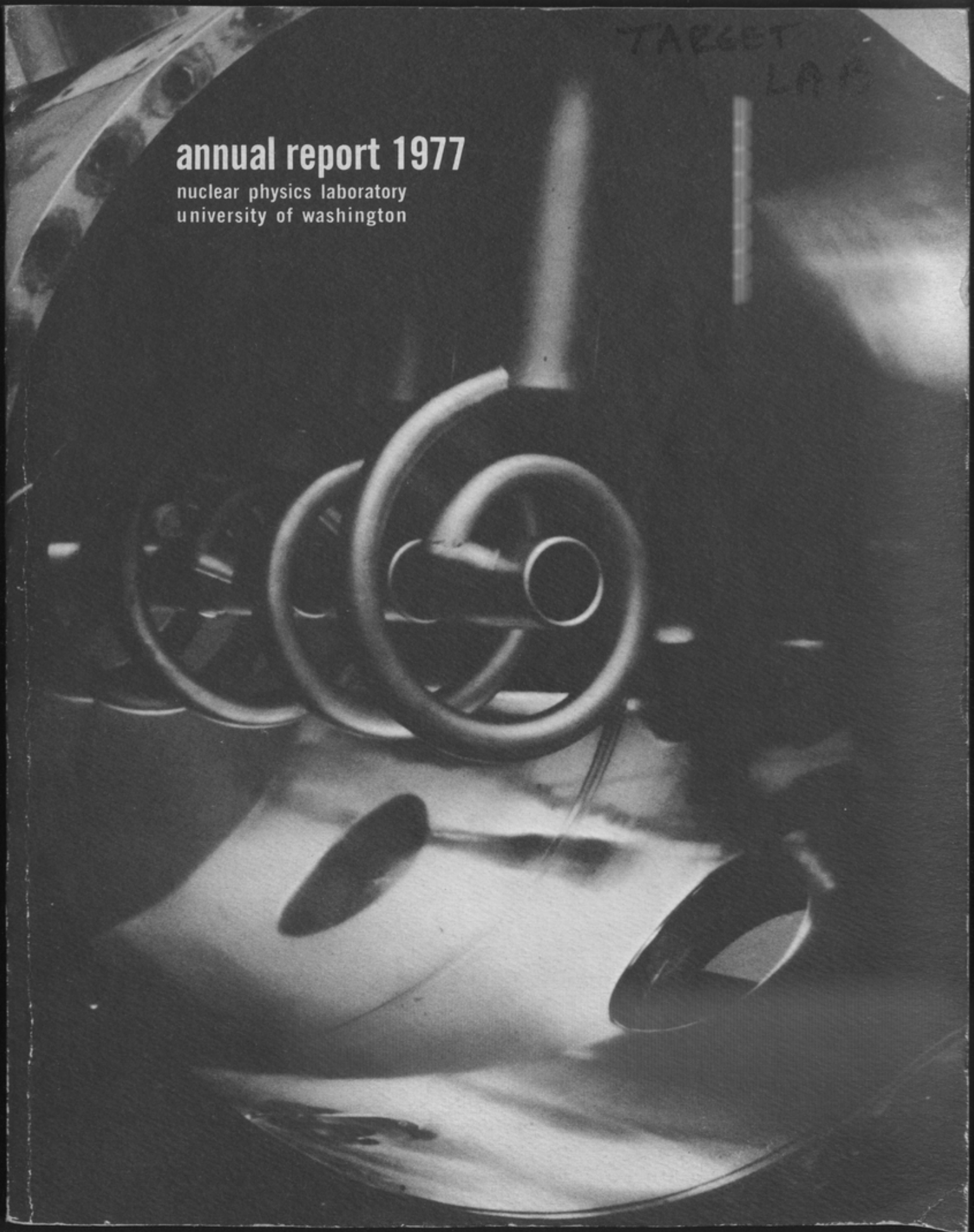

annual report 1977

nuclear physics laboratory
university of washington

Shirley Kellenberger

ANNUAL REPORT

Nuclear Physics Laboratory
University of Washington
June, 1977

Supported in part by the U. S. Energy Research and Development Agency under contract EY-77-C-06-1388 Program A.

INTRODUCTION

This Annual Report describes activities at our Laboratory for the period from Spring 1976 to Spring 1977.

The Laboratory continues to pursue an active program in many areas of nuclear science. There has been continued emphasis on the studies of fundamental symmetries in nuclei and on radiative capture. Another field of major interest is heavy ion reactions. These reactions are being studied using both beams from our own Van de Graaff and from accelerators at other laboratories such as the SuperHILAC. We also have an on-going program in medium-energy physics utilizing the LAMPF facilities. The continuing upgrading of our polarized ion source has facilitated a large number of reaction and structure experiments. We continue investigations in astrophysics and atomic physics.

In last year's report we discussed in some detail a preliminary design for a postaccelerator based on spiral resonator cavities. We have completed this stage of design and submitted a proposal for construction of such a device. We are also continuing a modest prototype cavity development project.

We close this introduction with the standard reminder that the articles in this report describe work in progress and are not to be regarded as publications nor quoted without permission of the investigators. The names of the investigators on each article have been listed alphabetically but where appropriate the name of the person primarily responsible for the report has been underlined.

As always, we welcome applications from outsiders for the use of our facilities. As a handy reference for potential users we list in the table on the following page the vital statistics of our accelerators. For further information please write or telephone Dr. W. G. Weitkamp, Technical Director, Nuclear Physics Laboratory, University of Washington, Seattle, WA 98195; (206) 543-4080.

THREE STAGE TANDEM VAN DE GRAAFF ACCELERATOR

(A High Voltage Engineering Corp. Model FN)

Completed: 1967

Funding: Purchased with NSF funds; maintained by ERDA funds and some funds from the State of Washington.

Beams currently available: (See also W.G. Weitkamp and F.H. Schmidt "The University of Washington Three Stage Van de Graaff Accelerator" Nucl. Instrum. Methods *122*, 65 (1974).

Ion	Typ.Current 2 stage(μA)	Max.Practical Energy 2 Stage (MeV)	Typ.Current 3 stage(μA)	Max.Practical Energy 3 Stage (MeV)
p,d	15	18	10	25
polarized p,d	0.1	18	--	--
^{3,4}He	3	27	--	--
^{6,7}Li	0.5	36	--	--
C	2	63	1	70
N	2	72	1	79
O	10	81	3	88
Si	0.2	90	--	--
Cl	0.2	117	0.2	124
Ni	0.5	117		
Br	0.1	125		
Ag	0.01	125		

CYCLOTRON

(A 60-inch fixed energy machine)

Completed: 1952

Funding: Constructed primarily with State funds and subsequently supported by AEC funds. Now sustained by funds from outside users.

Beams currently available:

Ion	Typical Current (μA)	Maximum Practical Energy (MeV)
p	100	11
d	150	22
^{4}He	30	42

TABLE OF CONTENTS

1. NUCLEAR ASTROPHYSICS AND COSMOLOGY

1.1 Cross Sections Relevant to Gamma-Ray Astronomy

D. Bodansky, D. Chiang, and P. Dyer

Measurements of gamma-ray production cross sections to complement astrophysical observations of nuclear gamma-ray lines are continuing. Indications of gamma-ray lines have been observed from astrophysical sites such as solar flares, the galactic center, and the radiogalaxy Centaurus A. [1,2,3] At such sites, energetic particles collide with nuclei in the ambient medium to yield nuclear gamma rays via reactions such as $^{12}C(p,p')^{12}C(4.44\ MeV)$ and $^{16}O(6.13\ MeV)$ and $^{16}O(p,p')^{16}O(6.13\ MeV)$. Observation of these gamma rays with spectrometers mounted in balloons and satellites makes it possible in principle to obtain information on the energy spectrum of the interacting particles, the relative abundances of nuclei in the ambient medium, and the directions of the projectiles. These investigations require accurate knowledge of nuclear cross sections and of gamma-ray lineshapes.

We have measured total cross sections for production of gamma rays by protons of 2 to 24 MeV, incident of ^{14}N, ^{20}Ne, ^{24}Mg, ^{28}Si, and ^{56}Fe. Survey

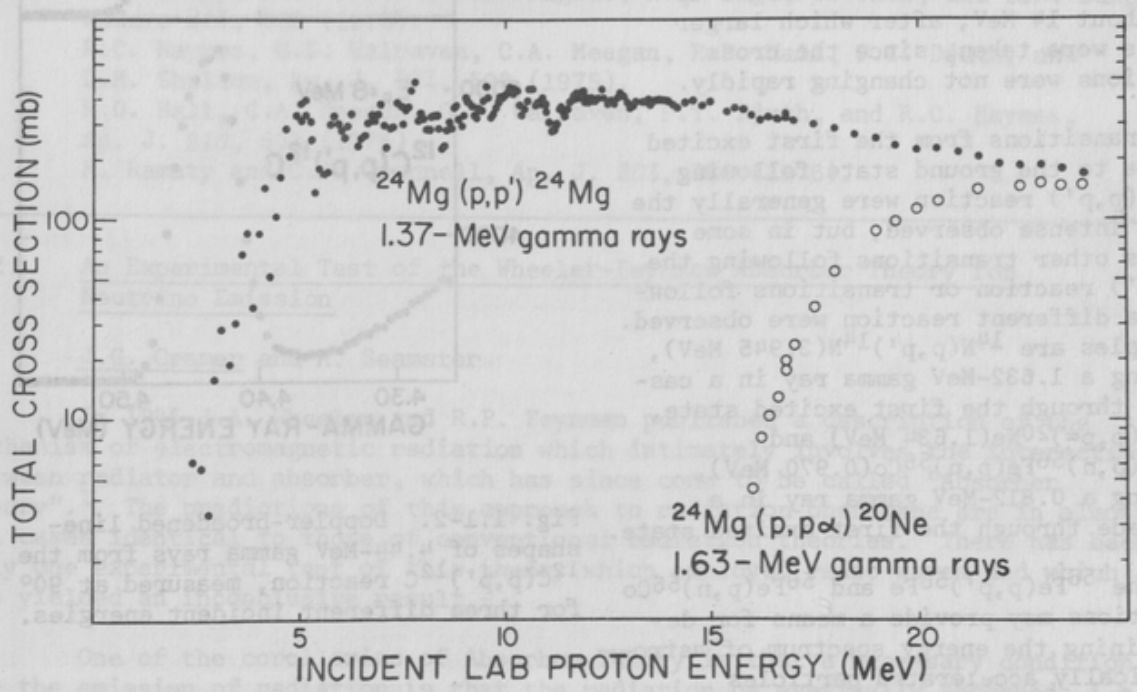

Fig. 1.1-1. Cross sections for production of 1.37-MeV gamma rays from the $^{24}Mg(p,p')^{24}Mg$ reaction and 1.63-MeV gamma rays from the $^{24}Mg(p,p\alpha)^{20}Ne$ reaction.

measurements have been made for ^{12}C and ^{16}O targets. These nuclei are the most abundant of the heavier isotopes in the universe. Two large Ge(Li) detectors were placed on a new angular distribution table 20 cm from the target at 30.5° and 109.9 from the beam axis, where the fourth order Legendre polynomial is zero. This geometry allows deterioration of the total cross section from measurements at two angles, as long as the gamma ray multipolarity order is 2 or less. The ^{24}Mg and ^{56}Fe targets were elemental and isotopic, the ^{28}Si target was elemental and natural, and the ^{14}N and ^{20}Ne targets were composed of natural gases enclosed in cells with nickel entrance and exit windows. Target thicknesses were in the range of 0.5 to 3 mg/cm^2. Energies were incremented in steps equal to the size of the energy loss in the target up to about 14 MeV, after which larger steps were taken, since the cross sections were not changing rapidly.

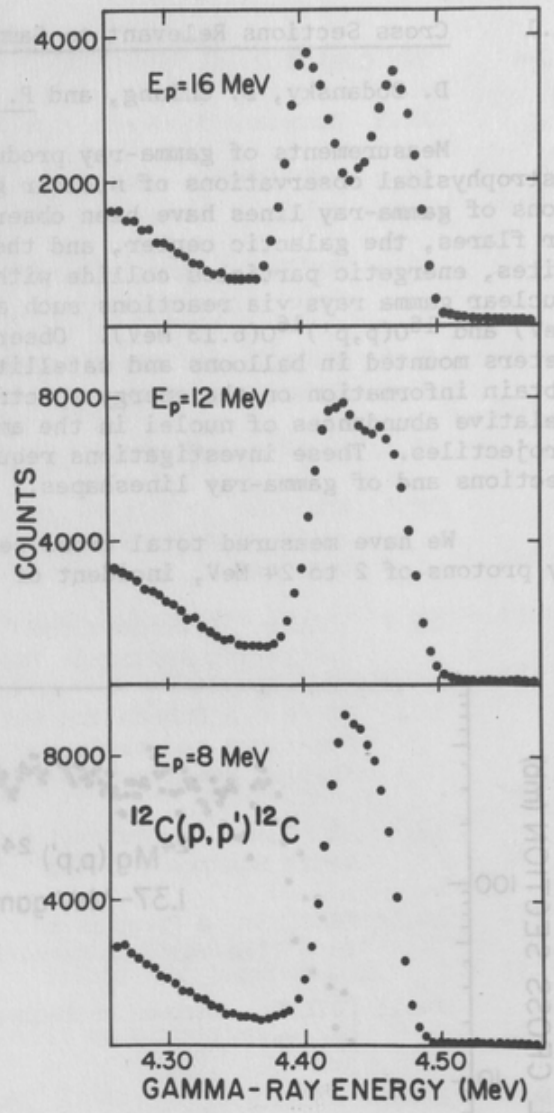

Fig. 1.1-2. Doppler-broadened lineshapes of 4.44-MeV gamma rays from the $^{12}C(p,p')^{12}C$ reaction, measured at 90° for three different incident energies.

Transitions from the first excited state to the ground state following the (p,p') reaction were generally the most intense observed, but in some cases other transitions following the (p,p') reaction or transitions following a different reaction were observed. Examples are $^{14}N(p,p')^{14}N(3.945\ MeV)$, giving a 1.632-MeV gamma ray in a cascade through the first excited state, $^{24}Mg(p,p\alpha)^{20}Ne(1.634\ MeV)$ and $^{56}Fe(p,n)^{56}Fe(p,n)^{56}Co(0.970\ MeV)$, giving a 0.812-MeV gamma ray in a cascade through the first excited state.

The $^{56}Fe(p,p')^{56}Fe$ and $^{56}Fe(p,n)^{56}Co$ reactions may provide a means for determining the energy spectrum of astrophysically accelerated particles independent of the absolute numbers of these particles. The astrophysically observed ratio of the number of 0.812-MeV gamma rays from (p,n) will depend on the shape of the proton energy spectrum. If an exponentially falling spectrum is assumed, $N(E)dE \propto E^{-s}dE$, then a 30% change in the exponent s would give about a 10% change in the ratio (near s=3).

The gamma ray line at 1.63 MeV, which has perhaps been observed in Centaurus A, will be a difficult line to interpret, since there are at least three different sources of gamma rays of this energy. The energies of the second excited to first excited state transition in ^{14}N and the first excited to ground state transition in ^{20}Ne are the same to within 2 keV. In addition, the ^{20}Ne state is populated above 15 MeV by the $^{24}Mg(p,p\alpha)^{20}Ne$ reaction as well as by the $^{20}Ne(p,p')^{20}Ne$ reaction. The $^{24}Mg(p,p')^{24}Mg$ and $^{24}Mg(p,\alpha)^{20}Ne$ excitation functions for production of 1.37 and 1.63-MeV gamma rays, respectively, are illustrated in Fig. 1.1-1. The cross section scale has not yet been determined better than 25%.

Directions of accelerated particles in astrophysical environments may be determined through Doppler shift measurements if high resolution Ge(Li) detectors are used in space.[4] We have begun measurements of Doppler-broadened lineshapes for the $^{12}C(p,p')^{12}C(4.44$ MeV) reaction as a function of proton energy and gamma-ray angle. Gamma-ray spectra at 90° for three proton bombarding energies are shown in Fig. 1.1-2. With increasing energy, there is a progression from a bell-shaped peak to a flat-topped peak, to a double peak, arising from the increasing Doppler broadening and the non-uniform population of magnetic substates that results from low spin-slip probabilities.

---

1. E.L. Chupp, D.J. Forest, P.R. Higbie, A.N. Suri, C. Tsai, and P.P. Dunphy, Nature *241*, 333 (1973).
2. R.C. Haymes, G.D. Walraven, C.A. Meegan, R.D. Hall, F.T. Djuth, and D.H. Shelton, Ap. J. *201*, 593 (1975).
3. R.D. Hall, C.A. Meegan, G.D. Walraven, F.T. Djuth, and R.C. Haymes, Ap. J. *210*, 631 (1976).
4. R. Ramaty and C.J. Crannell, Ap. J. *203*, 766 (1976).

1.2 An Experimental Test of the Wheeler-Feynman Absorber Theory for Neutrino Emission

J.G. Cramer and A. Seamster

In 1945 J.A. Wheeler and R.P. Feynman published a description of the mechanism of electromagnetic radiation which intimately involves the interaction between radiator and absorber, which has since come to be called "Absorber Theory".[1] The predictions of this approach to radiation phenomena are in almost all cases identical to those of conventional radiation theories. There has been only one experimental test of this theory which employed radio waves and which has yielded an inconclusive result.[2]

One of the corollaries of Absorber Theory is that a necessary condition for the emission of radiation is that the radiation be eventually absorbed, i.e., that there is a one-to-one correspondence between emission and absorption. If we apply this principle exclusively to electromagnetic radiation it is essentially impossible to test experimentally, since the probability of eventual absorption of any electromagnetic radiation emitted in any direction is essentially 1.0. On the other hand, we may adopt a more general view of the emission-absorption

correspondence principle: that it is not a statement about the electromagnetic interaction but about any process of radiation (perhaps even the emission of leptons and baryons.) If we consider possible tests of this generalized radiation correspondence principle, we should seek a kind of radiation which is (a) very easy to produce and (b) very weakly absorbed. Clearly, the outstanding example of such a radiation is the neutrino, which is readily produced by radioactive sources but has an extremely small absorption probability. We have thus designed an experiment to test the emitter-absorber correspondence principle as it may apply to neutrino emission.

Despite the relative ease with which neutrino emission can be produced with a k-capture or beta-decay radioactive source, it is relatively difficult to determine the direction in which the neutrino was emitted. Basically, there are two methods for doing this: (1) detect the direction of nuclear recoil following neutrino emission and (2) employ the strong electron neutrino angular correlation which is present for certain types of beta decay processes and detect the direction of emission of the beta particle. Although method (1) above gives the best angular determination of the neutrino emission angle, the recoil energy of the recoiling nucleus is typically only a few eV, making measurements very difficult. Therefore, we have elected to use method (2), observing the direction of beta emission and inferring the neutrino emission direction from this.

For a pure Fermi beta transition, the beta-neutrino angular correlation is given by:

$$P(\theta_{e\nu}) = [1 + \beta \mathrm{Cos}(\theta_{e\nu})] \text{ with } \beta = v_e/c \qquad (1)$$

If there is some anisotropy in the probability of neutrino emission δ_ν arising from a deficiency of absorption in some direction, the folding of the neutrino spatial anisotropy into a spatial anisotropy for the beta particles, the beta anisotropy will be $\delta_\nu\beta/3$. Thus the price paid for using the beta particles to infer the direction of neutrino direction is a factor of 3 in sensitivity. For a Gamow-Teller transition the correlation factor is similar to (1) except that the cosine term is negative and 1/3 as big, so that the beta anisotropy factor is $-\delta_\nu\beta/9$. We plan to look for spatial anisotropies in the emission of betas from both β^+ and β^- sources with pure Fermi and Gamow-Teller transitions. The sources to be used are ^{66}Ga(9.4 hr) Fermi β^+, ^{156}Eu(15.2 d) Fermi β^-, ^{68}Ge(275 d) Gamow-Teller β^+, and ^{100}Ru(367 d) Gamow-Teller β^-. The last of these can be ordered from ORNL while the other three must be produced by cyclotron bombardments. Preliminary cyclotron runs for source production indicate that all of these are quite feasible, but the Eu and Ge sources will probably require radiochemical separation after production.

Fig. 1.2-1 shows a photograph of the anisotropy counters mounted on a "polar mount" stand. The latter has been assembled by combining parts from an old television camera dolly and a surplus divider head. The counters themselves are NE-102 plastic scintillators with re-entrant backscatter wells mounted on RCA 8575 photomultiplier tubes. The beta decay source is mounted between the scintillators and is collimated so that the betas illuminate only the central region of the crystals. This apparatus is just being assembled.

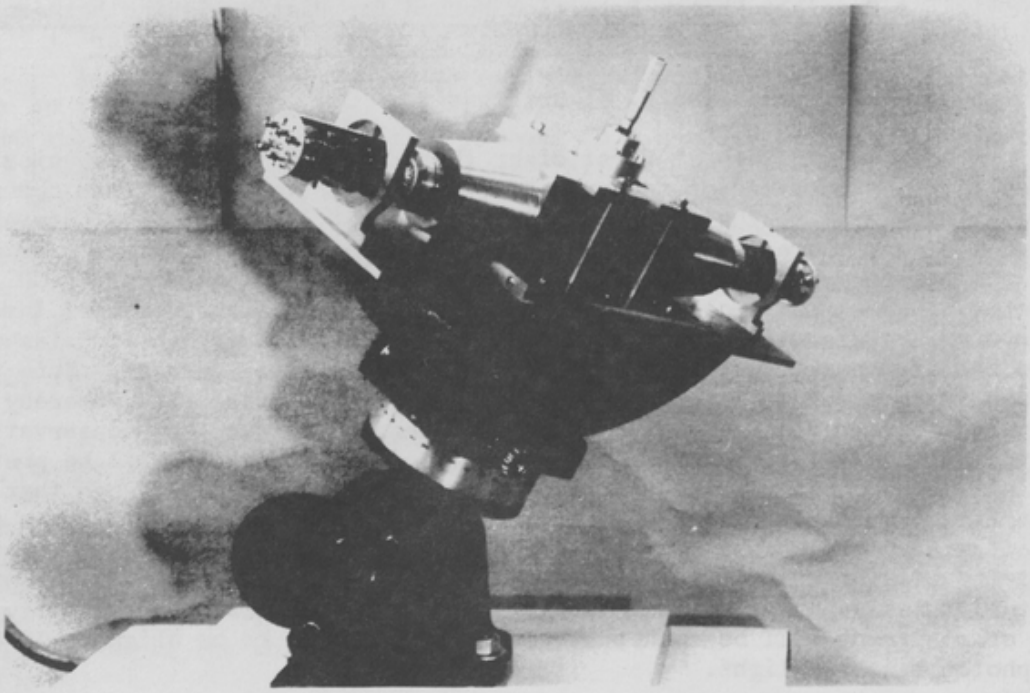

Fig. 1.2-1. Photograph of neutrino asymmetry apparatus, consisting of a pair of shielded scintillation counters mounted on a support with three variable angles.

We will operate it by establishing some fixed polar angle with respect to celestial north and allowing the symmetry axis of the counter to sweep out some conical locus as the Earth rotates. We will accumulate pairs of beta spectra at half hour intervals over a period of several days or weeks, changing sources, and then analyse these data for siderial correlations in the counting rate asymmetries between the two counters. For the present we will use only one pair of counters, but may later accumulate data simultaneously on a Fermi and Gamow-Teller source. We anticipate a sensitivity to spatial anisotropies in neutrino emission on the order of 10^{-5} or better. This should be sufficient to test simple cosmological models which account for neutrino emission-absorption and predict effects of 10^{-4} or larger. In the (likely) event that no anisotropies are observed to the sensitivity of the apparatus, it will be redesigned for an improved sensitivity in the 10^{-6} to 10^{-8} region, which is probably the best one can achieve with the present technique.

---

1. J.A. Wheeler and R.P. Feynman, Rev. Mod. Physics *17*, 157 (1945); Rev. Mod. Physics *21*, 425 (1949); also Phys. Rev. *59*, 683 (1941).

2. R.B. Partridge, Nature *244*, 263 (1973).

1.3 A Possible Photon-Detection Method for Distinguishing between Stars and Galaxies Composed of Matter and Antimatter

J. G. Cramer and W. J. Braithwaite*

It would seem at first sight that the symmetry of the physical processes in stars composed of matter and of antimatter would make them observationally identical so that no way could be found of distinguishing between them. However, there is one exception to this general symmetry which arises from the non-conservation of parity in the weak interactions and from CPT symmetry.[1] The thermonuclear processes which occur in stars, whether involving the hydrogen cycle, the carbon cycle, or nucleosynthesis of heavier elements up to the iron peak, systematically convert protons into neutrons. This conversion takes place at least partly through the weak interaction, thereby producing positrons and neutrinos. As a consequence of the non-conservation of parity, parity is violated maximally and all of the positrons will be preferentially in a "right" helicity state of polarization strength v/c such that their spins are aligned along their line of flight.[1] When these positrons are slowed in matter they are very likely to produce bremsstrahlung. The helicity of the positrons will be transferred to the bremsstrahlung, making them preferentially right circularly polarized.[2] In other words, the bremsstrahlung helicity like that of positrons will be such that the spin will tend to be aligned along the photon line of flight.

Another energy loss mechanism for the polarized positrons is annihilation in flight in which the energetic positron strikes an electron at rest, producing two photons, one along the line of flight of the positron and one in the opposite direction. This process is not unlikely since there are many "target" electrons available in a stellar plasma. The forward-going annihilation photon, which carries most of the energy, will preferentially have the same helicity as the positron.[3] Thus, both bremsstrahlung and annihilation in flight will give rise to energetic right-circularly polarized gamma rays.

If we consider antimatter stars, exactly the same processes will take place except that the burning processes convert antiprotons into antineutrons, producing antipositrons, i.e., electrons. As a consequence of CP symmetry these electrons will have their spins aligned <u>against</u> their line of flight and the bremsstrahlung and forward in-flight annihilation radiation produced will be <u>left</u> circularly polarized.[1] Thus the secondary energetic photons produced by thermonuclear processes in matter and antimatter stars will tend to be polarized with opposite helicities. Hence, a non-symmetry exists between matter and antimatter which, in principle, allows one to distinguish between the two without the necessity of annihilation between them.

One explanation of the occurrance of novae is that they may be produced in binary stars having one member which is a white dwarf. Hydrogen-rich material is transferred from the other member of the binary system to the white dwarf until its surface suddenly ignites in a thermonuclear explosion, producing the nova. In this scenario it is clear that a sizable quantity of positrons, and hence circularly polarized energetic photons, should be produced

at or near the stellar surface where these photons could readily escape without much degradation or depolarization.

Another possibility for direct observation of the matter/antimatter helicity is a type II supernova. It is believed that this type of stellar explosion takes place when the fusion process in a massive star has terminated with the production of a large quantity of ^{56}Ni. This decays by electron capture to ^{56}Fe.[4] This description ascribes a large fraction of the energy emitted after the supernova explosion to this decay sequence. Therefore, the probability of directly observing the polarized radiation produced by the positrons in the ^{56}Co decay in supernovae should be enhanced. As a benchmark for the difficulty of these measurements, however, it should be pointed out that even the direct gamma ray transitions accompanying the ^{56}Ni and ^{56}Co decays in supernovae have not yet been observed.[4]

The next step in our work on this problem will be a more detailed look at the problems of expected helicities and intensities and of polarimeter design, with specific attention to the detection of the helicity of x-rays and gamma rays in the energy range of interest. In particular, we will study the feasibility of constructing a space-mounted polarimeter array which would be able to make the determination of the helicity of the radiation from stars and to answer the question of whether there are antimatter stars and galaxies in our neighborhood of the universe.

---

*Permanent address: Department of Physics, University of Texas at Austin, Austin, Texas 78712

1. C.S. Wu and S.A. Moszkowski, Beta Decay (John Wiley & Sons, 1966), pp. 149 ff.

2. M. Goldhaber, L. Grodzins, and A.W. Sunyar, Phys. Rev. 106, 826 (1957); C. Fronsdal and H. Uberall, Phys. Rev. 111, 580 (1958).

3. L.A. Page, Phys. Rev. 106, 394 (1957); [Note: This paper uses a polarization convention which is opposite Basel convention used in the present work.]

4. D.D. Clayton, Proc. of Conf. on Explosive Nucleosynthesis, ed. by D.N. Schramm and W.D. Arnett (University of Texas Press, 1973).

---

2. FUNDAMENTAL SYMMETRIES IN NUCLEI

2.1 Parity Mixing in ^{18}F*

E.G. Adelberger, C.A. Barnes†, J. Davidson†, M.L. Lowry†, R.E. Marrs†, F.B. Morinigo††, and H.E. Swanson

The parity mixing of the 1081 keV 0+ T = 0 and the 1042 keV 0^+ T = 1 levels of ^{18}F provides one of the very few opportunities to measure directly the $\Delta I = 1$ parity violating N-N force. We are, in collaboration with physicists from the California Institute of Technology and California State University at Los Angeles (CSULA), trying to measure the parity violating circular polarization of the 1081 keV photons. The experiment is being performed at the high current KN4000 accelerator at CSULA. Since the motivation for this experiment and many of the experimental details are given in previous annual reports,[1] we shall restrict this discussion to some of the changes which have evolved over the last year.

(1) An improved, precision digital period generator has been constructed in Seattle and used at CSULA for ~1 year. This unit is based on a crystal oscillator and supplies signals for the polarimeter magnet supply, the routing of the digitized Ge(Li) signals and a "gate off" pulse that stops data acquisition during the polarimeter switching transients.

(2) Improved circuitry has been developed in Seattle for the polarimeter magnet supply and used for ~1 year at CSULA. The new circuitry greatly reduces magnetization correlated peak shifts in the Ge(Li) spectra. Such effects, which can lead to spurious asymmetries, were present in our first version of the electronics and were traced to ground loops involving the polarimeter supply.

(3) A new data acquisition facility for this experiment has been designed and constructed in Seattle and has been working successfully at CSULA for over half a year. The system is based on two independent, fast (100MHz ADC, ^ 2.5 μsec cycle time) ND2400 pulse height analysers and a PERTEC magnetic tape unit. The analysers are under the control of an automatic sequencer. In one complete cycle the sequencer starts the PHA's at the beginning of a polarimeter cycle, then upon receiving a pulse indicating a desired, elapsed time, stops the PHA's at the end of the next polarimeter cycle, increments a mag tape tagword by one, writes the contents of the 2 analysers three times on mag tape, and finally clears the analyser memories. All periods are switch selectable. This system was developed to replace a commercial ND4420 system where 2 ADC's are serviced by a single computer after tests with an intense ^{60}Co source at the target position revealed that the ND4420 system apparently injected subtle nonstatistical errors due to the display interrupts, and also introduced correlations between the dead times in the two ADC's. No such difficulties are observed using the new system which is functionally equivalent to the extensively tested system used at Seattle for the ^{19}F parity mixing experiment.

(4) In an attempt to improve the lifetime of the 7500Å thick Ni entrance foils NiOH was added to the distilled water used as the target. We observed that the (γ-ray counts)/(microcoulomb of integrated charge) increases as a foil is bombarded. This suggests that the foil becomes thinner due to erosion (which raises the effective ^3He energy and thus the counting rate) before finally rupturing.

On the basis of limited statistics the addition of NiOH seems to improve the foil lifetime.

(5) A redundant vacuum safety system consisting of a second fast-acting valve and trigger circuitry has been added to prevent foil ruptures from tripping the accelerator vacuum interlocks.

Our present statistical errors on the circular polarization of the 1081 keV γ-ray are approximately half the 0.6% value predicted using a Weinberg-Salam model of the weak interaction.[2] The data for this γ-ray along with the 937 keV E2 transition from the 937 keV state (which is expected to have a negligible circular polarization) are distributed statistically. However the data on the 1042 keV M1 γ-ray from the decay of the 0^+, T = 1 state show nonstatistical fluctuations which are not yet understood.

---

* Supported in part by National Science Foundation (California Institute of Technology, California State University of California and the State of California.

† California Institute of Technology, Pasadena, California.
†† California State University at Los Angeles, Los Angeles, California

1. E.G. Adelberger, C.A. Barnes, M.L. Lowry, R.E. Marrs, F.B. Morinigo, H.E. Swanson and H. Winkler, Nuclear Physics Laboratory Annual Report, University of Washington, (1976) p. 54.
2. M. Gari, J.B. McGrory and J. Offerman, Phys. Lett. *55B*, 277 (1975).

2.2 Parity Mixing in ^{19}F

E.G. Adelberger, Z. Iqbal, H.E. Swanson, T.A. Trainor and R. VonLintig

We are preparing an improved experiment to measure the parity mixing between the ground (1/2+) and 110 keV excited (1/2-) states of ^{19}F. Our previous measurement[1] did not have small enough errors to reliably distinguish between theories where the weak N-N force is due only to charged currents and those which include parity violating neutral currents as well. The new version of the experiment differs in the following ways from the first:

(1) the polarized ion source has been rebuilt to employ a "spin filter" and the Los Alamos-style fast-flip scheme.[2] This gives us 3 advantages:

a) the proton polarization is increased from 42% to 77% which is equivalent to a fourfold increase in counting statistics.

b) spin correlated modulations of the beam emittance and intensity are greatly reduced. This diminishes the most important sources of systematic errors.

c) the spin can be flipped at much higher frequencies (reversal delays $\lesssim$ 10 μsec) which permits us to run at frequencies well above the noisy region of the accelerator noise spectrum.

this part of the project has been completed, tested and works extremely well (see Sec. 12.3 of this report).

(2) A new 4 counter polarization monitor has been constructed.[3] The polarimeter contains a thin target consisting of ~5 $\mu g/cm^2$ of Au evaporated onto ~20 $\mu g/cm^2$ of C. Protons scattered at $\theta_L = 52°$ are detected in 4 counters spread equally around the aximuth. Each counter feeds two SCA's set on the scattering peaks from Au and C. The outputs of these SCA's are then routed into 2 sets of scalers according to the spin state of the beam. The 16 counting rates are continuously monitored by the on-line computer which determines the magnitude and direction of the proton spin in each spin state, the beam charge collected in each spin state, and the statistical errors in the above quantities. Apparatus has been constructed to allow the computer to rotate the Wein precessor so as to keep the proton spin "locked into" the polarimeter axis. This apparatus has been tested and works successfully. So far a digital feedback scheme on the proton spin direction has not proved necessary because the spin direction from the improved ion source appears to be stable enough.

(3) A new mechanical system for alignment of the gas cell, proton polarimeter, and the Ge(Li) counters has been designed and constructed. Refinements have been made to our technique of Ge(Li) alignment using radioactive sources. These changes greatly facilitate accurate alignment.

All the apparatus for our experiment has been constructed and we are ready to take data.

---

1. E.G. Adelberger, H.E. Swanson, M.D. Cooper, J.W. Tape and T.A. Trainor, Phys. Rev. Lett. *34*, 402 (1975).
2. "A Comparison of Sona and Spin-Filter Polarization Schemes for a Lamb-Shift Polarized Ion Source", T.A. Trainor, W.B. Ingalls, H.E. Swanson, and E.G. Adelberger, Proc. of the 1977 Particle Accelerator Conference, Chicago (1977), to be published in IEEE Transactions on Nuclear Science.
3. E.G. Adelberger and H.E. Swanson, Nuclear Physics Laboratory Annual Report, University of Washington, (1976), p. 36.

2.3 Lifetime of the 1042-keV State in ^{18}F

R.E. Marrs, E.G. Adelberger, A.B. McDonald and K.A. Snover

The lowest T = 1 state at 1042 keV in ^{18}F decays by a fast isovector M1 transition to the ground state. Its lifetime has previously been measured to be 4^{+3}_{-2} fs using the $^{18}O(p,n)^{18}F(1042)$ reaction and the Doppler shift attenuation method.[1] A more accurate measurement of this lifetime is important because of its role in a separate measurement of the parity-violating matrix element connecting the 1042- and 1081-keV states in ^{18}F.[2] In addition, the strength of the isovector M1 transition from the 1042-keV state may be compared with the analogous β decays of ^{18}Ne and ^{18}F. A comparison with shell-model predictions of the $^{18}F(1042)$ lifetime would also be interesting.

We are attempting to determine the $^{18}F(1042)$ lifetime from a coincidence study of the $^{16}O(^{3}He,p\gamma)^{18}F$ reaction at 5.0 MeV ^{3}He energy. Preliminary runs were done at the Kellogg Radiation Lab at the California Institute of Technology, and the main data run to date was done at the University of Washington. Protons were detected in an annular counter at ~170°, and Doppler-shifted rays were detected at 0° in a 15% Ge(Li) detector. The targets used were Ta_2O_5 (short slowing-down time) and ice (long slowing-down time). Although the ^{18}F recoil energy is ~10 times higher in the present measurement than in the previous $^{18}O(p,n)$ measurement, the 16-keV Doppler shift of the 1042-keV γray is attenuated by only 1% for the Ta_2O_5 target. The experiment is further complicated by the instability of our ice targets, which recrystalized during bombardment. This changes the effective target thickness, which in turn changes the ^{18}F recoil velocity. In our data analysis, we are attempting to correct for this effect by using the widths and centroids of groups in the proton spectra.

---

1. A.E. Blaugrund, D.H. Youngblood, G.C. Morrison, and R.E. Segel, Phys. Rev. *158*, 893 (1967).
2. See Sec. 2.1 of this report.

2.4 Isospin Forbidden Decays of T = 2 States in A = 4n Nuclei

E.G. Adelberger

Recent work on the isospin forbidden decays of T = 3/2 levels in A = 4n + 1 nuclei has revealed several striking and unexpected regularities.[1,2,3] These include a pronounced oscillation in the reduced widths for p_0 decay of the T_z =-1/2 isobars: the A = 4n + 1 nuclei with n odd have systematically larger decay widths than the nuclei with n even. (see Fig. 2.4-1) This periodicity is apparently not present in the p_1 decays, or in the n_0 decays of the T_z = +1/2 isobars. These phenomena have as yet not been explained. In order to explore what physics may be responsible for the regularities we have undertaken a systematic study of the isospin forbidden decays of the T = 2 states of the T_z = 0 nuclei. The program is based on resonance and β-decay studies performed in Seattle and coincidence measurements at the Princeton University Cyclotron. The Seattle based resonance studies are chosen to complement resonance experiments at Chalk River done by A.B. McDonald and collaborators. A summary of the known reduced width for p,d and α decays of T = 2 states is shown in Fig. 2.4-2. The following articles report on our studies of T = 2 in specific A = 4n nuclei.

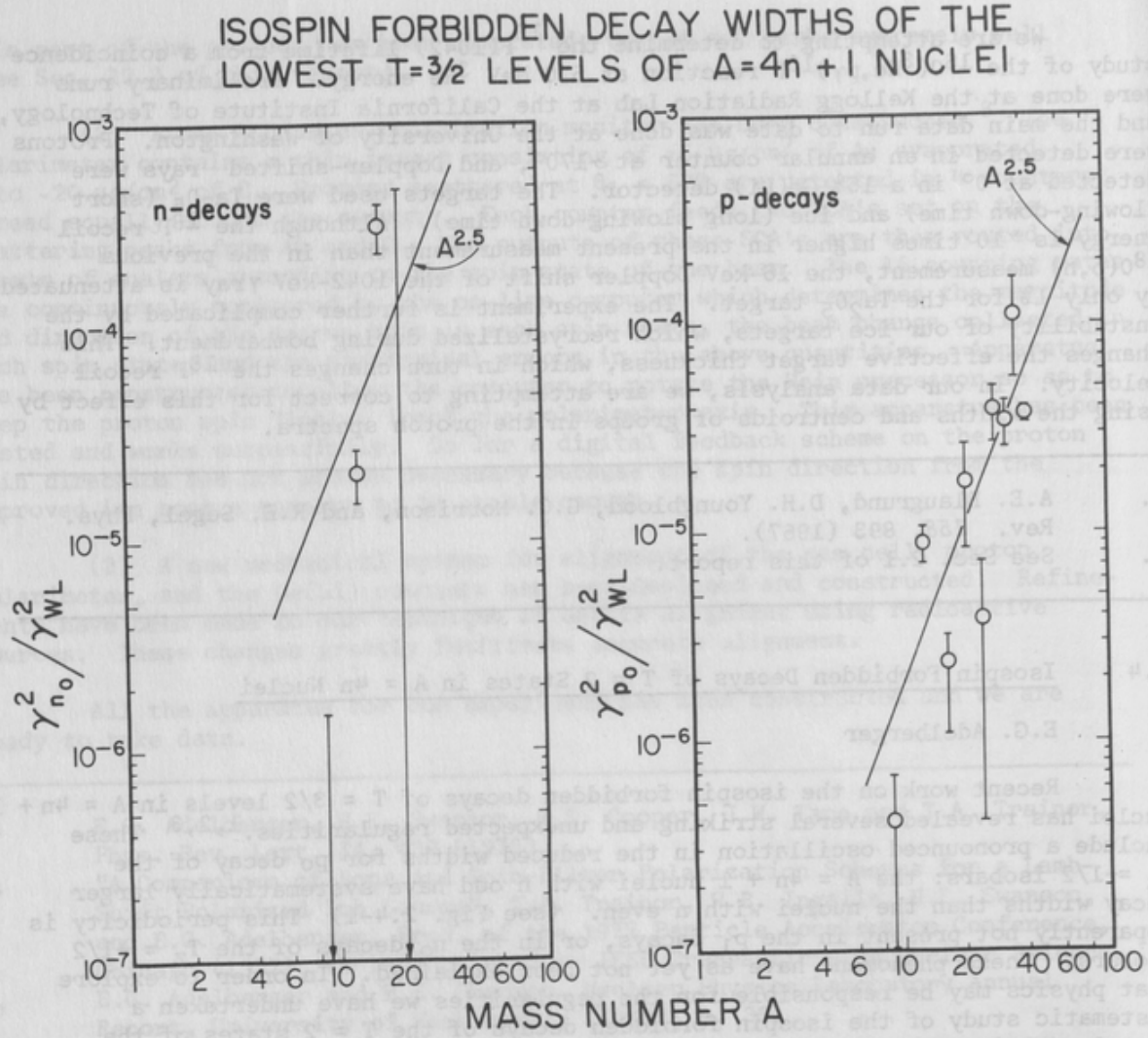

Fig. 2.4-1. Dimensionless reduced widths for isospin forbidden decays of the lowest T = 3/2 levels of the A = ^{4}n + 1 nuclei (taken from Ref. 2, more recent values for some of these widths can be found in Ref. 3).

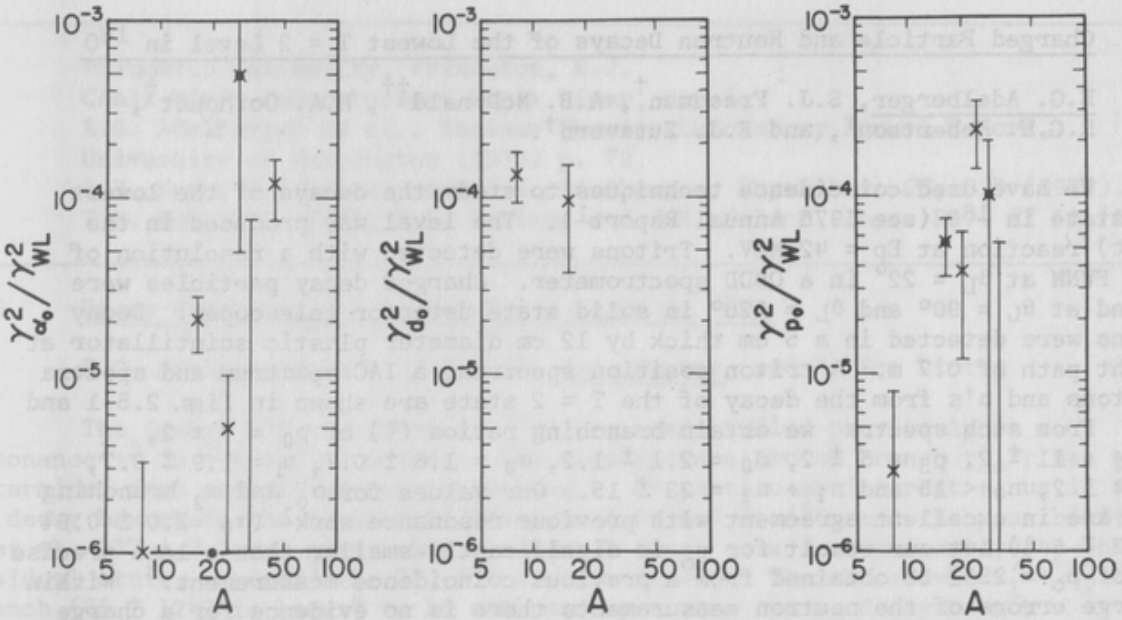

Fig. 2.4-2. Dimensionless reduced widths for isospin forbidden decays of the lowest T = 2 levels of the A = 4n nuclei.

---

1. T.A. Trainor, T.B. Clegg and W.J. Thompson, Phys. Rev. Lett. *33*, 229 (1974).
2. E.G. Adelberger, Proceedings Int. Conf. on Nucl. Structure and Spectroscopy, Amsterdam, 1974, ed. by H.P. Blok and A.G.L. Dieperink, Scholars Press, Amsterdam, 1974, p. 641.
3. P.G. Ikossi, W.J. Thompson, T.B. Clegg, W.W. Jacobs and E.J. Ludwig, Phys. Rev. Lett. *36*, 1357 (1976).

2.5 Charged Particle and Neutron Decays of the Lowest T = 2 Level in ^{16}O

E.G. Adelberger, S.J. Freedman[†], A.B. McDonald[††], M.A. Oothondt[†], R.G.H. Robertson[†], and F.J. Zutavern[†].

We have used coincidence techniques to study the decays of the lowest T = 2 state in ^{16}O (see 1976 Annual Report[1]). The level was produced in the $^{18}O(p,t)$ reaction at Ep = 42 MeV. Tritons were detected with a resolution of 25 keV FWNM at $\theta_L = 22^\circ$ in a QDDD spectrometer. Charged decay particles were detected at $\theta_L = 90^\circ$ and $\theta_L = 120^\circ$ in solid state detector telescopes. Decay neutrons were detected in a 5 cm thick by 12 cm diameter plastic scintillator at a flight path of 0.7 m. A triton position spectrum, a TAC spectrum and spectra of protons and α's from the decay of the T = 2 state are shown in Figs. 2.5-1 and 2.5-2. From such spectra we obtain branching ratios (%) of $p_0 = 7 \pm 2$, $p_1 + p_2 = 11 \pm 2$, $p_3 = 5 \pm 2$, $d_0 = 2.1 \pm 1.2$, $\alpha_0 = 1.6 \pm 0.7$, $\alpha_1 = 1.9 \pm 0.7$, $\alpha_2 = 14 \pm 2$, $n_0 < 15$ and $n_1 + n_2 = 23 \pm 15$. Our values for α_0 and α_2 branching ratios are in excellent agreement with previous resonance work[1] ($\alpha_0 = 2.0 \pm 0.6\%$ $\alpha_2 = 13 \pm 5$ %) but our result for p_0 is significantly smaller than a less precise value of $p_0 = 25 \pm 6\%$ obtained from a previous coincidence measurement.[3] Within the large errors of the neutron measurements there is no evidence for a charge asymmetry in the corresponding neutron and proton decays.

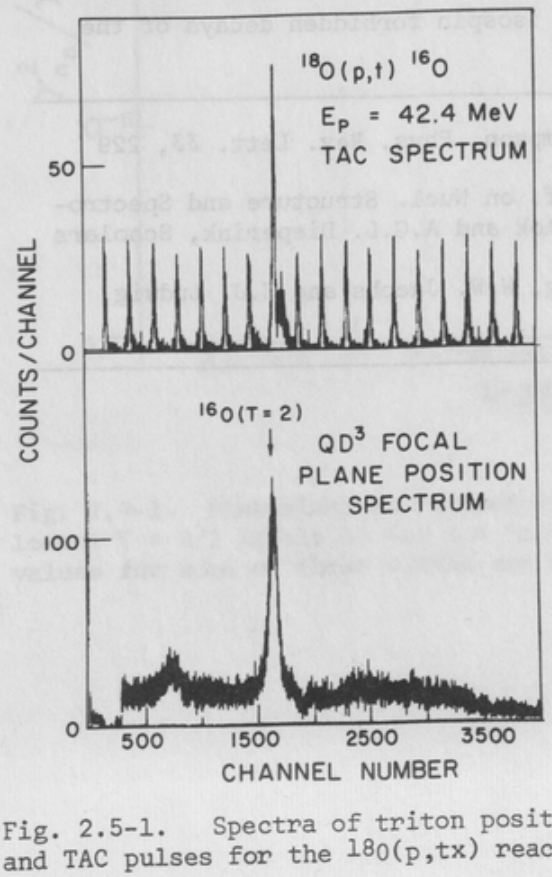

Fig. 2.5-1. Spectra of triton position and TAC pulses for the $^{18}O(p,tx)$ reaction.

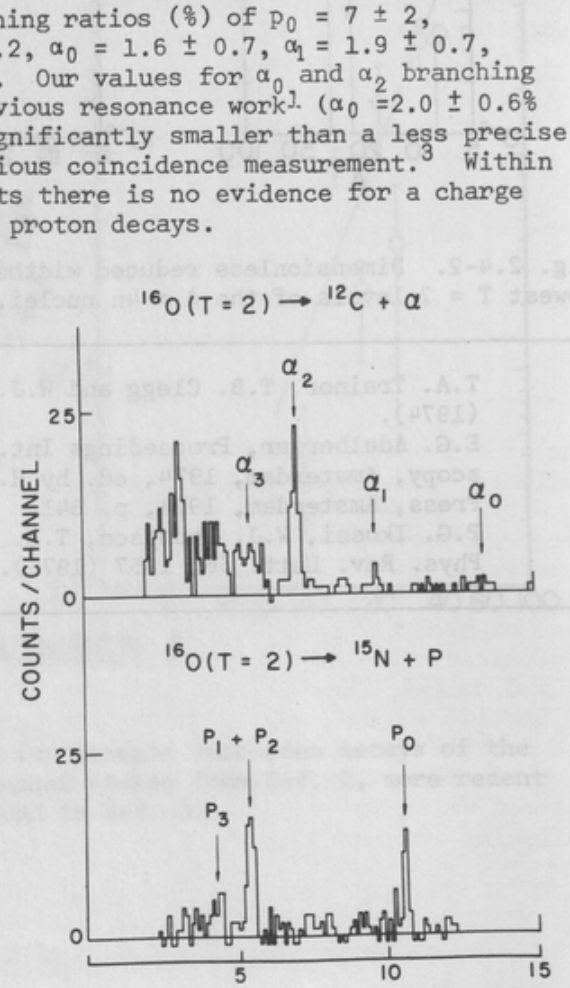

Fig. 2.5-2. Spectra of decay particles in coincidence with tritons populating the lowest T = 2 state of ^{16}O in the $^{18}O(p,t)$ reaction.

† Princeton University, Princeton, N.J.
†† Chalk River Laboratories, Chalk River, Canada.

1. E.G. Adelberger *et al.*, Nuclear Physics Laboratory Annual Report, University of Washington (1976) p. 72.
2. A.V. Nero, R.G. Pixley and E.G. Adelberger, Phys. Rev. *C6*, 679 (1972).
3. T.K. Koh, W.R. Falk, N.E. Davison and J.M. Nelson, Phys. Rev. *C7* 50 (1973).

2.6 Decay Widths of the Lowest T = 2 State in ^{20}Ne

E.G. Adelberger, A.B. McDonald, K.A. Snover, and R. Von Lintig

The lowest $0^+T = 2$ level in ^{20}Ne has been studied previously as a resonance[1,2] in ^{19}F + p reactions. The ground-state proton branch Γ_{p_0}/Γ has been determined from elastic proton scattering.[1] Of particular interest to us is the α_0 decay branch to the excited 0^+ level at 6.06 MeV in ^{16}O, and the possibility that the $0^+T = 2$ level might show a strong α decay to a (predominantly) 4p-4h residual state, as does[3] the 0^+, T = 2 state in ^{16}O. The unresolved $\alpha_1 + \alpha_2$ branch ($35 \pm 12\%$) is known[4] to be much stronger than the α_0 decay branch ($-6 \pm 5\%$). In principle, one should be able to extract reasonably unique values for the (p,α_0) and (p,α_1) resonance strengths (and hence obtain α decay widths) from resonance data, since the intrinsic spin sequence is simple for these reaction channels. Our data confirm the previous observation[2] that the $(p,\alpha_1 + \alpha_2)$ resonance anomaly is dominated at back angles by the α_2 yield. However, the α_1 branch may still be very important, since the nonresonant background (and hence the expected absolute size of the resonance anomaly for a given partial width) for α_1 is much smaller than for α_2. Data analysis is in progress.

1. R. Bloch, R.E. Pixley and P. Trual, Phys. Lett. *25B*, 2 (1967).
2. H.M. Kuan, D.W. Heikkinen, K.A. Snover, F. Riess and S.S. Hanna, Phys. Lett. *25B*, 217 (1967).
3. See Sec. 2.5 of this report.
4. R.L. McGrath, J. Cerny, J.C. Hardy, G. Goth and A. Arima, Phys. Rev. 184 (1970).

2.7 Width of the Lowest T = 2 State in ^{24}Mg

E.G. Adelberger, J.L. Osborne, K.A. Snover

From extrapolations of the known widths of the lowest T = 2 levels in ^{8}Be, ^{16}O and ^{20}Ne one expects the total width of the lowest T = 2 level in ^{24}Mg to be $\Gamma \sim 1$ keV. Previous experimental work[1] has established an upper limit of $\Gamma < 2$ keV. We have attempted a direct measurement of Γ by studying the level as a ^{23}Na(p,γ) resonance at $E_p = 3.906$ MeV. The width of the T = 2 state was inferred from the shape of thick-target yields. This method is practical only if the energy resolution function of the beam and target are well known and $\lesssim$ to the level width. To insure good beam energy resolution the full widths of the object and image slits of the 90° analyzing magnet were set to 0.76mm, the

insulating gas pressure in the tandem tank was lowered to 110 psi, a gas stripper operating at very low pressure was employed, and care was taken in the tuning of the beam optics and corona feedback stabilization. The 90° magnet was controlled by a feedback device on the NMR and the NMR frequency was continuously monitored by our on-line computer. Typical conditions were an injected beam of 15 μA and 0.5 μA on target (the small transmission was due to the very low stripper gas pressure). The beam energy resolution function was studied experimentally using a narrow $^{27}Al(p,\gamma)$ resonance at E_p = 3.671 MeV. Excitation functions of 10 MeV γ-rays observed from the bombardment of a 120 $\mu g/cm^2$ Al target are shown in Fig. 2.7-1. Note that the leading edge of resonance rises from 1/4 to 3/4 of the plateau value in only 380 ev. The smooth curves in Fig. 2.7-1 are yields calculated by taking account of the discontinuous nature of the proton energy loss mechanism. The overshoot on the leading edge is known as the "Lewis effect" and was discovered and explained many years ago in very beautiful work at Wisconsin (see Ref. 2). The calculated curves were computed following the methods of Ref. 2 using the Monte Carlo program RESONANCE YIELD[3] written by R.E. Marrs. The data is well fitted by a gaussian beam energy spread B = 550 ev and a resonance width Γ_{LAB} = 200 ev. It is interesting to note that the beam energy spread contains contributions not only from the beam resolution of the tandem but also from the thermal motion of the target atoms about their lattice sites. This latter process gives a gaussian contribution of 200 ev FWHM to the beam energy spread. (calculated according to Ref. 4) One should note that even though $\Gamma < B$ in this case, our data rules out larger values of Γ because they would cause a long "tail" on the low energy side of the resonance. In other words one is sensitive to small values of Γ because a Lorentzian "dies" much more slowly than a gaussian as one moves away from the resonance.

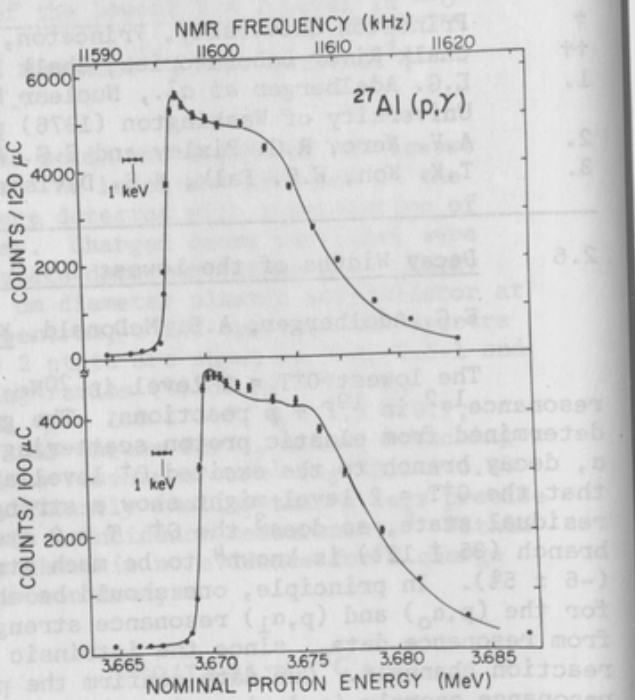

Fig. 2.7-1. Yield of 10 MeV rays from the 3.67 MeV $^{27}Al(p,\ )$ resonance. The smooth curve is calculated as described in the text.

Having measured and understood our resolution function we then proceeded to study the $^{23}Na(p,\gamma)$ resonance. Targets were prepared by evaporating metallic Na onto thick well cleaned W backings which were mounted directly onto a water cooled Cu block. Backings were made of W, and were selected because W has good thermal conductivity and does not alloy with Na. Targets were transferred under vaccuum from the evaporator to the target chamber. The target chamber contained a large LN_2 cooled plate in order to minimize target contamination. Resonance curves were run on six different targets. Excitation functions obtained with 3 of these

targets are shown in Fig. 2.7-2. The smooth curves were calculated as described above, and correspond to Γ_{cm} = 550 ev and B = 550 ev. We demonstrated that our results are not affected by a buildup of contaminants under bombardment by taking two passes over the resonance on the same target--in the first pass we increased the energy in small steps; in the second we decreased the energy. The good agreement of these two passes establishes that the targets did not deteriorate in the course of our measurements. Several of our earlier targets showed broader resonance rises.[5] Because we cannot be completely sure that our best Na targets did not contain "lumpy" contaminants which would give an additional broadening to our resolution function we quote our result as an upper limit

$$\Gamma \leq 550 \text{ ev}$$

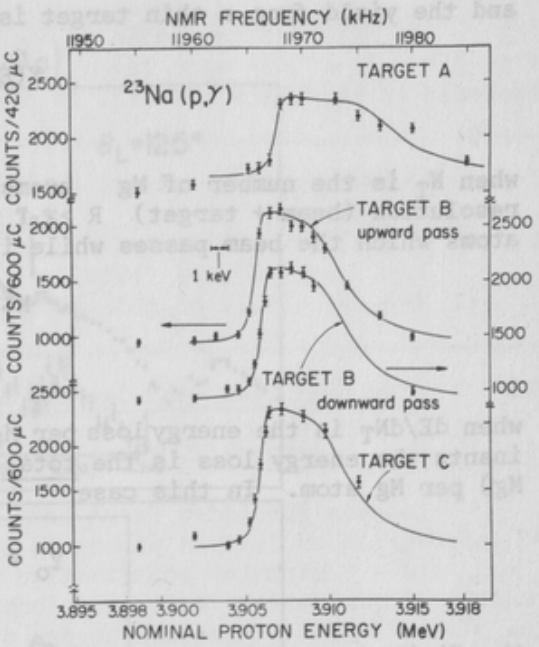

Fig. 2.7-2. Yield of 10 MeV rays from the E_p = 3.91 MeV ^{23}Na(p,γ) resonance corresponding to the lowest T = 2 state in ^{16}O. Data are shown from bombardment of those different targets. The smooth curves are calculated as described in the text.

1. F. Riess, W.J. O'Connell, D.W. Heikkinen, H.M. Kuan and S.S. Hanna, Phys. Rev. Lett. *19* 367 (1967).
2. D.G. Costello, J.G. Skofronick, A.L. Morsell, D.W. Palmer, and R.G. Herb, Nucl. Phys. *51*, 113 (1964) and references therein.
3. R.E. Marrs, E.G. Adelberger and K.A. Snover, submitted to Phys. Rev. C.
4. F. Hinterberger et al., Nucl. Phys. *A253*, 125 (1975).
5. J.L. Osborne and E.G. Adelberger, Bull. Am. Phys. Soc. *21*, 965 (1976).

2.8 Width of the Lowest T = 2 State in ^{28}Si

E.G. Adelberger, A.B. McDonald†, J.L. Osborne and K.A. Snover

Based on systematics of the known widths of other T = 2 levels, we expect the width of the T = 2 state in ^{28}Si will be too small to measure ($\Gamma \sim 0.1$ keV) by the methods used in ^{20}Ne and ^{24}Mg. Previous experimental work[1] has established an upper limit of $\Gamma \lesssim 2$ keV. Instead we chose to employ a method based on ^{24}Mg(α,α) scattering. The basic idea is easily understood by considering an isolated resonance. On resonance the cross section is

$$\sigma(E_r) \propto \frac{\Gamma \alpha^2}{\Gamma^2}$$

and the yield from a thin target is

$$Y(E_r) \propto \frac{\Gamma_\alpha^2}{\Gamma^2} N_T$$

when N_T is the number of Mg atoms in the target. Now if one has an energy resolution (beam + target) $R >> \Gamma$ the number N_T refers only to those target atoms which the beam passes while it has an energy within Γ of E_r. So

$$N_T^{eff} \propto \frac{\Gamma}{\frac{dE}{dN_T}}$$

when dE/dN_T is the energy loss per Mg atom. Note that if the target has contaminants the energy loss is the <u>total</u> energy loss (due to contaminants as well as Mg) per Mg atom. In this case

$$Y_o \propto \frac{\Gamma_\alpha^2}{\Gamma^2} \frac{dE}{dN_T}^{-1}$$

the finite energy resolution causes the observed width of the resonance W to be

$$W = N_T \frac{dE}{dN_T}$$

Note that the area under the resonance curve is

$$A = Y_o W \propto \frac{\Gamma_\alpha^2}{\Gamma} N_T$$

and that A does not depend on knowing dE/dN_T.

In our experiment we employed 5 counters. Excitation functions for $5.92 \leq E_L \leq 6.25$ MeV were taken with a pair of counters at $\theta_{LAB} = \pm 165°$, a pair at $\theta_{LAB} = \pm 145°$, and a single counter at $\theta_{LAB} = 125°$. Symmetric pairs of counters were employed to cancel the effects of any beam position and angle changes on the extracted cross sections. A target of 2.0 μg/cm^2 of enriched ^{24}Mg was evaporated on to 2.76 μg/cm of Bi which in turn was evaporated into thin carbon backings. Data in the vicinity of the T = 2 resonance was repeated with a similar target with a thickness of an 0.49 μg/cm of ^{24}Mg. The number of ^{24}Mg atoms N_T was determined from data at $E_L = 3.191$ and $E_L = 3.687$ MeV when the cross section was assumed to be Rutherford. Our excitation functions (obtained from the program VOYEUR[2]) are shown in Fig. 2.8-1. The T = 2 state is seen as a weak resonance in the midst of several much stronger (T allowed) resonances. It is fortunate that at $\theta_{LAB} = 165°$ a very deep valley occurs between these stronger resonances. This reduces our sensitivity to the background phase shifts. From the observed width of the T = 2 resonance bump it can be seen that our targets had large contaminants or were quite "lumpy". This demonstrates the importance of an analysis which does not depend on a knowledge of dE/dN_T.

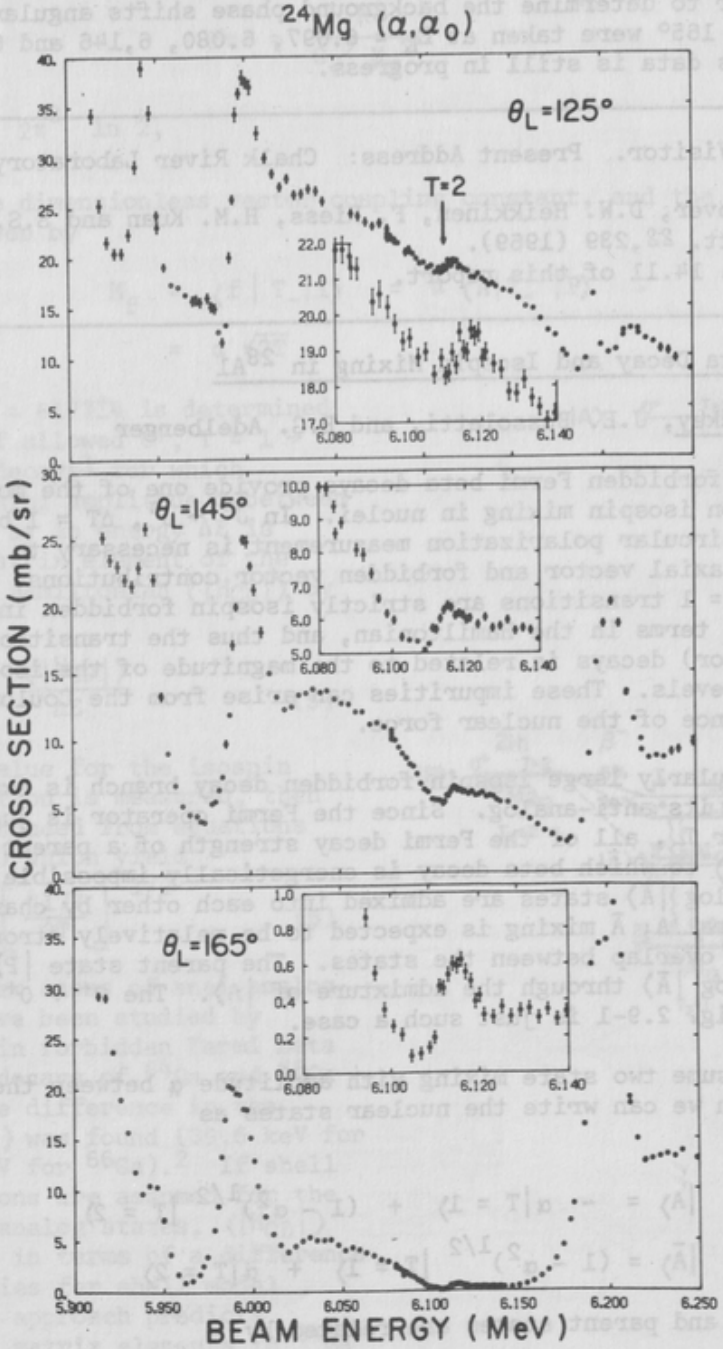

Fig. 2.8-1. Excitation function for elastic α scattering from a 2.0 μg/cm^2 ^{24}Mg target. The insets show a magnified view of the cross section in the vicinity of the resonance corresponding to the lowest T = 2 state of ^{28}Si.

In order to determine the background phase shifts angular distributions from $35° \leq \theta_L \leq 165°$ were taken at E_L = 6.097, 6.080, 6,146 and 6.129 MeV. Analysis of this data is still in progress.

---

† Summer Visitor. Present Address: Chalk River Laboratory, Chalk River, Canada.

1. K.A. Snover, D.W. Heikkinen, F. Riess, H.M. Kuan and S.S. Hanna, Phys. Rev. Lett. 22,239 (1969).

2. See Sec. 14.11 of this report.

2.9 ^{28}Mg Beta Decay and Isospin Mixing in ^{28}Al

P.A. Dickey, J.E. Bussoletti, and E.G. Adelberger

Isospin forbidden Fermi beta decays provide one of the most direct sources of information on isospin mixing in nuclei. In $J^\pi \to J^\pi$, $\Delta T = 1$ beta decays with $J \neq 0$, a $\beta - \gamma$ circular polarization measurement is necessary to separate the isospin allowed axial vector and forbidden vector contributions. In contrast, the $0^+ \to 0^+$, $\Delta T = 1$ transitions are strictly isospin forbidden in the absence of charge dependent terms in the Hamiltonian, and thus the transition rate for these pure Fermi (vector) decays is related to the magnitude of the isospin impurities in the nuclear levels. These impurities can arise from the Coulomb force or from a charge dependence of the nuclear force.

A particularly large isospin forbidden decay branch is expected between a parent state and its anti-analog. Since the Fermi operator is just the isospin lowering operator T_-, all of the Fermi decay strength of a parent state $|P\rangle$ lies in its analog $|A\rangle$ to which beta decay is energetically impossible. The analog $|A\rangle$ and anti-analog $|\bar{A}\rangle$ states are admixed into each other by charge dependent forces. In general A, $\bar{A}$ mixing is expected to be relatively strong because of the high spatial overlap between the states. The parent state $|P\rangle$ can then decay to the anti-analog $|\bar{A}\rangle$ through the admixture of $|A\rangle$. The $0^+ \to 0^+$ β^- decay of ^{28}Mg, shown in Fig. 2.9-1 is just such a case.

If we assume two state mixing with amplitude α between the analog and anti-analog, then we can write the nuclear states as

$$|A\rangle = -\alpha|T = 1\rangle + (1 - \alpha^2)^{1/2}|T = 2\rangle$$
$$|\bar{A}\rangle = (1 - \alpha^2)^{1/2}|T = 1\rangle + \alpha|T = 2\rangle \quad (1)$$

where the analog and parent states are related by

$$|A\rangle = \frac{T_-|P\rangle}{\sqrt{(T + T_z)(T - T_z + 1)}} = \frac{T_-|P\rangle}{\sqrt{2T}} \quad \text{for } T_z = T \quad (2)$$

For a pure Fermi transition:

$$ft = \frac{K}{G_v^2 M_f^2} \qquad (3)$$

in which $K = \frac{\hbar}{mc^2} 2\pi^3 \ln 2$,

G_v is the dimensionless vector coupling constant, and the Fermi matrix element M_f is given by

$$M_f = \langle f | T_- | i \rangle = \alpha \langle A | T_- | P \rangle$$
$$= \alpha \sqrt{2T}$$

A value of $K/G_v^2 = 6177 \pm 4$ is determined from ft values of allowed 0^+, T = 1 → 0^+, T = 1 Fermi decays[1] for which $M_f = \sqrt{2}$. The mixing amplitude α between states separated by an energy ΔE is related to the matrix element of the charge dependent Hamiltonian $\langle |H_{CD}| \rangle$ by the expression

$$\alpha = \frac{\langle |H_{CD}| \rangle}{\Delta E} \qquad (5)$$

Thus if the ft value for the isospin forbidden transition is measured, then $\langle |H_{CD}| \rangle$ can be deduced from equations (5), (4), and (3) which yield

$$\langle |H_{CD}| \rangle = \frac{\Delta E}{\sqrt{ft}} \left[\frac{6177}{2T} \right]^{1/2} \qquad (6)$$

Only a few cases of anti-analog-analog mixing have been studied by looking at isospin forbidden Fermi beta decays. In the decays of ^{64}Ga and ^{66}Ga a factor of three difference in the values of $\langle |H_{CD}| \rangle$ was found (39.6 keV for ^{64}Ga and 13.6 keV for ^{66}Ga).[2] If shell model wavefunctions are assumed for the analog and anti-analog states, $\langle |H_{CD}| \rangle$ can be expressed in terms of a difference in Coulomb energies for shell model orbitals.[3] That approach predicts nearly identical matrix elements in ^{64}Ga and ^{66}Ga, in conflict with experiment. No isospin mixing matrix elements greater than about 50 keV have been seen in beta decay experiments; however, much

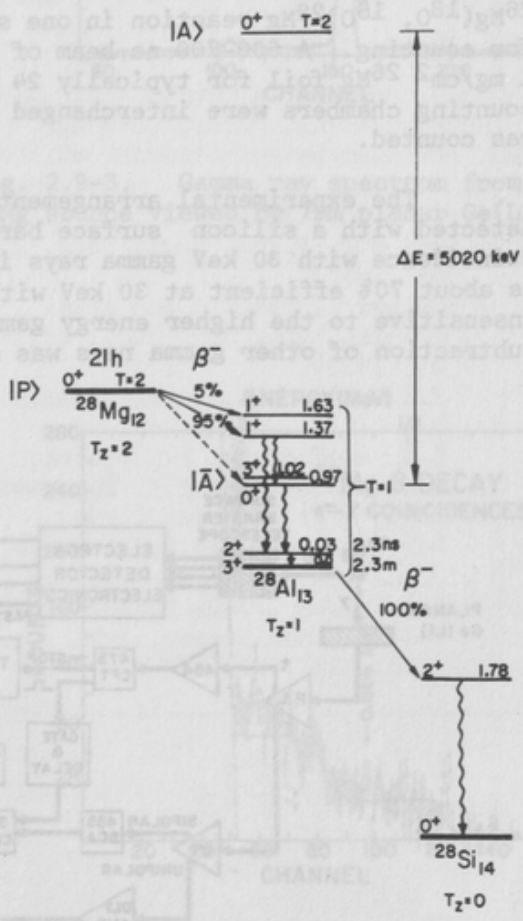

Fig. 2.9-1. Level schemes for mass 28 nuclei involved in ^{28}Mg beta decay. Dashed arrow indicates isospin forbidden 0^+, T = 2 → 0^+, T = 1 decay of interest.

larger matrix elements have been found by other methods in ^{8}Be(150 keV)[4] and ^{12}C(110 ± 30 keV).[5] At the present time there is insufficient data for a systematic understanding of these results.

We have chosen to study the isospin forbidden $0^+ \rightarrow 0^+$ β^- decay of ^{28}Mg because the analog-anti-analog mixing in ^{28}Al has never been measured. The allowed decays were studied by Alburger[6], but the experiment was not sensitive enough to detect a $\leq$ 1% branch to the 0.9 MeV 0^+ state, roughly the size expected for the forbidden decay. As seen in Fig. 2.9-1 the forbidden decay branch is the most energetic and is therefore favored by the phase space factor. Although ^{28}Al is β unstable, its 2.3 minute half life allows selection of the ^{28}Mg decays by a fast β-γ coincidence.

^{28}Mg has a 21 hour half life. The sources were made by the ^{26}Mg(^{18}O, ^{16}O)^{28}Mg reaction in one scattering chamber and transferred to another for counting. A 500-700 na beam of 54 MeV $^{18}O^{5+}$ ions bombarded a water cooled 1 mg/cm^2 ^{26}Mg foil for typically 24 hours before the foils in the scattering and counting chambers were interchanged and a new source made while the fresh source was counted.

The experimental arrangement is shown in Fig. 2.9-2. Electrons were detected with a silicon surface barrier telescope (described in Sec. 13.1) in coincidence with 30 keV gamma rays in a 7mm thick planar Ge(Li). The thin Ge(Li) is about 70% efficient at 30 keV with 1 keV resolution, but is relatively insensitive to the higher energy gamma rays emitted in ^{28}Mg decay. A precise subtraction of other gamma rays was done by placing windows above the 30 keV peak.

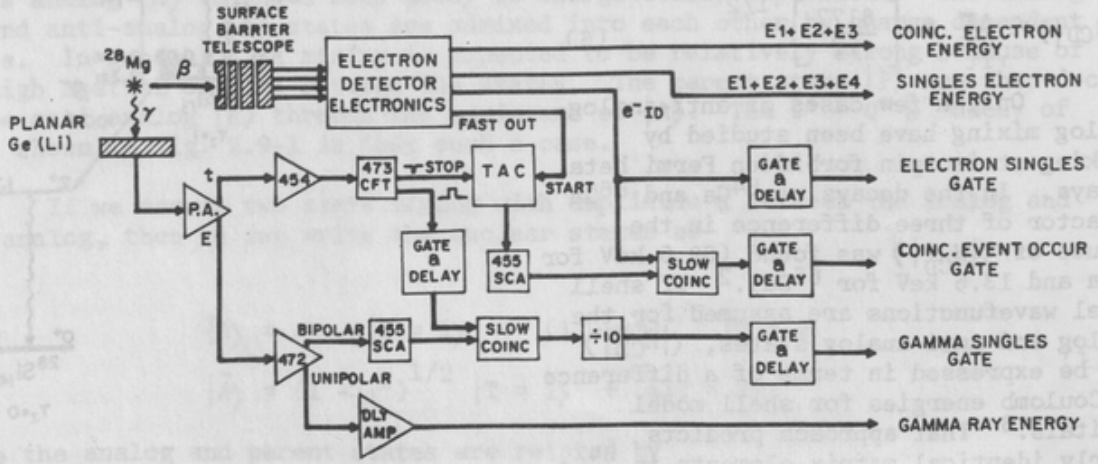

Fig. 2.9-2. Experimental arrangement and simplified electronics for ^{28}Mg beta decay experiment.

Fig. 2.9-3 shows a typical gamma spectrum in the planar Ge(Li). For a $0^+ \rightarrow 0^+$ transition no angular correlations exist, and so the β and γ detectors were placed at right angles to one another to minimize crosstalk from scattered electrons.

Data from a preliminary 24 hour run indicated a 1% upper limit for the $0^+ \rightarrow 0^+$ branching ratio[7], corresponding to $|H_{CD}| \leq 40$ keV. Some improvements were made in the apparatus, and the results of a recent run with the new setup are presented below.

The high energy portion of the electron spectrum in coincidence with 30 keV gamma rays is shown in Fig. 2.9-4. Most of the events above 466 keV can be attributed to 940 keV or 1340 keV gamma rays interacting in the telescope. The gamma ray contribution was measured by accumulating a spectrum with the ΔE-E coincidence requirement turned off. That spectrum, Fig. 2.9-5, was normalized to the electron coincidence spectrum by comparing the number of events above 866 keV, where no electrons are expected. The solid curve in Fig. 2.9-4 is a sketch of the gamma ray spectrum to be subtracted.

The electron detector response function distorts the beta spectrum shape so that only 13% of the isospin forbidden events protrude beyond 466 keV. Taking the detector response into account the excess counts above 466 keV represent a branching ratio of = $(2.1 \pm 1.2) \times 10^{-3}$ or a mixing matrix element of $17.0^{+4.2}_{-5.6}$ keV.

A check on the apparatus is provided by the allowed $0^+ \rightarrow 1^+$ branch shown in Fig. 2.9-6. The curves are calculations of the high energy portion of the allowed beta spectrum with different detector response functions. The normalization of the calculations to the data is absolute, based on the measured

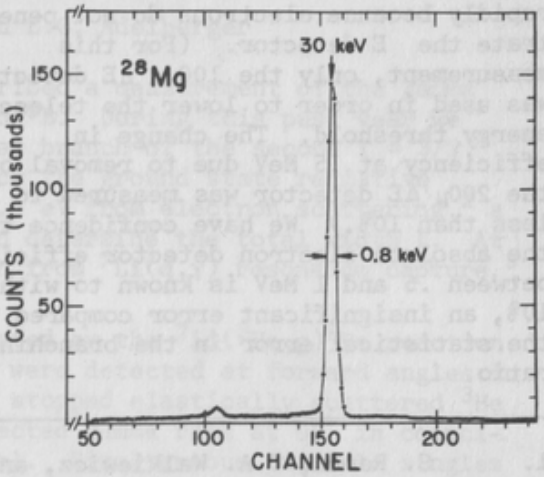

Fig. 2.9-3. Gamma ray spectrum from ^{28}Mg source viewed by 7mm planar Ge(Li).

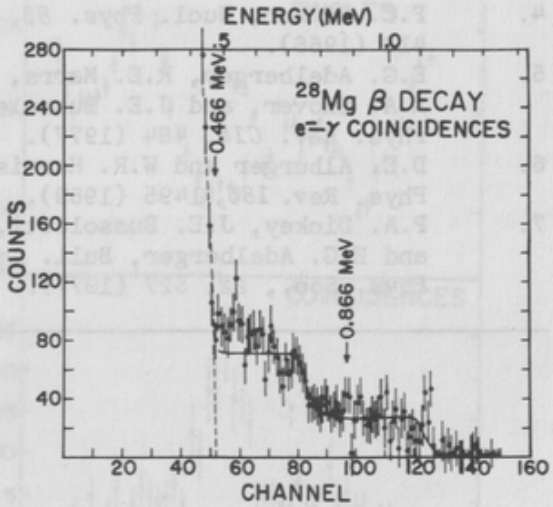

Fig. 2.9-4. High energy portion of electron detector spectrum in coincidence with 30 keV gamma rays. Solid curve is a sketch of the measured gamma ray contribution to the spectrum.

detector efficiency at 1 MeV. Below about 300 keV the efficiency falls rapidly because electrons do not penetrate the E detector. (For this measurement, only the 100 μ ΔE detector was used in order to lower the telescope energy threshold. The change in efficiency at .5 MeV due to removal of the 200μ ΔE detector was measured to be less than 10%.) We have confidence that the absolute electron detector efficiency between .5 and 1 MeV is known to within 10%, an insignificant error compared to the statistical error in the branching ratio.

1. S. Raman, T.A. Walkiewicz, and H. Behrens, Atomic Data and Nuclear Data Tables *16*, 451 (1975).
2. S.K. Bhattacherjee, S.K. Mitra, and H.C. Padhi, Nucl. Phys. *A96*, 81 (1967).
3. George F. Bertsch and Aram Mekjian, Ann. Rev. Nucl. Sci. *22*, 25 (1972).
4. F.C. Barker, Nucl. Phys. *83*, 418 (1966).
5. E.G. Adelberger, R.E. Marrs, K.A. Snover, and J.E. Bussoletti, Phys. Rev. *C15*, 484 (1977).
6. D.E. Alburger and W.R. Harris, Phys. Rev. *185*, 1495 (1969).
7. P.A. Dickey, J.E. Bussoletti, and E.G. Adelberger, Bull. Am. Phys. Soc., *22*, 527 (1977).

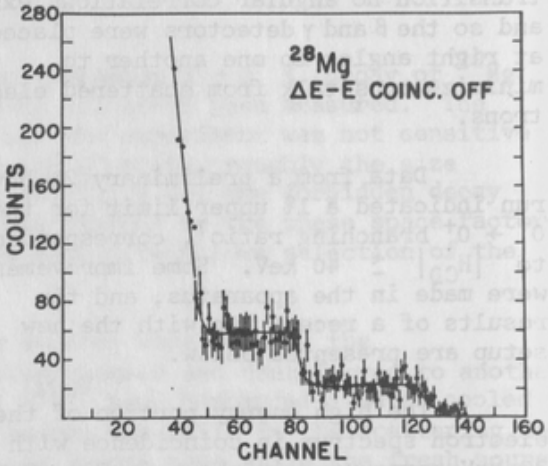

Fig. 2.9-5. Spectrum in electron detector with E-E coincidence off. Above 466 keV (channel 52) all the events are from gamma rays.

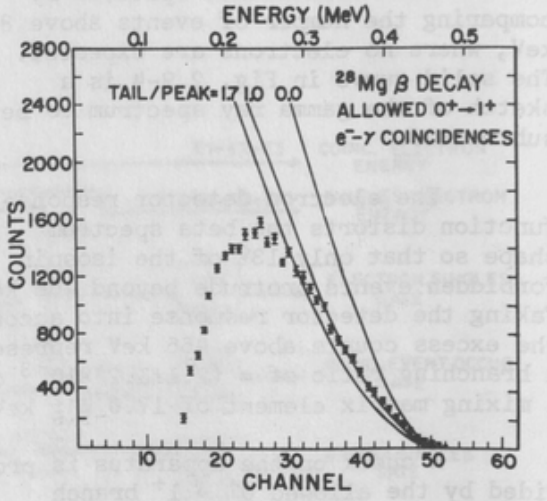

Fig. 2.9-6. Electron spectrum from allowed $0^+ \rightarrow 1^+$ ^{28}Mg beta decay. Solid curves are the result of calculations with different tail-peak area ratios for the detector response.

2.10 Gamma Decay of the Second T = 3/2 Level in ^{9}Be and a Search for a Possible New State in ^{9}Be near 3 MeV

P.A. Dickey, P. Dyer, K.A. Snover, and E.G. Adelberger

In last year's annual report[1] we described a measurement of the gamma decays of the lowest T = 3/2 levels in ^{9}Be and ^{9}B. During this past year we attempted to measure the ground state gamma ray branch of the second T = 3/2 state in ^{9}Be, a 1/2^{-} level at 16.98 MeV. Since the ground state radiative width Γ_{γ_0} of ^{9}Be(16.98) is known to be 11.5±1.4 eV from electron scattering,[2] a measurement of the branching ratio Γ_{γ_0}/Γ would determine the total width Γ. At present only an upper limit of 470 eV is known from ^{7}Li(d,γ) resonance capture.[3]

The 16.98 MeV T = 3/2 state was populated by the ^{7}Li(^{3}He,p)^{9}Be reaction at an incident ^{3}He energy of 13 MeV. Protons were detected at forward angles in a ΔE-E telescope behind Au and Ni foils which stopped elastically scattered ^{3}He ions. The NPL 10" ×10" NaI spectrometer detected gamma rays at 90° in coincidence with protons populating the T = 3/2 level. Simultaneous particle singles and coincidence spectra were recorded through the same ADC at several particle detector angles. Although γ decays of

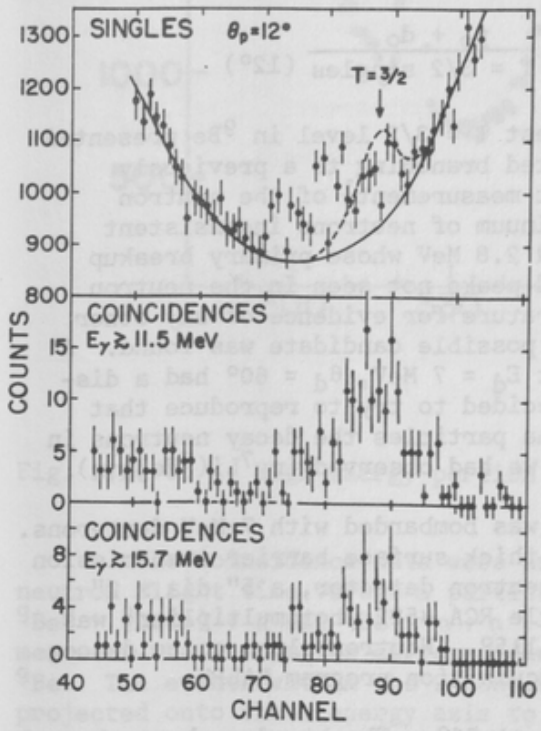

Fig. 2.10-1. Portion of singles and coincidence particle spectra from ^{7}Li(^{3}He,p)^{9}Be (16.98) → γ + ^{9}Be(g.s.), in which particles were detected at 12°. Arrow indicates expected location of T = 3/2 group. Dashed curve is an upper limit for the peak.

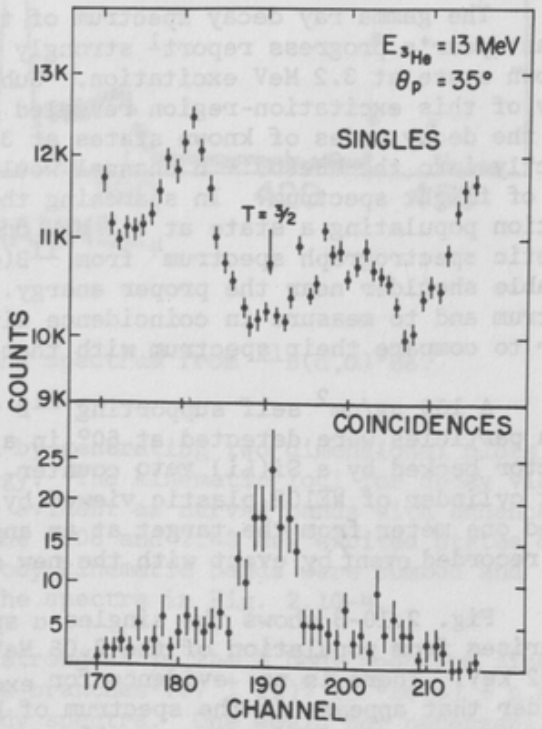

Fig. 2.10-2. Singles and coincidence particle spectra at 35°.

the 16.98 MeV state were readily identified in coincidence spectra, the T = 3/2 group could not be seen in the singles proton spectrum at any angle. Figs. 2.10-1 and 2.10-2 show portions of singles and coincidence particle spectra taken at 12° and 35°; the arrow indicates the expected location of the T = 3/2 group. In the 12° data the solid line is a possible background and the dashed line is an estimate of the upper limit for a peak of the proper width as determined from the coincidence spectra. This singles peak area along with the measured coincidence yield gives a lower limit for Γ_{γ_0}/Γ of $\geq$ 0.7%. If Γ_{γ_0} = 11.5 ev, then our upper limit for Γ is 1.7 keV, a value nearly four times the known upper limit. It is clearly necessary to identify the T = 3/2 group in a singles spectrum in order to improve our value.

We have normalized our T = 3/2 gamma ray coincidence yield at $E_{^3He}$ = 13 MeV, θ_p = 12° to the unresolved $^7Li(^3He,p_o)^9B$ and $^7Li(^3He,d_o)^8Be$ singles yields so that a future high resolution singles measurement of the $^7Li(^3He,p)^9Be^*(16.98)$ yield relative to $p_o + d_o$ could determine Γ_{γ_0}/Γ. Such an experiment would be relatively easy to do with a magnetic spectrometer. The expression for determining Γ_{γ_0}/Γ in the singles experiment is

$$\frac{\Gamma_{\gamma_0}}{\Gamma} = (2.8 \pm 0.6) \times 10^{-3} \times \frac{p_o + d_o}{\text{T = 3/2 singles}} (12°)$$

The gamma ray decay spectrum of the lowest T = 3/2 level in ^9Be presented in last year's progress report[1] strongly suggested branching to a previously unknown state at 3.2 MeV excitation. Subsequent measurement[1] of the neutron decay of this excitation-region revealed a continuum of neutrons inconsistent with the decay modes of known states at 3.06 and 2.8 MeV whose primary breakup directly into the $^8Be(0) + n$ channel would yield peaks not seen in the neutron time of flight spectrum. In searching the literature for evidence of any other reaction populating a state at 3.2 MeV only one possible candidate was found. A magnetic spectrograph spectrum[4] from $^{11}B(d,\alpha)$ at E_d = 7 MeV, θ_d = 60° had a discernable shoulder near the proper energy. We decided to try to reproduce that spectrum and to measure in coincidence with alpha particles the decay neutrons in order to compare their spectrum with that which we had observed in $^7Li(^3He,pn)$.

A 100 $\mu g/cm^2$ self supporting ^{11}B target was bombarded with 7 MeV deuterons. Alpha particles were detected at 60° in a 100 μ thick surface barrier transmission detector backed by a Si(Li) veto counter. The neutron detector, a 5" dia x 2" thick cylinder of NE102 plastic viewed by a single RCA 4522 photomultiplier, was placed one meter from the target at an angle of 115°. Neutron-alpha coincidences were recorded event by event with the new data acquisition program RALPH.

Fig. 2.10-3 shows the singles α spectrum at 60°. The broad peak at channel 250 arises from population of the 3.06 MeV $\frac{5}{2}^+$ level in ^9Be whose natural width is 292 keV. There is no evidence for excitation of a state at 3.2 MeV; the shoulder that appears in the spectrum of Bockelman et al[4] is absent in our data. If the shoulder did not come from $^{11}B(d,\alpha)$, then it would not have to appear at the same place in the spectrograph and the counter data.

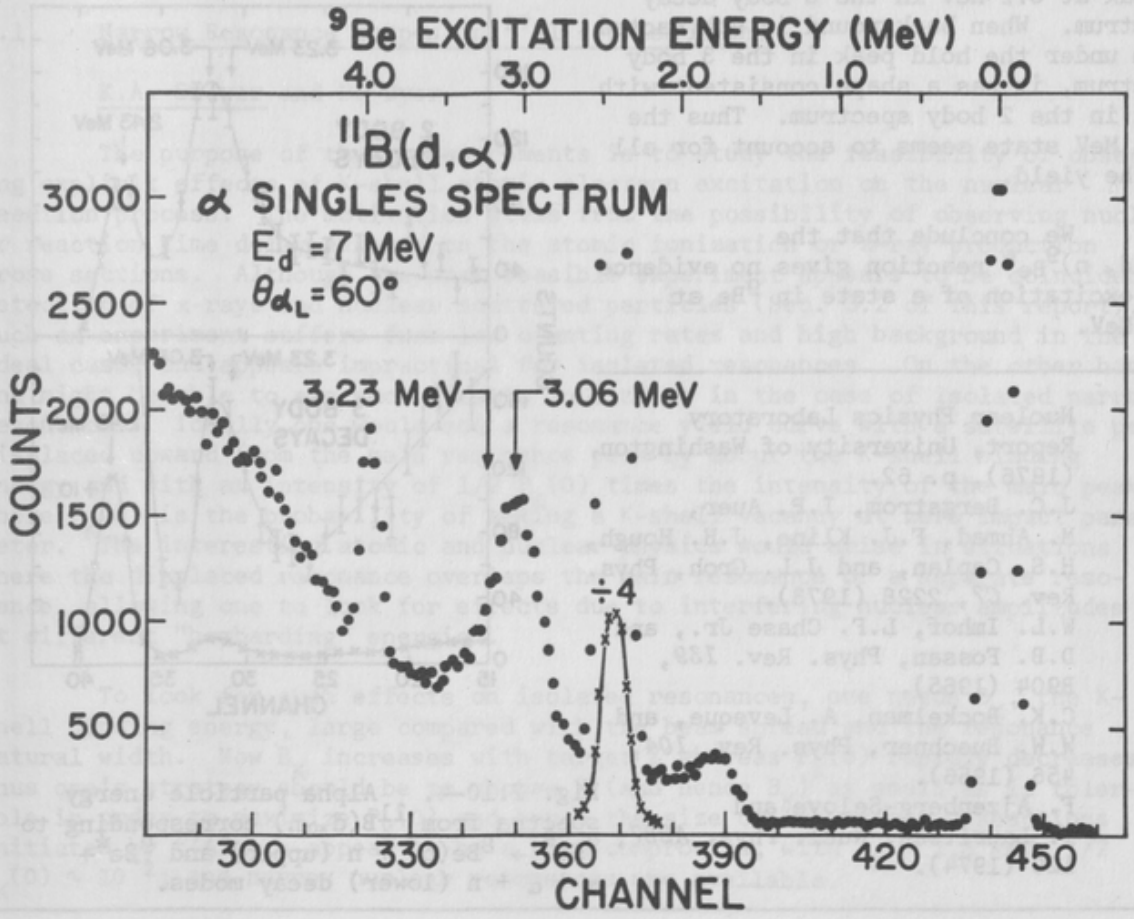

Fig. 2.10-3. High energy portion of alpha spectrum from $^{11}B(d,\alpha)^9Be$.

The coincidence data were analyzed by generating two dimensional plots of neutron flight time versus α particle energy. The kinematic loci for decay via $^9Be^* \rightarrow {}^8Be(o) + n$ and $^9Be^* \rightarrow \alpha + \alpha + n$ were evident as curved bands with enhancements at the α energies corresponding to the 3.06 and 2.43 MeV excited states of ^{9}Be. The events within the 2 body and 3 body kinematic bands were summed and projected onto the α energy axis to give the spectra in Fig. 2.10-4.

As expected the 2.43 MeV state is strongest in the 3 body spectrum since it has $\Gamma n_o/\Gamma = 6.4\%$.[5] The 3.06 MeV state branches[5] $(87 \pm 13)\%$ to $^8Be(o) + n$ and is quite prominent in both 2 body and 3 body spectra. One would not necessarily expect the 2 and 3 body yields to be in the ratio of 87:13 because the effects of angular correlations, center of mass to lab conversion, and energy dependence of the neutron detector efficiency have not been removed. There is no evidence for

a peak at 3.2 MeV in the 3 body decay spectrum. When background is subtracted from under the hold peak in the 3 body spectrum, it has a shape consistent with that in the 2 body spectrum. Thus the 3.06 MeV state seems to account for all of the yield.

We conclude that the $^{11}B(d, n)^{9}Be^{*}$ reaction gives no evidence for excitation of a state in ^{9}Be at 3.2 MeV.

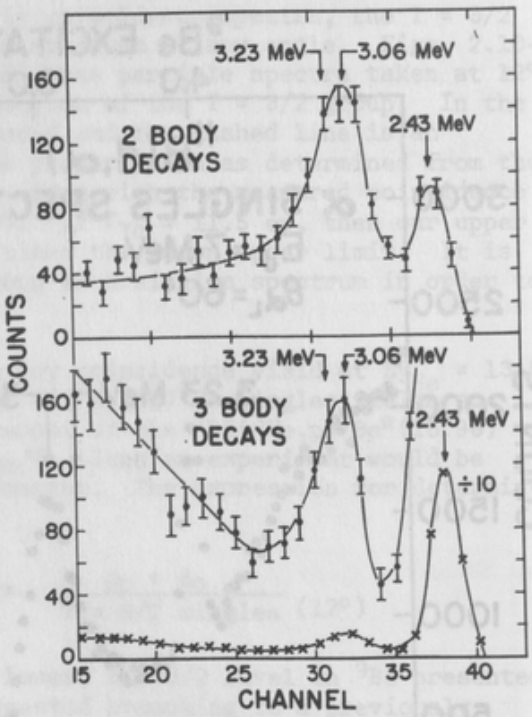

Fig. 2.10-4. Alpha particle energy spectra from $^{11}B(d,\alpha n)$ corresponding to $^{9}Be^{*} \rightarrow {}^{8}Be(o) + n$ (upper) and $^{9}Be^{*} \rightarrow \alpha + \alpha + n$ (lower) decay modes.

1. Nuclear Physics Laboratory Report, University of Washington, (1976), p. 62.
2. J.C. Bergstrom, I.P. Auer, M. Ahmad, F.J. Kline, J.H. Hough, H.S. Caplan, and J.L. Groh, Phys. Rev. *C7*, 2228 (1973).
3. W.L. Imhof, L.F. Chase Jr., and D.B. Fossan, Phys. Rev. *139*, B904 (1965).
4. C.K. Bockelman, A. Leveque, and W.W. Buechner, Phys. Rev. *104*, 456 (1956).
5. F. Ajzenberg-Selove and T. Lauritsen, Nucl. Phys. *A227*, 120 (1974).

3. NUCLEAR STRUCTURE

3.1 Narrow Resonance Shapes in ^{27}Al + p Reactions

K.A. Snover and P. Dyer

The purpose of these measurements is to study the feasibility of observing explicit effects of K-shell atomic electron excitation on the nuclear reaction process. The motivation stems from the possibility of observing nuclear reaction time delay effects on the atomic ionization or x-ray production cross sections. Although the most feasible experiment appears to be coincidence detection of x-rays and nuclear scattered particles (Sec. 3.2 of this report), such an experiment suffers from low counting rates and high background in the ideal case, and appears impractical for isolated resonances. On the other hand, one might be able to see such effects in singles in the case of isolated narrow resonances. Ideally one would see a resonance yield curve with a satellite peak displaced upward from the main resonance peak by about the K-shell binding energy and with an intensity of 1/2 $P_K(0)$ times the intensity of the main peak, where $P_K(0)$ is the probability of making a K-shell vacancy at zero impact parameter. The interesting atomic and nuclear physics would arise in situations where the displaced resonance overlaps the main resonance or a separate resonance, allowing one to look for effects due to interfering nuclear amplitudes at different "bombarding" energies.

To look for such effects on isolated resonances, one needs B_K, the K-shell binding energy, large compared with the beam spread and the resonance natural width. Now B_K increases with target Z whereas $P_K(0)$ rapidly decreases; thus one's strategy should be to choose Z (and hence B_K) as small as is tolerable in order to maximize $P_K(0)$ and hence the size of the effect. Reactions initiated by ^{27}Al + p appear to be a good compromise, with $B_K \sim 1.6$ keV, 1/2 $P_K(0) \sim 10^{-2}$; and narrow nuclear resonances are available.

Two resonances were examined, the first of which was the strong narrow (Γ = 150 eV) ^{27}Al (p,α) ^{24}Mg resonance at E_p = 1647 keV. Measurements were made at θ_α = 145° using a thin 20μ detector to eliminate elastic pile-up interference. Thick target (20μg/cm^2, $\Delta E \sim 2.6$ keV) yield curves showed a beam spread of ∿ 750 eV from the 1/8 - 7/8 rise. However, thin target (1.3 - 2.6μg/cm^2) yield curves showed substantial high energy tails, much larger than could be accounted for in terms of straggling caculations. The 1.3μg/cm^2 yield curve is shown in Fig. 3.1-1. The FWHM of 750 eV is equal to the beam spread deduced from the thick target, and the low energy side of the yield curve is consistent with a gaussian shape down to 10% of the maximum yield, but with a larger tail at lower energies. Fig. 3.1-1 also shows a thin target yield curve over the strong (p,γ2) resonance at Ep = 3.671 MeV for $\theta\gamma$ = 90°. It is clear that to detect a satellite peak requires reduction of the high energy tail in either case. This tail may be due to target non-uniformities or to a low energy tail on the proton beam as a result of upstream slit scattering. Straggling or energy broadening in the gas stripper due to failure to contain the gas within the terminal may contribute also (measurements with a 3μg/cm^2 C stripper foil showed larger tails). In the case of the (p,γ_2) resonance, the nonresonant background makes a substantial contribution.

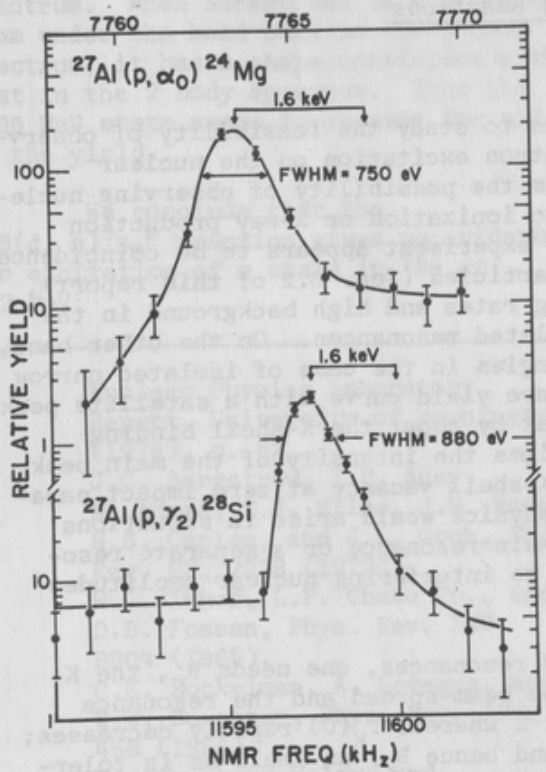

Fig. 3.1-1. *Upper curve and scale:* The ^{27}Al (p,α_0) ^{24}Mg reaction near E_p = 1647 keV. *Lower curve and scale:* the ^{27}Al (p,γ_2) ^{28}Si reaction near E_p = 3671 keV.

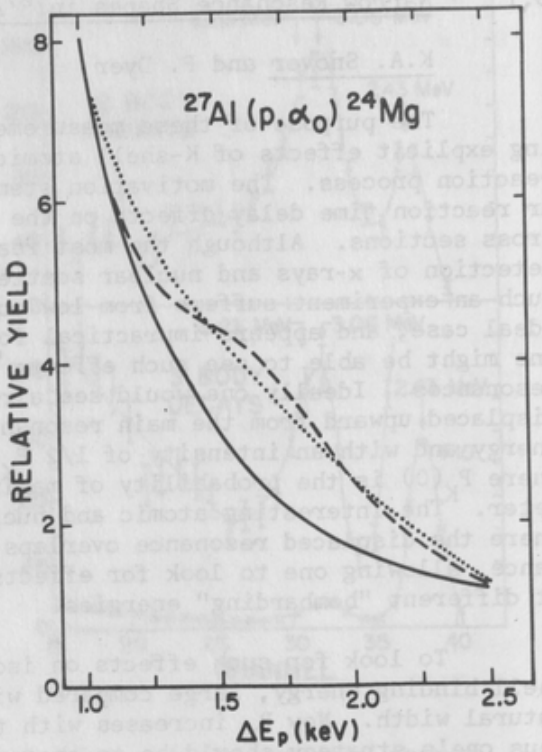

Fig. 3.1-2. "Calculated" satellite effect above the (p,α_0) resonance (see text). $\Delta E_p \equiv E_p - E_{p_{res}}$. The peak yield on resonance is 150 (relative units).

Fig. 3.1-2 shows the result of an idealized calculation (including straggling) of the effect above the 1647 keV resonance, assuming a 2μg/cm^2 target and a 500 eV gaussian beam spread. The figure depicts the region ∿ 1.6 keV above the main peak. The solid curve represents the calculated tail of the main peak; the dashed curve, a 1% satellite peak added on with the same shape as the main peak; and the dotted curve, the best smooth curve with a shape similar to the main peak tail. With very good statistics one might be able to tell the difference between the dotted and dashed curves near the leading edge of the satellite peak. However, any broadening of the leading edge, as one might expect from a spread in K-shell excitation energies, would wash out this difference.

3.2 K-Shell Ionization and Time Delays in Nuclear Reactions

J.S. Blair, P. Dyer, K.A. Snover, and T.A. Trainor

A new means of studying time delay in a compound nuclear reaction is being investigated. As a nuclear particle is scattered, an atomic K-shell vacancy may be created (in the same atom) by the incoming particle or by the outgoing particle. The incoming and outgoing amplitudes for this process interfere quantum mechanically, and the probability for the simultaneous nuclear-atomic event depends on the nuclear delay time through the phase difference.

If the vacancy is created by the incoming particle, that particle loses an amount of energy equal to the sum of the K-shell binding energy and the kinetic energy of the ejected electron. When the nuclear resonance width and the beam energy resolution are comparable to or less than the K-shell binding energy, this energy loss gives rise to a double-resonance structure in the atomic-nuclear excitation function. If A(klm) and B(klm) are the amplitudes for the atomic vacancy creation by the incoming and outgoing particles, respectively, and $f_{\beta\alpha}(\theta,E)$ is the nuclear scattering amplitude, then the probability that there is simultaneougly a nuclear scattering and a K vacancy creation may be calculated with time-independent perturbation theory to be

$$|A(klm)f_{\beta\alpha}(\theta,E-\hbar\omega) + B(klm)f_{\beta\alpha}(\theta,E)|^2$$

where k,l, and m are the wave number, angular momentum, and angular-momentum projection of the ejected electron, E is the energy of the incoming particle, θ is the scattering angle, $\hbar\omega$ is the energy transferred to the electron, and α and β symbolize a set of nuclear quantum numbers describing the initial and final states, respectively. Sums and averages over the appropriate quantum numbers and the electron kinetic energy must be performed to obtain the cross section. Specifically, the quantity we are measuring is the correlation between nuclear amplitudes at two different energies. The effects due to "time delay" are incorporated in the energy dependence of the reaction amplitudes, consistent with the Heisenberg uncertainty principle.

This technique is being tested by measuring the atomic-nuclear probability as a function of bombarding energy for the case of the $^{58}Ni(p,p)\,^{58}Ni$ reaction. At 3.14 MeV there is a large, isolated s-wave resonance (interfering with Coulomb scattering) of width 5.6 keV. The K-shell binding energy is 8.3 keV. This resonance is thus a case for which the nuclear resonance width and the K-shell binding energy are comparable. A target composed of 9 $\mu g/cm^2$ ^{58}Ni evaporated onto a 10 $\mu g/cm^2$ carbon backing was bombarded by a proton beam. The beam energy resolution was about 1 keV, and the energy loss in the target was 0.6 keV. A Si(Li) x-ray detector and a Si(Li) particle detector were placed at 90° with respect to the beam direction. The x-ray detector subtended a solid angle of 0.38 sr; the particle detector, 1.2 sr, with a spread in θ of $\pm$ 20°. With fast-timing techniques, coincidences between elastically scattered protons and Ni K x-rays were measured at four bombarding energies. Because of the small zero-impact-parameter ionization probability ($P_K(0)\sim 0.003$) and the high singles x-ray and particle counting rates, there is a high background of random events, and the statistical errors are large.

The proton singles excitation function, showing the s-wave resonance at 3.14 MeV, is illustrated in Fig. 3.2-1a. The measured number of coincidences are shown in Fig. 3.2-1b. For this test case, all quantities in the above formula are known except the phase difference between the two atomic amplitudes. The three curves in Fig. 3.2-1b are calculated for atomic phase differences of $\Delta\phi = 0°$, $+90°$, and $-90°$, for the specific case of monopole excitation only (l=m=0) for which A=B* and $\Delta\phi \equiv \tan^{-1}A/B$. The curves have been normalized to the average value of the two data points at 3.125 and 3.175 MeV. It can be seen that in addition to testing the concept of measuring nuclear time delays by this type of experiment, a precise experiment may be able to determine the atomic phase difference $\Delta\phi$.

We are now preparing to repeat these measurements with a Na(Tl) x-ray detector. With larger solid angles, possibly better time resolution, and longer counting times, we should be able to make much more precise measurements.

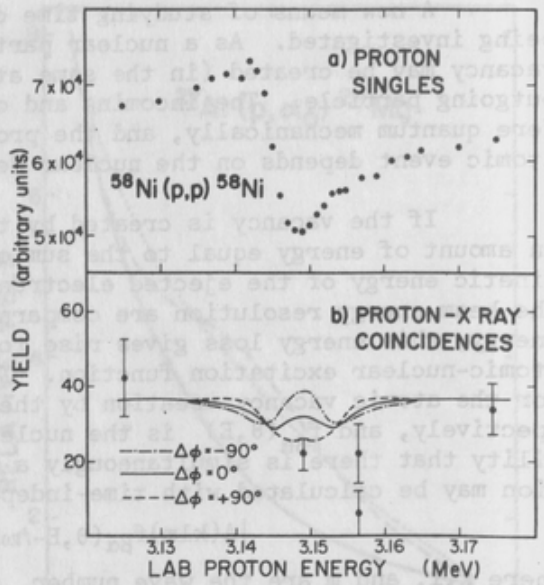

Fig. 3.2-1. a) Excitation function for elastic scattering of protons from ^{58}Ni. b) Yield of Ni K x-rays in coincidence with elastically scattered protons. Calculated curves for three atomic phase shifts are also shown (see text).

3.3 Search for Superheavy Elements

D. Burch, J.G. Cramer, P. Dyer

We have searched for superheavy elements in four samples by detecting characteristic x-rays induced by protons.

The first sample was a monazite mineral from Idaho.[1] Evidence for primordial superheavy elements in monazite inclusions showing giant halo formation in mica has been reported by Gentry et al.[2] The second sample was a piece of the Allende meteorite which fell in Mexico in 1969.[3] Anomalous abundances of the xenon isotopes 131, 132, 134 and 136 have been observed in this meteorite, and superheavy elements have been suggested as the progenitors of these isotopes.[4] The third sample was coral extracted from the Bikini thermonuclear bomb crater,[5] a possible source of man-made superheavy elements. The fourth sample was glass used on a University of Washington cosmic-ray experiment.[6] Emulsions on this glass had shown a few unexplained tracks from long-range alpha particles.

The samples were finely ground, slurried onto carbon backing foils, and bombarded with 2-MeV protons. X-rays were detected with an intrinsic germanium detector.

An x-ray spectrum for the monazite sample is shown in Fig. 3.3-1. K x-rays from Ce, La, and other rare earth elements are easily observed. Unfortunately, in the region where superheavy L_α x-rays would be observed, there is a

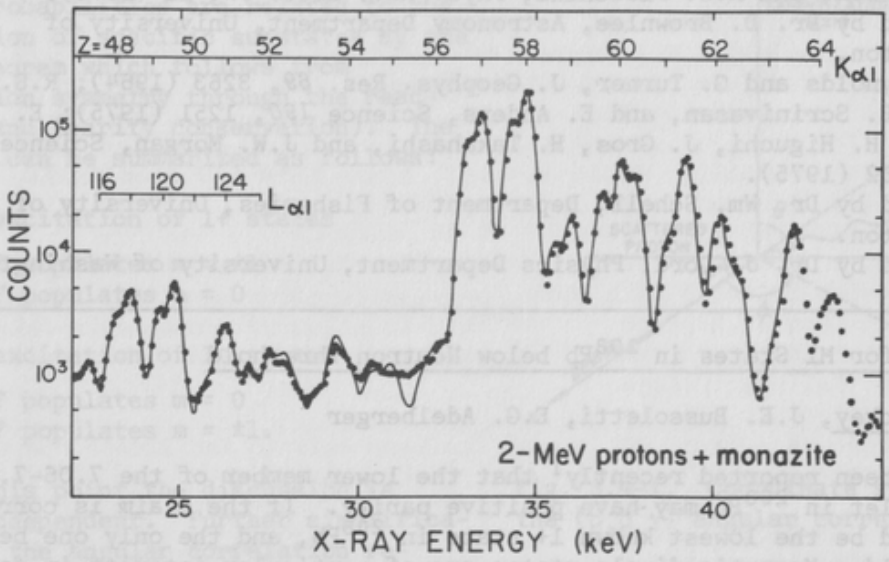

Fig. 3.3-1. Spectrum of x-rays induced in a monazite sample by 2-MeV protons. The solid line is a fit to the data. Positions of $K_{\alpha 1}$ lines for the Z's used in the fit and of a few $L_{\alpha 1}$ lines in the superheavy region are indicated. All structure in the indicated superheavy region can be accounted for by K x-rays or Ge K escape peaks from the rare earth elements.

large background from the Ge I escape peaks of the rare earth lines (about 10 keV below the full-energy peaks). The peak at 26.3 keV is from Sb K x-rays. A fit to the data is shown, for which the intensities of K x-rays of elements Z=46 and a constant background are free parameters. Lineshapes are gaussian with exponential tails. The positions and relative intensities of 6 components of the K x-ray line are fixed at their known values; the widths, the parameters describing the exponential tail, and the intensity ratios of the $Ge_\alpha K_\beta$ and K escape peaks to full-energy peaks are determined from measured lineshapes of several K x-rays in the region of interest. It can be seen, for example, that

the ratio of Z=126 $L_{\alpha 1}$ x-rays to cerium $K_{\alpha 1}$ x-rays is less than 5×10^{-4}. This sensitivity is several times greater than that of the experiment of Gentry et al.;[2] however, our monazite sample was a bulk sample rather than a giant halo inclusion, so our limit is not of great interest.

No superheavy elements were detected in any of the four samples at levels of a few parts per million.

---

1. Provided by Prof. B.W. Evans, Geology Department, University of Washington.
2. R.V. Gentry, T.A. Cahill, N.R. Fletcher, H.C. Kaufman, L.R. Medsker, J.W. Nelson, and R.G. Flocchini, Phys. Rev. Lett. *37*, 11 (1976).
3. Provided by Dr. D. Brownlee, Astronomy Department, University of Washington.
4. J.H. Reynolds and G. Turner, J. Geophys. Res. *69*, 3263 (1964); R.S. Lewis, B. Scrinivasan, and E. Anders, Science *190*, 1251 (1975); E. Anders, H. Higuchi, J. Gros, H. Takahashi, and J.W. Morgan, Science *190*, 1262 (1975).
5. Provided by Dr. Wm. Schell, Department of Fisheries, University of Washington.
6. Provided by Dr. J. Lord, Physics Department, University of Washington.

3.4 Search for M1 States in ^{208}Pb below Neutron Threshold

P.A. Dickey, J.E. Bussoletti, E.G. Adelberger

It has been reported recently[1] that the lower member of the 7.06-7.08 MeV spin 1 doublet in ^{208}Pb may have positive parity. If the claim is correct, that state would be the lowest known 1+ state in ^{208}Pb, and the only one below neutron threshold. Magnetic dipole states are of particular interest in doubly magic ^{208}Pb because the shall closure leaves unpaired the i 11/2 - i 13/2 neutron and h 9/2 - h 11/2 proton spin orbit partners, the only $0\hbar\omega$ one particle --one hole shell model configurations which can couple to 1+. Shell model calculations of the spectrum of 1+ states have been performed within a 1p-1h $0\hbar\omega$ + $2\hbar\omega$ basis (i 11/2 g $9/2^{-1}$ neutrons and j 13/2 h $11/2^{-1}$ neutrons included),[2,3] and very recently with the inclusion of 2p-2h excitations.[4] The results are sensitive to the basis and to the details of the residual interaction. This most recent calcuation[4] predicts strong 1+ states at 7.13 and 7.86 MeV with strengths in factor of two agreement with those of states at 7.06 MeV and 7.99 MeV seen in (γ,γ)[5] and (γ,n)[6] experiments. Because the existence of a 1+ state at 7 MeV would be of such importance, and because the results of Ref. 1 are not definitive, we have decided to try to repeat that measurement with better statistics and to make some further investigations.

The technique involves exciting the states of interest by the direct (p,p') reaction and measuring the correlation of de-excitation-gamma rays relative to the reaction-plane. The ratio of in plane to out of plane intensities determines the proton spin-flip probabilities, which are expected to be quite different for excitation of 1+ and 1$^-$ states. DWBA calculations are used to predict spin-flip probabilities for particular experimental conditions.

The general form of the gamma ray angular distribution for J=1→0 transitions can be written[7]

$$W_{J=1}(\theta,\phi) \propto (a_1^2 + a_{-1}^2)(1 + \cos^2\theta) + 2a_0^2 \sin^2\theta + 2a_1 a_{-1} \sin^2\theta \cos(\delta - 2\phi)$$

where the angles θ and ϕ are defined by the coordinate system of Fig. 3.4-1, the a_m are the amplitudes for populating the mth magnetic substate of the excited J=1 state, and δ is the relative phase between the m = ±1 amplitudes. The spin flip (SF) and non spin flip (NSF) probabilities are related to the population of specific substates by the Bohr theorem which follows from reflection symmetry through the reaction plane (parity conservation). The results can be summarized as follows:

for excitation of 1+ states

SF populates m = ±1
NSF populates m = 0

for excitation of 1⁻ states

SF populates m = 0
NSF populates m = ±1.

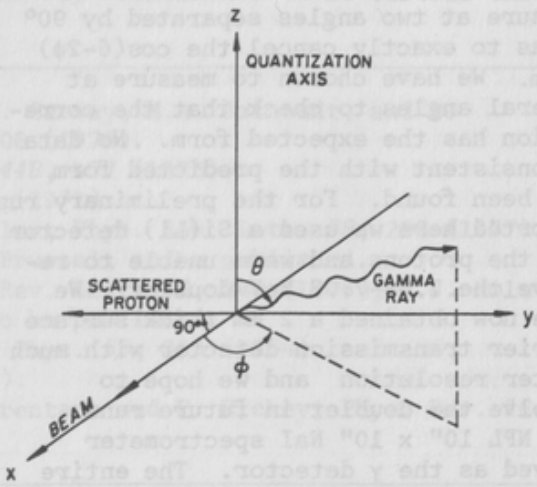

Fig. 3.4-1. Coordinate system for the (p,p′γ) angular correlation.

Up to this point the discussion is model independent. Further simplification of the angular correlation requires knowledge of the reaction mechanism.

It is expected that at forward angles the excitation of 1+ states by (p,p′) will proceed mainly by L = 0 transfer.[1] If L = 0 transfer is assumed, it can be shown that the $a_1 a_{-1}$ interference term vanishes because a particular projectile spin flip sequence excites a unique target substate. Furthermore, if spin-orbit distortion is neglected (it will be smallest at forward angles), the spin flip probability $a_1^2 + a_{-1}^2 = 2/3$. Under these assumptions, the 1+ → 0+ gamma ray yield is isotropic.

Electric dipole 1⁻ states can be excited only by L=1 transfer. In general the $a_1 a_{-1}$ interference does not vanish for L=1. The spin flip probability A_o^2 is expected to be small for 1⁻ states. The in plane to out of plane ratio thus becomes

$$\frac{\langle W_{IP} \rangle}{W_{OP}} = \frac{1 + a_o^2}{2(1 - a_o^2)} \simeq \frac{1}{2}$$

Fig. 3.4-2 shows the W_{OP}/W_{IP} ratio for 1^+ and 1^- states as a function of the

spin flip probability.

The experiment entails measuring, in coincidence with inelastically scattered protons, the yield of ground state γ rays in and perpendicular to the reaction plane. In order to correct for the in plane correlation function, one must either measure at several gamma ray angles and fit the results or measure at two angles separated by 90° so as to exactly cancel the $\cos(\delta-2\phi)$ term. We have chosen to measure at several angles to check that the correlation has the expected form. No data inconsistent with the predicted form has been found. For the preliminary run reported here we used a Si(Li) detector for the protons and were unable to resolve the 7.06-7.08 MeV doublet. We have now obtained a 2 mm thick surface barrier transmission detector with much better resolution and we hope to resolve the doublet in future runs. The NPL 10" x 10" NaI spectrometer served as the γ detector. The entire scattering chamber was rotated 90° around the beam axis to facilitate the out of plane measurement.

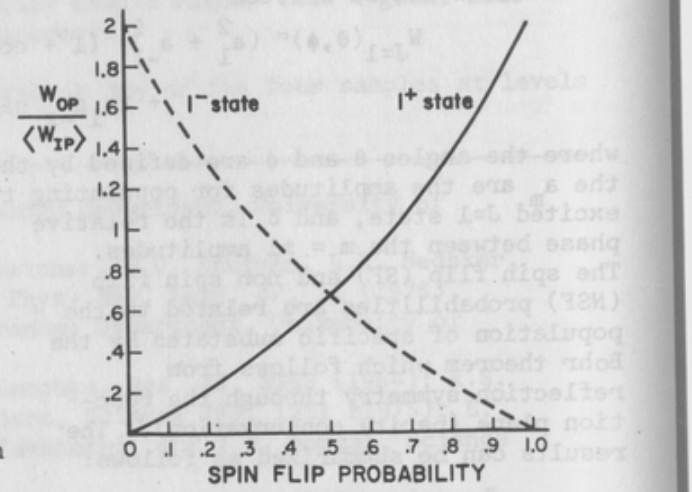

Fig. 3.4-2. Ratio of out of plane to average in plane gamma ray intensity as a function of proton spin flip for excitation of 1^+ and 1^- states.

It is advantageous to run at as high a proton bombarding energy and as forward a proton scattering angle as possible. The Princeton experiment[1] was performed at E_p = 24 MeV with $\phi_{p'}$ = 45°. At that energy we are still well above the analog resonance region, but it would be reassuring to show the results to be energy independent. In Fig. 3.4-3 our results are compared with those of Freedman et al.[1] The two sets of results are completely consistent for the 4.84, 5.51 and 6.31 MeV states. This gives us confidence that our assumptions about the reaction mechanism are still valid at lower energy and more backward angles, and justifies our effort to improve the proton resolution.

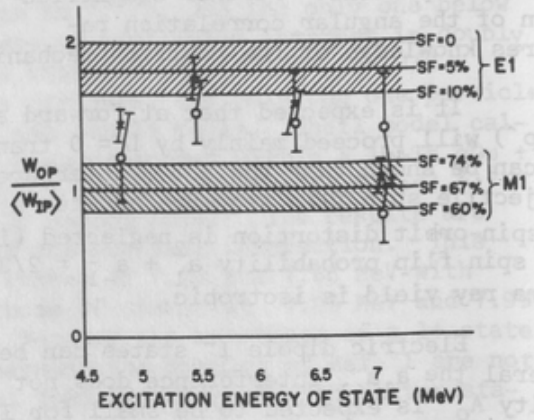

Fig. 3.4-3. The observed ratios $W_{OP}/\langle W_{IP} \rangle$ for states in ^{208}Pb. Points with crosses are our data; points with open circles are data of Ref. 1.

In a preliminary run with the new proton detector we failed to achieve

adequate energy resolution at the needed counting rate because of the tremendous elastic scattering at forward angles. It is clear that we must seek a maximum inelastic-to-elastic ratio at a more backward angle. DWBA calculations will be necessary to verify the validity of the L transfer and spin flip assumptions.

We plan one additional experiment to complement the correlation data. Data from (p,p′) near the $d_{3/2}$ analog resonance[9] indicate that the 7.06 MeV state may be enhanced on resonance. Such behavior would be unlikely for a 1^+ state because a $d_{3/2}$ neutron cannot couple with an available hole to give $J^\pi = 1^+$. The experiment should be repeated with the gamma ray coincidence to be certain that the states involved are the same.

1. S.J. Freedman, C.A. Gagliardi, G.T. Garvey, M.A. Oothoudt, and B. Svetitsky, Phys. Rev. Lett. *37*, 1606 (1976).
2. P. Ring and J. Speth, Phys. Lett. *44B*, 477 (1973).
3. J.D. Vergados, Phys. Lett. *36B*, 12 (1971).
4. J.S. Dehesa, J. Speth and A. Faessler, Phys. Rev. Lett. *38*, 208 (1977).
5. D.F. Coope, L.E. Cannell and M.K. Brussel, to be published.
6. R.J. Holt and H.E. Jackson, Phys. Rev. Lett. *36*, 244 (1976); R.J. Holt, R.M. Laszewski and H.E. Jackson, to be published.
7. J.G. Cramer and W.W. Eidson, Nucl. Phys. *55*, 593 (1964).
8. A. Bohr, Nucl. Phys. *10*, 486 (1959).
9. C.F. Moore, J.G. Kulleck, P. von Brentano and F. Rickey, Phys. Rev. *164*, 1559 (1967).

3.5 Heavy Ion Induced Reactions as a Tool for Studying Nuclear Quadrupole Moments of μsec Isomers by Recoil Implantation

K.G. Bernhardt, H. Bohn, Y-d Chan, B. Cuengco, K. Green, R. Sielemann

It has been shown recently that accurate time-differential measurements of nuclear quadrupole interactions can be made on isomeric nuclear states with nsec- and μsec-halflives by recoil-implantation into different metallic matrices.[1,2] α-particle induced reactions were used in connection with evaporated multi-layered sandwich targets[1] and also a ^{12}C beam[2] on a two-layer target. Using heavier ion beams at higher energies, this technique should be an extremely useful tool for measuring E2 moments, particularly for high-spin isomeric states which occur in great abundance throughout the periodic system. The recoil implantation technique allows one to choose the best possible environment, which has been found to be s-p electron-type metals like Cd, In, and Sn. A very high accuracy (1-2%) can be achieved by measuring relative moments of a particular element in the same environment.

Energy and beam current considerations for our FN tandem show that (Heavy ion, xn)-reactions are favorable for x=3 and 4 on medium weight nuclei. The Klystron-Buncher is capable of bunching the light heavy ion projectiles ^{12}C, ^{14}N, ^{16}O, and ^{18}O to packets of a few nanoseconds.[3]

In a first experiment we excited a $I^{\pi} = 11/2^-$ state with $T_{1/2} = 6$ μsec in ^{115}Te via the reactions ^{106}Pd(^{12}C,3n) and ^{102}Ru(^{16}O,3n). Both reactions populate the state strongly enough to perform an implantation experiment. As the state is rather long lived, the ^{102}Ru + ^{16}O reaction is advantageous because the ^{16}O beam is intense enough to be chopped with a very small duty cycle. Both experiments were made on natural targets. Enriched targets must be used for the implantation experiments because of the high background from the stopping metal used for the quadrupole interaction.

Our interest in the $11/2^-$ state of ^{115}Te is motivated by the recent measurement of E2 moments of $11/2^-$ states in Sn.[4] These $11/2^-$ states are largely of $h_{11/2}$ neutron single particle character, the properties of these states can be successfully described by the variation of occupation probabilities in different shells by pairing interaction. This is also true for the $h_{11/2}$ neutron state in ^{115}Te, but the quadrupole interaction of Te in Sn showed an enormous decrease of more than one order of magnitude compared to the interaction of the Sn states in Cd.[5] It is presently not clear at all, whether the addition of two protons to the magic Z=50 shell causes a large drop in nuclear deformation, but large changes in nuclear shapes might be expected near major shell closures. Another possible explanation might be a strong decrease of the Sn electric field gradient on the introduction of the Te atom in the Sn lattice. Implantation into suitable host lattices should clarify this point and help to determine whether a strong change in nuclear shape takes place between Z=50 and Z=52.

---

1. W. Bartsch, W. Leitz, H.-E. Mahnke, W. Semmler, R. Sielemann, and Th. Wichert, Z. Physik *B21*, 131 (1975).
2. C. Budtz-Jorgensen, K. Bonde Nielsen, F. Abildskov, T.K. Laursen, W. Semmler, R. Sielemann, and Th. Wichert, International Meeting on Hyperfine Interactions, Leuven, 1975 (unpublished).
3. See section 12.7 of this report.
4. F. Dimmling, D. Riegel, K.-G. Rensfelt, and C.-J. Herrlander, Phys. Lett. *55B*, 293 (1975).
5. E. Ivanov, W. Leitz, E. Recknagel, E. Schlodder, M. Ionescu-Bujor, A. Jordachescu, D. Plostinaru, S. Vajda, Annual Report Sektor Kernphysik am Hahn-Meitner-Institut für Kernforschung Berlin (1974), p. 81.

3.6 Isomeric Quasiparticle States in ^{174}Hf

H. Bohn,[†] Y-d Chan, H. Ejiri,[††] and R. Sielemann

Last year[1] we reported results of a search for isomeric quasiparticle states in the even-even deformed nucleus ^{174}Hf. We used the reaction ^{175}Lu(p,2n)^{174}Hf at bombarding energies 12-, 14-, and 16-MeV induced by a chopped proton beam. We found evidence for three isomeric states between 1.5- and 2-MeV excitation energy with half-lives of 0.18-, 1.4-, and 2.1 μsec. The 0.18 μsec halflife could be ascribed to a $J^{\pi}K = (6^+6)$ bandhead at 1549 keV which decays by K- forbidden transitions to be 6^+,4^+ members of the ground state rotational band. We could ascribe the 1.4 μsec halflife to a state at 1902 keV

decaying into the (6^+6) state via a 353 keV transition. The 2.1 μsec halflife was carried by a 188 keV transition which is known to connect the first excited state and the ground state of the band built on the (6^+6) state at 1549 keV. In addition to the delayed γ-rays a strong prompt component was visible.

Our subsequent data analysis of the low energy γ-rays revealed a line at 60 keV between the K_α and K_β x-rays of Hf with the halflife of the 188 keV transition (2.1 μsec). The x-rays clearly show a composite decay curve due to contributions from the different isomeric states. In addition, a weak line at 248 keV was found which has, within rather large error bars, the same life time of both the 188- and 60 keV transitions. This is likely to be the direct transition from the isomeric state to the (6^+6) state. We place this isomeric state with $T_{1/2}$ = 2.1 μsec at 1797 keV. Additional confirmation for this assignment comes from conversion electron data. Intensity balance shows that the 60 keV line is only weakly converted, therefore it should be a highly retarded E1 transition. Analogy with ^{176}Hf indicates that the isomeric state is probably the expected (8^-8) band head.

We note several features of particular interest:

The hindrance factor for the fourtimes-forbidden transition $(6^+6)\rightarrow(4^+0)$ (assuming E2 transition as in neighboring nuclei) is an order of magnitude smaller compared with the corresponding transition in ^{176}Hf and even more so compared with ^{174}Yb. This is strongly correlated with the amount of the two proton content of the wave function (almost pure [pp] in ^{174}Hf, almost pure [nn] in ^{174}Yb, strongly mixed in ^{176}Hf).[3]

In contrast to neighboring Hf isotopes which generally have two isomeric states under 2 MeV excitation energy, we observe three. The 1.4 μsec state at 1902 keV has no observable branches to either the 1797 keV state or the first excited state (7^+6) based on the 1549 keV state band. One reason might be that similar to the 1549 keV state the other isomeric states are high purity [pp] or [nn] bands so that interband transitions are additionally inhibited between different particle-type bands.

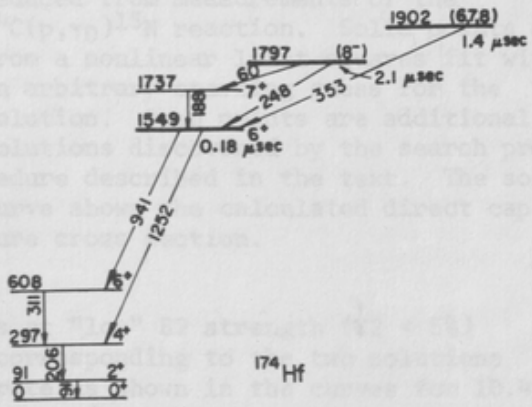

Fig. 3.6-1. Partial level scheme for ^{174}Hf showing the decay of the isomeric quasiparticle states.

---

† Permanent address: Institut für Kernphysik und Nukleare Festkörperphysik, Technische Univ. München, D-8046, Garching, Germany.

†† Permanent address: Department of Physics, Osaka University, Toyonaka, Osaka, Japan.

1. Nuclear Physics Laboratory Annual Report, University of

Washington (1976), p. 72.
2. J. Borggreen, N.J.S. Hansen, J. Pedersen, L. Westgaard, J. Zylicz, and S. Bjornholm, Nucl. Phys. *A96*, 561 (1967).
3. H. Ejiri, G.B. Hagemann, and T. Hammer, Proc. Int. Conf. on Nuclear Moments and Nuclear Structure, Osaka, 1972, p. 428.

3.7 Search for a Shape Isomeric State in ^{32}S

K.G. Bernhardt, H. Bohn, Y-d Chan, K. Green, and R. Vandenbosch

The existence of a secondary minimum in the potential energy surface of ^{32}S has been theoretically predicted in a number of independent calculations.[1-3] Although there is some disagreement on the numerical values, the consensus suggests a prolate isomeric minimum with deformation $\varepsilon \approx 0.6$ at 4 to 9 MeV above the ground state. It is not feasible to directly measure the lifetime of such a state as it is anticipated to be too short for conventional methods. Extrapolation of lifetimes from measurements on spontaneous fission isomers support this assumption. We are instead attempting to measure the alpha branching ratio ($\Gamma(\alpha)/\Gamma(\gamma)$) of states in the region 7-12 MeV in the hope of detecting anomolies indicative of possible shape isomerism. Preliminary particle spectra have been taken via the $^{24}Mg(^{12}C,\alpha)^{32}S^{*}(\alpha)^{28}Si$ reaction, the analysis of which is still in progress.

---

1. P.K. Sheline, I. Ragnarsson and S.G. Nilsson, Phys. Lett. *41B*, 115-121 (1972).
2. P.G. Zint and U. Mosel, Phys. Lett. *58B*, 269-272 (1975).
3. R.Y. Cusson, R. Hilko and D. Kolb, Nuclear Physics *A270*, 437-470 (1976).

4.1 Ambiguities in the Determination of Quadrupole Strength from $(\vec{p},\gamma_0)$ Studies

J. Bussoletti, K. Ebisawa, K. Snover, T. Trainor

Continuation of our studies (Ref 1) of $^{14}C\ (p,\gamma_0)^{15}N$ has revealed information which suggests that these types of experiments suffer from some ambiguities which weaken the realiability of the "model-independent" determination of the quadrupole (E2) capture cross section.

Shown in Fig. 4.1-1 is the excitation function of the E2 cross section as deduced by a fit to the measured yields and polarization asymmetries observed[1] in the $^{14}C(\vec{p},\gamma_0)^{15}N$ reaction. These results arise from a non-linear least squares fit which begins with an arbitrary starting guess. Two solutions are found with identical E2 cross sections; the solutions differ in the ratio of s-wave to d-wave dipole (E1) capture probability. Since the search procedure is a non-linear one, there is no assurance that other solutions do not exist.

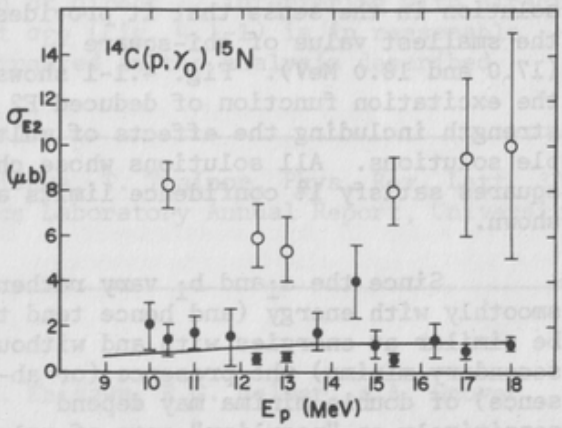

Fig. 4.1-1. E2 total cross sections deduced from measurements of the $^{14}C(p,\gamma_0)^{15}N$ reaction. Solid points are from a nonlinear least squares fit with an arbitrary starting guess for the solution. Open points are additional solutions discovered by the search procedure described in the text. The solid curve shows the calculated direct capture cross section.

We have investigated the possible existence of additional solutions by the following technique. The size of the E2 cross section is fixed at an arbitrary value. The best fit to the measurements is then obtained by allowing all other parameters to vary. The chi-square for the resulting fit is noted. The E2 cross section is stepped to a new value and the process is repeated. Thus the multidimensional chi-square surface is projected along the E2 strength axis. These projections are shown in Fig. 4.1-2.

All curves show a pair of solutions at "low" E2 strength (E2 < 5%) As the E2 strength increases the surfaces corresponding to the two solutions (dominant s-wave and dominant d-wave) separate as shown in the curves for 10.4 MeV and 12.37 MeV bombarding energy. In some cases (as at 11.0 or 13.7 MeV) an additional minimum appears after the curves have separated, though the minimum is at such a large value of chi-square that it can be excluded at some reasonable confidence level (1% for both 11.0 MeV and 13.7 MeV). However, additional cases occur as at 10.4, 12.37, 17.0 and 18.0 MeV where the additional solution cannot be excluded on statistical grounds and in fact is occasionally the preferred

Fig. 4.1-2. Projections of the multi-dimensional chi-square surface along the E2 strength axis. Note indications of multiple branches of the surface (E_p = 12.37 and E_p = 10.4 MeV). The solutions in all cases are doubly degenerate at the minimum indicated by the arrow. The 1% confidence limit (CL) value for the chi-square is indicated by the straight horizontal line in each graph.

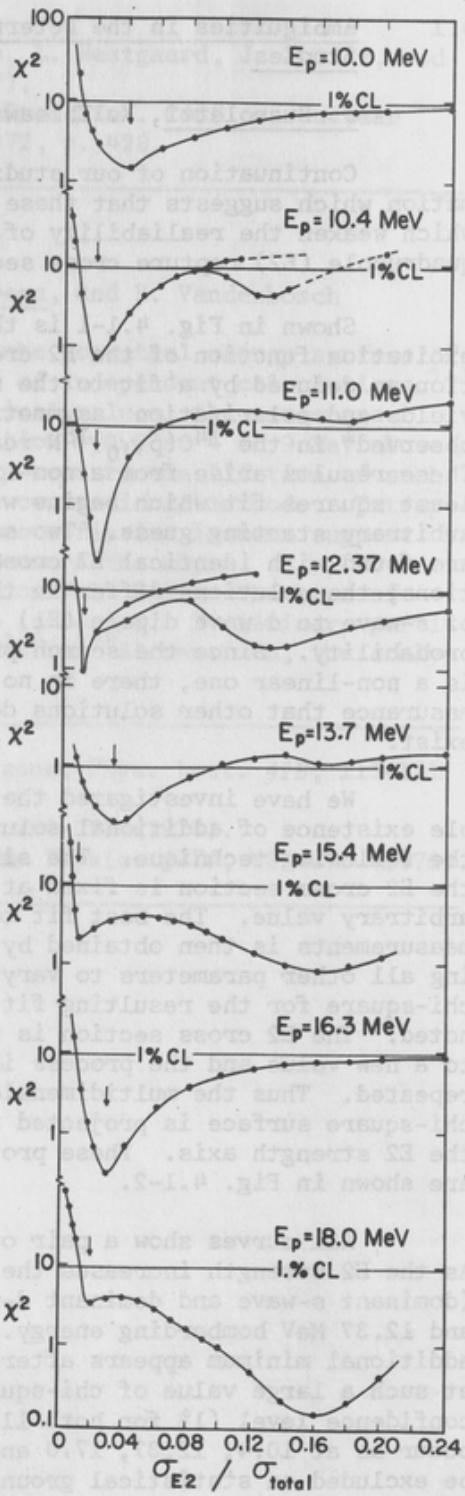

solution in the sense that it provides the smallest value of chi-square (17.0 and 18.0 MeV). Fig. 4.1-1 shows the excitation function of deduced E2 strength including the effects of multiple solutions. All solutions whose chi-squares satisfy 1% confidence limits are shown.

Since the a_i and b_i vary rather smoothly with energy (and hence tend to be similar at energies with and without secondary minima) the presence (or absence) of double minima may depend sensitively on "peculiar" sets of values and/or errors for the Legendre coefficients. We will investigate this possibility by examining the χ^2 plots corresponding to different data subsets at the same energy. We will also examine the possibility that double minima are a general consequence of the non-linear nature of the problem by seeing if different choices of starting parameters will bring out the secondary minima at energies where we have found only one minimum.

Our final understanding of this problem must await these further tests. However, based on what we know now, our results bias us toward the small σ_{E2} solution since (a) these solutions appear at every energy at a statistically acceptable level, whereas the large σ_{E2} solutions do not (indeed, at some energies the large σ_{E2} solutions corre-

spond to unacceptably poor χ^2, indicating they must not be the physical solution) and (b) the smooth variation of the a_i and b_i with energy would result naturally from a smooth variation in σ_{E2} (corresponding to the small solution everywhere) but would be peculiar if σ_{E2} varies strongly with energy.

It is clear in any case that the ambiguities discussed above make it difficult to make a definitive "model independent" statement about $\sigma E2$. This problem would be compounded by possible M1 effects which are ignored in the above treatment.

The strongest statement that one can make at this point about the capture process is a model dependent one, based on comparisons of direct-semidirect (DSD) calculations with experiment. As shown in Ref. 1, the measured a_i and b_i are in reasonably good agreement with a calculation of direct E2 interfering with direct plus resonance E1, and the calculated direct σ_{E2} (Fig. 4.1-1) is in reasonable agreement with the small solution values extracted in the analysis described above.

---

1. K.A. Snover, J.E. Bussoletti, K. Ebisawa, T. Trainor, Phys. Rev. Lett. *37* 273 (1976). Also see Nuclear Physics Laboratory Annual Report, University of Washington (1976), p. 81.

4.2 E1 and E2 Strength in $^{15}N(\vec{p},\gamma_0)^{16}O$

E.G. Adelberger, J.E. Bussoletti, K. Ebisawa, R.G. Helmer, K.A. Snover and T.A. Trainor

The results of our measurements[1] of $^{14}C(\vec{p},\gamma_0)^{15}N$ seemed to indicate that the E2 strength distribution in ^{15}N is qualitatively different than the E2 strength distribution in ^{16}O as reported by Stanford[2] in their measurements of $^{15}N(\vec{p},\gamma_0)^{16}O$. No strong evidence for a peak in the E2 strength was evident in the $^{14}C(\vec{p},\gamma_0)^{15}N$ measurements; the deduced strength was consistent with direct capture only, and exhausted less than 10% of the isoscaler (IS) energy weighted sum rule. Stanford reported from measurements on ^{15}N that $\sim$35% of the IS E2 sum rule was exhausted by the proton channel in ^{16}O. Their results suggest a peak in the E2 strength at about 24 MeV excitation energy. They attributed this peak to the giant guadrupole resonance (GQR). Since both of these measurements determine strength only in the proton channel (the neutron channel and the alpha channels would also be expected to contribute to the decay of an isoscalar E2 resonance) their analysis implies the presence of an E2 giant resonance which exhausts most of the energy weighted sum rule. If the giant E2 resonance is as universal a phenomenon as is the giant dipole resonance, then neighboring nuclei ought to exhibit similar behavior. Our analysis of the $^{14}C(\vec{p},\gamma_0)^{15}N$ measurements indicated that either this phenomenon is not as universal as supposed or that the strength is spread out over a much greater area in excitation in ^{15}N than in ^{16}O. Thus we have performed measurements of the $^{15}N(\vec{p},\gamma_0)^{16}O$ reaction to attempt to corroborate the Stanford results and define more clearly the problems of interpretation.

Our measurements followed the general scheme already described for our previous studies in ^{15}N (Ref. 1). At each bombardment energy four separate measurements were made of the yield and polarization asymmetry angular distributions of gamma rays emitted in the $^{15}N(p,\gamma_0)^{16}O$ reaction. The target was a gas cell filled with ^{15}N gas. A single large area kapton foil served as both the entrance and exit window. Two ΔE-E telescopes of silicon detectors at $\pm 160°$ were used to continuously monitor the beam polarization and target thickness. A composite peak consisting of elastic scattering of protons from the ^{15}N in the cell and the ^{12}C, ^{14}N and ^{16}O in the front and rear kapton foil was used to determine the beam polarization. (The analyzing power of the composite peak was measured in a separate experiment.) The reaction $^{15}N(p,\alpha_0)^{12}C$ was used to monitor the thickness of the ^{15}N target; the detector telescopes allowed a separation of the alpha reactions from the proton reactions. The collimation system for the charged particle detectors was designed so that the detectors viewed the same interaction volume in the gas cell as did the NaI crystal.

The four separate measurements of "spin-up" and "spin-down" yields at each angle were averaged together to provide an average yield to be used in a least squares analysis to determine the Legendre polynomial expansion coefficients at each energy. The averaging process rather closely resembles a one parameter fit to a set of four measurements. The distribution of chi-squares for "fits" of the yield and polarization asymmetry to their average quantities are shown in Fig. 4.2-1, along with the expected chi-square distribution for three degrees of freedom. Thus there is little evidence for nonstatistical behavior of the data.

The Legendre coefficients determined from the average yields are used in a non-linear least squares analysis to determine the capture amplitudes. In order to guarantee that the capture amplitudes which provide the best fit to the Legendre coefficients are the same set of numbers which provide the best fit to the original yield measurements, it is essential that the nonlinear fit be performed with a non-diagonal weight matrix. It can be proven that the appropriate weight matrix is the normal matrix for the fit that determines the Legendre coefficients. This fact seems not to have been appreciated in previous analyses.

In our analysis presented here we include all Legendre coefficients to determine the capture aplitudes. While omission of the a_1 and b_1 coefficients as done by Stanford[2] allows in principle some consistency test for the presence of M1 radiation, it places the burden of the extraction of the small E2 strength more upon those coefficients which depend on the E2 amplitudes in second order. This creates larger errors in the determined E2 strength. Moreover the non-linear fit becomes a problem with zero degrees of freedom when any pair of Legendre coefficients are omitted. This nullifies the usefulness of the chi-square magnitude to determine statistically significant solutions. In addition, omission of the a_1 and b_1 coefficients makes the minima in the chi-square surface extremely narrow; thus it may be easy to miss multiple solutions. To allow direct comparison with the results of Stanford we have nonetheless performed an analysis of our data in which we also exclude the a_1 and b_1 parameters from the fit. Preliminary analysis shows that some of our ^{16}O data exhibit the same multiplicities of solutions at a given energy that we have observed in our $^{14}C(\vec{p},\gamma_0)^{15}N$ data, though there presently are fewer energies where ambiguities have been found which are statistically significant. (See Section 4.1 of this report).

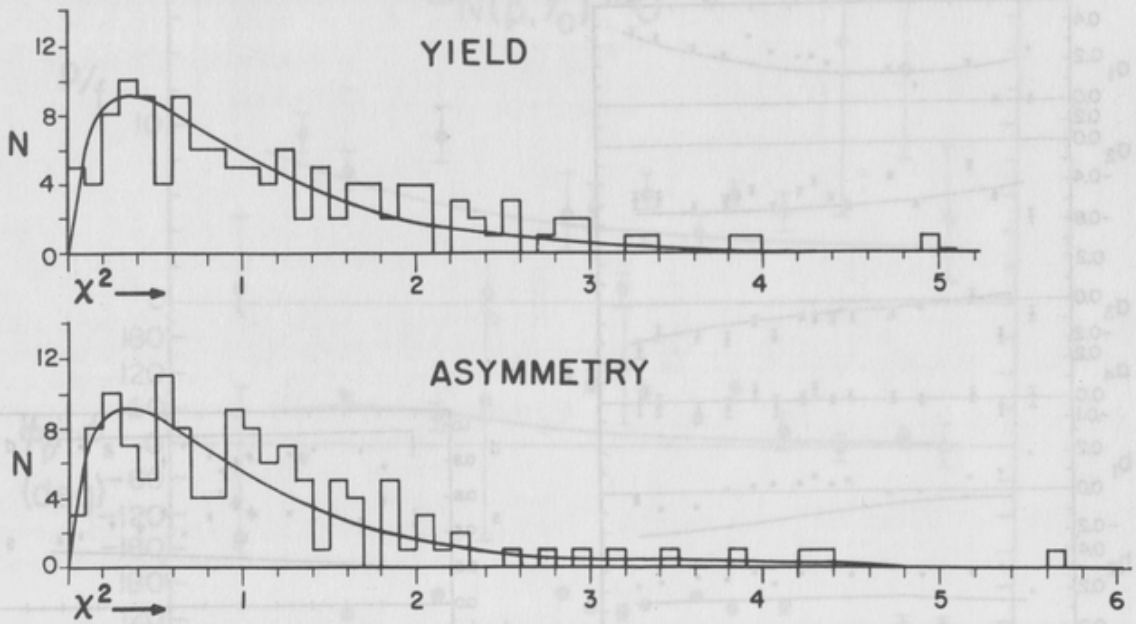

Fig. 4.2-1. Distributions of the χ^2 for the measured yields and asymmetrics compared to the mean (at each angle). The curves represent the expected χ^2 distribution for 3 degrees of freedom.

The excitation functions for the Legendre coefficients are shown in Fig. 4.2-2, along with the predictions of the values of the coefficients from direct-semidirect (DSD) model calculations[1,3]. Again we find as in the measurements of $^{14}C(p,\gamma_0)^{15}N$ that the Legendre coefficients are reasonably consistent with direct capture alone.

The E1 parameters are shown in Fig. 4.2-3. The generally featureless dependence on excitation energy of the $\phi_d-\phi_s$ phase difference is in agreement with the results reported by Stanford[1], as is the fluctuation in the relative magnitudes of s-wave and d-wave capture. The E2 amplitude ratio p/f and phase differences are shown in Fig. 4.2-4. In Fig. 4.2-5, the solid points show the E strength determined from the analysis which begins with the same arbitrary starting guess for the solutions and includes all Legendre coefficients. The open circles in Fig. 4.2-5 show the E2 strengths deduced by omitting the a_1 and b_1 coefficients. The presence of more than one solid point at several energies indicates statistically acceptable "second" solutions (see the preceding $^{14}C(p,\gamma)$ discussion). This analysis, including searches of our data for additional solutions has not yet been completed.

Our interpretation of these results is similar to the preceeding discussion regarding the $^{14}C(\vec{p},\gamma_0)^{15}N$ reaction. The existence of second solutions at

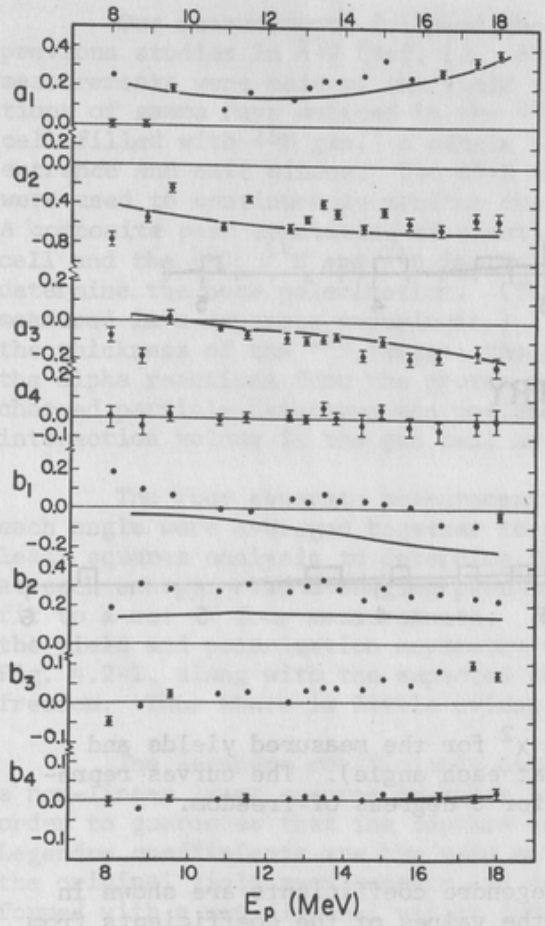

Fig. 4.2-2. Angular distribution coefficients for $^{15}N(\vec{p},\gamma_0)^{16}O$ versus lab bombarding energy. The solid curves here and in the following figures are from a DSD calculation (see text).

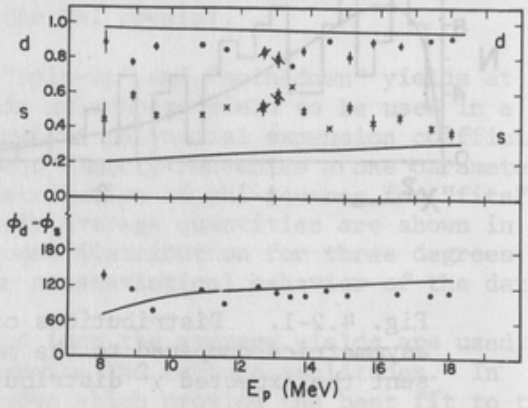

Fig. 4.2-3. E1 amplitudes and phase difference (dominant d-wave solutions) for the analysis of the results of Fig. 4.2-2.

some energies, and the possible contributions of M1 complicate attempts at a "model-independent" analysis of the data. At most energies the fits excluding a_1 and b_1 tend to give larger σ_{E2} (and larger errors). We are currently investigating whether this tendency can be accounted for solely in terms of statistics. The agreement with the DSD calculations (including direct E2 and direct plus resonance E1) is comparable with one $^{14}C(\vec{p},\gamma_0)$ case. From the analysis involving all coefficients, there is little evidence for a strong GQR, as reported previously[2], although there appears to be somewhat of an excess E2 cross section (relative to direct capture) near Ep = 9 MeV and 13.5 MeV.

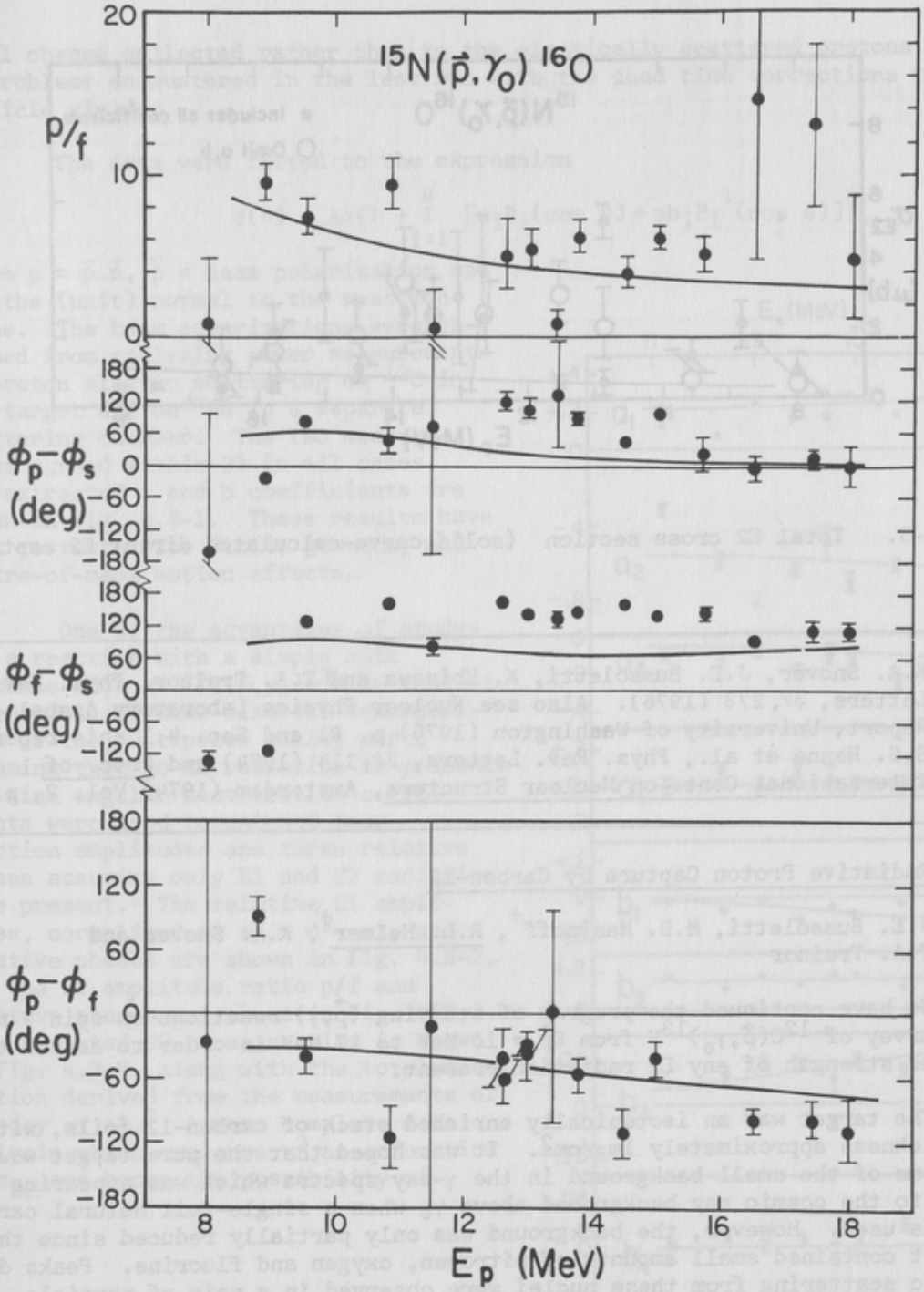

Fig. 4.2-4. E2 amplitude ratio p/f and phase differences.

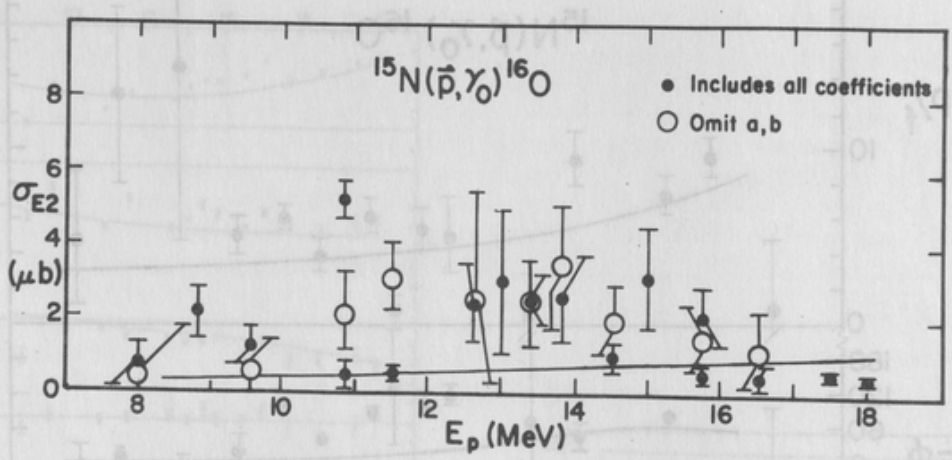

Fig. 4.2-5. Total E2 cross section (solid curve-calculated direct E2 capture).

---

1. K.A. Snover, J.E. Bussoletti, K. Ebisawa and T.A. Trainor, Phys. Rev. Letters, *37*, 273 (1976). Also see Nuclear Physics Laboratory Annual Report, University of Washington (1976) p. 81 and Sec. 4.1 this report.
2. S.S. Hanna et al., Phys. Rev. Letters, *32*, 114 (1974) and Proc. of International Cont. on Nuclear Structure, Amsterdam (1974) Vol. 2, p. 249.

4.3 Radiative Proton Capture by Carbon-12

J.E. Bussoletti, M.D. Hasinoff†, R.L. Helmer†, K.A. Snover and T.A. Trainor

We have continued the program of studying $(\vec{p},\gamma)$ reactions on spin 0 nuclei with a survey of $^{12}C(\vec{p},\gamma_0)^{13}N$ from $E\vec{p}$ = 10 MeV to 17 MeV in order to assess the nature and strength of any E2 radiation present.

The target was an isotopically enriched stack of carbon-12 foils, with total thickness approximately $1 mg/cm^2$. It was hoped that the pure target would reduce some of the small background in the γ-ray spectra which was appearing in addition to the cosmic ray background above γ_0 when a single-foil natural carbon target was used. However, the background was only partially reduced since the new target contained small amounts of nitrogen, oxygen and fluorine. Peaks due to elastic scattering from these nuclei were observed in a pair of particle detectors located at 160° to the beam direction. The final results are not very sensitive to the manner in which this background is treated.

The spectra were analyzed as described in last year's Annual Report.[1] It has been found more satisfactory to normalize the gamma ray yields to the

total charge collected rather than to the elastically scattered protons because of problems encountered in the last run with the dead time corrections to the particle yields.

The data were fitted to the expression

$$\sigma(\theta) = A\sigma\{1 + \sum_{i=1}^{4} [a_i P_i(\cos\theta) + pb_i P_i^1(\cos\theta)]\},$$

where $p = \vec{p}.\vec{n}$, $\vec{p}$ = beam polarization and $\vec{n}$ = the (unit) normal to the reaction plane. The beam polarizations were obtained from analyzing power measurements of proton elastic scattering on ^{12}C in the target and on ^{4}He in a separate scattering chamber. The two measurements agreed within 2% in all cases. The extracted a and b coefficients are shown in Fig. 4.3-1. These results have been corrected for finite geometry and centre-of-mass motion effects.

One of the advantages of studying a reaction with a simple spin sequence such as $^{12}C(\vec{p},\gamma_0)^{13}N$ is that it is possible to make discrete decomposition of the multipoles taking part, assuming that no M1 radiation is present. The nine angular distribution coefficients were used to extract four reaction amplitudes and three relative phases assuming only E1 and E2 radiation were present. The relative E1 amplitudes, normalized to $s^2 + d^2 = 1$, and relative phases are shown in Fig. 4.3-2, and the E2 amplitude ratio p/f and relative phases are shown in Fig. 4.3-3. The extracted E2 cross section is shown in Fig. 4.3-4, along with the total cross section derived from the measurements of Measday et al.[2] A more complete data analysis which explores χ^2 as a function of σ_{E2} and hence the possibility of

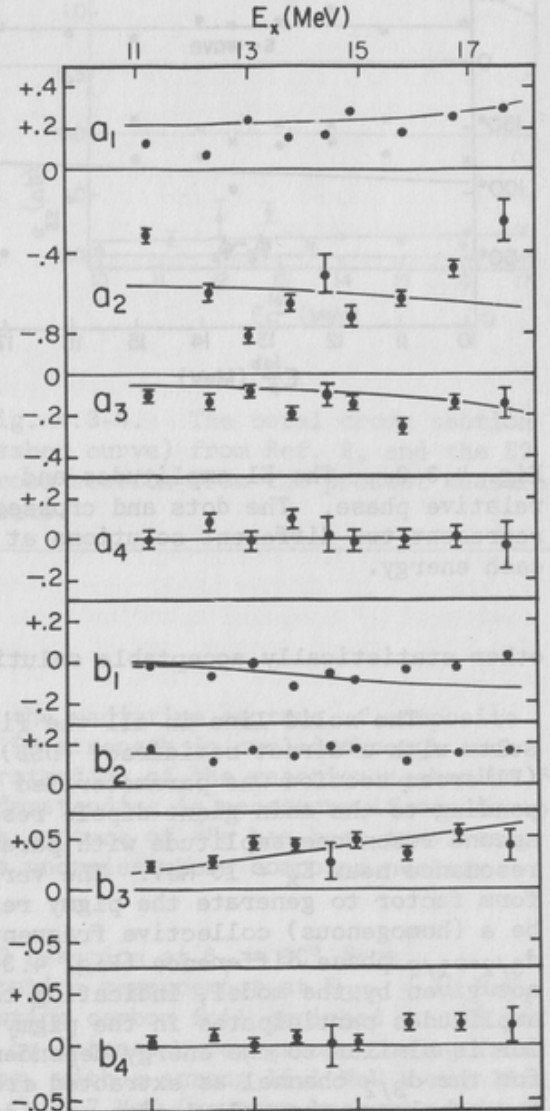

Fig. 4.3-1. Angular distribution coefficients for $^{12}C(\vec{p},\gamma)^{13}N$. The solid curves are from a first attempt to calculate the coefficients with a DSD model (see text).

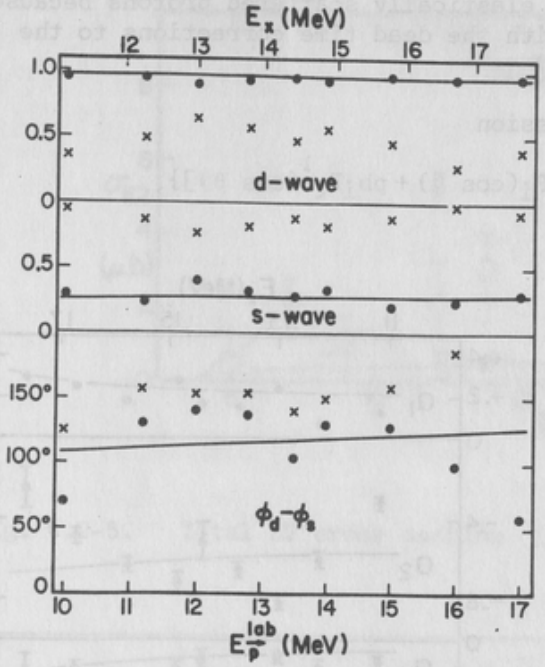

Fig. 4.3-2. The El amplitudes and relative phase. The dots and crosses represent two different solutions at each energy.

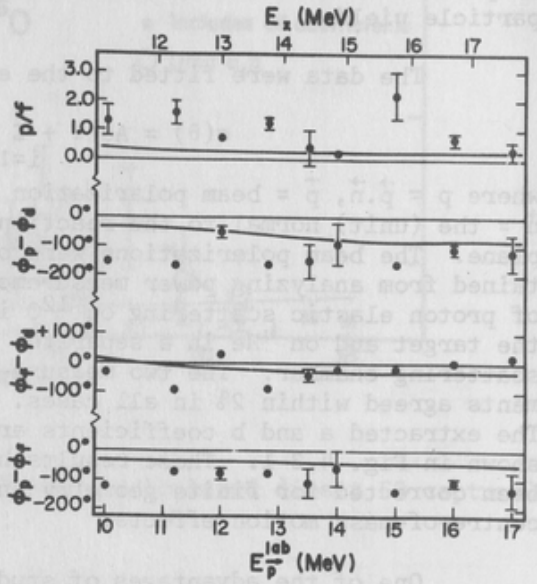

Fig. 4.3-3. The E2 amplitude ratio and relative phases.

other statistically acceptable solutions (see Sec 4.1) is in progress.

The solid line in all the figures is a first attempt at fitting the results with a direct-semidirect (DSD) model calculation.[3] The shape of the total (El) cross section was parameterized by including a resonant amplitude corresponding to the main giant-dipole resonance near E_x = 22 MeV, along with a second resonance amplitude with parameters adjusted to mock up the "pigmy" resonance near E_x = 13 MeV. The very large magnitude needed for the collective form factor to generate the pigmy resonance amplitude indicates that it cannot be a (homogenous) collective fragment of the GDR. Indeed, the experimental $d_{3/2}$-$s_{1/2}$ phase difference (Fig. 4.3-2) shows a resonance-like energy dependence not given by the model, indicating that perhaps only one of the El reaction amplitudes participates in the pigmy resonance. In fact, this resonance behavior is similar to the energy dependence of the partial absorption cross section for the $d_{3/2}$ channel as extracted from elastic proton scattering[4] on ^{12}C. Nevertheless, the calculation provides a reasonable rough parameterization of the El amplitudes and phases and the addition of direct (but no collective) E2 radiation provides a good description of the angular distribution coefficients as well as the extracted E2 cross section.

Efforts are currently under way to refine our theoretical description of the capture process in this energy region.

The energy weighted integral of σ_{E2} from 10 MeV to 17 MeV is $\int\sigma_{E2}(\gamma,p_o)dE/E^2 = 0.7 \pm 0.3$ μb/MeV, representing 14 ± 6% of the isoscalar sum rule.

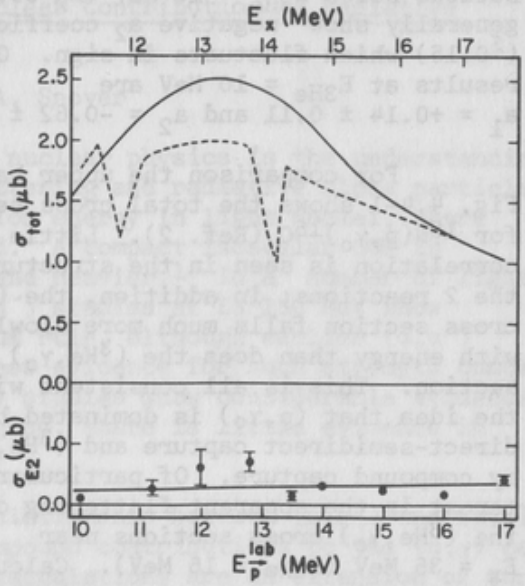

Fig. 4.3-4. The total cross section dashed curve) from Ref. 2, and the E2 cross section from the present measurements.

---

† Department of Physics, University of British Columbia, Vancouver, Canada.

1. Nuclear Physics Laboratory Annual Report, University of Washington (1975), p. 42.
2. D.F. Measday, M. Hasinoff and D.L. Johnson, Can. J. Phys. *51* 1227 (1973).
3. K.A. Snover and K. Ebisawa, Nuclear Physics Laboratory Annual Report, University of Washington, 1976, and to be published.
4. H. Meyer, private communication.

4.4 The $^{13}C(^3He,\gamma_o)^{16}O$ Reaction

K. Ebisawa and K.A. Snover

Our primary motivation in studying the radiative capture of composite particles is to see if one can leave about E2 strength in nuclei through such measurements. Of interest also is an understanding of the reaction mechanism for the capture process, and indeed such an understanding is necessary if one is to learn about nuclear E2 strength. Radiative capture of ^{3}He has been previously measured in several light nuclei at low ^{3}He energies where compound nuclear contributions are important.

We have measured the $^{13}C(^3He,\gamma_o)^{16}O$ reaction at $\theta_\gamma = 90°$ from $E_{3He} = 4$ to 18 MeV, with an angular distribution measurement at $E_{3He} = 10$ MeV. The target used was a 450 mg/cm^2 self-supporting carbon foil enriched to 97% ^{13}C. The data collection was count-rate limited by intense γ-ray groups coming from transfer reactions populating excited states, with a strong 15.1 MeV γ-ray line from (^{3}He,α) and a variety of lines below $\sim$10.7 MeV (neutron background in the spectrum was relatively weak). The results for the 90° cross section are shown in Fig. 4.4-1, along with previous measurements at lower energies.[1] The sharp resonance behavior of the cross section, with steep falloff at higher energies, indicates the reaction is dominated by compound-like processes. Angular distri-

butions below $E_{^3He}$ = 10 MeV (E_x=30.9 MeV) generally show[1] negative a_2 coefficients ($\lesssim$0.15) which fluctuate in sign. Our results at $E_{^3He}$ = 10 MeV are $a_1 = +0.14 \pm 0.11$ and $a_2 = -0.62 \pm 0.22$.

For comparison the upper half of Fig. 4.4-1 shows the total cross section for $^{15}N(p,\gamma_0)^{16}O$ (Ref. 2). Little correlation is seen in the structure in the 2 reactions; in addition, the (p,γ_0) cross section falls much more slowly with energy than does the $(^3He,\gamma_0)$ cross section. This is all consistent with the idea that (p,γ_0) is dominated by direct-semidirect capture and $(^3He,\gamma_0)$ by compound capture. Of particular interest is the apparent flattening out of the $(^3He,\gamma_0)$ cross sections near E_x = 36 MeV ($E_{^3He}$ = 16 MeV). Calculations are in progress to see whether this could be due to a direct-semidirect component.

The nonzero a_1 coefficients indicate the presence of E2/M1 radiation, and the fluctuating sign indicates rapid phase variations which would result from either the E1 or the E2/M1 capture being dominated by compound contributions. The E2/M1 cross section can be crudely estimated to be $\sim 10^{-2}$ times smaller than σ_{E2} in (p,γ_0) from a comparison of A_0 and a_1 coefficients for the 2 reactions. Since σ_{E2} in (p,γ) is very roughly 2% of the E2 sum rule per MeV in the giant-dipole-resonance region, σ_{E2} in $(^3He,\gamma_0)$ is quite small indeed.

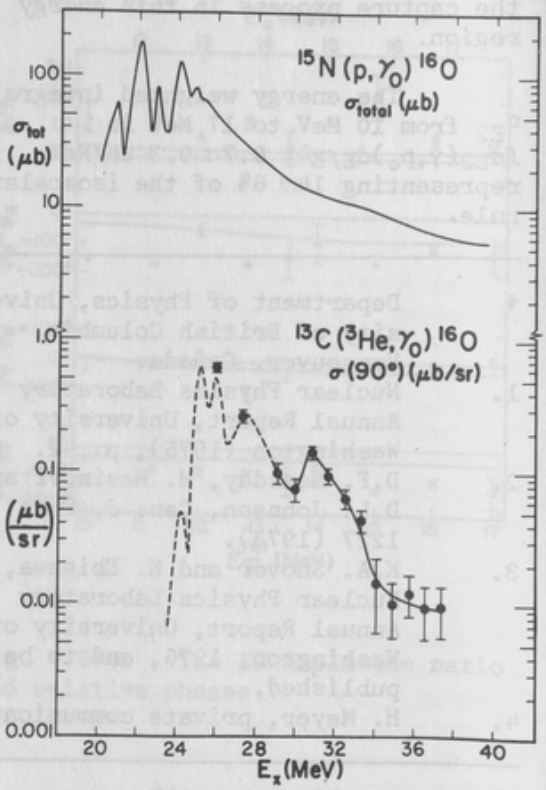

Fig. 4.4-1. Lower half: the 90° cross section for $^{13}C(^3He,\gamma_0)^{16}O$ versus excitation energy in ^{16}O. Data points and solid curve-present results; dashed curve-Ref. 1. Upper half: total cross sections for $^{15}N(p,\gamma_0)^{16}O$ -Ref. 2.

1. E. Ventura et al, Stanford Univ. Prog. Report, 1972.
2. P. Paul, K.A. Snover, J. Noe and E.K. Warburton, to be published; W.J. O'Connell, Ph.D. thesis, Stanford Univ., 1969.

4.5 Direct, Semi-direct and Compound Nuclear Contribution to Radiative Alpha Particle Capture

J.E. Bussoletti, K. Ebisawa, and K.A. Snover

An issue of outstanding interest in nuclear physics is the understanding of the relation between inelastic alpha scattering and radiative alpha particle capture in the region of 10-30 MeV excitation energy in light nuclei, where collective isoscalar E2 strength is expected. A compact isoscalar GQR is observed in (α, α') in nuclei near mass 40 and heavier.[1] In a number of light nuclei, including ^{16}O and ^{20}Ne, recent (α, α') studies at $E\alpha \sim 150$ MeV show evidence[2,3,4] for a GQR with $\sim$30% of the sum rule, although earlier (α,α') studies at lower bombarding energies show less evidence for such strength concentrations. On the other hand, although (α,γ) studies show considerable evidence for E2 strength spread out below the GQR region, there is little evidence in general from such studies for a compact GQR.

In order to better understand the relationship between (α,α') and (α,γ), we have calculated direct-semidirect and compound contributions to the (α,γ) capture process, for both E2 and E1. The DSD calculations are an extension of our previous work[5] on (p,γ). In the semidirect process, the reaction proceeds via 1-step excitation of the collective resonance with an amplitude proportional to the matrix element of the collective form factor taken between the initial scattering state and final bound state of the particle. This amplitude is closely related to the amplitude calculated in DWBA for (α,α') excitation of the same collective resonance as a final state, the main difference being that in the latter case the initial and final α particle states are in the continuum at high energies.

Here we report such calculations for E2 radiation in $^{12}C(\alpha,\gamma_0)^{16}O$ and $^{16}O(\alpha,\gamma_0)^{20}Ne$ and for E1 and E2 radiation in $^{14}C(\alpha,\gamma_0)^{18}O$, and compare with experiment. Measurements of the $^{12}C(\alpha,\gamma_0)^{16}O$ reaction have been reported[6] which show that the E2 strength from Ex = 12 to 28 MeV amounts to 17% of the isoscalar energy weighted sum rule (EWSR) in the α_0 channel. These results are shown in Fig. 4.5-1. A concentration of E2 strength in this region has also been reported from inelastic α-scattering[2,3] and inelastic electron scattering.[7]

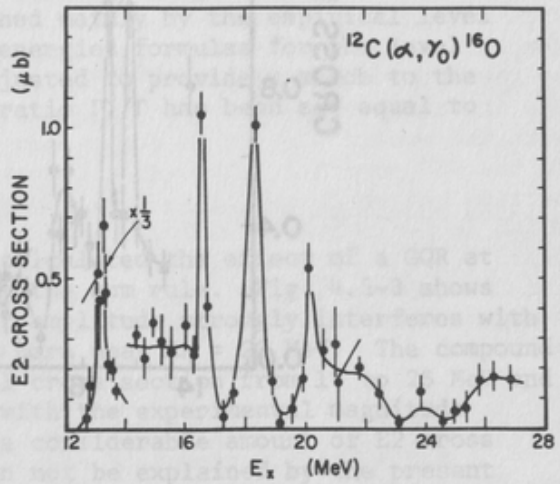

Fig. 4.5-1. Total E2 cross section for $^{12}C(\alpha,\gamma_0)^{16}O$ from Ref. 1.

Recently we measured the cross section for the $^{16}O(\alpha,\gamma_0)^{20}Ne$ reaction from E ~8 to 25 MeV using a 930 Mg/cm^2 Ta_2O_5 target and the 10 in x 10 in. Na(I) detector with anti-coincidence shield.

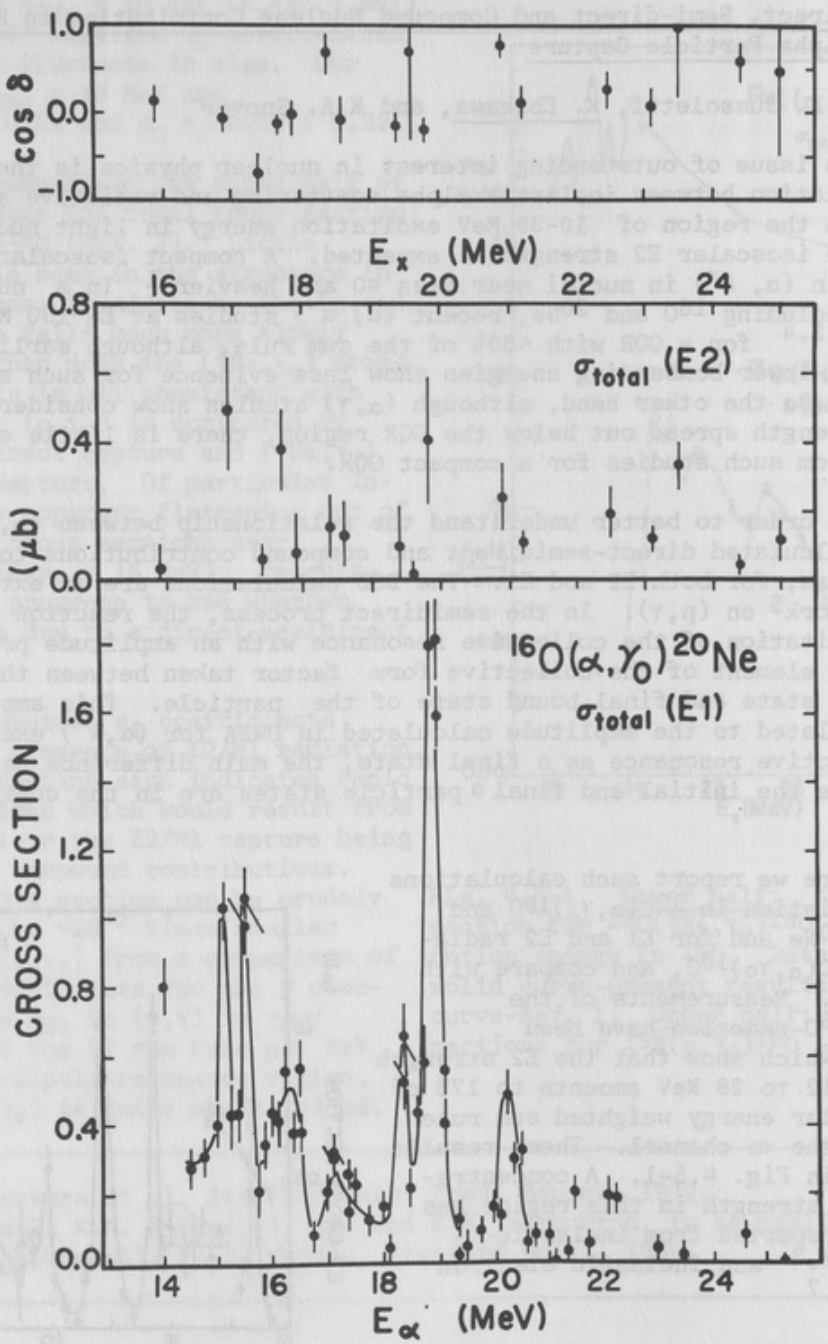

Fig. 4.5-2. E1, E2 total cross section and relative phase cos δ for $^{16}O(\alpha,\gamma_0)^{20}Ne$.

For Ex 10-14 MeV the gamma rays from inelastic scattering pile up into the γ_0 energy region. In addition to the 90° yield which was reported in the 1974 Annual Report (page 141) we have measured three-point angular distributions at a number of energys and extracted E1, E2 cross sections and the relative phase as shown in Fig. 4.5-2. The energy spacing of the data points is so coarse that we don't get much information about possible narrow structure. It is apparent that the E2 cross section is ~0.2 μbarn for E_x = 17-25 MeV.

The DSD calculations were performed in a manner similar to that described for proton capture.[5] Optical potentials derived from the work of Goldberg[8] were used to generate bound state and scattering state wave functions. For the bound state the node number N was determined from the relation

$$2N + L = \sum_{i=1}^{4} (2n_i + l_i)$$

where the sum is over the last 2 protons and 2 neutrons, yielding for the (L=0) ground state N = 2 for ^{16}O and N = 4 for ^{20}Ne. The spectroscopic factors were taken to be[9] S = 0.23 for both ^{16}O and ^{20}Ne. The form factor for the semidirect process is assumed to be proportional to dV(r)/dr where V(r) is the real central potential.

The compound E2 cross section can be written as

$$\sigma(\alpha,\gamma) = \pi \lambda^2 (2J+1) \frac{\Gamma \Gamma_\gamma^\circ}{(E_x - E_R)^2 + \Gamma^2/4} \left(\frac{E_x}{E_R}\right)^5 \left(\frac{\Gamma^\downarrow}{\Gamma}\right) B(\alpha_o)$$

where $B(\alpha_o)$ is the statistical decay probability into the α_o channel calculated numerically by a computer code.[10] $\Gamma^\downarrow$ is the spreading width of the doorway state and Γ_γ° is the doorway radiation width evaluated at E = E_R. For $E_x \leq$ 21 MeV in ^{12}C and ^{16}O the statistical decay is determined mainly by the empirical level densities of the residual nuclei; at higher energies formulas for the level densities[11] were employed with parameters adjusted to provide a match to the empirical densities at lower energies. The ratio $\Gamma^\downarrow/\Gamma$ has been set equal to unity for simplicity (see below).

(1) The $^{12}C(\alpha,\gamma_0)^{16}O$ Reaction

For demonstration purposes, we have calculated the effect of a GQR at 22 MeV with a total width of 4 MeV and 50% of the sum rule. Fig. 4.5-3 shows calculations of each process. The semidirect amplitude strongly interferes with the direct one producing a maximum of ~0.02 μbarn near Ex = 23 MeV. The compound process on the other hand dominates the total cross section from 13 to 26 MeV and reaches as large as 0.2 μbarn, which agrees with the experimental magnitude around 20~24 MeV. It is no surprise that the considerable amount of E2 cross section between 13 to 20 MeV (Fig. 4.5-1) can not be explained by the present simple Breight-Wigner approximation. If one takes the maximum E2 strength between 18~28 MeV as determined in (α,α') (Ref. 3) and assume compound prosses only, one obtains an improved (α,γ_0) yield as shown by the heavy solid line in Fig. 4.5-3. Thus compound nuclear formation can be considered to be a major

process, and is one order of magnitude larger than the DSD cross section. It also should be noted that 17% of the sum rule for Ex = 12 to 28 MeV in the α_o channel[1] is equivalent to 100% of the sum rule in all channels if the decays are statistical. Along with 25% of the sum rule below E_x 13 MeV, this would imply $\sim$25% of the sum rule strength below 28 MeV. It is always possible, of course, that there is less E2 strength in the high energy region, and that this strength decays with an enhanced α_o decay probability.

(2) $^{16}O(\alpha,\gamma_o)^{20}Ne$

Here we illustrate the effects of GQR in ^{20}Ne and 24 MeV width and 50° of the sum rule (Fig. 4.5-4). The factor direct cross section here is a factor of 2 large than in the ^{16}O case, slightly increasing in the calculated region. Here the semidirect amplitude interferes destructively with the direct amplitude. The DSD differences in $^{16}O(\alpha,\gamma_o)$ versus $^{12}C(\alpha,\gamma_o)$ are due mainly to the node number difference in the final state (N = 4 vs. N - 2). A somewhat different optical potential (Ref. 3) gives quite similar results, with a magnitude difference of 20%. The compound cross section here is reduced by factor of 4 compared to ^{16}O due to the increased number of open channels, with the result that it is comparable to the DSD process. The over-all cross section ranges from 0.03 to 0.05 μ barn which is far below the measurements (Fig. 4.5-2). This would appear that the E2 strength in this region must decay with an enhanced α_o decay probability.

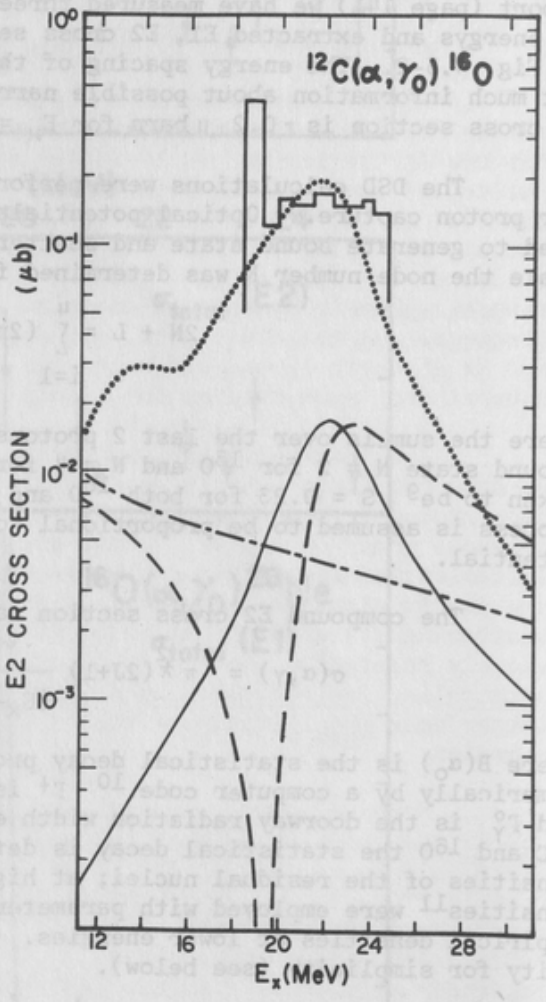

Fig. 4.5-3. Calculated E2 cross sections. Dash-dot: direct E2, fine-solid: semidirect E2, dashed: direct + semidirect E2, dotted: compound (Breit-Wigner), heavy solid: compound (derived from Ref. 3).

(3) $^{14}C(\alpha,\gamma_o)^{18}O$

Since the ^{14}C target is not a self conjugate nuclei, the E1 component of the GDR can in principle be excited in (α,γ). The differential cross section at one angle has been measured and reported previously.[12] As seen in Fig. 4.5-5 there is no prominent yield in the GDR region, E_α=18-23 MeV as contrasted with (p,γ), which typically has a peak cross section of $\sim$10 barn. The semidirect process for (α,γ) does not contribute to the GDR, since the isovector E1 form factor is

derived from the isospin-dependent part of the projectile-target interaction (the optical potential) which vanishes for the α particle. The other processes such as direct E1, direct E2, and semi-direct E2 (50% sum rule) are calculated and give about 0.06 barn to the total cross section near the GDR. (see Fig. 4.5-6) The actual DSD cross sections are likely to be smaller since the results illustrated in Fig. 4.5-6 are for the spectroscopic factor S = 1. Thus the DSD process alone fails to provide much yield for E_α=10-19 MeV. For the compound process, E2 capture is negligible, as shown, whereas E1 capture (assuring the GDR is at 23 MeV with Γ = 4 MeV) is apparently overestimated by at least a factor of 20 in the GDR region, as compared with experiment (Fig. 4.5-5). These results imply that the probability for compound decay of the GDR (taken to be unity to obtain the results shown in the figures) must be $\Gamma\downarrow/\Gamma \leq 0.05$, a limit that is not unreasonable for such a light nucleus. Such an inhibition appears unnecessary at lower energies, perhaps due to fragmentation of E1 strength. The secondary peak near E_α = 8 MeV in the compound curves (Fig. 4.5-6) is an artifact of the energy dependence of the compound branching ratio.

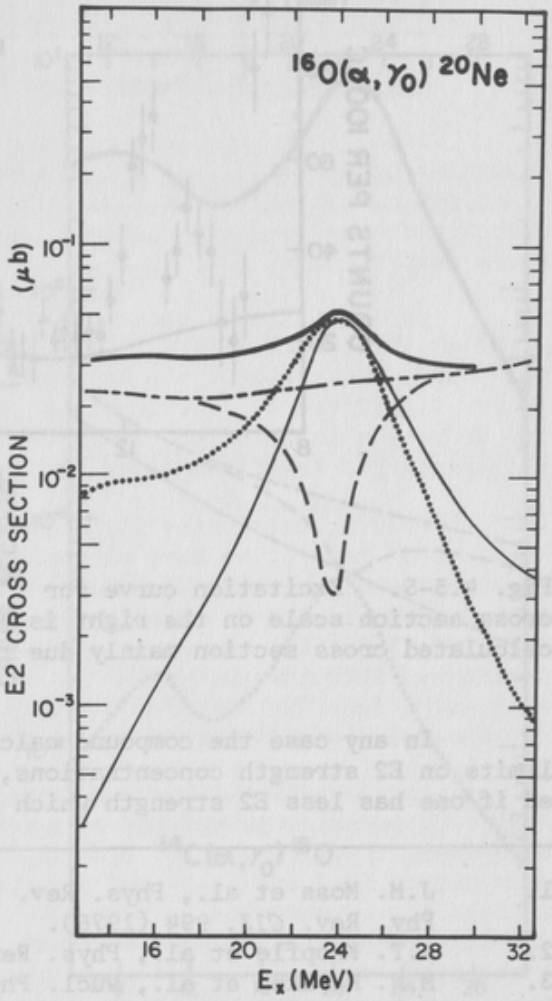

Fig. 4.5-4. Calculated E2 cross section for $^{16}O(\alpha,\gamma_0)\ ^{20}Ne$. Same notation as Fig. 4.5-3 except that heavy solid line is a sum of compound and DSD process.

The major thrust of this work is the discovery that the direct-semidirect process plays a very minor role in α-capture in the cases considered, as contrasted with (p,γ), where it is the dominant process in the giant resonance region. A previous attempt to calculate these processes for (α,γ) near A = 40 resulted in substantial DSD contributions to E2 capture.[13] However, these authors considered the α-potential depth as ambiguous and chose a shallow depth so as to best reproduce (α,γ) data, whereas we have done calculations with deep potentials ($V_o \sim 115$ MeV) chosen to fit high energy scattering data. It will be interesting to see if our potentials imply small DSD (α,γ) cross sections in this higher mass region.

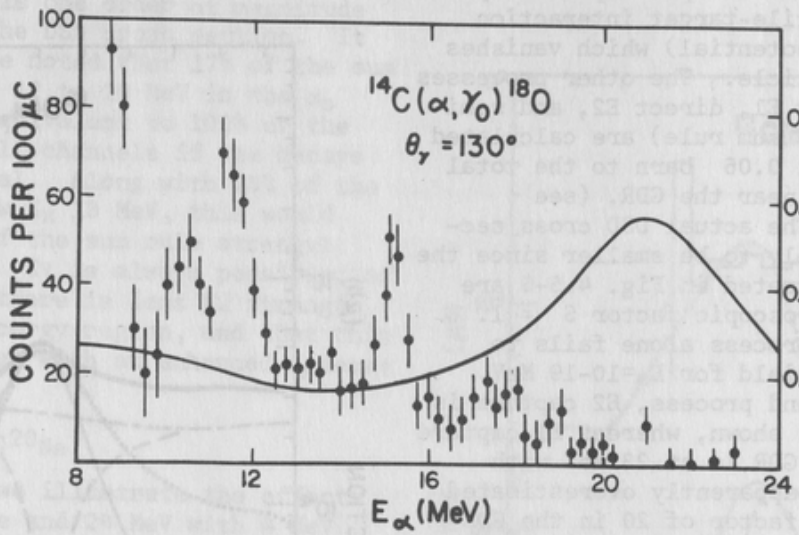

Fig. 4.5-5. Excitation curve for $^{14}C(\alpha,\gamma_0)^{18}O$ at θ_γ = 130°. The absolute cross section scale on the right is accurate to ±40%. The solid curve is a calculated cross section mainly due to the compound GDR (see text).

In any case the compound calculation can be used only to set upper limits on E2 strength concentrations, since similar cross sections may be obtained if one has less E2 strength which decays with an enhanced α_0 rate.

1. J.M. Moss et al., Phys. Rev. Lett. *34*, 748 (1975), D.H. Youngblood et al., Phy. Rev. *C13*, 994 (1976).
2. K.T. Knopfle et al., Phys. Rev. Lett. *35*, 779 (1975).
3. M.N. Harakeh et al., Nucl. Phys. *A265*, 189 (1976).
4. K.T. Knopfle et al., Phys. Rev. Lett. *64B*, 263 (1976).
5. Nuclear Physics Laboratory Annual Report, University of Washington (1975) p. 152, and (1976) p. 84.
6. K.A. Snover, E.A. Adelberger, and D.R. Brown, Phys. Rev. Lett. *32*, 1061 (1974).
7. A. Hotta, K. Itoh, and T. Saito, Phys. Rev. Lett. 33, 790 (1974).
8. D.A. Goldberg, Phys. Lett. 55B, 59 (1975).
9. D. Kurath, Phys. Rev. C7, 1390 (1973), A. Arima et al., Advances in Nuclear Physics, Vol. 5, Plenum Press (1972).
10. STAT 2 by R. Stokstad, Oak Ridge National Laboratory, unpublished.
11. A. Gilbert, and A.G.W. Cameron, Can. J. Phys. *43*, 1446 (1965), U. Facchini and E. Saetta-Menichella, Energia Nucleare *15*, 54 (1968).
12. Nuclear Physics Laboratory Annual Report, University of Washington (1975) p. 161.
13. N. Shikazono, and T. Terasawa, Nucl. Phys. *A250*, 260 (1975).

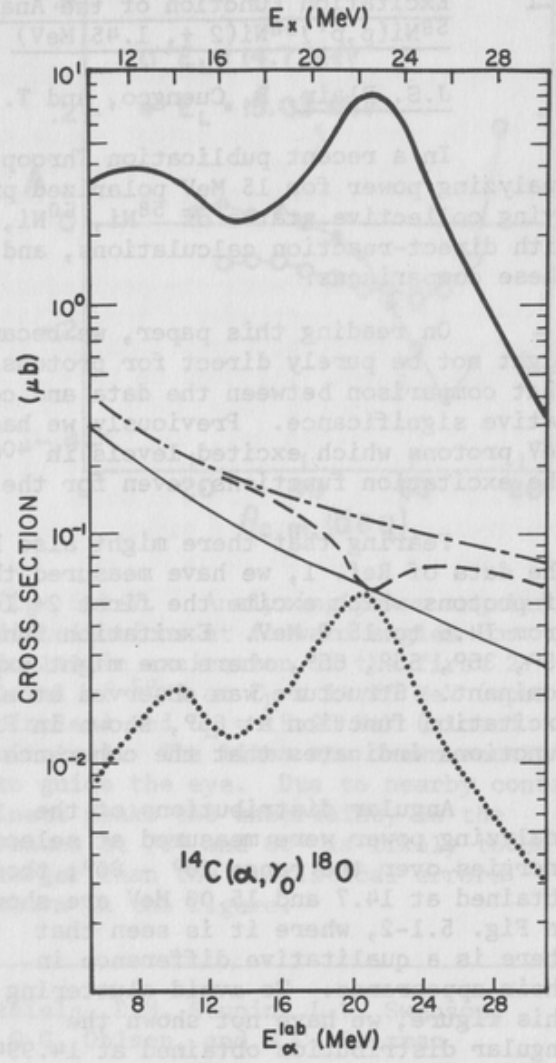

Fig. 4.5-6. Calculated cross section for $^{14}C(\alpha,\gamma_0)^{18}O$. Fine-solid: direct E1, dot-dash: direct E1 + direct E2, dashed: direct E1 + E2 + semidirect E2, dotted: compound GQR, heavy solid: compound GDR (Ex = 23 MeV, Γ = 4 MeV, 100% of sum rule)

5. REACTIONS WITH POLARIZED PROTONS AND DEUTERONS

5.1 Excitation Function of the Analyzing Power in the Reaction $^{58}Ni(p,p')^{58}Ni(2+, 1.45\ MeV)$

J.S. Blair, B. Cuengco, and T. Trainor

In a recent publication Throop, *et al.*,[1] reported measurements of the analyzing power for 15 MeV polarized protons which inelastically excited the low-lying collective states of ^{58}Ni, ^{60}Ni, and ^{64}Zn. These data were then compared with direct-reaction calculations, and a number of conclusions were drawn from these comparisons.

On reading this paper, we became apprehensive that the reaction mechanism might not be purely direct for protons of this energy bombarding such targets and that comparison between the data and calculations might, at best, have only qualitative significance. Previously we had studied[2] the analyzing power of 16-18 MeV protons which excited levels in ^{40}Ca and had found considerable structure in the excitation functions, even for the collective octupole vibration at 3.73 MeV.

Fearing that there might also be significant non-direct contributions to the data of Ref. 1, we have measured the energy dependence of the analyzing power of protons which excite the first 2+ level of ^{58}Ni for incident energies ranging from 14.6 to 15.3 MeV. Excitation functions were obtained at the forward angles 25°, 35°, 55°, 65°, where one might expect a direct-reaction mechanism to be dominant. Structure was observed at all angles and was most pronounced in the excitation function at 65°, shown in Fig. 5.1-1; inspection of the excitation functions indicates that the coherence widths are as small as 5 keV.

Angular distributions of the analyzing power were measured at selected energies over the range 20° - 80°; those obtained at 14.7 and 15.03 MeV are shown in Fig. 5.1-2, where it is seen that there is a qualitative difference in their appearance. To avoid cluttering this figure, we have not shown the angular distribution obtained at 14.994 MeV; it is fair to say, however, that this is very much closer to that found at 14.7 MeV than that at 15.03 MeV, only 36 keV higher in incident energy.

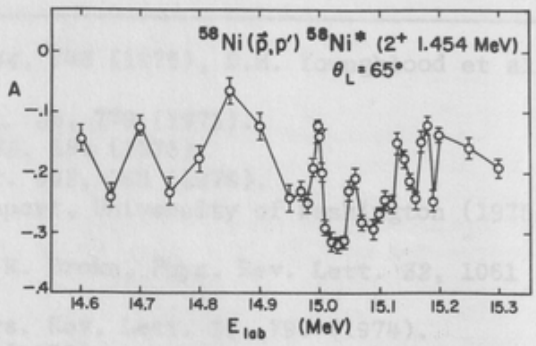

Fig. 5.1-1. Analyzing power at θ_L=65° for excitation of the first 2+ level of ^{58}Ni as a function of incident proton energy. The lines are drawn merely to guide the eye.

Excitation functions and angular distributions were similarly obtained for the elastic analyzing power. Again, structure was found in the excitation functions but, unlike the case for inelastic scattering, this did not lead to any qualitative change in the angular distributions.

When the inelastic angular distributions of Fig. 5.1-2 are compared to Figure 1 of Ref. 1, it is seen that there is not much point in applying direct interaction calculations to the data obtained at incident energies near 15 MeV. The differences between the data at differing energies are as large as the differences between contending theoretical calculations and between calculations and data. The observed angular distributions for the analyzing power at some energies do not conform to even the qualitative features of the standard DWBA calculations: the observed, nearly flat, forward angular distribution at 14.7 MeV does not emerge from any of the calculations.

It is possible that the energy variations we have observed for ^{58}Ni and ^{40}Ca are peculiar to only a few target nuclei, at or near shell closure. In view of our results, however, we believe it is advisable to verify first that the variation in inelastic analyzing power with incident energy is slow for any intermediate mass target under investigation, when E_L < 20 MeV, before interpreting the results of such experiments purely in terms of direct-reaction theories.

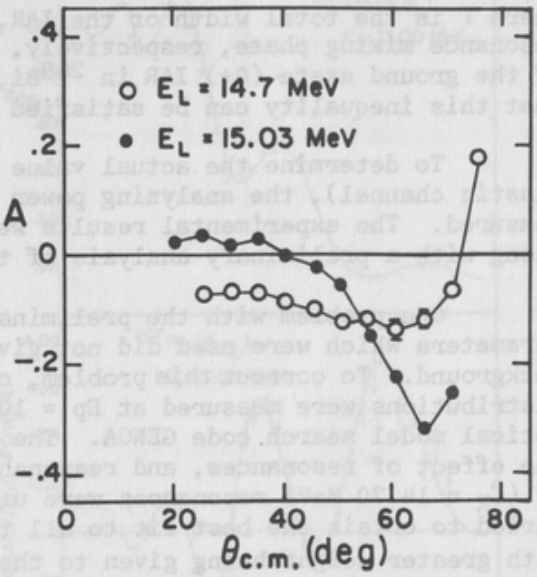

Fig. 5.1-2. Analyzing power angular distributions at forward angles for inelastic excitation of the first 2+ level of ^{58}Ni at E_L = 14.70 MeV (open circles) and E_L = 15.03 MeV (closed circles). The lines are drawn merely to guide the eye. Due to nearby contaminant peaks the uncertainty in the values at 75° and 80° is likely to be larger than the statistical errors shown in the figure.

1. M.J. Throop, Y.T. Cheng, D.K. McDaniels, D.M. Stupin, L.W. Swenson, N. Jarmie, J.H. Jett, P.A. Lovoi, G.G. Ohlsen, and G.C. Salzman. Phys. Rev. Lett. *35*, 16 (1975).
2. Nuclear Physics Laboratory Annual Report, University of Washington (1975), p. 101.

5.2 Analyzing Power in the ^{207}Pb($\vec{p}$,p_o)^{207}Pb Reaction Near the $3P_{1/2}$ Isobaric Analog Resonance

N.L. Back, J.G. Cramer, W.G. Lynch, and T.A. Trainor

Recent calculations based on S-matrix theory[1] predict that the parameters of an isobaric analog resonance (IAR) satisfy the following inequality:

$$\Gamma \geq 2 \overline{\cos(2\phi_c)} \sum_c \Gamma_c \qquad (1)$$

where Γ is the total width of the IAR, and Γ_c and ϕ_c are the partial width and resonance mixing phase, respectively, of the IAR in the channel c. In the case of the ground state (0+) IAR in ^{208}Bi, the published values[2] of Γ and Γ_c are such that this inequality can be satisfied only if $2\phi_c \geq 36° \pm 6°$.

To determine the actual value of ϕ_R (the resonance mixing phase in the elastic channel), the analyzing power in the reaction ^{207}Pb($\vec{p}$,p_o) has been measured. The experimental results were reported in last year's Annual Report,[3] along with a preliminary analysis of the data.

One problem with the preliminary analysis was that the optical-model parameters which were used did not give an adequate fit to the non-resonant background. To correct this problem, cross-section and analyzing-power angular distributions were measured at Ep = 10 MeV and 13 MeV and were analyzed with the optical model search code GENOA. The program was modified to take into account the effect of resonances, and reasonable parameters for the 0+ and the 5^- (E_R = 14.70 MeV) resonances were used. The optical model parameters were varied to obtain the best fit to all the angular distribution data ($\theta_{lab} \geq 60°$), with greater weight being given to the analyzing power-data. The resulting parameter set is given in Table 5.2-1. The angular distributions are shown in

Table 5.2-1. Optical model parameters used in analysis of ^{207}Pb($\vec{p}$,p_o) data

U	$= 65.54 - .59 * Ep$
r_R	$= 1.256$
a_R	$= 0.667$
W_s	$= -7.00 + 1.80 * Ep$
W_v	$= 0$
r_I	$= 1.288$
a_I	$= 0.343$
$U_{s.o.}$	$= 5.81$
$r_{s.o.}$	$= 1.131$
$a_{s.o.}$	$= 0.651$
r_c	$= 1.190$

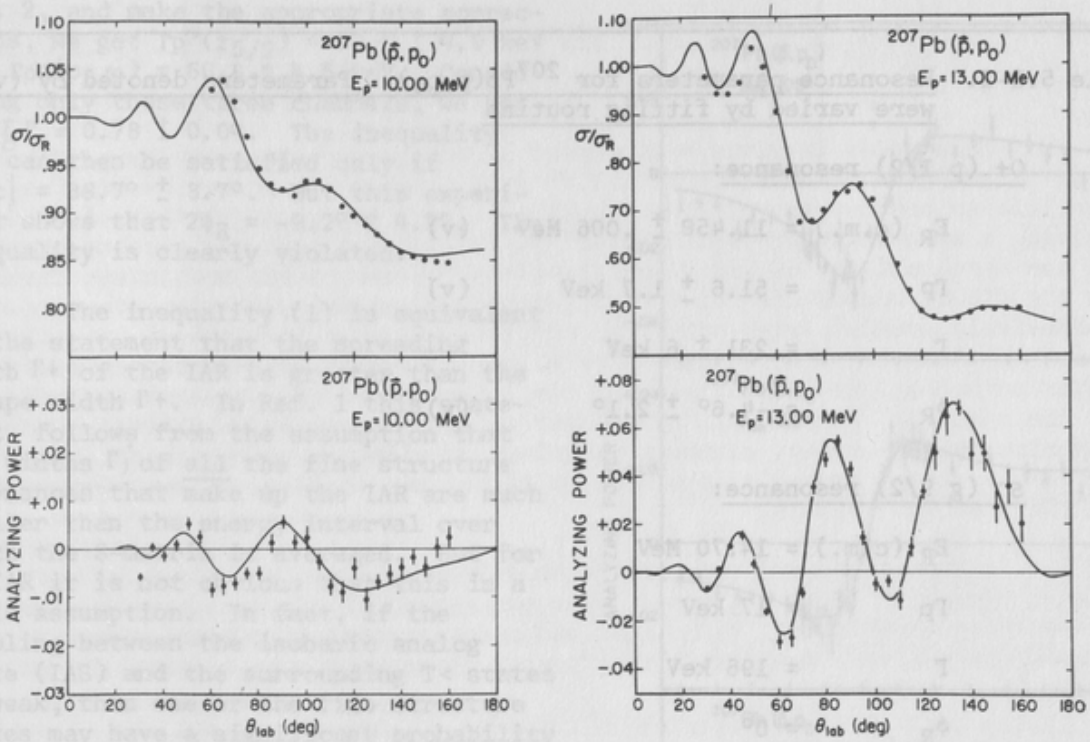

Fig. 5.2-1. Off-resonance cross section and analyzing power angular distributions for ^{207}Pb(p̄,p$_0$).

Fig. 5.2-1, where the curves represent the best fit.

To assist in finding the resonance parameters, the program RESFIT was revised to include a search routine.[4] The resonance energy E_R, partial width Γ_p, and mixing phase ϕ_R were varied to obtain the best fit to the three analyzing power excitation functions in the vicinity of the resonance. The total width Γ was fixed at a value determined from analysis of the inelastic scattering cross sections.[2] In addition, the 5^- IAR was included; the parameters are those of Ramavatram et al.,[5] except that ϕ_R was taken to be 0° rather than 15°. All data between $E_R - \Gamma$ and $E_R + \Gamma$ were used in the search. The resulting set of resonance parameters is given in Table 5.2-2; the analyzing power excitation functions at θ_{lab} = 105°, 120°, and 135° are shown in Fig. 5.2-2, with the curves representing the best fit. The reduced χ^2 of the fit was 1.034; the probability of exceeding this χ^2 is 39%.

The errors quoted for the resonance parameters deserve some comment. Potential sources of error include: (a) systematic errors in the data, (b) statistical errors in the data, (c) uncertainty in the background parameterization, and (d) other known errors. (a) An analysis of overlap points, including some points that were measured in two different runs one month apart, indicates that the

Table 5.2-2. Resonance parameters for $^{207}Pb(p,p_o)$. Parameters denoted by (v) were varied by fitting routine

0+ (p 1/2) resonance:

E_R (c.m.)	= 11.458 ± .006 MeV	(v)
Γp	= 51.6 ± 1.7 keV	(v)
Γ	= 231 ± 6 keV	
ϕ_R	= -4.6° ± 2.1°	(v)

5⁻ (g 9/2) resonance:

E_R (c.m.)	= 14.70 MeV	
Γp	= 17 keV	
Γ	= 196 keV	
ϕ_R	= 0°	

scatter in the analyzing power data is purely statistical; this is also suggested by the value of χ^2. Therefore systematic errors were not considered. (b) The statistical error in the resonance parameters depends on the statistical error in the data points, the number of data points used, and the curvature of the χ^2-hypersurface near the minimum. The procedure used to determine the errors is given by Bevington[6]; the approximate effect of incrementing each parameter by its statistical error is to increase the total χ^2 by one. As a check on these errors, the following test was made. The analyzing power data are actually a composite of two sets of data taken a month apart. A search was made on each data set separately, and the resulting parameter sets agreed with each other and with the "overall" set to within the statistical error. (c) The errors due to the background are difficult to determine. What was done was to generate different optical model sets, which gave small but noticeable degradations in the fit to the angular distributions, and to find the optimum resonance parameters with respect to these sets. Typically, the shifts in Γp were negligible, and the shifts in E_R and ϕ_R were comparable to the statistical errors. (d) The error in E_R due to uncertainty in machine calibration was taken to be < 1 keV (based solely on the error in the calibration constant), and so was ignored. Finally, it turns out that the largest source of error in Γp comes from the uncertainty in Γ, since this experiment is sensitive only to the ratio $\Gamma p/\Gamma$. The errors given in Table 5.2-2 include contributions from all of these sources.

The value of Γp is considerably lower than previously published values.[2] Consequently, the actual values of the inelastic partial widths $\Gamma p'$ are higher than the published values, since inelastic scattering cross sections measure only the product $\Gamma p \Gamma p'$. If we start with the values for Γp and $\Gamma p'$ given in

Ref. 2, and make the appropriate corrections, we get $\Gamma p'(f_{5/2}) = 29.5 \pm 4.0$ keV and $\Gamma p'(p_{3/2}) = 66.8 \pm 4.6$ keV. Considering only these three channels, we get $\Gamma/2 \sum_c \Gamma_c = 0.78 \pm 0.04$. The inequality (1) can then be satisfied only if $|2\phi c| = 38.7° \pm 3.7°$. But this experiment shows that $2\phi_R = -9.2° \pm 4.2°$. The inequality is clearly violated.

The inequality (1) is equivalent to the statement that the spreading width $\Gamma\downarrow$ of the IAR is greater than the escape width $\Gamma\uparrow$. In Ref. 1 this statement follows from the assumption that the widths Γ_j of all the fine structure resonances that make up the IAR are much smaller than the energy interval over which the S-matrix is averaged. But for an IAR it is not obvious that this is a valid assumption. In fact, if the coupling between the isobaric analog state (IAS) and the surrounding T< states is weak, then one of the fine structure states may have a significant probability for containing the IAS. This state will then have a large width. Indeed, this is one of the characteristic features of the IAR: because the T> and T< states are coupled only through the residual Coulomb interaction, the spreading width is much smaller than one would expect on the basis of the density of states.

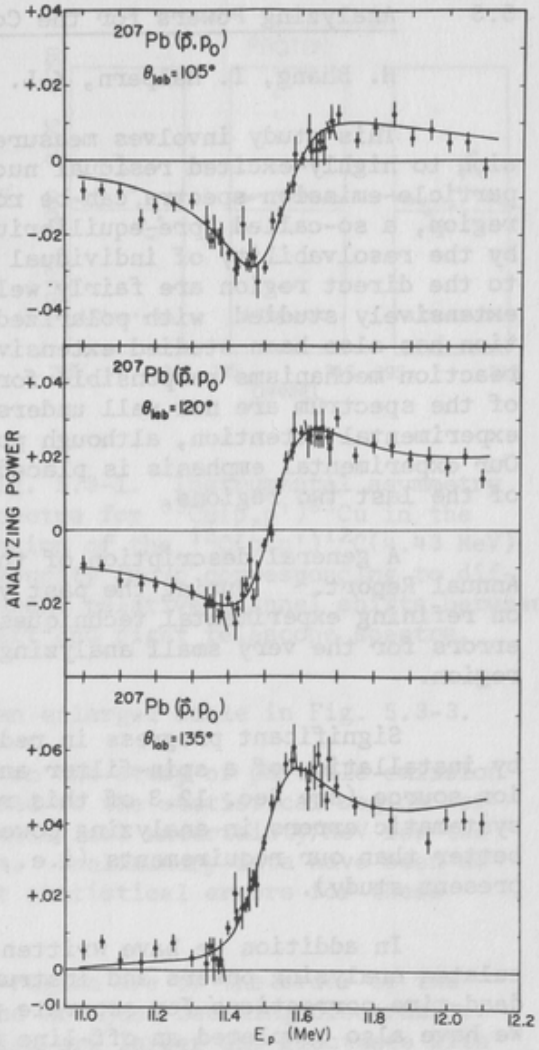

Fig. 5.2-2. Analyzing power excitation functions for ^{207}Pb($\vec{p}$,p_0) in the vicinity of the g.s. (0+) IAR.

1. P. von Brentano in *Proceedings of the Europhysics Study Conference on Intermediate Processes in Nuclear Reactions*, ed., N. Cindro (Springer-Verlag, New York, 1973), p.267.
2. E.C. Booth and B.S. Madsen, Nuclear Phys. *A206*, 293 (1973).
3. Nuclear Physics Laboratory Annual Report, University of Washington (1976), p. 102.
4. See Sec. 14.4 of this report.
5. K. Ramavataram, S. Ramavataram, W.G. Davies, A.J. Ferguson, and J.S. Fisher, Phys. Rev. *C10*, 632 (1974).
6. *Data Reduction and Error Analysis for the Physical Sciences* by Philip R. Bevington (McGraw-Hill Book Company, New York, 1969) p. 222.

5.3 Analyzing Powers for the Continuum Portions of Particle Emission Spectra

H. Bhang, I. Halpern, K-L. Liu, W. Lynch, and T.A. Trainor

This study involves measurement of analyzing powers for particle emission to highly-excited residual nuclei with a polarized proton beam. The particle-emission spectra can be roughly divided into a statistical emission region, a so-called "pre-equilibrium" region and a direct region characterized by the resolvability of individual levels. The excitation mechanisms leading to the direct region are fairly well understood at this time, and they have been extensively studied with polarized projectiles. The statistical emission retion has also been studied extensively, but only with unpolarized beams. The reaction mechanisms responsible for the intermediate or "pre-equilibrium" portion of the spectrum are not well understood and have received relatively little experimental attention, although polarization effects are reasonably large there. Our experimental emphasis is placed on techniques leading to an understanding of the last two regions.

A general description of the experimental setup was given in last year's Annual Report.[1] During the past year our major efforts have been concentrated on refining experimental techniques and reducing statistical and systematic errors for the very small analyzing powers observed in the statistical-emission region.

Significant progress in reduction of systematic errors has been achieved by installation of a spin-filter and rapid spin-reversal system on the polarized ion source (see Sec. 12.3 of this report). This installation has reduced systematic errors in analyzing power measurements below the 10^{-5} level, far better than our requirements (i.e., the expected statistical accuracy of the present study).

In addition we have written a particle-identification program which calculates analyzing powers and instrumental asymmetries on-line and makes system dead-time corrections for separate particle telescopes and spin orientations. We have also completed an off-line analysis program which smooths spectra, performs channel-by-channel calculations of analyzing powers and instrumental asymmetries, accurately matches different spectra to each other in terms of effective gain and offset and performs subtraction of impurity spectra associated with carbon and oxygen contamination of the target.

An example of the gain matching and impurity-peak stripping technique which we have developed is shown in Fig. 5.3-1. Here is shown the instrumental asymmetry calculated from spectra obtained for $^{63}Cu(p,p)^{63}Cu$ in a region of the spectrum surrounding the 4.43 MeV level from carbon contamination of the target. The sequence of three different segments corresponds to three different offsets (0.5, 0, -0.5 channels) between left and right telescope spectra. The center spectrum segment corresponds to proper matching of the left and right spectra. Simultaneous matching of several sharp lines in the spectra, such as carbon (4.43 MeV) and various elastic and other inelastic groups allows gain matching between spectra to at least second order in the channel number.

This technique also gives us a sensitive method for stripping impurity

groups resulting from carbon and oxygen contamination. Left and right spectra are purposely shifted by several channels and dispersion shapes, as in Fig. 5.3-1, appear in the instrumental asymmetry spectrum at each sharp line in the yeild spectrum. An impurity spectrum (e.g., carbon target) is then subtracted, with the relative yield (e.g., carbon/copper) as an adjustable parameter. This parameter is varied until there is no significant departure from a uniform instrumental asymmetry in the region of the contamination peak. When impurities have been removed as described above the stripped spectra of interest are restored to proper correspondence, smoothed with a several-channel wide gaussian function, and final channel-by-channel analyzing powers and instrumental asymmetries are calculated. Typical results of such a process are shown in Fig. 5.3-2. The analyzing power for a portion of the proton spectrum is shown on an enlarged scale in Fig. 5.3-3.

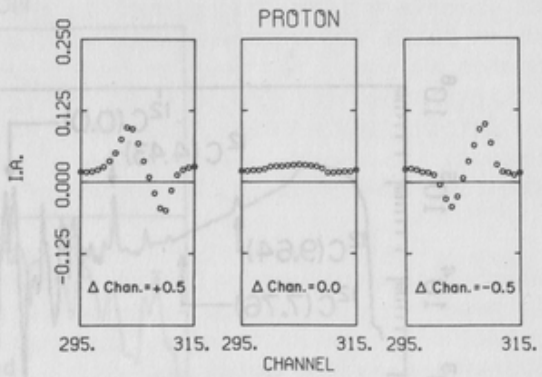

Fig. 5.3-1. Instrumental asymmetry spectra for $^{63}Cu(p,p')^{63}Cu$ in the region of the $^{12}C(p,p')^{12}C(4.43\ MeV)$ impurity group corresponding to different relative channel shifts between left and right telescope spectra.

Our major emphasis to date has been on the study of particle emission from ^{64}Zn (^{63}Cu target) which has a high yield to the statistical region for both proton and α-particle spectra. The statistical uncertainty/MeV for the proton spectra is of order 2×10^{-4} at present. Preliminary data have been acquired also with targets of ^{64}Zn and Ag, but statistical errors for these targets are still only of order 10^{-3}/MeV.

Analyzing powers in the evaporation region are of the order of the statistical uncertainty in the ^{63}Cu study and are just becoming discernable. Analyzing powers in the pre-equilibrium region are larger and fluctuate with residual excitation energy.

We plan to establish upper limits on the analyzing power in the evaporation region, or measure it should it prove to be large enough. Since the analyzing powers in the pre-equilibrium region of the proton spectrum are of order 10^{-2} - 10^{-1} it is easy to determine their values, and it is possible to test proposed models for the emission process. One approach which we are considering involves calculation of polarization effects due to a statistical distribution of levels of various spins and parities appropriate to the residual nucleus and excitation in question.

We also intend to accumulate data with ^{64}Zn and heavier targets such as Ag until statistical errors comparable to those for ^{63}Cu are achieved. This will provide further information on the dependence of polarization effects on target mass and charge.

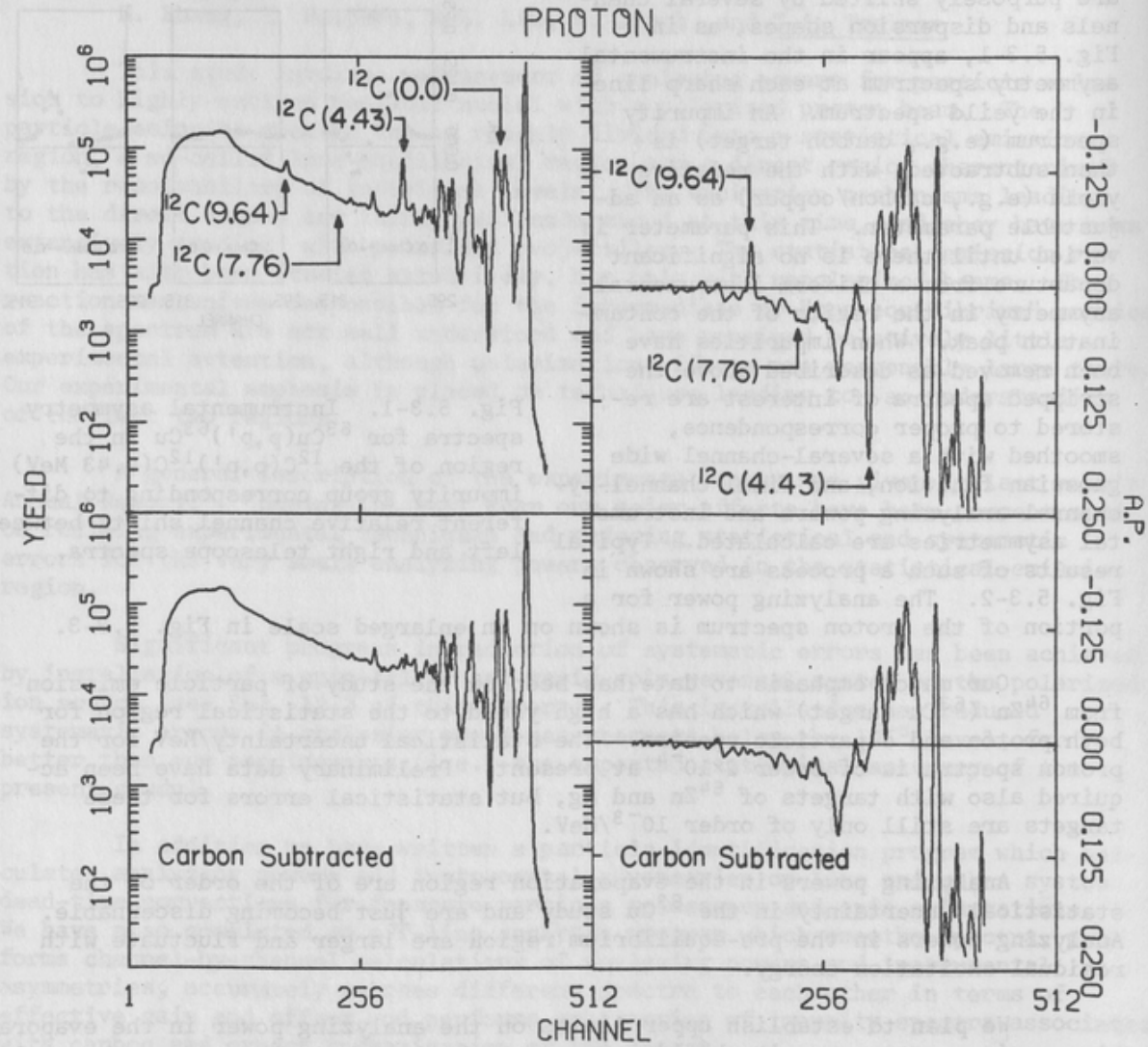

Fig. 5.3-2. Analyzing-power and yield spectra for $^{63}Cu(p,p)^{63}Cu$ at Ep = 18 MeV and $\theta_{lab} = 60°$.

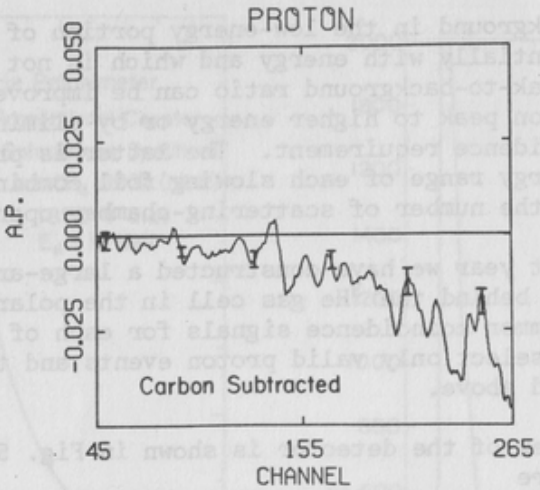

Fig. 5.3-3. Analyzing power for $^{63}Cu(p,p)^{63}Cu$ at Ep = 18 MeV and θ_{lab} = 60° in the statistical-emission and pre-equilibrium regions of the spectrum.

---

1. Nuclear Physics Laboratory Annual Report, University of Washington (1976), p. 105.

5.4 Deuteron Beam Tensor Polarimeter

N.L. Back, W.B. Ingalls, L.D. Knutson, W. Lynch, T.A. Trainor and W.G. Weitkamp

Last year we reported the construction and calibration of a tensor polarimeter based on the $^{3}He(d,p)^{4}He$ reaction.[1] This polarimeter consists of a beam-defining aperture, ^{3}He gas cell, electron suppressor and an array of five Si(Li) detectors. The Si(Li) detectors detect outgoing protons at lab angles of 0° and 20°. The four 20° detectors are equally spaced about the azimuth: left right, up and down.

Because of the large positive Q value of the analyzer reaction the protons must be slowed considerably in stainless steel foils placed between the gas cell and detectors so that they will lose a large fraction of their energy in the detectors. Different combinations of slowing foils must be used to cover different incident deuteron beam energy ranges.

It is desirable to minimize the number of slowing-foil changes required, and this depends directly on the quality of the proton spectra. Peaks in the proton spectra are severely broadened by energy straggling in the slowing foils. In addition, peaks in the 20° spectra suffer considerable kinematic broadening. Therefore, if there is an appreciable background contribution to the spectra in the region of the peak of interest the efficiency of the polarimeter is reduced.

We observe a large background in the low-energy portion of the proton spectra which falls off exponentially with energy and which is not associated with real proton events. The peak-to-background ratio can be improved by changing slowing foils to move the proton peak to higher energy or by eliminating the background by introducing a coincidence requirement. The latter is preferred because it extends the useful energy range of each slowing foil combination by several MeV and therefore reduces the number of scattering-chamber openings.

During the past year we have constructed a large-area proportional counter which fits immediately behind the ^{3}He gas cell in the polarimeter. This detector is meant to provide common coincidence signals for each of the five Si(Li) detectors in order to select only valid proton events and thereby eliminate the background events noted above.

An exploded view of the detector is shown in Fig. 5.4-1. The detector case and cover plate are constructed of brass. The center electrode consists of five equally spaced parallel wires spot-welded on a stainless steel annulus. The wire diameter is 1 mil. The center electrode is isolated from the case by an epoxy housing and teflon ring. The detector withstands bias voltages greater than 2 kV without breakdown.

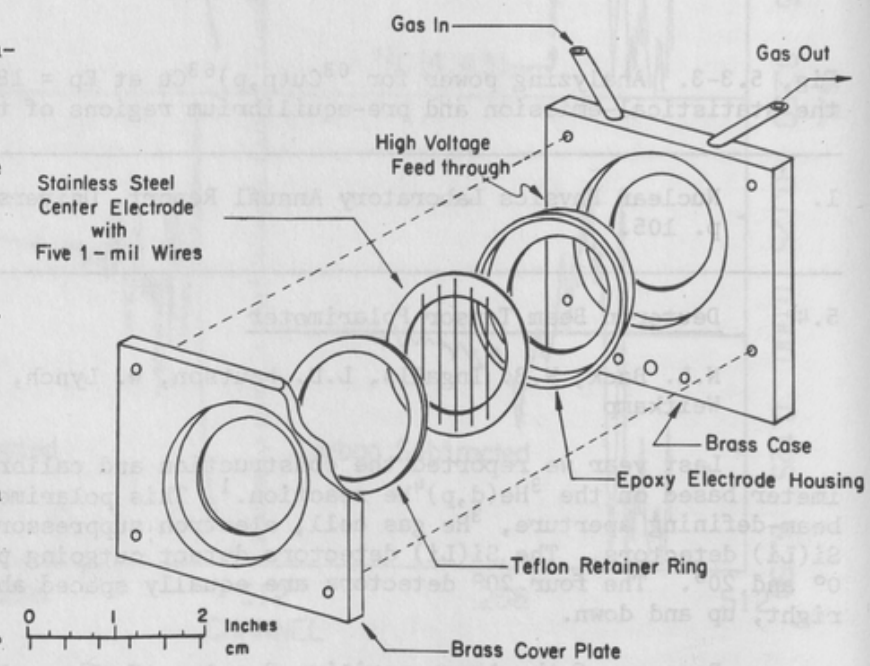

Fig. 5.4-1. Exploded view of deuteron polarimeter proportional counter.

The gas mixture is 10% methane-90% argon at one atmosphere. Entrance and exit windows are 1 mil stainless steel foils soldered to the brass case and cover plate. The vacuum seal is provided by a 1/16" o-ring in the cover plate.

The active diameter of the detector is 1-3/8". The uniformity of the detector response over this diameter was checked with a collimated α source and 0.1 mil aluminum entrance window. The detector response was found to be uniform to 1% over this diameter.

A typical proportional counter proton spectrum is shown in Fig. 5.4-2. The detector bias is 1850 volts, and the multiplication factor at this bias is slightly greater than 100. The peak in the spectrum corresponds to a proton

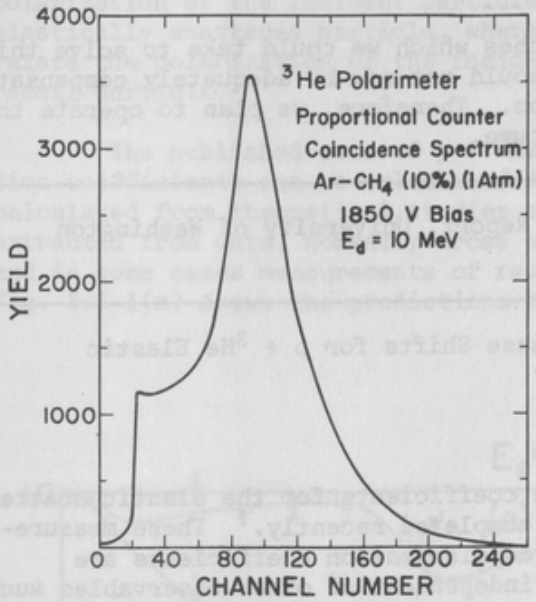

Fig. 5.4-2. Proportional counter coincidence spectrum.

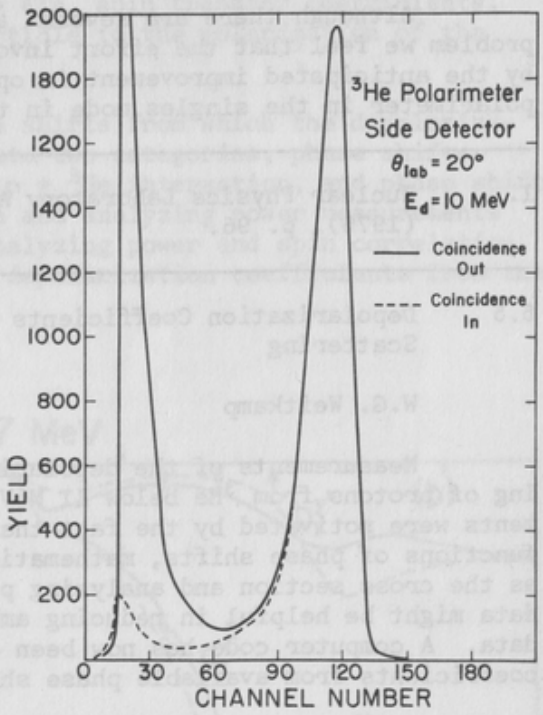

Fig. 5.4-3. Polarimater side-detector spectra with and without coincidence condition.

energy loss of about 30 keV. The spectrum represents coincidences between the proportional counter and all five polarimeter Si(Li) detectors.

A typical spectrum for one of the 20° Si(Li) detectors is shown in Fig. 5.4-3. The solid curve is obtained with no coincidence requirement between proportional counter and Si(Li) detector while the dashed curve is obtained with a coincidence requirement. These spectra illustrate nicely the elimination of the large, low-energy background component by the coincidence requirement. This extends the useful energy range for this particular slowing-foil arrangement by several MeV. Because of the poor timing quality of the proportional counter signal at large bias voltage the coincidence was done with slow timing signals (0.8 μS resolution).

Unfortunately, the improved spectrum quality which we observe is accompanied by an undesired effect. The count rate in the proportional counter is 50-100 kHz for reasonable rates in the Si(Li) detectors. At these high rates we observe a significant rate-dependent gain shift in the proportional counter spectrum. This is equivalent to a rate or beam-intensity dependence in the efficiency of the polarimeter because some valid events do not pass the lower-level discriminator in the propostional counter system. The result is introduction of a random error in the beam polarization inferred from the Si(Li) detector yields comparable to or greater than the reduction in error corresponding to the reduced spectrum background.

Although there are several approaches which we could take to solve this problem we feel that the effort involved would not now be adequately compensated by the anticipated improvement in operation. Therefore, we plan to operate the polarimeter in the singles mode in the future.

---

1. Nuclear Physics Laboratory Annual Report, University of Washington (1976), p. 96.

5.5 Depolarization Coefficients and Phase Shifts for p + ^{3}He Elastic Scattering

W.G. Weitkamp

Measurements of the depolarization coefficients for the elastic scattering of protons from ^{3}He below 11 MeV were completed recently.[1] These measurements were motivated by the fact that the depolarization coefficients are functions of phase shifts, mathematically independent of other observables such as the cross section and analyzing power, so that depolarization coefficient data might be helpful in reducing ambiguities in phase shifts extracted from data. A computer code has now been completed which calculates depolarization coefficients from available phase shift sets.

The depolarization coefficient is defined formally as[2]

$$D_j^{k'}(\theta) = \frac{\mathrm{Tr}\, M\sigma_j\, 1M^+\sigma_{k'}1}{\mathrm{Tr}\, MM^+} \qquad (1)$$

where σ represents a Pauli spin matrix, j and k represent the directions x, y, or z, and the primes indicate the spin direction of the scattering particle. The M matrix in eq. (1) can be written in terms of products of Paul spin matrices as

$$M = A + B\sigma_y 1 + C1\sigma_{y'} + D\sigma_y\sigma_{y'} + E\sigma_x\sigma_{x'} + F\sigma_z\sigma_{x'} + G\sigma_x\sigma_{z'} + H\sigma_z\sigma_{z'} \qquad (2)$$

The M matrix in this form can be related to phase shifts through the channel spin form of the M matrix. (See for example ref. 3). In those cases where phase shifts are coupled because two channels lead to the same value of total angular momentum, the coupling scheme of ref. 4 can be used.

The depolarization coefficients measured in ref. 1 are related to the coefficients of eq. (2) by the following expressions

$$D_y^{y'} = |A|^2 + |B|^2 + |C|^2 + |D|^2 - |E|^2 - |F|^2 - |G|^2 - |H|^2$$

$$D_x^{x'} = |A|^2 - |B|^2 + |C|^2 - |D|^2 + |E|^2 - |F|^2 + |G|^2 - |H|^2$$

$$D_z^{x'} = -2\mathrm{Im}\,(A^*B + C^*D) + 2\mathrm{Re}\,(E^*F + G^*H)$$

It should be noted that the $D_j^{k'}$ calculated here are not the same as the $K_j^{k'}$ calculated in ref. 2. The D's, depolarization coefficients, relate the

polarization of the incident particle to the polarization of the outgoing elastically scattered particle, whereas the K's, spin transfer coefficients, relate the polarization of the incident particle to the polarization of the recoil particle.

The published sets of p + ^{3}He phase shifts from which the depolarization coefficients can be calculated fall into two categories, phase shifts calculated from theoretical studies of the p + ^{3}He interaction, and phase shifts extracted from data, normally cross section and analyzing power measurements and in some cases measurements of recoil analyzing power and spin correlation. Fig. 5.5-1(a) shows the predictions of the depolarization coefficients from the

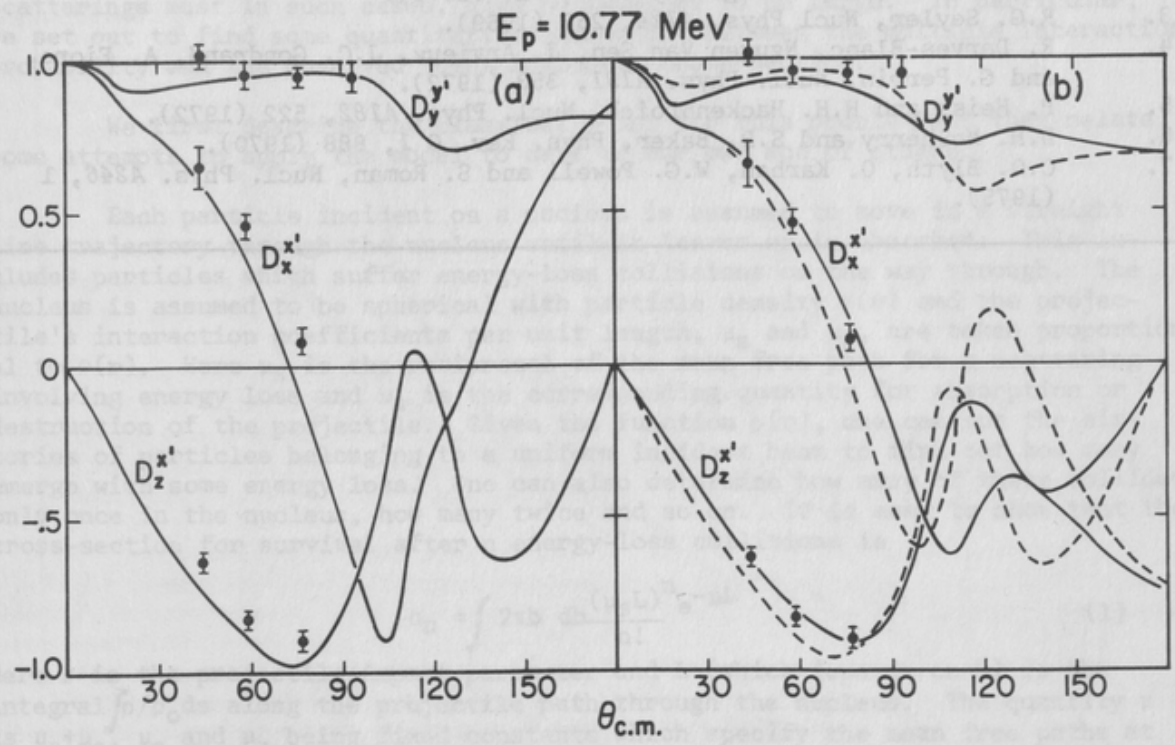

Fig. 5.5-1. Comparison of measured depolarization coefficients with those calculated from phase shifts: (2) from ref. 5, (b) solid line, from ref. 6, dashed line, set SL from ref. 7.

theoretical study of p + ^{3}He scattering by Heiss and Hackenbroich.[5] These phase shifts were obtained in a calculation of p- ^{3}He scattering states starting with a soft core nucleon-nucleon potential. Fig. 5.5-1(b) shows a comparison of the measured depolarization coefficients with values calculated from two sets of empirically determined phase shifts.[6,7] These phase shift sets differ rather

markedly, e.g., the $^1P_1$ and $^3P_1$ coupling parameters differ by nearly 70°. Although the data and calculations from both sets of phase shifts are in qualitative agreement, it is clear that phase shifts extracted from data including these measurements might be expected to have substantially smaller uncertainties. It is, of course, unfortunate that the angular region $\theta > 90°$, where the largest difference in observables calculated from the phase shift sets appear, is inaccessible to the type of measurement described in ref. 1.

---

1. W.G. Weitkamp, W. Grüebler, V. König, P.A. Schmelzbach, R. Risler, and B. Jenny, Proceedings of the Fourth International Symposium on Polarization Phenomena in Nuclear Reactions, eds. W. Grüebler and V. König, Birkhauser Verlag, Zürich, 1975, p. 514.
2. G.G. Ohlsen, Rep. Prog. Phys. *35*, 717 (1972).
3. R.G. Seyler, Nucl Phys. *A124*, 253 (1969).
4. R. Darves-Blanc, Nguyen Van Sen, J. Arvieux, J.C. Gondrand, A. Fiore, and G. Perrin, Nucl. Phys. *A191*, 353 (1972).
5. P. Heiss and H.H. Hackenbroich, Nucl. Phys. *A182*, 522 (1972).
6. D.H. McSherry and S.D. Baker, Phys. Rev. C *1*, 888 (1970).
7. C.O. Blyth, O. Karban, W.G. Powell and S. Roman, Nucl. Phys. *A246*, 1 (1975).

---

6. HEAVY ION ELASTIC AND INELASTIC SCATTERING

6.1 A Classical Model Connecting the Chance for Multiple Scattering within a Nucleus to the Total Inelastic Cross-Section

H. Wieman† and I. Halpern

We report here some of the basic features of a classical model for estimating the magnitudes of the partial inelastic cross-sections, σ_n. Here n gives the *number* of separate inelastic interactions that an inelastically scattered particle suffers as it passes through the nucleus. The original motivation for the model came from the observation that integrated inelastic cross-sections can sometimes be as large as half the geometric cross-section and that consequently the relative probability for multiple (i.e., $n \geq 2$) scatterings must in such cases, also be expected to be large. In particular, we set out to find some quantitative connection between the multiple interaction probability and the observed total inelastic cross-section.

We first describe the classical model for this problem and then relate some attempts to apply the model to data of our own and of others.

Each particle incident on a nucleus is assumed to move in a straight line trajectory through the nucleus until it leaves or is absorbed. This includes particles which suffer energy-loss collisions on the way through. The nucleus is assumed to be spherical with particle density $\rho(r)$ and the projectile's interaction coefficients per unit length, μ_s and μ_a, are taken proportional to $\rho(r)$. Here μ_s is the reciprocal of the mean free path for a scattering involving energy loss and μ_a is the corresponding quantity for absorption or destruction of the projectile. Given the function $\rho(r)$, one can sum the histories of particles belonging to a uniform incident beam to find out how many emerge with some energy loss. One can also determine how many of these collided only once in the nucleus, how many twice and so on. It is easy to show that the cross-section for survival after n energy-loss collisions is

$$\sigma_n = \int 2\pi b \; db \frac{(\mu_s L)^n}{n!} e^{-\mu L} \tag{1}$$

Here b is the projectile impact parameter and L (which depands on b) is the integral $\int \rho/\rho_o ds$ along the projectile path through the nucleus. The quantity μ is $\mu_s+\mu_a$, μ_s and μ_a being fixed constants which specify the mean free paths at the central density, ρ_o. It follows from (1) that the total inelastic scattering cross-section

$$\sigma_T = \sum_{n=1}^{\infty} \sigma_n = \int 2\pi b \; db \left[e^{-\mu_a L} - e^{-\mu L} \right] \tag{2}$$

To evaluate the integral in (2) one must specify $\rho(r)$ in order to determine L(b). A particularly convenient form for $\rho(r)$ is

$$\rho_N(r) = A_N P_N(r) e^{-\alpha_N r^2} \tag{3}$$

where P_N is the polynomial giving the first N terms of $e^{+\alpha_N r^2}$. The constants A_N and α_N are set by the values of the total number of particles in the nucleus

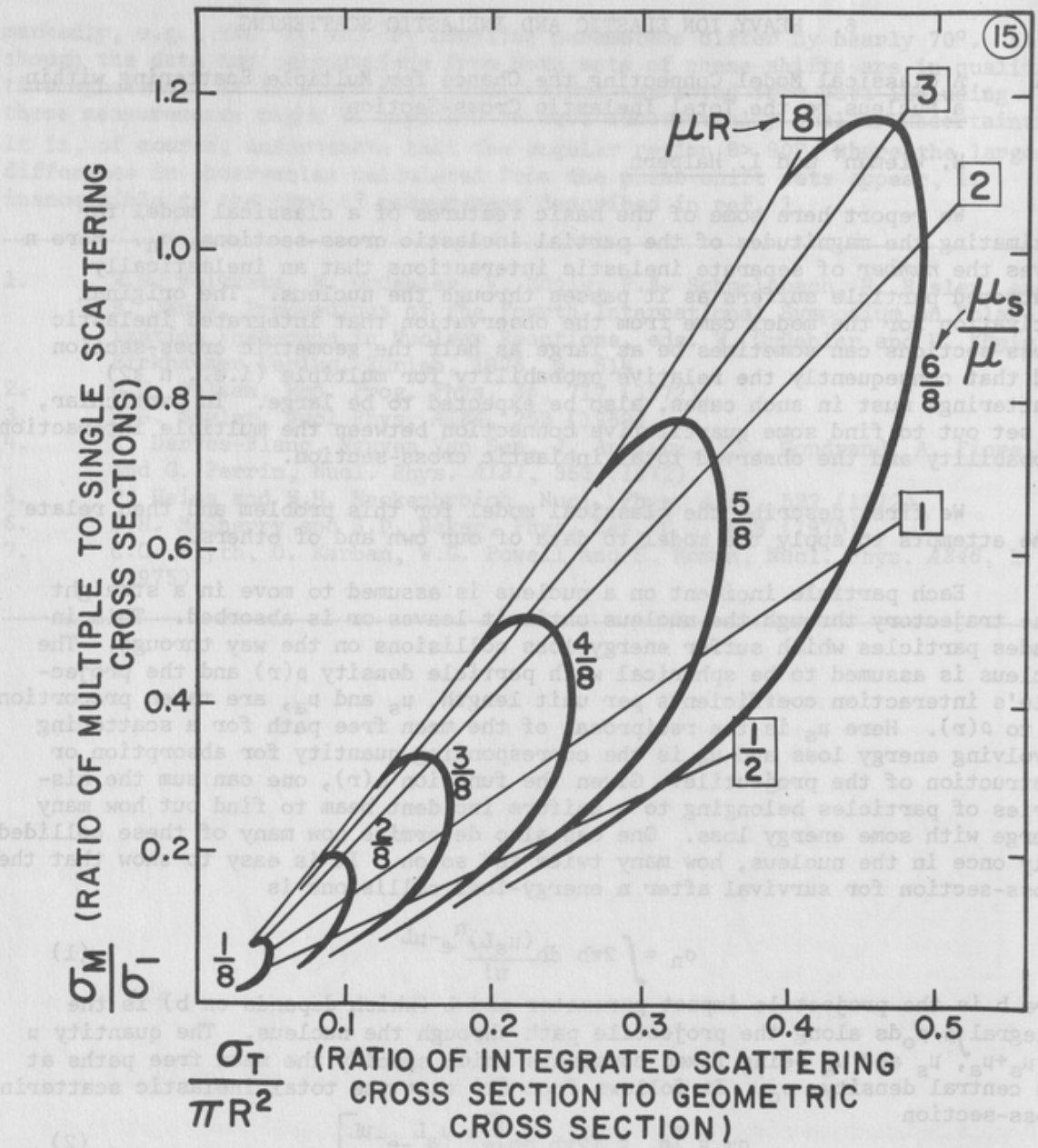

Fig. 6.1-1. The connection between the ratio of multiple to single scattering, on the way through a nucleus, to the size of the total inelastic scattering cross-section. These quantities depend, in the model described, on only the two parameters shown in the figure: μR is the ratio of the nuclear radius to the mean free path for removal from the elastic channel. μ_s/μ is the ratio of this mean free path to one for scattering rather than destruction of the projectile in an encounter inside the nucleus.

and by their root mean square radius, R. Measured density distributions for light nuclei are closely reproduced by (3) with N = 2 or 3. For rather heavy nuclei N is about 7.

Figure 6.1-1 is a way of representing some of the implications of this model for a medium weight (N=5) nucleus. The ordinate gives the ratio of multiple ($n \geq 2$) to single scattering probabilities for inelastically scattered particles. The abscissa is the total inelastic cross-section in units of π times the mean square radius of the nucleons in the nucleus. The values of ordinate and abscissa depend in the model on just two quantities, the value of μR for the nucleus and the value of the ratio μ_s/μ. Curves of constant μR and μ_s/μ are shown in the figure.

Values of μR for various projectiles which are consistent with the imaginary potentials in optical models range from $\sim 1/2$ to ~ 3. The values of μ_s/μ (i.e., of the relative chance for a scattering rather than an absorption in a collision) are not known and it is, in fact, a main point of the present discussion to suggest that μ_s/μ values can be determined from measured values of the total inelastic cross-section, σ_T. It is seen from the figure that this cross-section (normalized to πR^2) depends essentially on the value of μ_s/μ alone in the range of common μR values. It is not sensitive to the values of μR within this range. One can see why qualitatively. Suppose one increases μ_a in some nucleus. This reduces the total scattering cross-section since fewer projectiles survive passage through the nucleus. One can restore the cross-section by increasing μ_s. Thus an increase of both μ_s and μ_a means a small change in σ_T, a small change in μ_s/μ and a large change in μR.

Once one has determined a value of μ_s/μ from the total cross-section, even a rough value for μR allows one to make useful estimates of the partial scattering cross-sections, σ_n. The figure shows how the ratio $\sum_{n\geq 2}\sigma_n/\sigma_1$ depends on μ_s/μ and on μR. It is seen how a measurement of σ_T can lead to an estimate of this ratio, an estimate which improves as ones knowledge of μR improves.

The model just described should be most applicable at moderately high incident energies--say 200 MeV protons--but we have been unable to find sufficiently comprehensive sets of data to permit us to determine the total inelastic cross-section.

We have instead applied the model to lower energy scattering of protons, deuterons and α particles. Here the assumption of straight line trajectories is clearly invalid. To include the effects of Coulomb and other distortions, the outgoing intensities, $|\eta_\ell|^2$ of elastically scattered particles were determined from optical models in each case studied. This quantity corresponds, in the classical model to $e^{-\mu L(b)}$ where b is the impact parameter which corresponds to ℓ. With this association, it is easy to show that equations (1) and (2) translate to

$$\sigma_{n=1} = \pi\lambda^2\sum_\ell (2\ell+1)\frac{\mu_s}{\mu}(-\ell n|\eta_\ell|^2)|\eta_\ell|^2 \qquad (1a)$$

$$\sigma_T = \pi\lambda^2\sum_\ell (2\ell+1)\left\{|\eta_\ell|^2(1-\frac{\mu_s}{\mu})-|\eta_\ell|^2\right\} \qquad (2a)$$

From (2a) one can determine the value for μ_s/μ that (together with optical model values of the $|\eta_\ell|^2$) gives the measured value of σ_T. Listed in Table 6.1-1 are the values of μ_s/μ so determined for a number of bombardments.

Table 6.1-1. Relative Probabilities, $\frac{\mu_s}{\mu}$, for Scattering In Nuclear Collisions

Target	Proj	Ref	Projectile Energy (MeV)	Measured σ_T (mb)	$\frac{\mu_s}{\mu}$	$\Sigma\sigma_n / \sigma_1$ $n>2$
^{27}Aℓ	p	1	62	430±40	.95±.06	.79±.07
^{89}Y	p		62	610±15	.72±.01	1.04±.03
^{197}Au	p		62	640± 3	.63±.01	1.15±.01
^{66}Zn	d	2	22	35±15	.07±.03	.06±.03
^{89}Y	d		22	32± 6	.06±.01	.05±.01
^{107}Ag	d		22	32±11	.06±.02	.04±.02
^{27}Aℓ	d	2	45	110±40	.25±.08	.21±.09
^{90}Zr	d		45	100±40	.19±.07	.17±.07
^{197}Au	d		45	100±20	.16±.03	.12±.03
^{208}Pb	d		45	140±30	.20±.03	.16±.04
^{208}Pb	^{3}He	3	75	230±60	.36±.06	.35±.09
^{197}Au	^{4}He	3	65	330±50	.62±.04	.80±.10

It is seen that the values for μ_s/μ in any one type of bombardment are not very dependent upon the size of the nucleus involved. This is as it should be and is an encouraging support for the validity of the model. It is also seen that protons, ^{3}He's and α particles exhibit relatively high scattering probabilities whereas deuterons (especially lower energy deuterons) are much more likely to be destroyed instead.

The μ_s/μ value for ^{27}Al + p at 62 MeV is disconcertingly large. This may reflect our having taken too large a value for σ_T here. In determining the values of σ_T to use in our analyses we subtract any evaporated particles from the measured σ_T but do not correct for any knock-ons in the inelastic spectrum. This neglect can be justified for deuterons, ^{3}He and ^{4}He particles,[2,3] but may not be so reasonable for protons especially in light nuclei like aluminum. It should be pointed out here that our estimate for σ_2/σ_1 for scattering of 62 MeV protons from gold is very close to that recently obtained by Tamura et al. for 62 MeV protons on bismuth in an analysis very different from the present one.

Our result is 0.57 for σ_2/σ_1. The corresponding value deduced from the paper of Tamura et al. is 0.64 for bismuth.[4]

Clearly, the model we have discussed here needs more critical examination and refinement before it can be safely relied on to supply multiple scattering probabilities. Yet it may represent a reasonable beginning on a question where even order of magnitude estimates have been unavailable.

---

† Now at Lawrence Berkeley Laboratory, Berkeley, California.
1. F.E. Bertrand and R.W. Peelle, Phys. Rev. *C8*, 1045 (1973).
2. H. Wieman, Ph.D. Thesis, University of Washington (1975).
3. G. Chenevert, Ph.D. Thesis, University of Washington (1969).
4. T. Tamura, T. Udagawa, D.H. Feng and K.-k. Kan (private communication).

6.2 The Elastic Scattering of ^{16}O by ^{14}C

K.G. Bernhardt,† K.A. Eberhardt,† R. Vandenbosch, and M.P. Webb††

In addition to the excitation functions presented in the previous Annual Report, we have measured angular distributions at $E_{c.m.}$ = 21.6 and 23.2 MeV, using the setup described previously. The results are given in Fig. 6.2-1. The general rise in cross sections beyond $\theta_{c.m.} = 90^{\circ}$ is probably due to two-proton elastic transfer.

The peak-to-valley ratio of the excitation functions is comparable to the $^{16}O + ^{16}O$ case, as shown in Fig. 6.2-1. The structures match in energy since the difference in Coulomb barriers is about the size of the periodicity. It has been suggested previously that the observation of the large, oscillatory elastic cross sections in the $^{16}O + ^{16}O$ system is a consequence of the lack of channels which are able to carry away the grazing angular momentum.

Since the first excited states in the $^{14}C + ^{16}O$ system are equally high and the Q-values for direct reaction channels are only slightly more favorable, a similar behavior can be expected. This view is supported by our data.

More extensive optical model searches, and Hauser-Feshback calculations and DWBA calculations of the two-proton elastic transfer are planned.

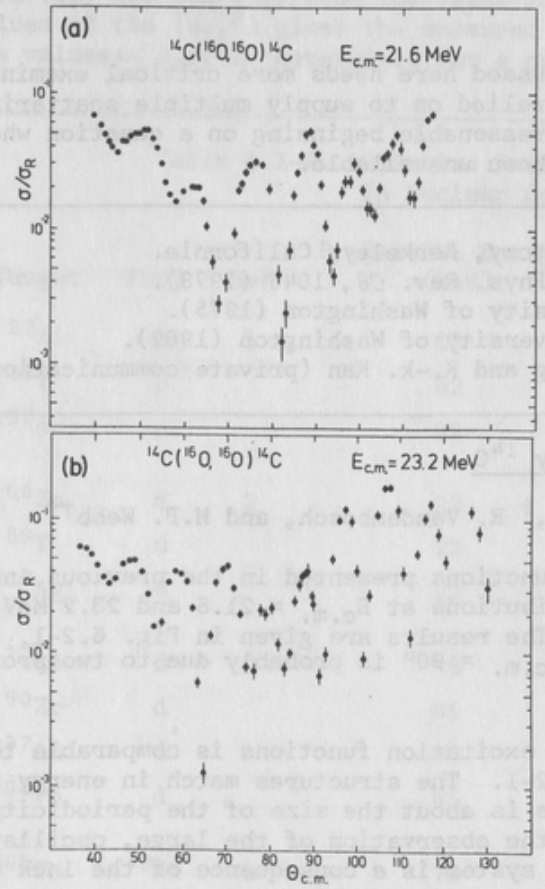

Fig. 6.2-1. Angular distribution of elastic scattering of ^{16}O from ^{14}C at $E_{c.m.}$ = 21.6 and 23.2 MeV.

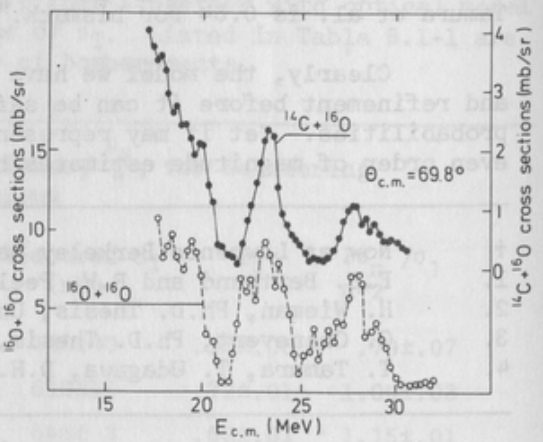

Fig. 6.2-2. Comparisons of the elastic cross sections of ^{14}C + ^{16}O (top) and ^{16}O + ^{16}O (bottom) at $\theta_{c.m.}$ = 69.8°. Note the different scales.

† Now at Sektion Physik der Universität München, D-8046 Garching, Germany.

†† Now at Oak Ridge National Laboratory, Oak Ridge, Tenn.

1. Nuclear Physics Laboratory Annual Report, University of Washington (1976), p. 125.

2. R.H. Siemssen et al., Phys. Rev. Lett. *19*, 369 (1967).

3. R. Vandenbosch, W.N. Reisdorf, and P.H. Lau, Nucl. Phys. *A230*, 59 (1974).

6.3 Measurements of the Elastic Scattering of ^{12}C from ^{28}Si at 131.5 MeV and 186.4 MeV in the Rainbow Scattering Region

J. G. Cramer, R.M. DeVries,† D.A. Goldberg,†† and M.S. Zisman†††

In previous investigations we have established that when data from near-Coulomb-barrier elastic scattering, scattering in the strong absorption region, and scattering in the rainbow region are simultaneously analyzed with a global energy-independent Woods-Saxon potential for the ^{16}O + ^{28}Si system, a "unique" optical potential is determined.[1] This potential is very shallow, with a real depth of only 10 MeV. A similar approach applied to the analysis of the ^{4}He + ^{28}Si system leads to potentials with real well depths of about 135 MeV.[2] The

principal difference between the data from these two systems is the presence of a pronounced back angle "rainbow" enhancement of the cross section in the high energy ^{4}He scattering data and the absence of the same type of enhancement in the ^{16}O scattering data. Thus there is a qualitative difference between the scattering of ^{4}He and ^{28}Si which bears further investigation.

In the present work we have pushed into the "gap" region between these two projectiles by investigating the rainbow scattering of ^{12}C (and ^{6}Li as discussed in section 6.4 below). This work has been performed in collaborative experiments: at 131.5 MeV with the ORIC cyclotron at ORNL in collaboration with R. G. Stokstad, and at 186.4 MeV using the 88" cyclotron at LBL in collaboration with J. A. Watson. These data are shown in Fig. 6.3-1. Also shown are optical model calculations with potentials H9 and L6 given in Table 6.3-1. As can be seen the calculations with potential H9, which has a central depth of 10 MeV, gives a qualitatively better fit than that calculated with the 100 MeV deep potential L6. Low energy data (not shown here) is also in much poorer agreement with L6 than with H9.

Thus we conclude that the situation for the scattering of ^{12}C from ^{28}Si is much the same as for ^{16}O scattering from the same target, i.e., a global fit to high and low energy data leads to a very shallow potential which is a reflection of the absence of prominent rainbow scattering at back angles in the high energy scattering measurements. In other words, ^{12}C and ^{16}O are qualitatively similar in their scattering properties, and both are qualitatively different in this respect from ^{4}He; C and O are heavy ions while ^{4}He is a light ion.

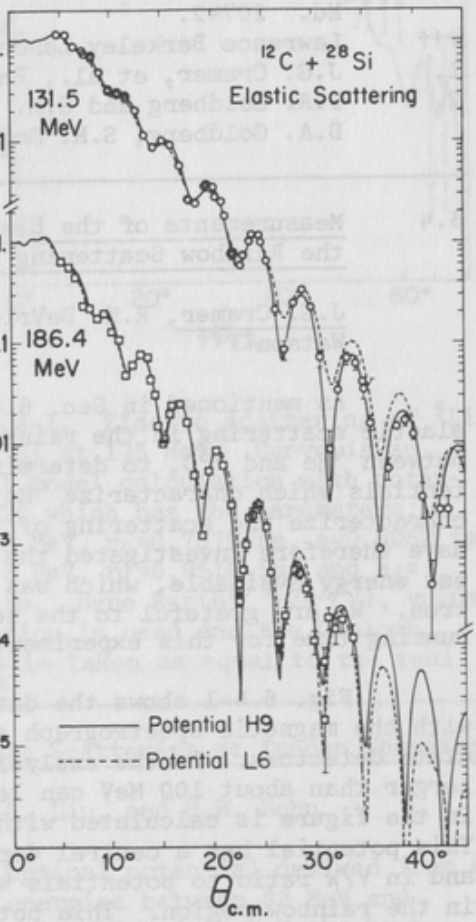

Fig. 6.3-1. Elastic scattering of ^{12}C from ^{28}Si at 131.5 MeV and 186.4 MeV. Curves are optical model fits with potentials H9 (Vo=10 MeV) and L6 (Vo=100 MeV).

Table 6.3-1. Potentials for $^{12}C + ^{28}Si$ Scattering

Potential	V_o (MeV)	r_r (fm)	a_r (fm)	W_o (MeV)	r_i (fm)	a_i (fm)
H9	10.0	1.329	0.6285	28.33	1.175	0.5990
L6	100.0	0.8628	0.8600	37.19	1.111	0.7194

† NSRL, University of Rochester, Rochester, NY 14627.
†† Dept. of Physics and Astronomy, University of Maryland, College Park, Md. 20742.
††† Lawrence Berkeley Laboratory, Berkeley, CA 94720.
1. J.G. Cramer, et al., Phys. Rev. *C14*, 2158 (1976).
2. D.A. Goldberg and S.M. Smith, Phys. Rev. Lett. *29*, 500 (1972).
D.A. Goldberg, S.M. Smith, and G.F. Burdzik, Phys. Rev. *C10*, 1367 (1974).

6.4 Measurements of the Elastic Scattering of ^{6}Li from ^{28}Si at 135 MeV in the Rainbow Scattering Region

J.G. Cramer, R.M. DeVries,† D.A. Goldberg,†† M.S. Zisman,††† and J.A. Watson††††

As mentioned in Sec. 6.3 above, we are embarked on a program of studying elastic scattering in the rainbow region for projectiles in the "gap" region between ^{4}He and ^{16}O, to determine where the transition occurs between deep potentials which characterize ^{4}He scattering and the shallow potentials which characterize the scattering of ^{16}O,[1] and ^{12}C, (as discussed in Sec. 6.3). We have therefore investigated the elastic scattering of ^{6}Li from ^{28}Si at the highest energy available, which was the 135 MeV $^{6}Li^{3+}$ beam from the LBL 88" cyclotron. We are grateful to the scientific staff of the 88" cyclotron for providing running time for this experiment.

Fig. 6.4-1 shows the data which was obtained on two runs, one performed with the magnetic spectrograph and the other performed with an array of solid state detectors. In the analysis of these data we find that any potential depth larger than about 100 MeV can lead to satisfactory fits. The solid line shown in the figure is calculated with potential R20 which is given in the caption. This potential has a central depth of 150 MeV and is very similar in geometry and in V/W ratio to potentials which have been used to fit ^{4}He scattering data in the rainbow region. This potential gives about the same χ^2 value as several other "deep" potentials which we have investigated, but it is presented here in preference because the fit looks better to the eye.

Thus we conclude that the scattering of ^{6}Li in the rainbow region is qualitatively similar to ^{4}He scattering, and if done at somewhat higher energies than that used here would probably lead to a unique determination of the potential. Therefore the transition from shallow to deep potentials has been narrowed from somewhere between ^{4}He and ^{16}O to somewhere between ^{6}Li and ^{12}C.

We plan further studies in the coming year to investigate the scattering of ^{9}Be and ^{10}B ions.

† NSRL, University of Rochester, Rochester, NY 14627.

†† Dept. of Physics and Astronomy, University of Maryland, College Park, MD 20742.

††† Lawrence Berkeley Laboratory, Berkeley, CA 94720

†††† Dept. of Physics, University of California at Davis, Davis CA 95616

1. J.G. Cramer, et al., Phys. Rev. *C14*, 2158 (1976).

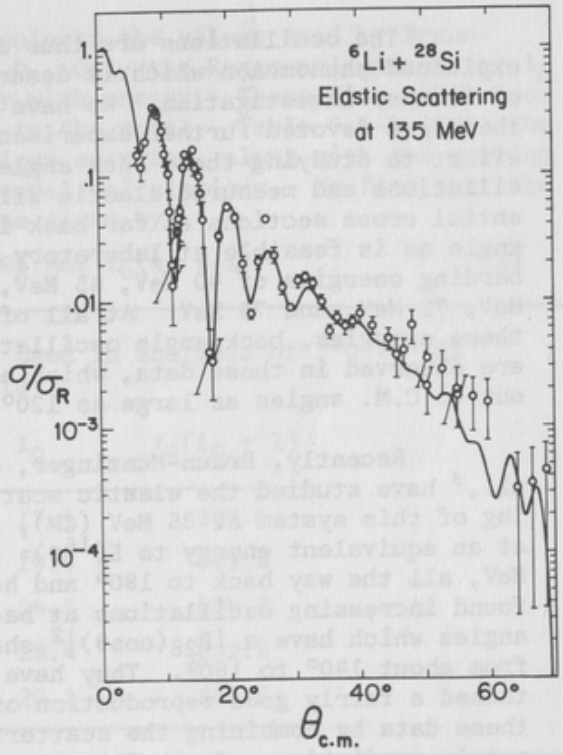

Fig. 6.4-1. Elastic scattering of ^{6}Li from ^{28}Si at 135 MeV. Curve is an optical model calculation with potential R20 which has the parameters: V=150.0 MeV, r_o=0.7079 fm, a=0.9062 fm, W=38.53 MeV, r_i=0.9510 fm, and a_i= 1.012 fm. Here $R=r(6^{1/3}+28^{1/3})$, volume absorption is used and the Coulomb radius is taken as equal to the real radius.

6.5 Further Measurements of ^{16}O + ^{28}Si Elastic Scattering at Tandem Energies

J. C. Wiborg, J.G. Cramer, Y.D. Chan, K-L. Liu, and H.H. Bohn

In our recent publication of a "unique" optical potential derived from an analysis of ^{16}O + ^{28}Si scattering at laboratory energies between 33 MeV and 215.2 MeV, we have noted that at energies between 50 MeV and 81 MeV the back angles of the measured angular distributions contain oscillations which are not reproduced by the optical model calculation.[1] An attempt to reproduce these oscillations with other potentials has been largely unsuccessful, in that "reflective" potentials which produce oscillations tend to make stronger oscillations as the bombarding energy is increased, while the experimental data indicates that the strength of the oscillations tends to *decrease* with energy.[2]

The oscillations are thus an unexplained phenomenon which is deserving of further investigation. We have therefore devoted further experimental effort to studying these back angle oscillations and measured elastic differential cross sections as far back in angle as is feasible at laboratory bombarding energies of 40 MeV, 45 MeV, 55 MeV, 72 MeV, and 76 MeV. At all of these energies, back-angle oscillations are observed in these data, which extend out to C.M. angles as large as 120°.

Recently, Braun-Munzinger, et al.,[3] have studied the elastic scattering of this system at 35 MeV (CM), i.e., at an equivalent energy to $E(^{16}O) = 55$ MeV, all the way back to 180° and have found increasing oscillations at back angles which have a $|P_{26}(\cos\theta)|^2$ shape from about 140° to 180°. They have obtained a fairly good reproduction of these data by combining the scattering matrix predictions of our E18 global potential[1] with an explicit Regge pole term in the S-matrix of the form:

$$S_\ell + S_\ell^o \left\{1 + i \frac{iD(\ell)\exp(2i\phi)}{[\ell-\ell_o-i\Gamma(\ell)/2]^{\frac{1}{2}}}\right\}$$

$$\text{with } D(\ell) = D_o(1 - |S_\ell^o|) ; \qquad (1)$$

$$\Gamma(\ell) = \Gamma_o(1 - |S_\ell^o|).$$

Because of the success of this form of analysis on the Braun-Munzinger data, we have attempted the same form of analysis on the data mentioned above. The results are shown in Fig. 6.5-1. The dashed curve in this figure shows the predictions of potential E18 alone, while the solid curve shows the predictions of potential E18 combined with a single Regge pole of the form given in equation (1) above. In this analysis,

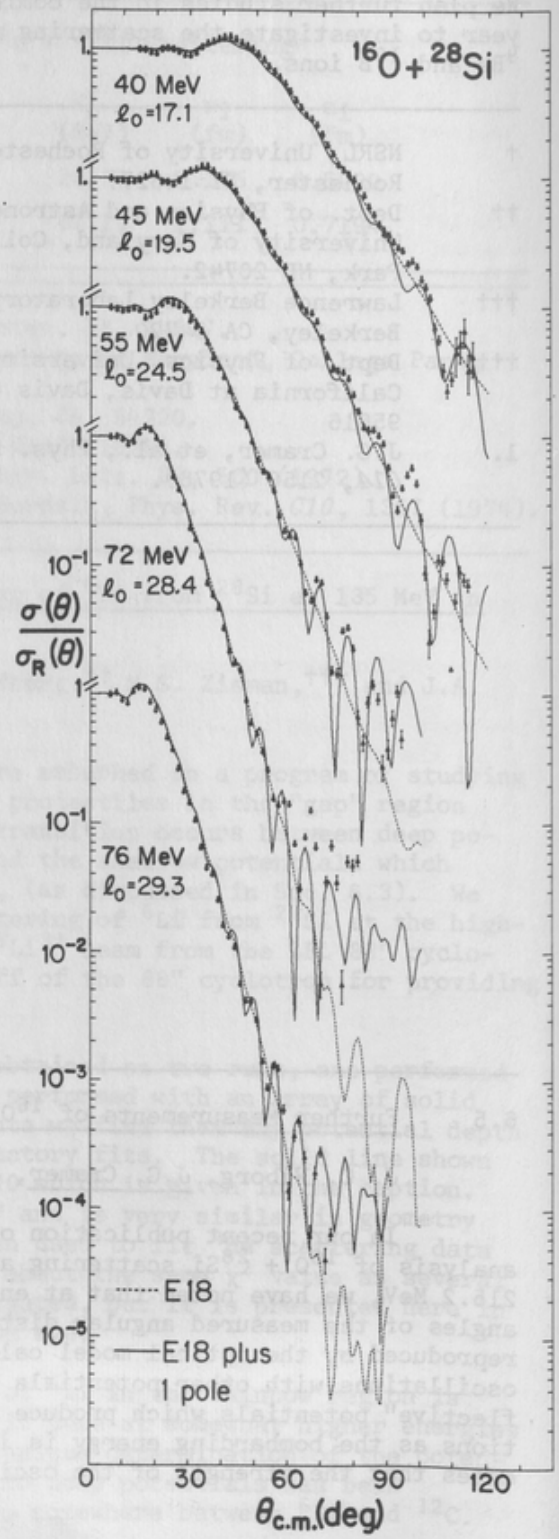

Fig. 6.5-1. $^{16}O + ^{28}Si$ Elastic scattering data with fits by optical model and optical model + Regge pole.

we restricted the parameters of the Regge pole to the values used by Braun-Munzinger, i.e., D_o=0.8, Γ_o=6.0, and ϕ = 0.0. Only the Regge pole parameter ℓ_o was taken as adjustable and allowed to vary with energy. These fits, while not of the highest quality, give some credence to the model. Table 6.5-1 gives the values of the ℓ_o parameter used at the various energies, along with the grazing partial wave ℓ_g as taken from the optical model calculations. We find that the quantity $\ell_o(\ell_o + 1)$ falls on a straight line given by

$$E_{CM} \cong 12.5 \text{ MeV} + 0.0395 \text{ MeV } \ell_o(\ell_o + 1) \qquad (2)$$

Table 6.5-1. Regge pole parameters used in analysis of $^{16}O + ^{28}Si$ Elastic Scattering Data

E_{lab}	E_{CM}	ℓ_g(E18)	ℓ_o	$\ell_o(\ell_o + 1)$
40	25.5	17.2	17.1	309.5
45	28.6	20.2	19.5	399.8
55	35.0	25.1	24.5	624.8
72	45.8	31.5	28.4	832.6
76	48.4	32.8	29.3	886.6

We also note that in Table 6.4-1, the Regge pole position approximates the grazing partial wave at the lower energies, but at the higher energies it becomes several units less than the grazing partial wave. This has the effect, as seen in the data, of reducing the oscillations with increasing energy because the Regge term is multiplied by S_ℓ^o, which becomes very close to zero for partial waves which are less than the grazing partial wave.

Despite the success of the approach described above, we find it rather unsatisfactory for the following reasons: (1) The *ad hoc* introduction of a Regge pole in the S-matrix may provide fits to the elastic scattering cross section but it does not provide wave functions which can be used for other kinds of calculations, e.g., inelastic scattering and transfer reaction analysis; and (2) the shallow E18 potential does not have a "pocket" in the effective potential for partial waves around the grazing wave, and thus cannot produce the kind of orbiting that the presence of a Regge pole suggest. Thus we are not merely "helping" the potential to provide orbiting, but introducing a phenomenon with which the potential itself is inconsistent. We intend to investigate the back-angle oscillation phenomenon further, both experimentally and theoretically. We plan to obtain more data and to seek a potential description of the phenomenon which includes the needed orbiting without the necessity of employing Regge poles explicitly in the S-matrix.

1. J.G. Cramer, et al., Phys. Rev. *C14*, 2158 (1976).
2. Nuclear Physics Laboratory Annual Report, University of Washington (1974), Sec. 10.8, p. 108.
3. P. Braun-Munzinger, et al., Phys. Rev. Lett. *38*, 944 (1977).

6.6 Klein-Gordon Coulomb Effects in Heavy Ion Scattering and Reactions

J.G. Cramer, W.G. Lynch, and J.G. Wills†

As discussed in Sections 14.5, 14.6, 14.7 and 9.4, the Coulomb wave functions and Coulomb phase shifts derived from the Coulomb Klein-Gordon equation are different from those derived from the Schrödinger Coulomb equation in that the effective angular momemtum value λ is no longer an integer, but is given by:

$$\lambda = [(\ell + \tfrac{1}{2})^2 - (ZZ'\alpha)^2]^{\frac{1}{2}} - \tfrac{1}{2} \qquad (1)$$

where ℓ is the orbital angular momentum, ZZ' is the product of charges for the projectile and target, and α is the fine structure constant or about 1/137. It would be expected that for heavy ions at energies below 10 MeV/nucleon such relativistic effects would not be important because the velocities of the ions are low. However, we note in equation (1) that the modification of the effective angular momentum by the factor $ZZ'\alpha$ is independent of energy but is strongly dependent on the charge of the system. Further, when $ZZ'>137/2$, λ will become a complex number for the lower partial waves, and this could have observable consequences in heavy ion scattering and reactions. Thus it might be possible to observe effects in heavy ion scattering and reactions which are the consequence of a relativistically invariant wave equation, perhaps even at non-relativistic energies.

As described in Sections 14.5, 14.6, 14.7, we have written a group of programs to investigate this phenomenon and have calculated a number of cases of heavy ion elastic scattering below the Coulomb barrier. These calculations indicate that there should be experimentally observable effects in the Rutherford cross section for these cases, and further that the deviations from Schrödinger-Rutherford scattering increase with energy. The phase differences between the relativistic and non-relativistic amplitudes, moreover, may become very large, particularly for the lower partial waves, so that observable effects in Coulomb-nuclear interference situations are to be expected above the Coulomb barrier.

We have investigated both the effects on the absolute cross section and the effect on the interference pattern in identical particle scattering. The latter appears as an angle-shift in the interference oscillations at angles away from 90°.

We have made preliminary measurements for sub-Coulomb scattering of $^{16}O + {}^{208}Pb$ in order to test these predicted effects, at bombarding energies in the vicinity of 40 MeV. Here a deviation in the back angle cross section of a few percent is expected. Predictions of similar deviations from Rutherford scattering can be found in the literature, arising from molecular potentials,[1,2]

electron vacuum polarization,[3] and nuclear polarization from Coulomb excitation. The contemplated experiment will thus require a careful design to observe unambiguous effects of this order and to distinguish between the various effects which might contribute to observed deviations.

---

† Department of Physics, Indiana University, Bloomington, IN 47401.

1. J. Rafelski, B. Müller, and W. Greiner, Lettere al Nuovo Cimento *4*,469 (1972).
2. B. Müller, J. Rafelski, and W. Greiner, Physics Letters *47B*,5 (1973).
3. J. Rafelski and A. Klein, Phys. Rev. *C9*,9 (1974).

---

7. HEAVY ION DEEPLY INELASTIC AND FUSION REACTIONS

7.1 Angular Momentum Transfer in the Deeply Inelastic Scattering of 610-MeV ^{86}Kr by ^{209}Bi

P. Dyer, R. J. Puigh, T. D. Thomas[+], R. Vandenbosch, and M. S. Zisman[++]

The reaction cross section for 610-MeV ^{86}Kr + ^{209}Bi is dominated by the deeply inelastic scattering process, which is characterized by strong damping of the initial kinetic energy, little net charge or mass transfer, and angular distributions peaked near the grazing angle.[1,2] In classical descriptions of the reaction mechanism, phenomenological viscous friction forces, with radial and tangential components, are used to describe the dissipation of initial kinetic energy and angular momentum into internal degrees of freedom. We are studying the angular momentum transfer in order to determine the strength of the tangential friction. This is done by measuring angular correlations of fragments from fissioning heavy reaction products relative to the recoil axis.

The geometry of the experiment is shown in Fig. 7.1-1. Fission fragments were detected in coincidence with the projectile-like reaction product, and correlations in and out of the reaction plane were measured. A 610-MeV ^{86}Kr beam from the LBL Super-HILAC was incident on a target consisting of 300 $\mu g/cm^2$ ^{209}Bi on a 50 $\mu g/cm^2$ carbon backing. Light (projectile-like) products were detected by a semiconductor counter telescope fixed at 40° lab, where the deeply inelastic scattering cross section is at a maximum. Two single counters detected fission fragments, one of which was mounted on an arm that could be moved to various out-of-plane angles. Timing signals from each detector were fed into time-to-amplitude converters (TAC's), so that each event was characterized by four linear signals, ΔE, E+ΔE, fission fragment energy, and TAC, which were digitized and recorded event-by-event. In a two-dimensional array of counts versus telescope energy and fission fragment energy (after a subtraction of random events), the events of interest were easily separable from other events.

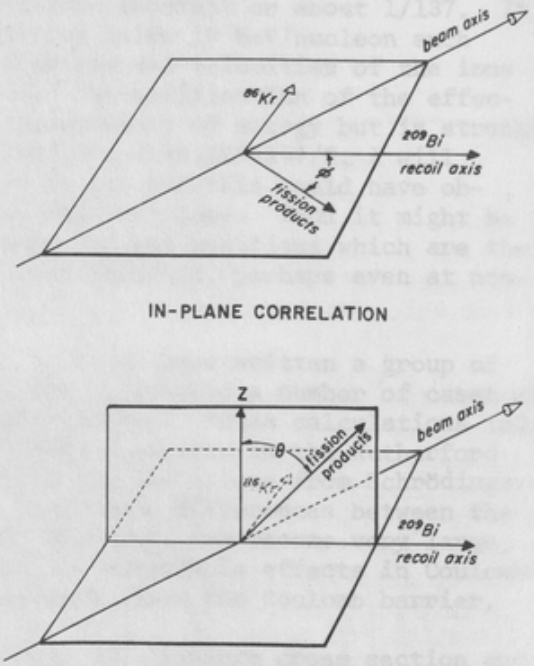

Fig. 7.1-1. Geometry of the experiment.

The angular distribution, with respect to a space-fixed z axis, of

fission fragments from a nucleus having quantum numbers J, M, and K is given by

$$W^{J}_{MK}(\theta) = \frac{(2J+1)}{2} \left| d^{J}_{MK}(\theta) \right|^{2}$$

where J is the intrinsic angular momentum of the fissioning nucleus, M is the projection of J on the z axis, K is the projection of J on the nuclear symmetry axis, θ is the angle measured from the z axis, and the $d^{J}_{MK}(\theta)$ are rotational wave functions. In order to calculate a family of angular correlation curves which can be compared to experimental data, it is necessary to sum the above distribution over J, M, and K with the appropriate weighting functions. The K distribution depends only on the properties of the fissioning nucleus, and is taken from previous experiments. The J and M distributions depend on the reaction mechanism; these are to be determined from the present experiment. The out-of-plane correlation is more sensitive to the J distribution; the in-plane, to the M distribution. In the limit of M=J (that of equatorial collisions in the classical limit) the in-plane correlation would be isotropic and the out-of-plane correlation would be anisotropic, with the anisotropy increasing with increasing J.

A Gaussian distribution of K values is assumed. The parameter K_0^2 characterizing the width of the distribution is taken from previous measurements of fragment correlations from fissioning compound nuclei.[3-6] We use $K_0^2=132$. No further assumptions about the properties of the fissioning nucleus are required.

For the J distribution, we take $P(J) \propto (2J+1)$ up to some maximum J_{max}, where there is a sharp cutoff. This form follows from a model in which all partial waves up to some maximum ℓ give rise to particles scattered to about 40° lab (an assumption supported by the sharply peaked differential cross section) and in which the fraction of orbital angular momentum transferred into intrinsic angular momentum is the same for all partial waves (an assumption which holds in the rolling or sticking friction limits).

The measured in and out-of-plane fission correlations are shown in Fig. 7.1-2. Lab angles and cross

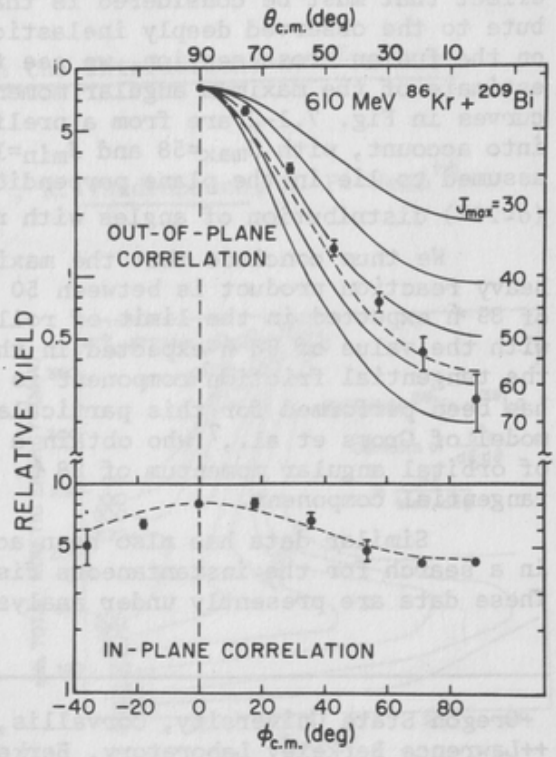

Fig. 7.1-2. Fission angular correlations measured in and out of the reaction plane. The family of solid curves are calculated for the out-of-plane case with M=J, $K_0^2 = 132$. The dashed curve is with $J_{min} = 18$, $J_{max} = 58$ and with contributions from M≠J (see text).

sections have been converted to those of the ^{209}Bi center-of-mass coordinate system. Also shown for the out-of-plane case are a family of curves calculated for $K_0^2=132$, M=J, and varying J_{max}. The large out-of-plane anisotropy is a direct indication of sizeable angular momentum transfer with the resulting intrinsic angular momentum being predominantly oriented perpendicular to the reaction plane. Comparison of the anisotropy with the model calculations just described leads to an initial estimate of the angular momentum transferred to the recoil of 55 $\hbar$.

Two corrections to this result are presently being estimated. We believe the anisotropy in the in-plane correlation arises from interactions (such as those of non-equatorial collisions) that lead to angular momentum vectors whose projections in the reaction plane are not isotropically distributed. Comparison of the out-of-plane correlation data to the family of curves in Fig. 7.1-2 then results in an underestimate of J_{max} by 15 to 20 units. Another effect that must be considered is that partial waves of small ℓ may not contribute to the observed deeply inelastic cross section. Considering upper limits on the fusion cross section, we see that such an effect could lower our estimate of the maximum angular momentum transfer by 10 to 15 units. The dashed curves in Fig. 7.1-2 are from a preliminary calculation taking these factors into account, with $J_{max}=58$ and $J_{min}=18$. The angular momentum vectors were assumed to lie in the plane perpendicular to the recoil axis with a Gaussian ($\sigma=27°$) distribution of angles with respect to the z axis.

We thus conclude that the maximum angular momentum transferred to the heavy reaction product is between 50 and 70 $\hbar$. This is higher than the value of 39 $\hbar$ expected in the limit of rolling friction, and is less than but consistent with the value of 68 $\hbar$ expected in the sticking limit. The result implies that the tangential friction component is very important. The only calculation that has been performed for this particular system and bombarding energy is a friction model of Gross et al.,[7] who obtain a total loss (that going into both fragments) of orbital angular momentum of 38 $\hbar$. This calculation thus underestimates the tangential component.

Similar data has also been acquired for the 730-MeV ^{86}Kr + ^{238}U reaction in a search for the instantaneous fission predicted by Deubler and Dietrich[8]. These data are presently under analysis.

+Oregon State University, Corvallis, Oregon
++Lawrence Berkeley Laboratory, Berkeley, California

1. K. L. Wolf, J. R. Huizenga, J. Birkelund, H. Friesleben, and V. E. Viola, Phys. Rev. Lett. *33*, 1105 (1974).

2. R. Vandenbosch, M. P. Webb, and T. D. Thomas, Phys. Rev. *C14*, 143 (1976).

3. R. Chaudhry, R. Vandenbosch, and J. R. Huizenga, Phys. Rev. *126*, 220 (1962).

4. L. G. Moretto, R. C. Gatti, and S. G. Thompson, LBL Report No. LBL 1666, unpublished.

5. S. S. Kapoor, H. Baba, and S. G. Thompson, Phys. Rev. *144* 965 (1966).

6. R. G. Clark, W. G. Meyer, M. M. Minor, C. T. Roche, and V. E. Viola, Z. für Physik, *274*, 131 (1975).

7. D. H. E. Gross, H. Kalinowski, and J. N. De, in "Classical and Quantum Mechanical Aspects of Heavy Ion Collisions", H. L. Harney, P. Braun-Munzinger and C. K. Gelbke, ed. Lecture Notes in Physics, Vol. 33, p. 194 (Springer-Verlag, Berlin-Heidelberg-NewYork, 1975).

8. H. H. Deubler and K. Dietrich, Phys. Lett. *62B*, 369 (1976).

7.2 Energy Dependence of Energy Loss in the Interactions of ^{86}Kr with ^{139}La

P. Dyer, R. J. Puigh, T. D. Thomas[+], R. Vandenbosch, M. P. Webb[++] and M. S. Zisman[+++]

Our previous studies[1] of the Kr +La system at 710 MeV have been extended to lower bombarding energies. The primary motivation of this extension was to see how the double-peaked energy spectra observed at the higher energy change in character with decreasing energy. We also wished to see if we could test the presumed dependence of the energy loss on the relative velocity of the two reactants.

We have made new measurements at 610 MeV and 505 MeV. The energy spectra obtained at 610 MeV exhibit two components at certain angles although not as prominently as at 710 MeV. The overall features of the dependence of energy loss on angle at 610 MeV and 505 MeV are shown in Figs. 7.2-1 and 2.

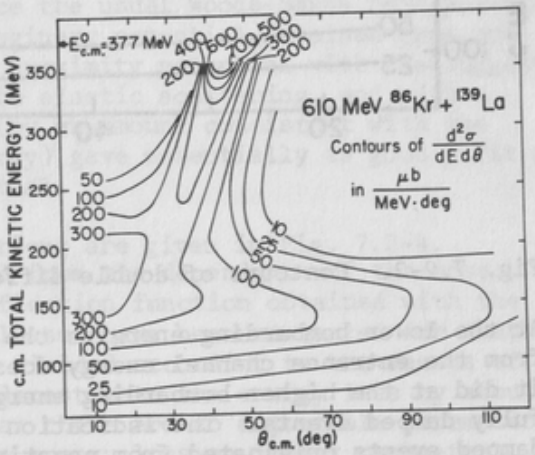

Fig. 7.2-1. Contours of double differential cross section $\frac{d^2\sigma}{dEd\theta}$ in $\mu b\ MeV^{-1}\ deg^{-1}$. The ordinate is the total kinetic energy in the exit channel derived from the light-particle kinetic energy with the assumption of no net mass transfer. No corrections for neutron emission have been made.

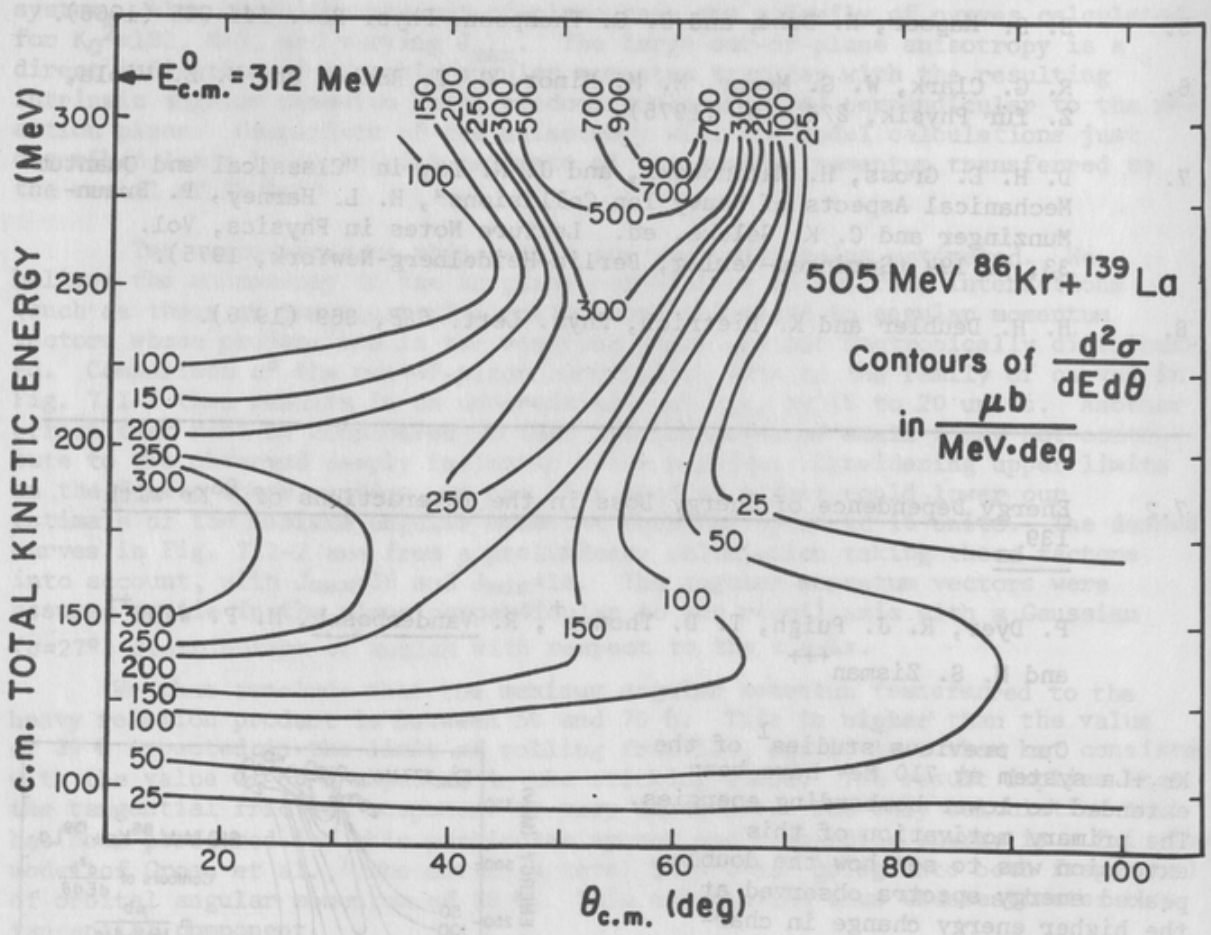

Fig. 7.2-2. Contours of double differential cross section as in Fig. 7.2-1.

At the lower bombarding energies the quasi-elastic ridge running down in energy from the entrance channel energy does not move forward in angle as rapidly as it did at the higher bombarding energy. It also merges more quickly with the fully damped events. The indication at the higher energy that the fully damped events originated from negative deflection angles is less clear. A deflection function giving the nuclear rainbow at a small (<10°) positive or negative angle could be consistent with the observations. The two possibilities would lead to ridge lines in a contour plot given by either the dashed or full curves in Fig. 7.2-3.

In order to understand the processes responsible for the energy loss in these reactions we have undertaken some calculations of the energy loss associated with one-body dissipation. Swiatecki[2] has derived a simple "window" formula from which one can calculate the energy loss due to transfer of nucleons

between two nuclei moving with a relative velocity $\vec{\mu}$. Randrup[3] has recently generalized this using a proximity model to obtain the dependence of the dissipation on the separation between the nuclei. The model takes into account the radius of curvature of the two nuclei, the surface diffusivity, and the transparency of the "window" between the two nuclei to particle transfer. We have integrated the dissipation predicted by the resulting dissipation function along various classical trajectories using the trajectory program described in section 14.5 of this report. The trajectory calculations performed thus far have neglected the effect of energy loss and orbital angular momentum loss on the trajectories. Sample calculations indicate these corrections largely cancel for the relatively small energy losses for which the generalized window treatment might be expected to be valid.

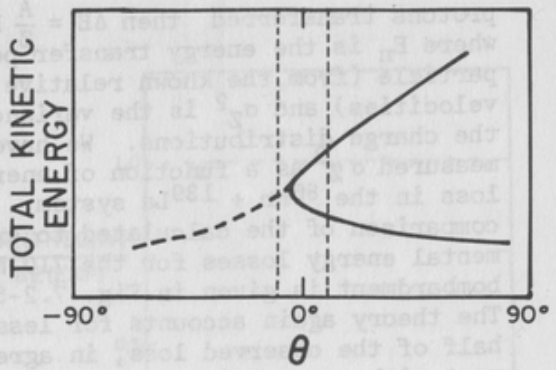

Fig. 7.2-3. Two possible trajectories of the ridge line in and E va. θ cross section countour diagram.

The calculations are quite sensitive to the conservative potential determining the trajectories. For self-consistency we have used the proximity potential.[4] As a partial test of the validity of this potential we have modified our optical model code so as to replace the usual Woods-Saxon real potential with the proximity potential. With the imaginary potential retained from previous fits to the elastic data, use of the proximity potential with the suggested parameters gave a satisfactory fit to the elastic scattering, and with a slight adjustment of the radius parameter (by an amount consistent with the uncertainty in the absolute bombarding energy) gave essentially as good a fit as the three-parameter Woods-Saxon real potential.

The results of some of the calculations are given in Fig. 7.2-4. The experimental energy losses are obtained from the dependence of the most probable energy loss on angle using the deflection function obtained with the proximity potential. The apparent energy losses have been corrected for neutron emission assuming the excitation energy is divided according to the masses of the products. The calculations seem to underestimate the energy loss by about a factor or two. It must be emphasized that there are no adjustable parameters in this calculation. The dependence of the energy loss on impact parameter (or ℓ) and on the bombarding energy seems to be qualitatively correct.

A more model-independent test of the importance of one-body dissipation via nuclear transfer can be performed by deducing the number of particles transferred from the variance of the experimental charge distributions at a particular energy loss. From the number of particles transferred and the known relative velocity the expected energy transfer can be calculated and compared with the measured energy loss. If neutrons and protons are transferred independently and if the total number of particles transferred is A/Z times the number

protons transferred then $\Delta E = \frac{A}{Z} E_n \sigma_Z^2$ where E_n is the energy transfer per particle (from the known relative velocities) and σ_Z^2 is the variance of the charge distributions. We have measured σ_Z^2 as a function of energy loss in the $^{86}Kr + ^{139}La$ system. A comparison of the calculated to experimental energy losses for the 710 MeV bombardment is given in Fig. 7.2-5. The theory again accounts for less than half of the observed loss, in agreement with our previous calculations. We emphasize that the latter comparison employing the variances of the charge distribution is independent of any assumptions about the form factor of the dissipation function or the influence of the conservative potential on the trajectory. (For larger energy losses than considered here one would have to worry about nuclear deformations and their effect on the Coulomb interaction potential and hence the relative velocity of the nuclei in the interaction region). We conclude from the comparison given here that the transfer component of one-body dissiation is incapable of explaining the energy loss. Whether other one-body effects such as energy exchange generated by the deformation of the potential walls during the collision or two-body mechanisms are responsible for the energy loss is not clear.

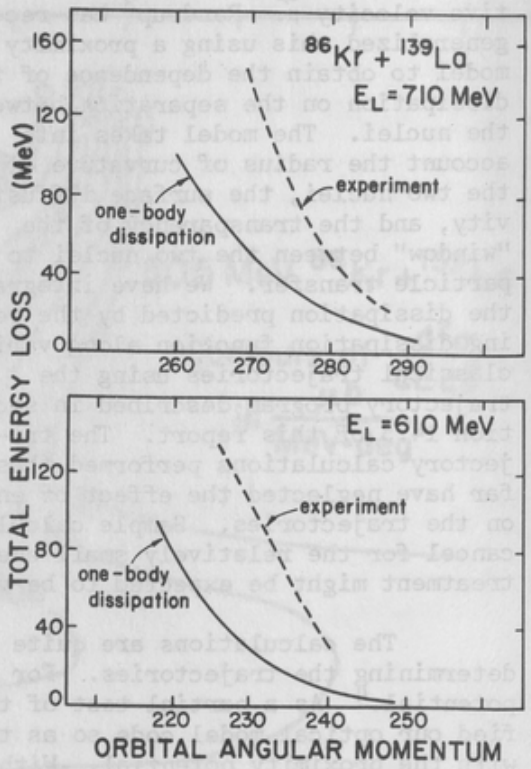

Fig. 7.2-4. Comparison of observed energy loss (corrected for neutron emission) with that calculated using one-body proximity friction at two bombarding energies.

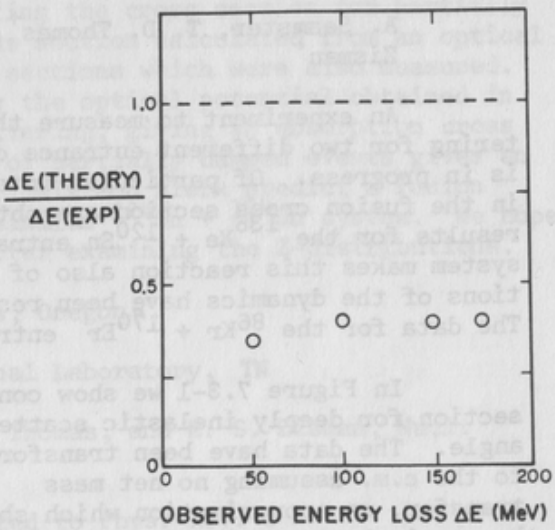

Fig. 7.2-5. Dependence of the ratio of calculated to experimental energy loss as a function of observed energy loss for 710 MeV ^{86}Kr + ^{139}La.

+ Oregon State University, Corvallis, OR 97331.

++ Present address: Oak Ridge National Laboratory, Oak Ridge, TN 37831.

+++ Lawrence Berkeley Laboratory, Berkeley, CA 94720

1. M. P. Webb. R. Vandenbosch, and T.D. Thomas, Phys. Letters *62B*, 407 (1976).

2. W. J. Swiatecki, J. de Physique Colloque *C5*, 45 (1972).

3. J. Randrup, to be published.

4. J. P. Blocki, J. Randrup, W. J. Swiatecki, and C. F. Tsang, Ann. Phys., to be published.

7.3 Deeply Inelastic Scattering of ^{136}Xe by ^{120}Sn

A. Seamster, T. D. Thomas[+], R. Vandenbosch, M. P. Webb[++] and M.S. Zisman

An experiment to measure the characteristics of deeply inelastic scattering for two different entrance channels leading to the same compound nucleus is in progress. Of particular interest would be to see what differences in the fusion cross section are obtained. We report here preliminary results for the ^{136}Xe + ^{120}Sn entrance channel. The near-symmetry of this system makes this reaction also of interest because most theoretical calculations of the dynamics have been restricted thus far to symmetric systems. The data for the ^{86}Kr + ^{170}Er entrance channel has yet to be analyzed.

In Figure 7.3-1 we show contours of the double differential cross-section for deeply inelastic scattering as a function of c.m. channel energy and angle. The data have been transformed to the c.m. assuming no net mass transfer, an approximation which should be particularly valid in this near-symmetric situation. No corrections have been made for particle emission from the fragments. The quasi-elastic events are strongly peaked at an angle slightly forward of the quarterpoint angle for elastic scattering. The quasielastic ridge bends slightly forward for larger energy losses, characteristic of smaller-impact trajectories pulled more forward by the attractive nuclear potential. The flatter plateau for the lowest kinetic energies extending to more backward angles may be due to either fully damped deeply inelastic events or to fission fragments. We have yet to analyze Z-distribution data which may shed some light on this problem, although it will be difficult to distinguish between the two kinds of events in this near-symmetric situation.

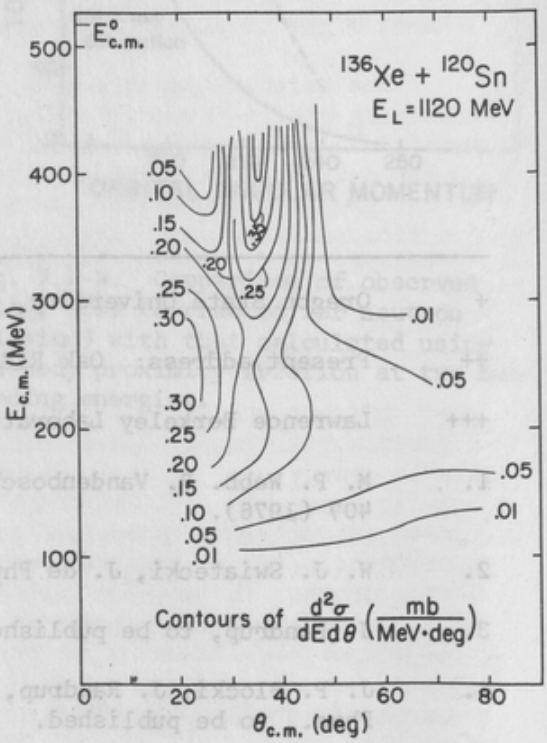

Fig. 7.3-1. Contours of double differential cross section as a function of total exit channel kinetic energy and angle.

An integration of the angular distribution over the angular region between 9° and 25° in the laboratroy system (or approximately 23° to 70° in the c.m. system) yields an integrated cross section of 2,000 ± 400 mb. An upper limit to the fusion-fission cross section is obtained from the more backward angles dominated by low energy events which could be either

fusion-fission or fully damped events if one assumes a $1/\sin\theta$ angular distribution for the fusion-fision events. A better upper limit for the fusion-fission events can be obtained by subtracting the cross section for partially damped events from the total reaction cross section calculated from an optical model fit to the elastic scattering cross sections which were also measured. The latter cross sections were well fit by the optical potential obtained in a previous study [1] of Xe + Pb elastic scattering, giving an absorption cross section of 2700 mb. Subtracting 1600 mb of partially damped events gives an upper limit for fusion-fission of 1100 mb. Nix and Sierk predict a fusion cross section of less than 50 mb for the similar $^{124}Sn + ^{124}Sn$ system. We hope to be able to set a more accurate limit after examining the Z-distributions.

+ Oregon State University, Corvallis, Oregon

++ Present address: Oak Ridge National Laboratory, TN

1. R. Vandenbosch, M. P. Webb, T. D. Thomas, and M. S. Zisman, Nucl. Phys. *A269* 210 (1976).

2. J. R. Nix and A. J. Sierk, submitted to Phys. Rev. C

7.4 Does the $^{4}He + ^{24}Mg$ Fusion Cross Section Exhibit Oscillations like that of $^{12}C + ^{16}O$?

K. G. Bernhardt, H. Bohn, Y-d Chan, J. G. Cramer, K. C. Green Sielemann, R. Weisfield and R. Vandenbosch

The recent observation[1,2] of oscillations in the fusion cross section for the $^{12}C + ^{16}O$ system at energies well in excess of the barrier is as yet not understood. The periodicity of the structure is suggestive of an odd-even effect, with the absorption less than average when an odd partial wave is grazing. One can envision two general kinds of effects which might be operative. One of these would be an entrance channel effect where the dynamics of fusion is affected by the parity associated with the entrance channel partial wave. Such an effect might arise, for example, from an alpha exchange mechanism. It has been shown that alpha exchange can lead to a parity-dependent effective potential.[3,4]

Another type of effect which might limit the fusion cross section would be an inability of the compound nucleus to accomodate all of the entrance channel angular momentum. Such an effect might occur if the yrast levels of odd spin and parity were higher in energy than for even spin and parity. If this effect were operative the fusion cross section for other entrance channels leading to the same compound nucleus might show similar oscillations if the grazing angular momenta were the same at bombarding energies which matched the compound nucleus excitation energy.

In order to try to distinguish between entrance channel effects and compound nuclear yrast level effects we have attempted to look for fluctuations in the fusion cross section for another system which leads to the same compound nucleus. A plot of the grazing angular momentum (taken here to be that angular momentum for which the optical model transmission coefficient is equal to ½) versus compound nuclear excitation energy for the $^{12}C + ^{16}O$ and $^{4}He + ^{24}Mg$ entrance channels shows that the grazing angular momenta are equal when the c.m. entrance channel energy for the former channel is 14.5 MeV and is 21.3 MeV for the latter channel. Thus if the origin of the oscillations were due to a compound nuclear effect one might expect to see oscillations in the $^{4}He + ^{24}Mg$ fusion cross sections correlated in compound nuclear excitation energy with those of the $^{12}C + ^{16}O$ system for energies in the vicinity of the matching point. Since the alpha exit channel of the compound nucleus showed more dramatically the fluctuation in the fusion cross section, we have measured excitation functions associated with this channel. Two approaches have been taken. In one approach the yield of the $2^{+} \rightarrow 0^{+}$ and $4 \rightarrow 2^{+}$ transitions in ^{24}Mg have been measured in a manner similar to that used in our studies of the $^{12}C + ^{16}O$ system. There is some concern about this approach in that these transitions can arise not only following compound nuclear alpha decays but also following direct inelastic excitations. The dependence of the latter effect on bombarding energy might then overshadow possible compound nucleus effects. The direct cross section might even exhibit oscillations out of phase with the compound nuclear cross section if the total absorption cross section varies smoothly with energy. Direct contributions should be less important for processes leading to the

$4^+ \rightarrow 2^+$ gamma transition than for $2^+ \rightarrow 0^+$ transition. To minimize the effect of direct processes we have also measured the yield of alpha particles to discrete states in ^{24}Mg at backward direction where direct contributions are minimized. To suppress the effect of fusion functions we have averaged over a range of angles and final states. Ericson fluctions were taken at approximately 5° intervals between 80° and 175°. The angular distributions were consistent with expectations for compound nuclear processes, rising at backward angles. We have summed the yields to all states at or below 6.4 in ^{24}Mg.

The results obtained thus far are shown in Fig. 7.4-1. Here we compare the excitation functions for the $4^+ \rightarrow 2^+$ transition in ^{24}Mg for both the $^{24}Mg + {}^4He$ and $^{12}C + {}^{16}O$ entrance channels. Also shown are the results of Sperr et. al. for the total fusion cross section for the $^{12}C + {}^{16}O$ system. The measurements of the γ - yields for the $^4He + {}^{24}Mg$ entrance channel was terminated prematurely due to accelerator failure and does not cover all of the desired energy range. Finally we compare the trend-reduced angle-and state-integrated cross sections for the (α,α') reaction to the lowest 6 states of ^{24}Mg. We find no evidence for a correlation between the excitation functions for the $^{12}C + {}^{16}O$ system and the $^4He + {}^{24}Mg$ systems. We therefore conclude that we have no evidence that compound nuclear yrast level limitations are likely to be causing the observed oscillations in the $^{12}C + {}^{16}O$ fusion cross section. The origin of the structure in the angle-and-state integrated cross sections for the Mg (α,α') reaction is not clear. It may reflect a lack of complete damping of Ericson fluctuations. An integration over a larger number of states would be desirable.

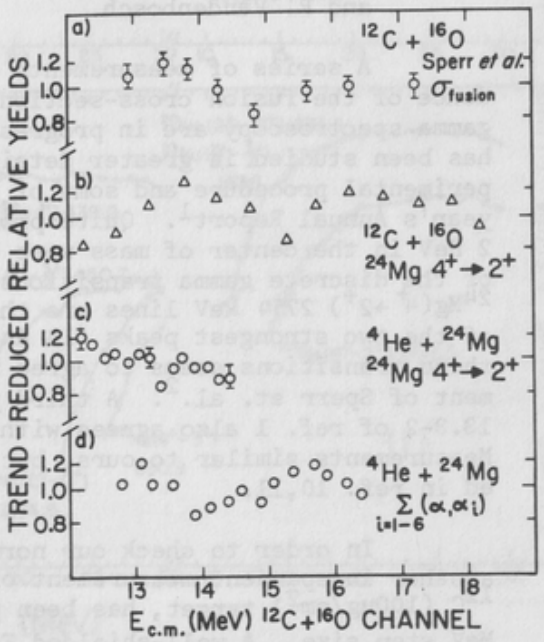

Fig. 7.4-1. Comparison of trend-reduced fusion or reaction channel excitation functions for the $^{12}C + {}^{16}O$ and $^4He + {}^{24}Mg$ systems as a function of the $^{12}C + {}^{16}O$ c.m. channel energy.

1. P. Sperr, S. Vigdor, Y. Eisen, W. Henning, D. G. Kovar, T. R. Ophal, and B. Zeidman, Phys. Rev. Lett. *36*, 405 (1976).

2. Nuclear Physics Laboratory Annual Report, University of Washington (1976), p. 139.

3. R. C. Fuller and K. W. McVoy, Phys. Lett. *41B*, 257 (1972).

4. H. Yoshida, Nucl. Phys. *A257*, 348 (1976).

7.5 On the Observation of Gross Structures in the Gamma Ray Yields following the $^{16}O + ^{12}C$ Reaction

K. G. Bernhardt, H. Bohn, Y-d Chan, J. G. Cramer, L. Green, R. Sielemann and R. Vandenbosch

A series of measurements intended to study the fine scale energy dependence of the fusion cross-section for reactions between light heavy-ions by gamma spectroscopy are in progress. In particular, the $^{16}O + ^{12}C$ reaction has been studied in greater detail between $E_{c.m.}$ = 6.2 and 29.8 MeV. The experimental procedure and some of the results have been reported in last year's Annual Report[1]. Quite prominent structures with widths between 1 to 2 MeV in the center of mass were observed in the excitation function for some of the discrete gamma transitions, of which the ^{24}Mg ($2^+ \rightarrow 0^+$) 1368 keV and the $^{24}Mg(4^+ \rightarrow 2^+)$ 2754 keV lines are the most significant. The location in energy of the two strongest peaks (14 and 16 MeV) in the excitation function for these transitions seems to agree with those reported from the particle measurement of Sperr et. al.[2]. A third peak at $E_{c.m.}$ = 11.5 MeV as shown in Fig. 13.3-2 of ref. 1 also agrees with a later measurement of Fröhlich et. al.[3] Measurements similar to ours, but covering different energies, are also reported in ref. 10,11.

In order to check our normalization and beam integration system another independent measurement of the same reaction, but with an unbacked ^{12}C (100μg/cm^2) target, has been performed from E_{lab} = 20-45 MeV, with 0.5 MeV step size. A well-shielded Faraday cup, located 6 meters away from the target, was used to collect the total charge in this case. Data analysis has been completed and is summarized in the following sections.

Excitation functions for gamma transitions following the $^{16}O + ^{12}C$ reaction are summarized in Figure 7.5-1. At low bombarding energies, the proton (^{27}Al) and alpha (^{24}Mg) channels are the strongest. As energy goes up, transitions from ^{20}Ne and ^{23}Na become important. At still higher incoming energy the yield cross-section is completely dominated by the $^{20}Ne + \alpha\alpha$ channel. This is in general agreement with what one would expect from particle evaporation.

In order to extract the absolute cross section, the overall detection

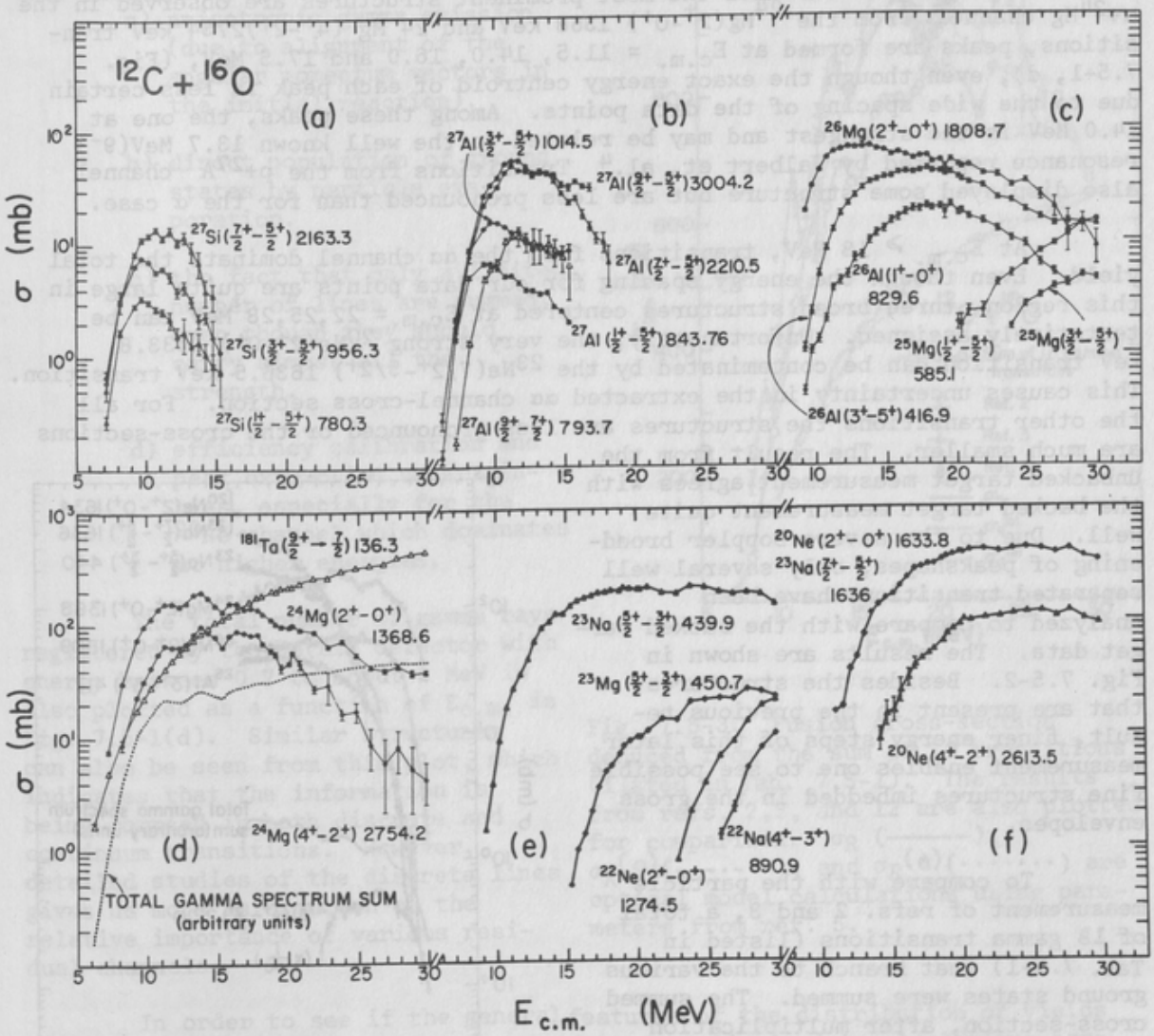

Fig. 7.5-1. Strong discrete gamma transitions observed following the ^{16}O + ^{12}C reaction. The $^{181}Ta(9/2^+ - 7/2^+)$ 136.3 keV Coulomb excitation line and spectra sum of gamma rays with energy between 0.7 to about 8 MeV (dotted line) are also plotted in (d) for comparison. Average beam energy loss due to target thickness has been accounted for. Only statistical errors are shown.

efficiency of the Ge(Li) detector has to be determined. In our case, the relative efficiency for $E\gamma$ = 800 keV to 3.5 MeV was measured by a ^{56}Co source prepared using our cyclotron, and the absolute efficiency was determined by standard calibrated gamma spectroscopy sources. In obtaining the cross section, we have

also made the approximation that all gamma rays are emitted isotropically.

According to our data the most prominent structures are observed in the $\alpha+^{24}Mg$ channel. From the $^{24}Mg(2^+-0^+)$ 1368 keV and 24 Mg $(4^+-2^+)2754$ keV transitions, peaks are formed at $E_{c.m.}$ = 11.5, 14.0, 16.0 and 17.5 MeV, (Fig. 7.5-1, d), even though the exact energy centroid of each peak is less certain due to the wide spacing of the data points. Among these peaks, the one at 14.0 MeV is the strongest and may be related to the well known 13.7 MeV(9^-) resonance reported by Halbert et. al.[4] Transitions from the $p+^{27}A$ channel also displayed some structure but are less pronounced than for the α case.

At $E_{c.m.} \geq$ 18 MeV, transitions from the αα channel dominate the total yield. Even though the energy spacing for our data points are quite large in this region, three broad structures centered at $E_{c.m.}$ = 22,25,28 MeV can be tentatively assigned. Unfortunately, the very strong $^{20}Ne(2^+-0^+)$ 1633.8 keV transition can be contaminated by the $^{23}Na(7/2^+-5/2^+)$ 1636.5 keV transition. This causes uncertainty in the extracted αα channel-cross section. For all the other transitions the structures are less pronounced or the cross-sections are much smaller. The result from the unbacked target measurement agrees with the backed target measurement quite well. Due to the severe Doppler broadening of peakshapes, only several well separated transitions have been analyzed to compare with the backed target data. The results are shown in Fig. 7.5-2. Besides the structures that are present in the previous result, finer energy steps of this later measurement enables one to see possible fine structures imbedded in the gross envelopes.

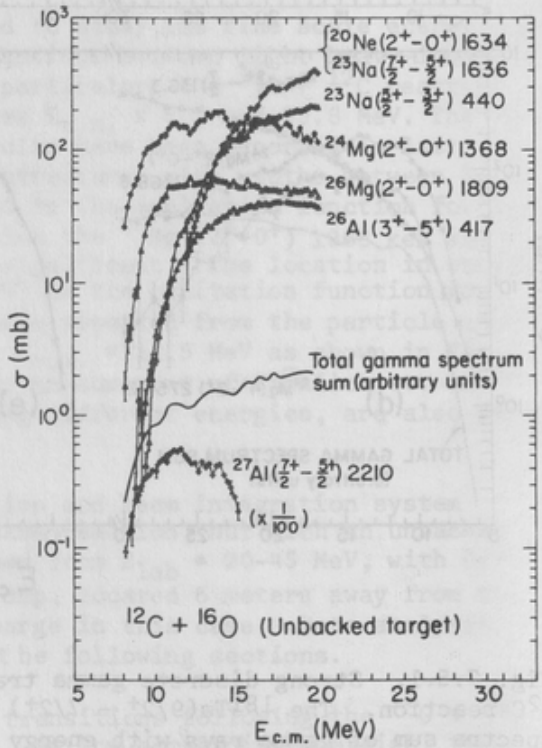

Fig. 7.5-2. Gamma yields from the unbacked ^{12}C target. Solid curve is the total gamma spectra sum.

To compare with the particle measurement of refs. 2 and 3, a total of 18 gamma transitions (listed in Tab. 7.5-1) that branch to the various ground states were summed. The summed cross-section, after multiplication by 4π, is shown in Fig. 7.5-3. Both particle and gamma data show maxima at $E_{c.m.}$ = 11.5, 14.0, and 16.0 MeV, which are also the energies at which strongest peaks appeared for the $^{24}Mg(2^+ -0^+)$ 1368 keV transition. For other regions, the agreement is only fair. Actually at about 19.5 MeV, these two data sets behave quite differently.

The fusion cross-section deduced from the gamma data is about

20% smaller than the particle result. The following factors could cause this discrepancy:

a) anisotropic gamma emission (due to alignment of the angular momentum vectors in the initial reaction).

b) direct population of ground states by particle evaporation.

c) the fact that only a limited number of lines are summed, even though they should carry almost all the strength.

d) efficiency calibration and peak extraction uncertainties, especially for the ^{20}Ne channel which dominates at higher energies.

The total number of gamma rays registered by the Ge(Li) detector with energy between 0.7 to about 8 MeV is also plotted as a function of $E_{c.m.}$ in Fig. 7.5-1(d). Similar structures can also be seen from this plot, which indicates that the information is being carried in both discrete and continuum transitions. However, detailed studies of the discrete lines gives us more information on the relative importance of various residual channels.

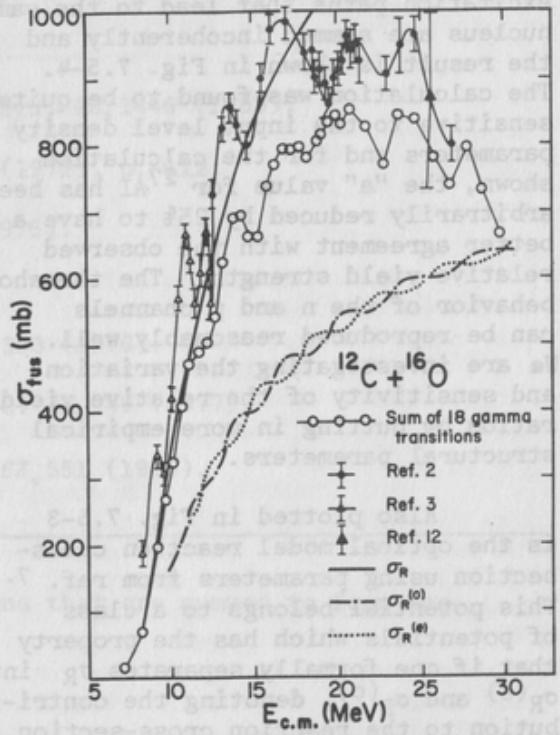

Fig. 7.5-3. Fusion cross-section deduced from the sum of 18 transitions (listed in Tab. 7.5-1). The results from refs. 2,3, and 12 are also plotted for comparison. σ_R (———), $\sigma_R^{(o)}$(-·-·-·-), and $\sigma_R^{(e)}$(·····) are optical model calculations using parameters from ref. 5.

In order to see if the general features of the distribution of yields between exit channels can be understood, evaporation model calculations have been performed using the computer code[5] GROGI2. This code allows competition between γ, n, p and α emissions at each stage of the de-excitation process, with the daughter-parent population related by the usual Hauser-Feshbach formula. Initial population, transmission coefficients, Q-values and structural level density parameters are required as inputs for the calculations. In our case, a rigid body moment of inertia (r_o=1.2 fm) was used for all the nuclei involved. The level density parameters a, were taken from ref. 6.

The initial spin population was calculated using optical model parameters from ref. 7 ($V=7.5 + 0.4E_{c.m.}$, $W=0.4 + 0.12\ E_{c.m.}$, $r_V = r_W = 1.34$, $a_V = a_W = 0.45$). Reaction channel transmission coefficients are calculated with parameters

quoted in ref. 12. Different de-excitation paths that lead to the same nucleus are summed incoherently and the result is shown in Fig. 7.5-4. The calculation was found to be quite sensitive to the input level density parameters and for the calculation shown, the "a" value for ^{27}Al has been arbitrarily reduced by 25% to have a better agreement with the observed relative yield strength. The threshold behavior of the n and p channels can be reproduced reasonably well. We are investigating the variation and sensitivity of the relative yield ratios by putting in more empirical structural parameters.

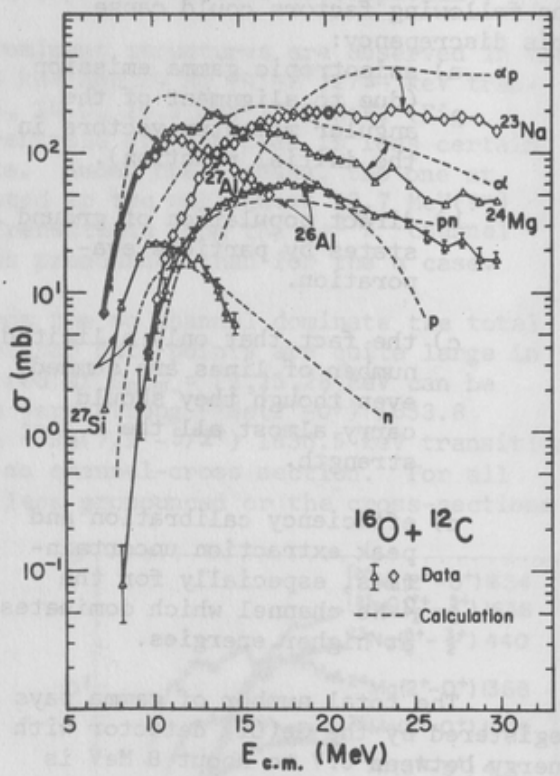

Fig. 7-5.4. Results from statistical calculations. The reaction channel and sequence of particle emission are indicated for each curve. See text for the explanation of parameters used.

Also plotted in Fig. 7.5-3 is the optical model reaction cross-section using parameters from ref. 7. This potential belongs to a class of potentials which has the property that if one formally separates σ_R into $\sigma_R^{(e)}$ and $\sigma_R^{(o)}$, denoting the contribution to the reaction cross-section from the even and odd partial waves, then both $\sigma_R^{(e)}$ and $\sigma_R^{(o)}$ display some moderate oscillatory-like structure. However the relative behavior of the even and odd part is such that the sum of the two is a smooth monotonous curve. This suggests that a parity dependent mechanism (e.g. core-exchange effects[8], odd-even yrast level effects[9], etc.) could cause these broad structures. A comparison with the data seems to suggest that the even contributions are somehow suppressed. This indication is dependent on the details of the optical model potential. Since this potential predicts a smaller total absorption cross-section than the experimental[2] fusion cross-section at low energies, caution must be exercised. More quantitative studies are underway.

---

1. Nuclear Physics Laboratory Annual Report, University of Washington (1976) p. 139.

2. P. Sperr et al. Phys. Rev. Lett. *36*, 405 (1976).

3. H. Fröhlich et al. Phys. Lett. *64B*, 408 (1976).

4. M. L. Halbert et al. Phys. Rev. *162*, 899 (1967).

5. GROGI2 by J. Gilat, BNL5024(T-580).

6. A Gilbert and A. Cameron, Can. J. Phys. *43*, 1446 (1965).

7. R. E. Malmin thesis, ANL PHY-1972F (1972), p. 112.

8. H. Yoshida, Nucl. Phys. *A257*, 348 (1976).

9. See section 7.4 of this report.

10. J.J. Kolata et al. Phys. Lett. *65B*, 333 (1976).

11. Z.E. Switkowski et al., Phys. Rev. C. *15*, 449 (1977).

12. A. Weidinger et al., Nucl. Phys. *A263*, 551 (1976).

Table 7.5-1. List of 18 discrete transitions that are summed to form the fusion cross-section. (Backed ^{12}C target).

Nucleus	Transitions ($J_i^\pi - J_f^\pi$) $E\gamma$(keV)
^{27}Si	$(^{1+}/_2 - ^{5+}/_2)780$; $(^{3+}/_2 - ^{5+}/_2)956$; $(^{7+}/_2 - ^{5+}/_2)2163$
^{27}A	$(^{1+}/_2 - ^{5+}/_2)844$; $(^{3+}/_2 - ^{5}/_{2+})1014$; $(^{7+}/_2 - ^{5+}/_2)2210$; $(^{9+}/_2 - ^{5+}/_2)3004$
^{26}A	$(1^+-0^+)830$; $(3^+-5^+)417$
^{26}Mg	$(2^+-0^+)1809$
^{25}Mg	$(1/2^+ - ^{5+}/_2)585$; $(^{3+}/_2-^{5+}/_2)975$
^{24}Mg	$(2^+-0^+)1368$
^{23}Mg	$(^{5+}/_2 - ^{3+}/_2)451$
^{23}Na	$(^{5+}/_2 - ^{3+}/_2)440$
^{22}Na	$(4^+-3^+)891$
^{22}Ne	$(2^+-0^+)1275$
^{20}Ne	$(2^+-0^+)1634$ $(+^{23}Na(^{7}/_{2+} - ^{5+}/_2)1636)$

7.6 Further Studies on Gamma Ray Yields Following the $^{18}O + ^{12}C$, $^{16}O + ^{13}C$ and $^{16}O + ^{28}Si$ Reactions

K. G. Bernhardt, H. Bohn, Y-d Chan, J. G. Cramer, L. Green, W. Lynch, R. Sielemann and R. Vandenbosch

The $^{18}O + ^{12}C$ and $^{16}O + ^{13}C$ Reactions

Gamma ray yields following the ^{18}O induced reactions on ^{12}C have been measured to compare with results from the $^{16}O + ^{12}C$ experiment.[1] According to the particle measurement of Sperr et al.[2], no comparable structure to that seen in $^{16}O + ^{12}C$ was observed in the fusion cross-section in this case. The systematic trend is not understood. It is therefore interesting to compare gamma results, which give more specific information about different exit channels.

Both backed[1] and unbacked ^{12}C targets were used in the experiment. The details of the backed target run has been described in ref. 1 and will not be reported here. For the unbacked ^{12}C target measurement, in addition to the Ge(Li) detector, a 10" x 10" NaI crystal[3] was also set up to detect gamma rays over a wide energy range. This is motivated by the previous result for the ^{16}O case that the gross structures observed in the discrete transitions are also present in a plot of the total gamma ray yield as a function of bombarding energy. Actually the excitation function of the higher energy gammas seem to display an even larger peak to valley ratio than the lower energy ones. It is therefore desirable to look into the high energy region of the gamma specta, and the NaI detector was chosen because of its better efficiency for high energy gamma rays.

The time of flight technique was applied to reduce neutron-induced gamma background since we were interested in the total spectrum sum. A bunched ^{18}O beam was used. A flight path of 58cm, which is the maximum one can have due to present geometrical constraints for the NPL 10" x 10" NaI system, was used to separate the prompt gamma rays from the neutron-induced ones. The time resolution was about 8-13 ns depending on the buncher tuning. By gating the gamma energy spectra by the prompt part of the TAC peak, the neutron-induced background was reduced by more than 50%. This could be much improved if a longer flight path was available. In order not to cause severe deadtime problems for the Ge(Li) detection system due to the pulsed beam, the beam current was limited to below 50 nA. The detection solid angle was also reduced by a factor of 4 compared to the previous measurements.

As expected with an unbacked target the peakshapes are very much Doppler broadened and only lines that were well separated from each other were analyzed. Excitation functions for discrete transitions are shown in Fig. 7.6-1. Excitation functions for the total gamma spectrum sum are also shown for both $^{18}O + ^{12}C$ and $^{16}O + ^{12}C$. The general behavior of the transition lines, neither the discrete transition nor the the total gamma yield for $^{18}O + ^{12}C$ indicates any structure of comparable strength to that for ^{16}O. This result supports the observations of Sperr et al.[2]

As has been suggested in ref. 4, the absence of structure in $^{18}O + ^{12}C$ could be due to the two extra neutrons that ^{18}O has. These neutrons might help to form strong doorways for fusion and conceivably damp away any similar structure. This idea can be tested from another point of view by adding neutrons to the ^{12}C core instead, e.g. $^{16}O + ^{13}C$, $^{16}O + ^{14}C$, etc. An experiment has been planned to study the gamma yields following the $^{16}O + ^{13}C$ reaction and a preliminary run has been performed at E_{lab}=40.5 MeV. The presence of ^{12}C contamination in the target causes an additional uncertainty in extracting the yields.

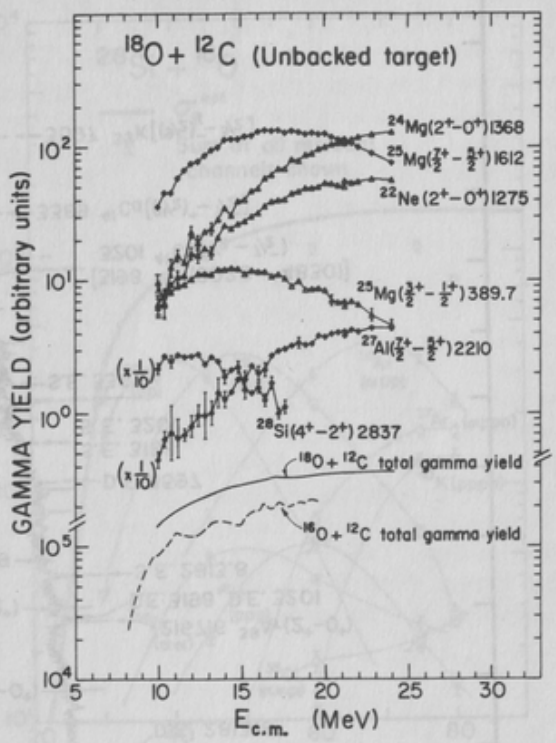

Fig. 7.6-1. Discrete transition gamma ray yields for the $^{18}O + ^{12}C$ reaction. Also shown are the total gamma spectrum count sum yields for $^{18}O + ^{12}C$ (solid curve) and $^{16}O + ^{12}C$ (dashed curve).

The $^{18}O + ^{28}Si$ Reaction

This experiment was an attempt to extend our fusion gamma ray study to targets belonging to the s-d shell, where extensive optical model studies have been made.[5] The measurement of fusion cross-sections would provide information to compliment that from elastic data.

Experimental set-up and procedures were very similar to the previous ones. The target was made by evaporating Si onto a thick tantalum backing. Measurements at E_{lab}= 30,45,60,70, 80 MeV have been completed and a typical spectrum with identified transitions coming from ^{28}Si is shown in Fig. 7.6-2. The gamma spectra are more complex than the lighter target case but still many transitions are well separated. The predominent channels are $2p(^{42}Ca)$, $3p(^{41}K)$, $\alpha p(^{39}K)$ and $\alpha pp(^{38}Ar)$ etc. Part of the analyzed lines are shown in Fig. 7.6-3 together with results of the optical model calculation using parameters from ref. 5. Our energy range partly overlaps with the work of Dauk et al.[6] In order to look for possible structures, finer step measurements will be pursued.

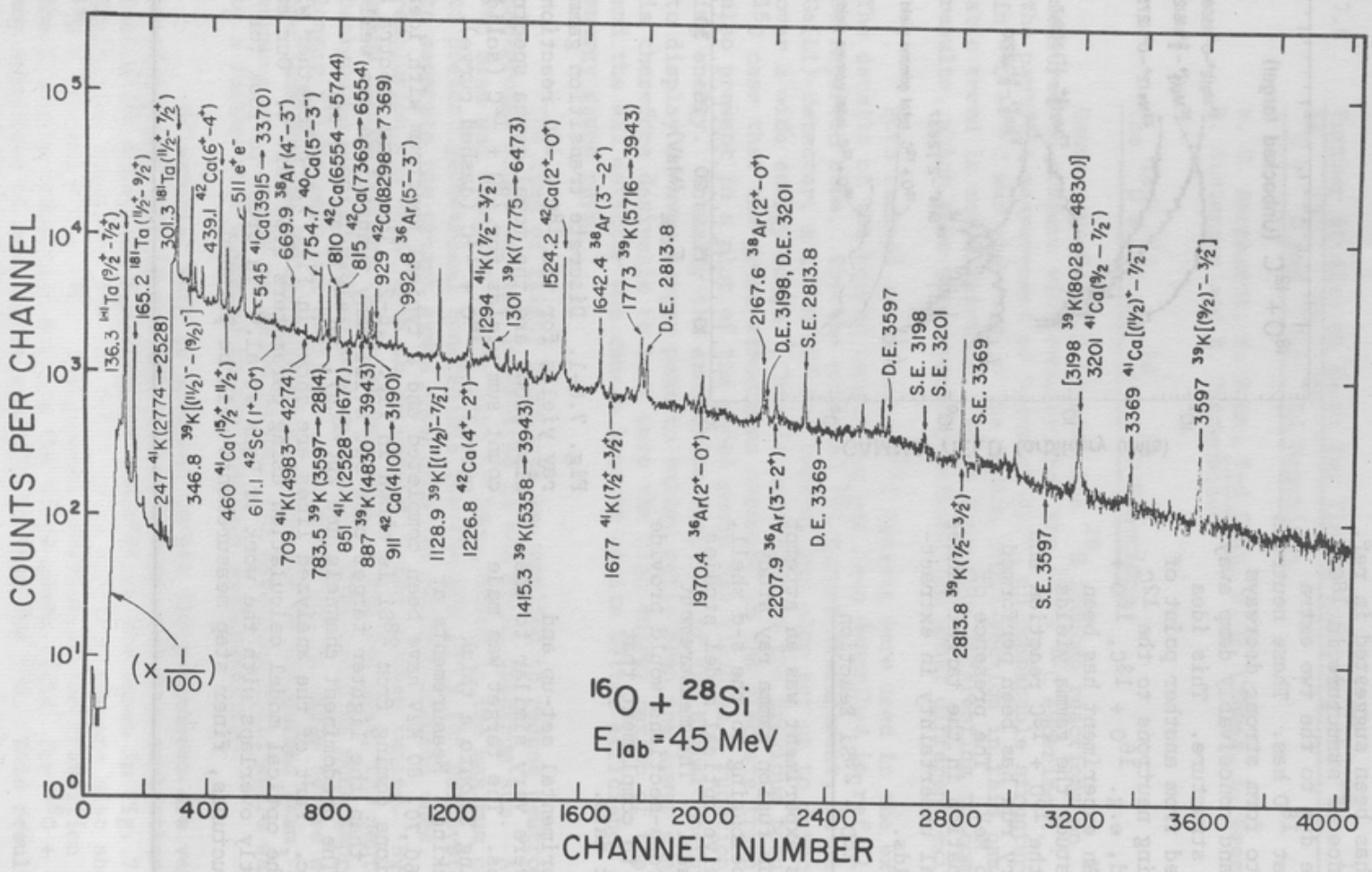

Figure 7.6-2

Gamma energy spectrum for the $^{16}O + ^{28}Si$ reaction at E_{lab}=45 MeV. Identified lines are indicated. In case the spin and parity of a level is unknown, the level energy is specified.

1. Nuclear Physics Laboratory Annual Report, University of Washington (1976) p. 139.

2. P. Sperr et al., Phys. Rev. Lett. *37*, 321 (1976).

3. M. Hasinoff et al., Nucl. Instr. Methods *117*, 375 (1974).

4. J. Schiffer, pre-print.

5. Nuclear Physics Laboratory Annual Report, University of Washington (1975) p. 128 and section 6.5 of this report

6. J. Dauk et al., Nucl. Phys. *A241*, 170 (1975).

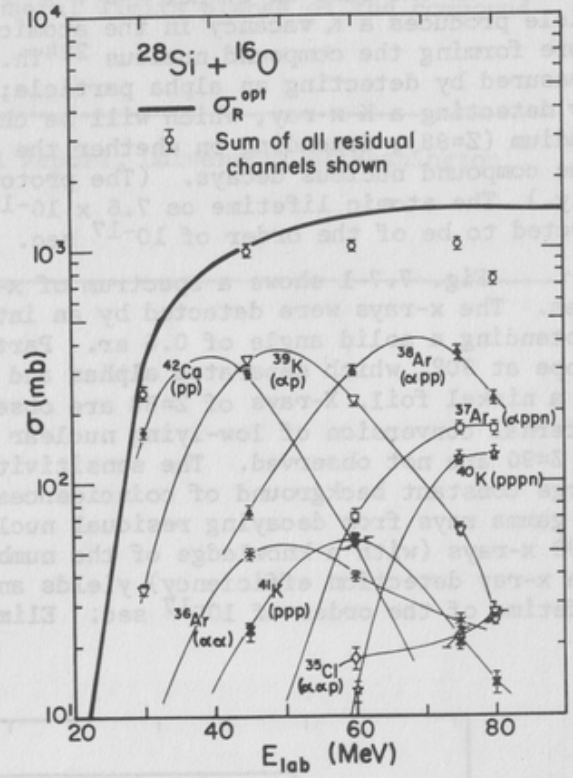

Fig. 7.6-3. Gamma ray yield cross-section for $^{16}O + ^{28}Si$. The solid curve is the predicted optical model reaction cross-section using parameters from ref. 5. Thin solid lines are drawn to guide the eye only.

7.7 X-Ray Technique for Measurement of Compound Nuclear Lifetimes

D. Burch, P. Dyer

Investigations of a new technique for measuring compound nuclear lifetimes in the 10^{-16} to 10^{-18} sec range have continued.[1] If a compound nucleus and an atomic K vacancy are created simultaneously, a measurement of how often the excited nucleus decays before the atomic excited state decays can determine the unknown nuclear lifetime relative to the known atomic lifetime. We measure characteristic K x-rays in coincidence with a product of the compound nuclear decay. If the compound nucleus decays first, the K x-ray is characteristic of the residual nucleus; if the atomic vacancy is filled first, the x-ray is characteristic of the compound nucleus.

Targets of ^{208}Pb, ^{197}Au and ^{181}Ta have been bombarded by ^{12}C and ^{16}O beams. In the case of 87-MeV ^{16}O + ^{208}Pb, for example, the incident ^{16}O particle produces a K vacancy in the atomic shell about once in 1500 times before forming the compound nucleus ^{224}Th. Decay of the compound nucleus is measured by detecting an alpha particle; decay of the atomic state is measured by detecting a K x-ray, which will be characteristic of thorium (Z=90) or radium (Z=88), depending on whether the K vacancy is filled before or after the compound nucleus decays. (The proton decay experiment is done simultaneously.) The atomic lifetime os 7.6×10^{-18} sec; the nuclear lifetime is expected to be of the order of 10^{-17} sec.

Fig. 7.7-1 shows a spectrum of x-rays in coincidence with alpha particles. The x-rays were detected by an intrinsi Ge detector placed at 90°, subtending a solid angle of 0.6 sr. Particles were detected by a counter telescope at 90°, which separated alphas and protons. Heavy particles were stopped by a nickel foil. X-rays of Z=88 are observed; however, most of these come from internal conversion of low-lying nuclear states of the residual nucleus. X-rays of Z=90 are not observed. The sensitivity of the experiment is limited by the large constant background of coincidences which probably arises from Compton tails of gamma rays from decaying residual nuclei. An upper limit on the number of Z=90 x-rays (with a knowledge of the number of alpha particles measured and of the x-ray detection efficiency) yields an upper limit on the compound nuclear lifetime of the order of 10^{-17} sec. Elimination of background by a technique

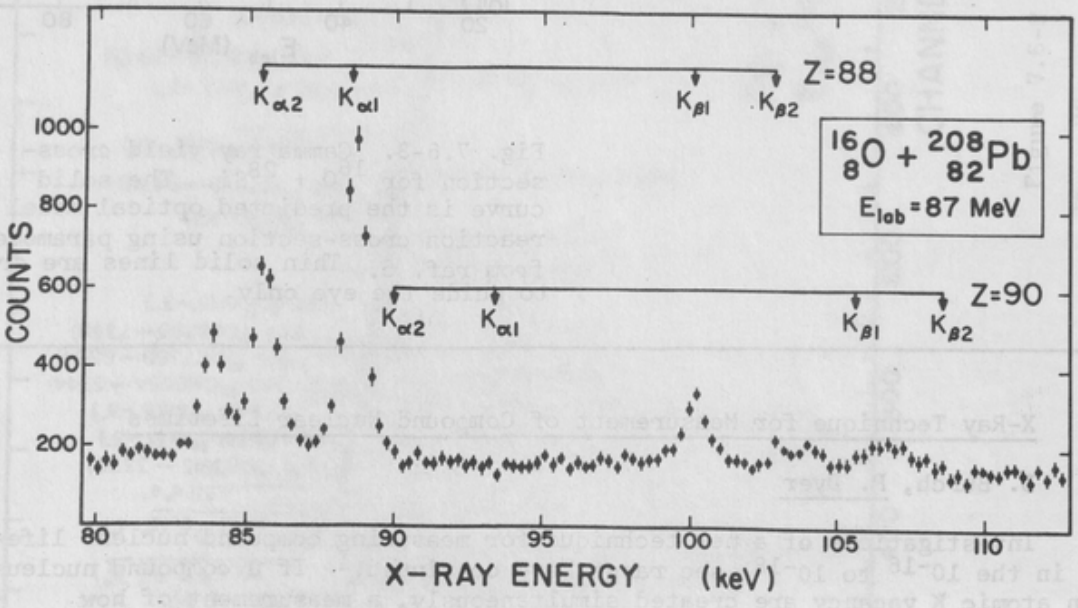

Fig.7.7-1. Energy spectrum of x rays coincident with alpha particles from the reaction 87-MeV ^{16}O + ^{208}Pb. Energies characteristic of the compound (Z=90) and residual (Z=88) nuclei are indicated. The peak at 84 keV is a gamma ray, probably from a Z=88 nucleus.

such as use of anticoincidence shielding will be required before compound nuclear x-rays can be observed and more useful limits placed on the compound nuclear lifetime.

---

1. Nuclear Physics Laboratory Annual Report, University of Washington (1976), p. 137.

---

8. HEAVY ION TRANSFER REACTIONS

8.1 The $^{29}Si + ^{14}N$ Stripping and Pickup Reaction

Y-d Chan, J.G. Cramer, B. Cuengco, K-L Liu, W. Lynch, and J. Wiborg

Since an anomalous angular distribution was reported in the $^{12}C(^{14}N, ^{13}N)^{13}C_{2s1/2}$ reaction,[1] other ℓ=1 transfer reactions have been studied to investigate the range of applicability of the finite-range distorted wave Born approximation. One class of reactions appropriate for this study is transfer reactions involving s-d shell nuclei, particularly in the s subshell. Since the orbital angular momentum transfer $\Delta\ell$ is restricted by the condition

$$|\ell_1-\ell_2| \leq \Delta\ell \leq \ell_1+\ell_2,$$

having the transferred particle going into an s-orbit (ℓ_1 or ℓ_2 = 0) limits $\Delta\ell$ equal to the orbital angular momentum of the transferred particle in the interacting partner, thus only one single $\Delta\ell$ is allowed for each reaction. Since only ground states are involved in these transfer reactions, larger cross sections should be expected compared with the $^{12}C(^{14}N,^{13}N)^{13}C_{2s1/2}$ reaction where excitation of the residual nuclei was required to produce the unique ℓ transfer condition.

The reactions $^{28}Si(^{14}N,^{15}N)^{28}S$, and $^{29}Si(^{14}N,^{13}C)^{30}P$ were chosen for this study. A self-supported ^{29}Si target was bombarded with a 53.5 MeV ^{14}N beam. A time-of-flight counter telescope was employed for separation of isotopes. The elastic scattering differential cross sections were measured down to about 10^{-3} of Rutherford, and computer code Genoa was used to search for the optimum optical potential parameters. These data and the optical model fit are shown in Fig. 8.1-1. With these parameters, the DWBA code LOLA was used to calculate the transfer angular distribution. A comparison of the data and the DWBA predictions is shown in Fig. 8.1-2.

This comparison shows some evidence for an anomaly in the angular distribution of the pick-up reaction (^{28}Si), but not in the stripping reaction (^{30}P). The fact that finite-range DWBA is adequate in describing the stripping reaction indicates the parameters chosen for the calculation

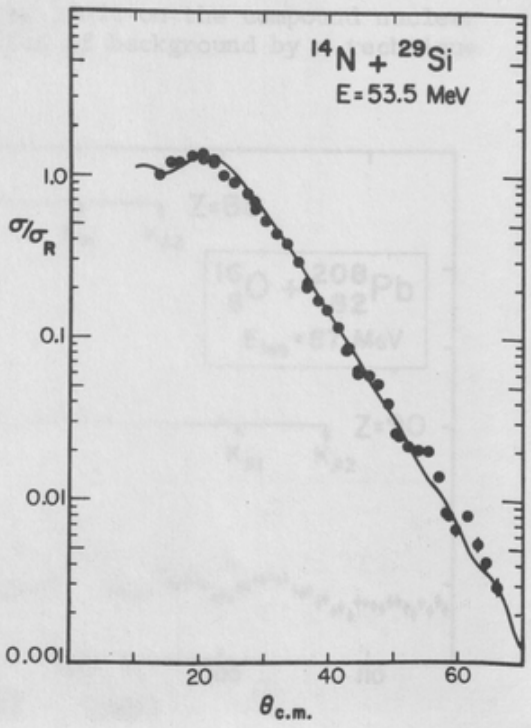

Fig. 8.1-1. Angular distribution for the $^{29}Si(^{14}N,^{14}N)^{29}Si$ scattering. The Solid line is the result of the optical model calculation with V_o = 100 MeV, W_o = 61.5 MeV r = 1.02fm and a = 0.69fm.

are reasonable. Other arbitrarily chosen parameters also fail to produce an anomaly in the stripping reaction.

This result coincides with the finding from the $^{13}C + {}^{40}Ca$ reaction,[2] where DWBA was found to be successful in describing the stripping reaction, but not the pick-up reaction. In that case coupled channel calculations indicated that in the $^{13}C + {}^{40}Ca$ transfer reaction multi-step processes via the 3^- and 5^- states were the probable cause of the discrepancy.

Although CCBA calculations have not been undertaken in our study, similar criteria exist here to make multi-step processes more important in the pick-up reaction. For the ^{29}Si $(^{14}N,{}^{15}N)^{28}Si$ reaction, if ^{29}Si is first inelastically excited, the binding energy for the transferred neutron would be smaller than if ^{29}Si is in its ground state. Since the tail region of the wave function of the transferred particle increases for decreasing binding energy and the transfer reaction is very sensitive to the tail region, the effect of core excitation is to dramatically enhance the stripping reaction cross section.

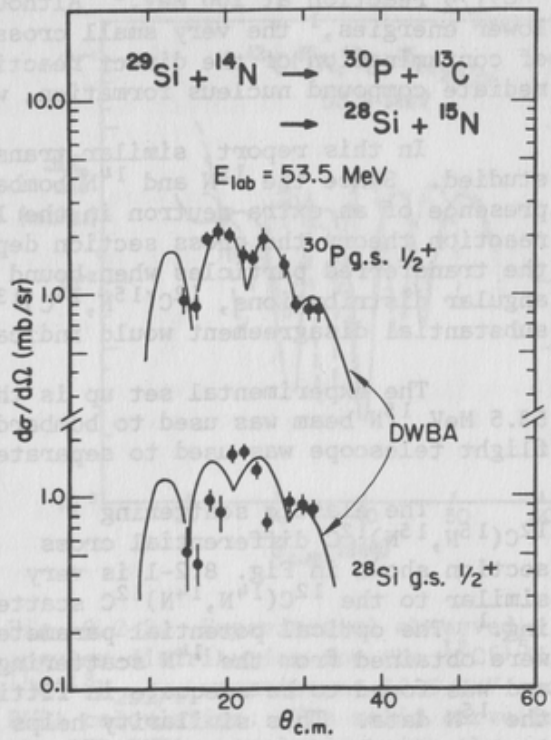

Fig. 8.1-2. Experimental transfer angular distributions for ^{29}Si $(^{14}N, {}^{13}C)^{30}P_{g.s.}$ and $^{29}Si(^{14}N,{}^{15}N)^{28}Si_{g.s.}$ and corresponding EFR DWBA calculations.

On the other hand, the excitation of ^{29}Si will not affect the transferred proton in the $^{29}Si(^{14}N,{}^{13}C)^{30}P$ reaction. As a result, multi-step effects should not be important for the stripping reaction.

1. R.M. DeVries *et al.*, Phys. Rev. Lett. *32*, 680 (1974.
2. P.D. Bond *et al.*, Phys. Rev. Lett. *36*, 300 (1976).

8.2 The Study of Anomalous Angular Distributions with ^{15}N-Induced Reactions

Y-d Chan, J.G. Cramer, B. Cuengco, L. Green, K-L Liu, and W. Lynch

The anomalous angular distribution of $^{12}C(^{14}N,{}^{13}N)^{13}C^*_{2s1/2}$ and $^{12}C(^{14}N, {}^{13}N,{}^{13}C)$ $N^*_{2s1/2}$ at 53.5 MeV was reported in the last annual report.[1] The purpose of this study of transfer reactions at low energy is to explore the extent of the anomaly which had been found in the angular distribution of $^{13}C(^{14}N,{}^{13}N)$

$^{13}C^{*}_{2\,1/2}$ reaction at 100 MeV.[2] Although a similar anomaly was also found at lower energies,[1] the very small cross sections there were obscured by sources of contamination of the direct reaction mechanisms, such as effect of intermediate compound nucleus formation, which can dominate the low energy spectra.

In this report, similar transfer reactions initiated by a ^{15}N beam were studied. Since the ^{15}N and ^{14}N bombarding particles differ principally by the presence of an extra neutron in the $1p_{1/2}$ shell in ^{15}N, and since in direct reaction theory the cross section depends principally on the configuration of the transferred particles when bound to the two cores, we should expect similar angular distributions, $^{12}C(^{15}N,^{14}C)^{13}N_{2s1/2}$ and $^{12}C(^{13}N,^{13}C)^{13}N_{2s1/2}$. Any substantial disagreement would indicate problems with direct reaction theory.

The experimental set up is the same as the $^{12}C(^{14}N,^{13}N)^{13}C$ study.[1] A 53.5 MeV ^{15}N beam was used to bombard a self-supporting ^{12}C target. A time-of-flight telescope was used to separate the detected particles.

The elastic scattering $^{12}C(^{15}N,^{15}N)^{12}C$ differential cross section shown in Fig. 8.2-1 is very similar to the $^{12}C(^{14}N,^{14}N)^{12}C$ scattering.[1] The optical potential parameters were obtained from the ^{14}N scattering and was found to be adequate in fitting the ^{15}N data. This similarity helps to support the argument that the distorted waves should not be very sensitive to the extra neutron in the ^{15}N nucleus. There has been a suggestion that the anomaly in the angular distribution can be removed by changing the optical parameters in the outgoing channels, the rationale being that the exit channels have different interacting particles from the entrance channels. The similarity between the distorted waves for ^{15}N and ^{14}N scattering shows this hardly to be the case.

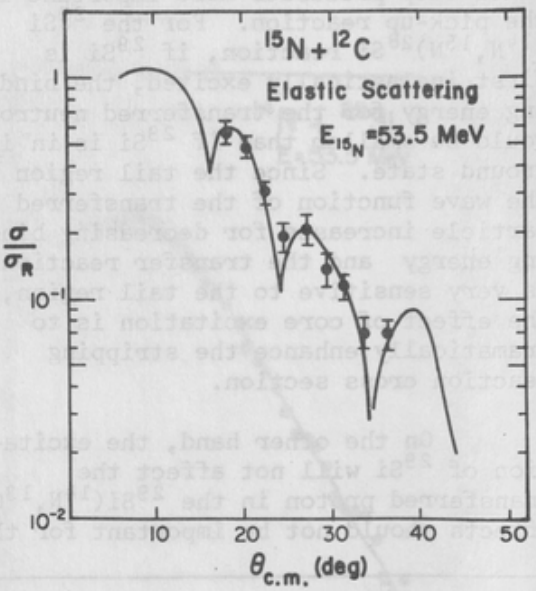

Fig. 8.2-1. Elastic scattering of $^{12}C(^{15}N,^{15}N)^{12}C$ at 53.5 MeV with optical model calculation

V = 145 MeV r_r = .925fm a_r = .816fm

W = 35.3 MeV r_i = 1.30fm a_i = .178fm

The angular distribution of the $^{12}C(^{15}N,^{14}C)^{13}N_{2s1/2}$ is shown in Fig. 8.2-2. The solid curve is the DWBA calculation for the unique ℓ=1 transfer reaction, which is performed by assuming a binding energy of 0.1 MeV for the unbound state. The validity of this approximation has been verified for other reactions.

The dotted curve indicates the result of a finite-range DWBA calculation using the radius of the imaginary part of the exit channel potential

different from that obtained from the elastic scattering as prescribed by Kubo. For the reaction studied here, the T-matrix for the proton stripping reaction is not sensitive to variation of this parameter. Thus modifying the exit imaginary radius parameters does nothing to shift the phase of the oscillation of the DWBA calculation.

On the contrary, the dashed curve, corresponding to the forbidden $\Delta\ell=0$ transfer DWBA calculation, again gives a better chi square for fitting the experimental results. In conclusion, it is shown that DWBA calculations fail to produce the fine structures of the angular distributions, for a variety of transfer reactions in the region of energies where oscillation is a distinctive feature of the cross sections, and that modifying the exit-channel imaginary radius does not permit fits to the data.

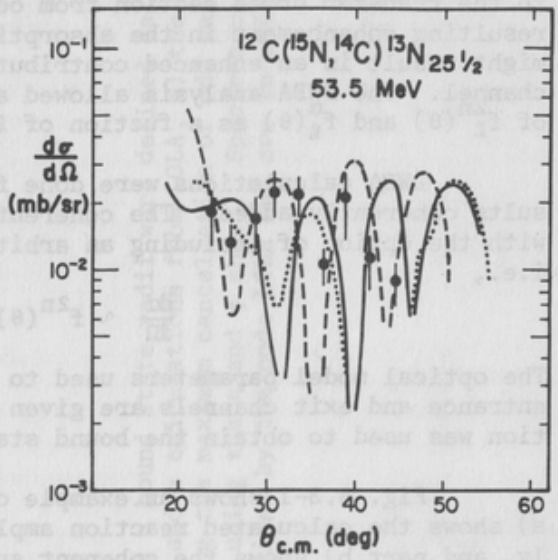

Fig. 8.2-2. Experimental observed angular distribution for the $^{12}C(^{15}N, ^{14}C)^{13}N_{2s1/2}$ reaction at 53.5 MeV and DWBA calculation. The solid curve is the EFR DWBA calculation with the parameters obtained from elastic scattering. The dotted curve is the result using a modified imaginary radius in the exit channel. The dashed curve is the forbidden $\Delta\ell=0$ transfer calculation.

1. Nuclear Physics Laboratory Annual Report, University of Washington (1976), p. 149.
2. R.M. DeVries et al., Phys. Rev. Lett. *32*, 680 (1974).

8.3 Interference of the 2n and α Transfer Channels in the $^{18}O+^{12}C$ System

K.G. Bernhardt,† H. Bohn,† K.A. Eberhard,† R. Vandenbosch, and M.P. Webb††

We have measured angular distributions for the 2n-α transfer channel of the $^{18}O+^{12}C$ system at $E_{c.m.}$=16.6, 19.8, 20.4 and 21.8 MeV and have carried out a DWBA analysis of the results. This program was undertaken in order to test the hypothysis[1] that the dominance of odd spin, intermediate structure resonances in the elastic scattering of ^{18}O from ^{12}C might be caused by the preferential absorption of even partial waves into the ^{2n}-α channel. Since both 2n and α transfer in this system produce the same final state ($^{16}O+^{14}C$), the reaction amplitude is a coherent sum of the amplitudes for both processes

$$f(\theta) = \sum_{\ell} \left[f_{\ell}^{2n}(\theta) + (-)^{\ell} f_{\ell}^{\alpha}(\theta) \right]$$

If the 2n and α amplitudes were of similar magnitude and phase, contributions to the transfer cross section from odd partial waves would be inhibited. The resulting enhancement in the absorption of even partial waves into this channel might result in an enhanced contribution from odd partial waves in the elastic channel. The DWBA analysis allowed an investigation of the magnitude and phase of $f_\ell^{2n}(\theta)$ and $f_\ell^{\alpha}(\theta)$ as a fuction of ℓ.

DWBA calculations were done for both the 2n and α transfer and the results coherently added. The coherent addition of the two amplitudes was made with the option of including an arbitrary scale factor (η) and phase angle (ϕ), i.e.,

$$\frac{d\sigma}{d\Omega} \sim \left| f^{2n}(\theta) + \eta e^{i\phi} f^{\alpha}(\pi-\theta) \right|^2 .$$

The optical model parameters used to generate the distorted waves in the entrance and exit channels are given in reference 2). The cluster approximation was used to obtain the bound state wave functions.

Fig. 8.3-1 shows an example of the results obtained at 19.0 MeV. Part a) shows the calculated reaction amplitudes for the 2n and α processes separately, and part b) shows the coherent sum with η and ϕ values which produced the maximum cancellation of the odd ℓ contributions. Unfortunately, at these energies the two processes showed a significant interference only in a rather narrow angular region (∿10°) about 90°. Qualitatively, it appeared that the use of η and ϕ values which produced the maximum amount of cancellation of the odd ℓ contributions fit the data a little better near 90°. It can be seen from the figure that even without arbitrary adjustment of η and ϕ there is a significant cancellation of the amplitudes for the odd partial waves.

It was also found that a decrease in the α bound state radius (to r_o = 1.05 fm) relative to that of the 2n bound state changed the magnitude and phase of the $f_\ell^{\alpha}(\theta)$ such that they were in phase with the $f_\ell^{2n}(\theta)$. The coherent addition of these reaction amplitudes required that ϕ=0 for the best fit. In addition, the absolute magnitude of the cross section depended very sensitively on the choice of the bound state radii. The optical model parameters were not varied in these studies.

Estimates of the possible effect of this channel on the elastic channel (by comparing the angle integrated cross section for the 2n-α process to the total cross section for the relavent partial wave and by calculation of the S-matrix elements) showed that the 2n-α channel accounted for only 3-4% of the flux for a given partial wave. However, optical model calculations made with the inclusion of a party-dependent surface term in the imaginary potential showed that significant enhancements in the back angle elastic cross section could be obtained with a surface term which increased the absorption of the even partial waves by only a few percent over that obtained with a parity independent volume absorption only. Thus it appeared as if a small *parity-dependent* change in the absorption had a significant effect on the elastic scattering at back angles (>90°).

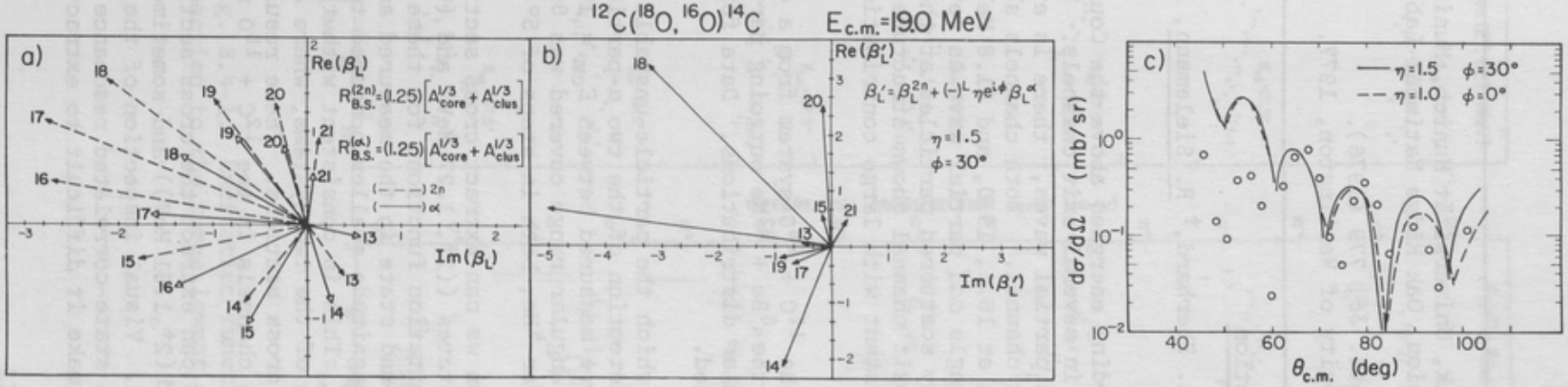

Fig. 8.3-1. DWBA results at 19.0 MeV where both the 2n and α bound state radii were defined as $R = (1.25\ fm)(A_{core}^{1/3} + A_{clus}^{1/3})$. a) shows the β_ℓ for the 2n and α calculations from LOLA, b) the coherent addition of the amplitudes for the η and φ yielding the maximum cancellation of odd partial wave contributions and c) fits to the angular distribution using the η and φ shown. Spectroscopic factors are discussed in the text. The amplitudes are as given by the code LOLA and are in units of MeV $fm^{1/2}$.

† Present address: Sektion Physik, Universität Munich, Munich, Germany.
†† Present address: Physics Division, Oak Ridge National Lab, Oak Ridge, Tn. 37831.

1. M.P. Webb et al., Phys. Rev. Lett. *36*, 779 (1976).
2. M.P. Webb, Ph.D. Thesis, University of Washington, 1977.

8.4 The $^{12}C + ^{18}O \rightarrow ^{8}Be + ^{22}Ne$ Reaction

K.G. Bernhardt,† H. Bohn,†† K.A. Eberhard,† R. Sielemann, R. Vandenbosch, and M.P. Webb†††

The system $^{12}C + ^{18}O$ for bombarding energies above the Coulomb barrier exhibits remarkably different behavior in several exit channels. The elastic scattering seems to be dominated by odd partial waves,[1] there is evidence that this is also true for the $\alpha + ^{26}Mg$ exit channel.[1] Both channels show nonstatistical intermediate structure resonances at 16.6, 19.0, and 21.8 MeV; these structures seem to be dominated by a single *odd* partial wave as revealed in angular distributions of the elastically scattered particles at the resonance energies. In contrast, the $^{16}O + ^{14}C$ exit channel shows structure in the angular distribution at 16.6 and 19.0 MeV consistent with large contributions from *even* partial waves.[2]

To obtain more information on the $^{12}C + ^{18}O$ system from a different exit channel we started an investigation of the $^{8}Be + ^{22}Ne$ outgoing particles by measuring excitation functions and angular distributions. Data for the $\alpha + ^{26}Mg$ channel were simultaneously recorded.

We used an 8-detector array in which the particle-unstable ^{8}Be nucleus was identified through the coincident detection of the two α-particles by which it decays. The excitation functions were measured between E_{cm} = 15 MeV and 22.4 MeV in ΔE_{cm} = 200 keV steps. The angular range covered was θ_{LAB} = 7.5° to 37.5° for ^{8}Be and θ_{LAB} = 5° to 40° for ^{4}He, both in steps of 5°.

In the $^{12}C(^{18}O,^{8}Be)^{22}Ne$ reaction we can extract cross sections for the (0^+, g.s.) and the two lowest excited states ((2^+, 1.27 MeV) and (4^+, 3.36 MeV)) quite easily. Fig. 8.4-1 shows the excitation functions for these three states in ^{22}Ne. The cross section for the ground state in the measured angular- and energy interval is up to one order of magnitude smaller compared to the $^{12}C(^{16}O, ^{8}Be)^{20}Ne$ reaction to the ground state.[3] This is consistent with the ground state alpha exit channel cross sections of the two systems, where again the $^{12}C + ^{18}O$ system exhibits much smaller cross sections. These results are consistent with the greater number of open channels in the $^{12}C + ^{18}O$ system.

In the $\alpha + ^{26}Mg$ exit channel we can extract the cross sections for the two lowest states in ^{26}Mg ((0^+,g.s.) and (2^+,1.81 MeV)) and sometimes also for the second excited state (2^+, 2.94 MeV). Visual inspection of the excitation functions shows evidence for angle- and state-correlated resonance structures at 16.6 and 19.0 MeV. Poor statistics make it difficult to extract information at 21.8 MeV.

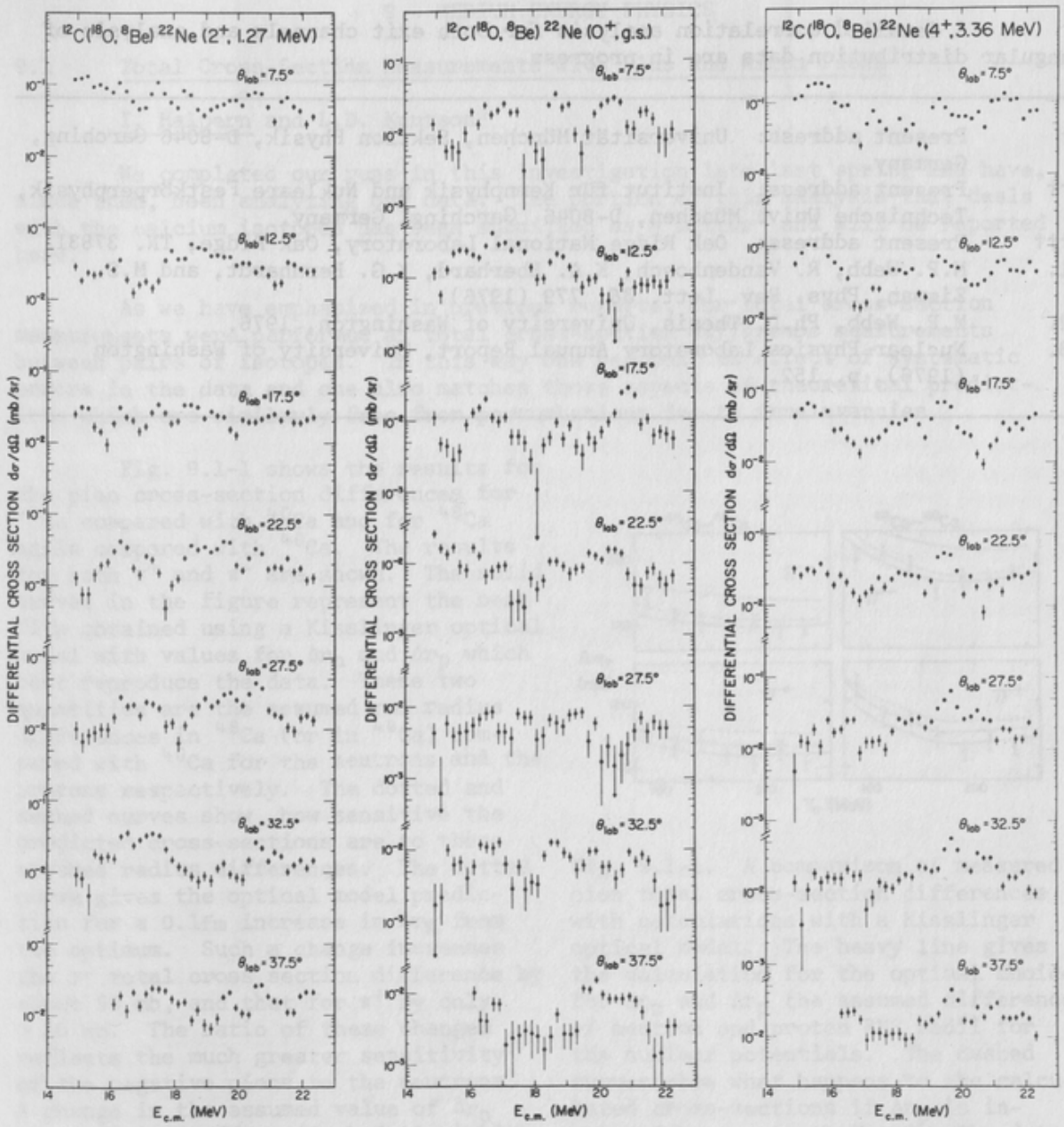

Fig. 8.4-1. Excitation functions of the $^{12}C(^{18}O, ^{8}Be)^{22}Ne$ reaction to the three lowest states in ^{22}Ne.

A detailed correlation analysis for both exit channels and analysis of angular distribution data are in progress.

---

† Present address: Universität München, Sektion Physik, D-8046 Garching, Germany.

†† Present address: Institut für Kernphysik und Nukleare Festkörperphysik, Technische Univ. München, D-8046 Garching, Germany.

††† Present address: Oak Ridge National Laboratory, Oak Ridge, TN. 37831.

1. M.P. Webb, R. Vandenbosch, K.A. Eberhard, K.G. Bernhardt, and M.S. Zisman, Phys. Rev. Lett. *36*, 779 (1976).

2. M.P. Webb, Ph.D. Thesis, University of Washington, 1976.

3. Nuclear Physics Laboratory Annual Report, University of Washington (1976), p. 152.

---

9. MEDIUM ENERGY PHYSICS

9.1 Total Cross-Section Measurements with Plus and Minus Pions

I. Halpern and L.D. Knutson*

We completed our runs in this investigation late last spring and have, since then, been analyzing our data. The portion of this analysis that deals with the calcium isotopes has been submitted as a Letter[1] and will be reported here.

As we have emphasized in previous reports, our total cross-section measurements were performed as total cross-section *difference* measurements between pairs of isotopes. In this way one reduces the effect of systematic errors in the data and one also matches those aspects of theoretical predictions which are similarly free from perturbations due to irrelevancies.

Fig. 9.1-1 shows the results for the pion cross-section differences for ^{44}Ca compared with ^{40}Ca and for ^{48}Ca again compared with ^{40}Ca. The results for both π^+ and π^- are shown. The solid curves in the figure represent the best fits obtained using a Kisslinger optical model with values for Δr_n and Δr_p which best reproduce the data. These two quantities are the assumed rms radius differences in ^{48}Ca (or in ^{44}Ca) compared with ^{40}Ca for the neutrons and the protons respectively. The dotted and dashed curves show how sensitive the predicted cross-sections are to these assumed radius differences. The dotted curve gives the optical model prediction for a 0.1fm increase in Δr_n from the optimum. Such a change increases the π^- total cross section difference by about 50 mb, and that for π^+ by only $\sim$ 10 mb. The ratio of these changes reflects the much greater sensitivity of the negative pions to the neutrons A change in the assumed value of Δr_p has a similar effect (dashed line) with the effect larger this time for the positive pions.

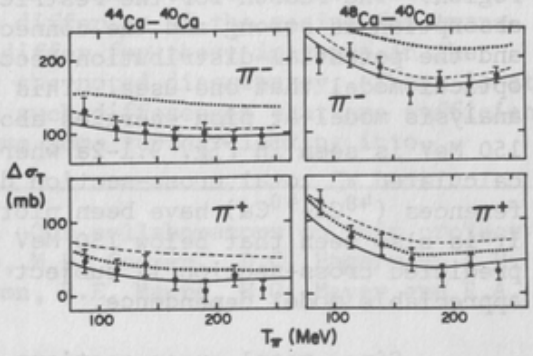

Fig. 9.1-1. A comparison of measured pion total cross-section differences with calculations with a Kisslinger optical model. The heavy line gives the calculation for the optimal choice for Δr_n and Δr_p the assumed difference of neutron and proton RMS radii for the nuclear potentials. The dashed curves show what happens to the calculated cross-sections if Δr_p is increased by one tenth fermi. The dotted curves are the same for an equal increase in Δr_n.

The calcium isotopes (in particular ^{40}Ca and ^{48}Ca) have been among those favored by theorists in their attempts to account for nuclear shapes and sizes in terms of the known forces between nucleons. There have been a number of Hartree-Fock calculations for the calcium isotopes and the main interest in total pion cross-section data, at present, is in their implications with regard

to those things that the Hartree-Fock calculations predict.

Since a total cross-section is but one number, it is clear that it cannot provide us with much detail about the nuclear size and shape. Moreover, even to obtain the information that it does in principle provide, one must unfold the effects of the strength and range of the probe-nucleon interaction. More crisply put, the Hartree-Fock calculations make predictions about neutron and proton *density* distributions. The pion-nucleus cross-sections on the other hand can be used to map out aspects of nuclear *potential* distributions. To confront the theory one therefore has to make the connection somehow between the effective optical model potentials and the actual distributions of the nucleons that give rise to these potentials.

In order to minimize the uncertainties connected with this problem, we have restricted the data examined in the present analysis to the (3,3) resonance region (∿100 to 250 MeV) although we have also taken data below this region. The reason for the restriction is that in the resonance region the absorption is strong and the connection between particle density distribution and the potential distribution becomes rather independent of the particular optical model that one uses. This independence of the cross-section on the analysis model at pion energies above 150 MeV is seen in Fig. 9.1-2a where calculated π^- total cross-section differences (^{48}Ca-^{40}Ca) have been plotted. It is also seen that below 150 MeV the predicted cross-section is subject to appreciable model dependence.

Since total cross-sections provide but a single number, one might be concerned that a change in rms radius could be compensated by a change in the general shape of the particle distribution when one calculates a predicted cross-section. This turns out not to be the case. If the total number of nucleons and their rms radius is fixed and, in addition, one specifies that the shape of the nucleon distribution be "reasonable" (any commonly assumed parameterization is reasonable) then one finds that the total cross-section is quite well determined. This is shown in Fig. 9.1-2b. All told, one therefore has some confidence in the comparison of radius differences of optical models matched to pion cross-section data with the same differences obtained in Hartree-Fock calculations for nucleon distributions.

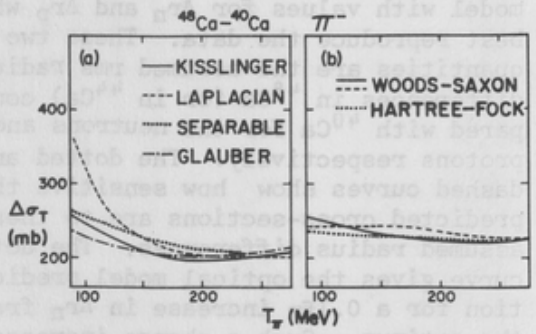

Fig. 9.1-2. a) Results of calculations of total cross-section differences with various models. Above 150 MeV there is very little difference between the various models for given values for Δr_n and Δr_p. b) Results of calculations of total cross-section differences for different reasonable shapes of nucleon distributions having the same total number of nucleons and the same rms radius. There is little difference in the predictions of the various shapes.

The present measurements give $\Delta r_p = -0.06 \pm 0.07$fm for ^{48}Ca-^{40}Ca which overlaps the electron scattering measurements,[2] $\Delta r_p \sim 0.01$fm. For Δr_n our measurements give 0.14 ± 0.05fm. Here there are of course no electron-scattering radii. The Hartree-Fock predictions[3] for Δr_n are typically near 0.25 fm, somewhat larger than the experimental result. In support of our experimental value we can cite two recent measurements, one with α particles and the other with high energy protons.

α particles[4]	$\Delta r_n = 0.08 \pm 0.08$ fm
1 GeV protons[5]	$\Delta r_n = 0.16 \pm 0.02$ fm

Although both these probes are, like the pions, strong interaction probes and involve some sort of unfolding to obtain *density* parameters from *potential* parameters, the fact that all three results are in substantial agreement despite their different character suggests, perhaps, that some difficulties remain in the Hartree-Fock calculations. It should be mentioned, however, that there may be another way out. In all of the experimental fits the potential distributions for the calcium isotopes which were fitted were taken to be of the same *form*. If the basic forms for ^{40}Ca and ^{48}Ca should differ or if the recipe for translating from densities to potentials should differ for these isotopes in the tail region, one could possibly account for the noted discrepancy. There is at the moment no evidence that there should be such differences that are sufficiently large, but these possibilities may deserve some further looking into.

---

* Now at the University of Wisconsin. Our collaborators on this project include G.R. Burleson, J.R. Calarco, M.D. Cooper, D.C. Hagerman, R.H. Jeppesen, K.F. Johnson, M.J. Jakobson, R.E. Marrs, H.O. Meyer and R.A. Redwine.

1. Submitted to Phys. Rev. Letters.
2. R.F. Frosch et al., Phys. Rev. *174*, 1380 (1968), R.D. Ehrlich, Phys. Rev. *173*, 1088 (1968). See also W. Bertozzi et al., Phys. Lett. *41B*, 408 (1972) for a correction to these papers for effects of nucleon size.
3. Reviewed in R.C. Barrett, Rep. Prog. Phys. *37*, 1 (1974). Se also J.W. Negele and D. Vautherin, Phys. Rev. *C5*, 1472 (1972).
4. G.M. Lerner et al., Phys. Rev. *C12*, 778 (1975).
5. G.D. Alkhazov et al., Nucl. Phys. *A274*, 443 (1976).

9.2 Inelastic Scattering of Pions to the Continuum

D. Chiang, I. Halpern, L. Knutson,† G.A. Miller, and Collaborators*

We have pointed out in earlier reports that inelastically scattered pions have the advantage (as probes for giant resonances) over other strongly interacting particles that they are lighter and therefore excite fewer multipoles in any given excitation region. Late last fall we had a first run on the π,π' reaction to continuum excitations. The run was carried out in collaboration with the Carnegie-Mellon group and they provided the intrinsic germanium detector telescope used in these measurements.[1] Positive pions of 60 MeV were incident on a large area target (typical thickness ~ 1 gm/cm^2) viewed by a

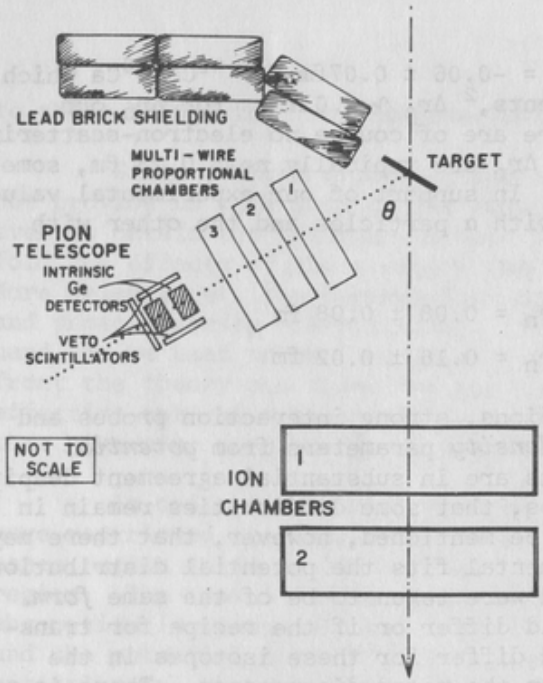

Fig. 9.2-1. Arrangement of detectors and shielding for the measurement of π,π' spectra to the continuum. The detector array includes a monitor counter (not shown) which sits out of the scattering plane. ●

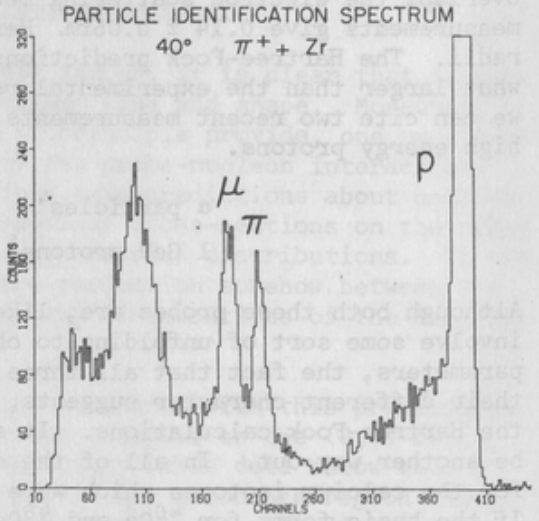

Fig. 9.2-2. The output of the particle-identifier in a typical run for particles passed by the wire-chambers as having come from the target. Elastic pions do not contribute to this spectrum. They are vetoed by the scintillator behind the telescope. The incident pion energy was 60 MeV and the telescope was at 40°. It is seen that the pion and muon peaks are adequately separated.

system (Fig. 9.2-1) consisting of wire chambers (to restrict accepted particles to those coming from the target) and a telescope that could identify pions of energies between ∿38 MeV and 52 MeV. This corresponds to excitation energies ranging from 8 to 22 MeV. A typical particle-identification spectrum is shown in Fig. 9.2-2. It is seen from the figure that muons, the most troublesome contaminant, are quite distinguishable from the pions. At forward angles the upper limit for muon contamination in the pion spectrum is about 10%. It is smaller at backward angles.

Spectra were taken for targets of Ni, Zr, Sn and Pb at most of the following angles: 40°, 70°, 90°, and 120°. The results are shown in Fig. 9.2-3. The statistical accuracy of the data shown there is not quite good enough to permit one to reliably identify any bumps in the spectra.

One of the more striking features seen in Fig. 9.2-3 is the strong backward peaking of the inelastic spectra integrated over the observed energy interval. We had done some DWIA calculations of expected spectra before the first run, using both Kisslinger and local Laplacian optical models with parameters derived from free pion-nucleon scattering. These integrated spectra showed a fairly symmetric minimum at 90° instead of a backward peak. This

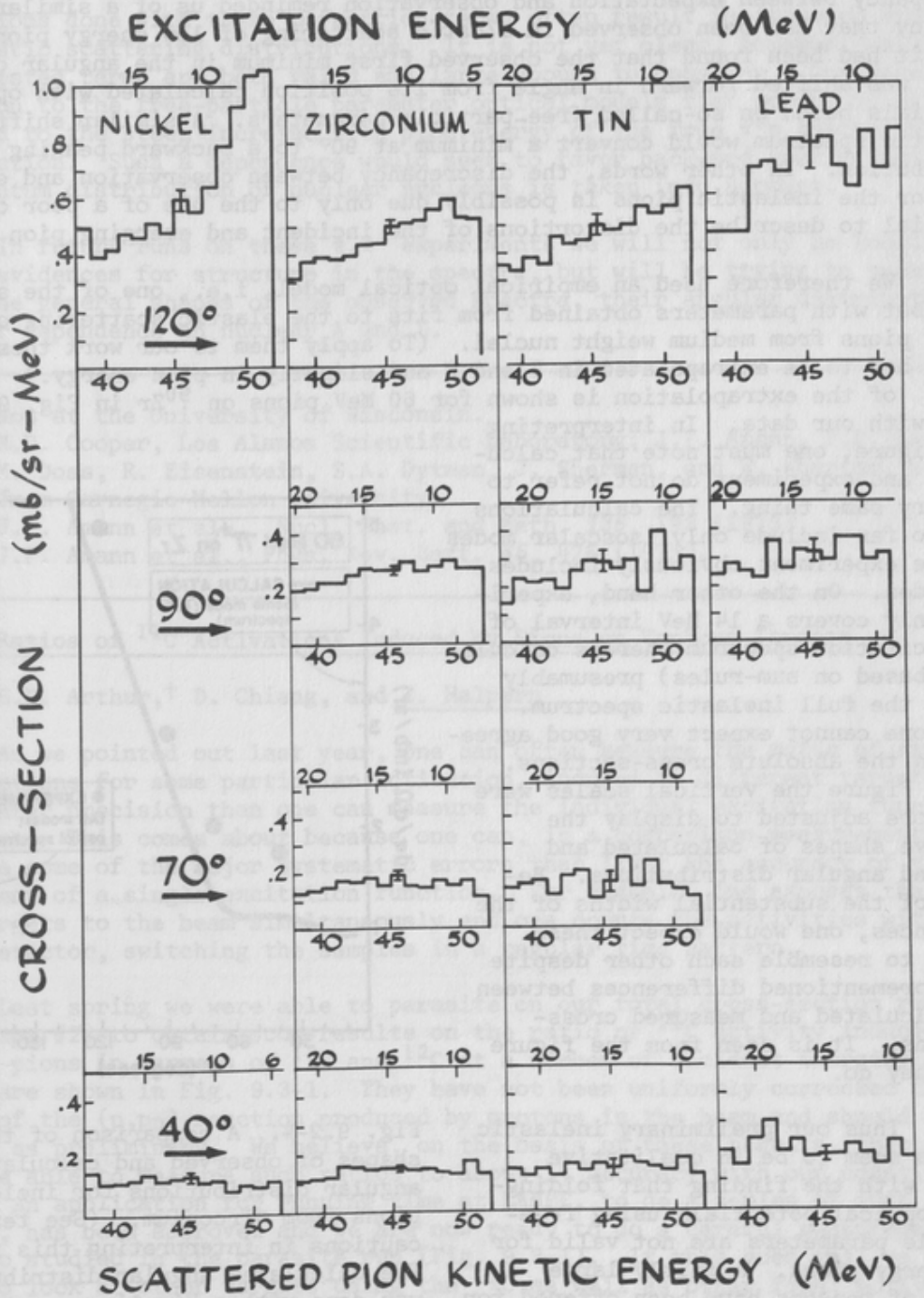

Fig. 9.2-3. Spectra of inelastically scattered positive pions observed in our first run. The incident pion energy was 60 MeV. Typical statistical accuracies are ∿10% per MeV interval.

discrepancy between expectation and observation reminded us of a similar discrepancy that had been observed in *elastic* scattering of low energy pions.[2] There it had been found that the observed first minimum in the angular distribution was shifted forward in angle from its position calculated with optical potentials based on so-called free-particle parameters. A similar shift for the inelastic spectrum would convert a minimum at 90° to a backward peaking angular distribution. In other words, the discrepancy between observation and calculation for the inelastic pions is possibly due only to the use of a poor optical potential to describe the distortions of the incident and emerging pion waves.

We therefore used an empirical optical model, i.e., one of the standard forms but with parameters obtained from fits to the elastic scattering of low energy pions from medium weight nuclei. (To apply them to our work these parameters had to be extrapolated in Z and N and slightly in pion energy.) The result of the extrapolation is shown for 60 MeV pions on ^{90}Zr in Fig. 9.2-4 along with our data. In interpreting this figure, one must note that calculation and experiment do not refer to the very same thing. The calculations done so far include only isoscalar modes and the experiment obviously includes all modes. On the other hand, experiment only covers a 14 MeV interval of the excitation spectrum whereas calculation (based on sum-rules) presumably covers the full inelastic spectrum. Thus, one cannot expect very good agreement on the absolute cross-sections. In the Figure the vertical scales were therefore adjusted to display the relative shapes of calculated and observed angular distributions. Because of the substantial widths of the resonances, one would expect these shapes to resemble each other despite the aforementioned differences between the calculated and measured cross-sections. It is seen from the figure that they do.

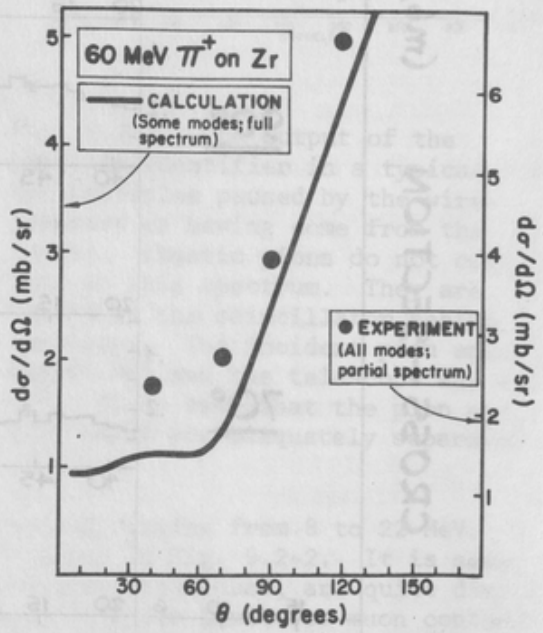

Fig. 9.2-4. A comparison of the shapes of observed and calculated angular distributions for inelastic pions from zirconium. (See text for cautions in interpreting this figure.) The calculated angular distribution was done with a Kisslinger optical model using parameters obtained from a fit to elastic scattering on iron rather than from free pion-nucleon cross-sections.

Thus our preliminary inelastic results seem to be in qualitative accord with the finding that folding-model optical potentials using free-particle parameters are not valid for low energy pions. A fairly large number of reasons have been offered for this failing and there have been many suggestions for correction terms to add the free-particle parameter optical potentials reflecting these reasons.

Calculations done with these correction terms often result in improved agreement with elastic scattering distributions. It is not yet clear, however, which of the suggested terms are both valid and large enough to consider. One possible correction to the free-particle parameter optical models that occurs to us is connected to the steep increase with pion energy of the free π^+p scattering cross-section. Such a dependence would seem to favor backward scatterings when the momentum distribution of nuclear nucleons is taken into account.

In future runs on these π,π' experiments we will not only be looking for clearer evidences for structure in the spectra, but will be trying to understand better the general shapes of the observed spectra, their angular distributions and their dependence on nuclear A and Z.

---

† Now at the University of Wisconsin.

* M.D. Cooper, Los Alamos Scientific Laboratory; J.F. Amann, P.D. Barnes, M. Doss, R. Eisenstein, S.A. Dytman, J. Sherman, and W. Wharton, all from Carnegie-Mellon University.

1. J.F. Amann et al., Nucl. Inst. and Meth. *126*, 193 (1975).
2. J.F. Amann et al., Phys. Rev. Lett. *35*, 426 (1975).

9.3 Ratios of ^{11}C Activations Induced by Pions on Various Targets

E.D. Arthur,† D. Chiang, and I. Halpern

As we pointed out last year, one can often measure the *ratio* of excitation functions for some particular activation, induced in different targets, with much greater precision than one can measure the individual excitation functions themselves. This comes about because one can, in a comparison measurement, eliminate some of the major systematic errors that limit the accuracy of the measurement of a single excitation function. For example, one exposes the compared targets to the beam simultaneously and one counts the activities with a single detector, switching the samples in a regular time pattern.

Last spring we were able to parasite on our total cross-section run at LAMPF (Expt #2) to obtain some results on the ratio of ^{11}C activity induced by positive pions in targets of ^{13}C and ^{12}C at a number of incident energies. These results are shown in Fig. 9.3-1. They have not been uniformly corrected for effects of the (p,pn) reaction produced by protons in the beam and should be regarded as preliminary. We believe, on the basis of these results, that we should be able to measure such ratios to about 1% accuracy with our counting system. An application for running time at LAMPF, to do a series of such comparisons, has been approved and we are now ready to do a careful measurement of the ratio studied in the parasite run (Fig. 9.3-1). If this goes well we would expect to look at other targets using the ^{11}C as well as other final activities.[1]

As we mentioned last year, an accurate curve for the ratio of excitation functions can allow us to compare shapes and positions of the (3,3) resonance for different reactions, and it can also provide evidence for any intermediate structure in this resonance.

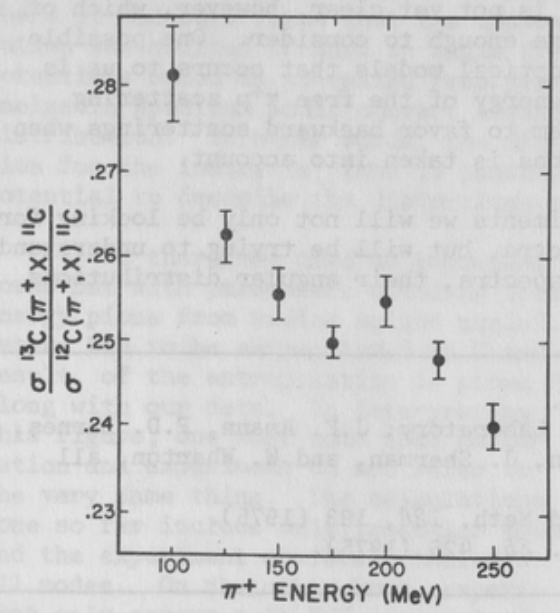

Fig. 9.3-1. Preliminary results for the ratio of the 20 min ^{11}C activity from ^{13}C and ^{12}C function of incident pion energy. The activity counter was a pair of NaI crystals observing the annihilation radiation from the stopped positrons. These results have not been fully corrected for activity induced by beam protons and secondary particles. They should be regarded as preliminary.

† Los Alamos Scientific Laboratory.

1. N.P. Jacob Jr. and S.S. Markowitz, Phys. Rev. *13C*, 754 (1976).

9.4 Relativistic Coulomb Effects in Pion Scattering

J.G. Cramer, W.J. Lynch, and J.G. Wills†

The Coulomb wave functions and Coulomb phase shifts normally employed in the analysis of the scattering of charged particles are solutions of the Coulomb Schrödinger equation. However, in the analysis of the scattering of pions a more appropriate wave equation is one such as the Klein-Gordon equation which is relativistically invariant. If we solve for the Coulomb solutions of the Klein-Gordon equation, we obtain relativistic Coulomb functions which are the same as the more familiar Coulomb functions with two exceptions: 1) the ρ and η values used must be characteristic of relativistic kinematics, and 2) the effective angular momentum value λ is no longer an integer, but is given by:

$$\lambda = [(\ell + \tfrac{1}{2})^2 - (ZZ'\alpha)^2]^{\frac{1}{2}} - \tfrac{1}{2}$$

where ℓ is the orbital angular momentum, ZZ' is the product of charges for the

projectile and target, and α is the fine structure constant or about 1/137. The origin of this modified angular momentum is in the term in the Klein-Gordon equation which is the square of the Coulomb potential, i.e., a $1/r^2$ potential. This term can be viewed as an *attractive* centrifugal potential and λ is the effective angular momentum which characterizes the net centrifugal potential. We should also note that when $ZZ'>137/2$, the $\ell=0$ value of λ becomes a complex number. This will occur for π^+ scattering from targets with $Z \gtrsim 69$, i.e., thulium or heavier.

We have investigated the numerical problems presented by these relativistic Coulomb functions, and have prepared numerical subroutines for 1) computing Coulomb phase shifts of non-integer and complex angular momentum values (see Sec. 14.6), 2) computing Coulomb wave functions of non-integer and complex angular momentum values (see Sec. 14.8), and 3) computing the Rutherford amplitude which is characteristic of the relativistic Coulomb wave equation (see Sec. 14.7). Fig. 9.4-1 shows the Rutherford scattering cross section calculated with the Schrödinger equation and the Klein-Gordon equation for 70 meV (CM) π^+ on ^{208}Pb. For the latter we have treated $\ell=0$ phase shift by analytically continuing the Coulomb phase shift to complex angular momentum but using only the real part of the phase shift in the calculation. Other procedures are possible which give somewhat different predictions.

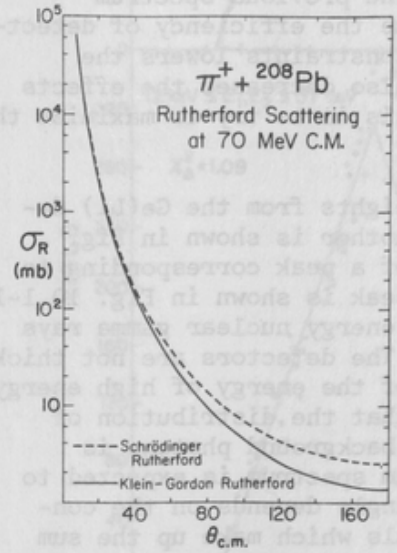

Fig. 9-4-1. Rutherford scattering comparison for 70 MeV $\pi^+ + {}^{208}$Pb.

We are presently preparing an optical model program for pion scattering employing these relativistic Coulomb functions in collaboration with G.A. Miller and M.D. Cooper. This will allow the investigation of these relativistic Coulomb effects in the presence of the nuclear force, with correct treatment of nuclear-Coulomb interference.

---

† Indiana University, Bloomington, Indiana 47401, U.S.A.

---

10. ATOMIC PHYSICS

10.1 Branching Ratio for the Two Photon Decay of the Atomic ^{208}Pb K-shell Vacancy

D. Burch and J. Bussoletti

The data from previous measurements[1] have been completely reanalyzed in an effort to determine the best upper limit on the branching ratio for two photon decay of the $(1S)^{-1}$ state of the ^{208}Pb atom. The measurements were performed with two planar Ge(Li) detectors separated by a lead shield in a 90° geometry. The K-vacancies were produced by a ^{207}Bi radioactive source. Coincident pulses from the Ge(Li) detectors were event-recorded along with a signal indicating the relative time difference between the pulses from each detector. The reanalysis consists of imposing a series of constraints on the event-recorded data which should be satisfied only by two-photon decay signals. The reanalysis is necessary because a large background is present in the previous spectrum generated by the choice of constraints which maximize the efficiency of detecting the two-photon signals. A different choice of constraints lowers the efficiency of detecting the two-photon signals but also decreases the effects of the background. The intent of the further analysis is to try to maximize the two photon signal to background ratio.

A spectrum consisting of the sum of pulse heights from the Ge(Li) detectors which were in prompt coincidence with one another is shown in Fig. 10.1-1. The arrow indicates the expected position of a peak corresponding to two-photon events. The expected line shape of the peak is shown in Fig. 10.1-1. The background is due to Compton scattering of high energy nuclear gamma rays which are in prompt coincidence with one another. (The detectors are not thick enough to collect with significant probability all of the energy of high energy photons, i.e., $E \gtrsim 200$ keV.) Under the assumption that the distribution of pulse heights from the Ge(Li) crystals due to these background photons is rectangular, (i.e., random), the background in the sum spectrum is expected to be triangular. The location of the peak of the triangle depends on the constraints which have been imposed on the energy signals which make up the sum spectrum. For example, if events E_1 and E_2 are random variables on an interval (0,1) then the event $E_0 = E_1 + E_2$ such that $E_{low} \leq E_1, E_2 \leq E_{high}$ will be distributed with a triangular distribution whose peak will occur at $E_{low} + E_{high}$ and whose base will extend from $2 \times E_{low}$ to $2 \times E_{high}$.

A triangle centered at the expected location is fit to each sum spectrum which is generated by a particular choice of constraints on the energy signals. Channels in the region of the expected two-photon peak are excluded from the fit. The chi-square for each fit is given in Fig. 10.1-1. The expected location of the two-photon peak is indicated by an arrow in the same figure.

A line shape for 75 keV photons was extracted from a spectrum of singles data which was collected simultaneously with the event-recorded coincidence data.[2] This line shape was broadened by $\sqrt{2}$ to account for the effects of adding two events from distributions of finite but equal widths. The resultant peak shape was normalized to unit area. This line shape defines the expected peak shape for the two-photon signals.

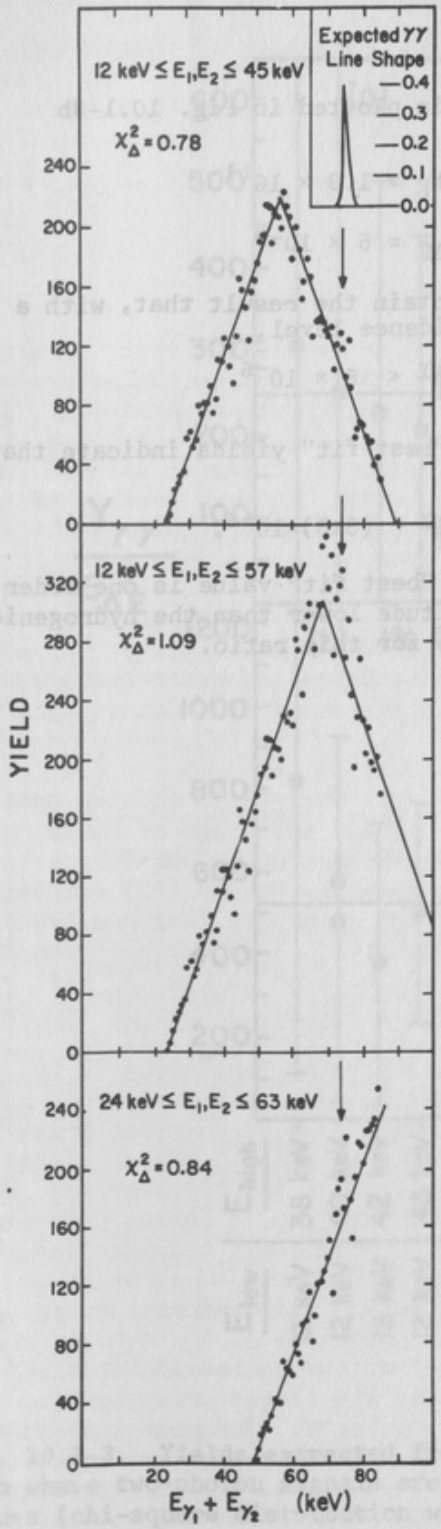

Fig. 10.1-1. Sum spectra of two Ge(Li) detectors. The arrow indicated the expected position of the two-photon peak. The chi-square shown is for a fit of a triangle to the back-ground in the spectrum.

The spectrum resulting from the subtraction of the best fit triangular background from the sum spectrum is illustrated in Fig. 10.1-2. The peak shape for two-photon events was fit to this residuals spectrum. Both a "best-fit" and a one per cent confidence level fit were extracted from these spectra. Fig. 10.1-3a shows the extracted "best-fit" yields divided by the calculated detection efficiency for a variety of choices of constraints. Fig. 10.1-3b illustrates the corresponding one per cent confidence limit yields. The errors in the plotted points include the statistical error in the original measurements, the effects of subtraction of a random background from the coincident energy signals and the effects of the subtraction of the triangular background.

The results from each choice of constraint have been averaged together to obtain the best estimate for the two-photon yield. As most "best-fit" yields are consistent with zero, we interpret our results to provide an upper limit for the two photon branching ratio at a one per cent confidence level. The two-photon branching ratio is given by:

$$\frac{\Gamma_{\gamma\gamma}}{\Gamma} = \frac{1}{N_K} \frac{1}{\varepsilon_{\Delta\Omega}} \frac{Y_{\gamma\gamma}}{\varepsilon_{\Delta E}}$$

where

N_K is the number of K vacancies created,

$\varepsilon_{\Delta\Omega}$ is the solid angle efficiency,

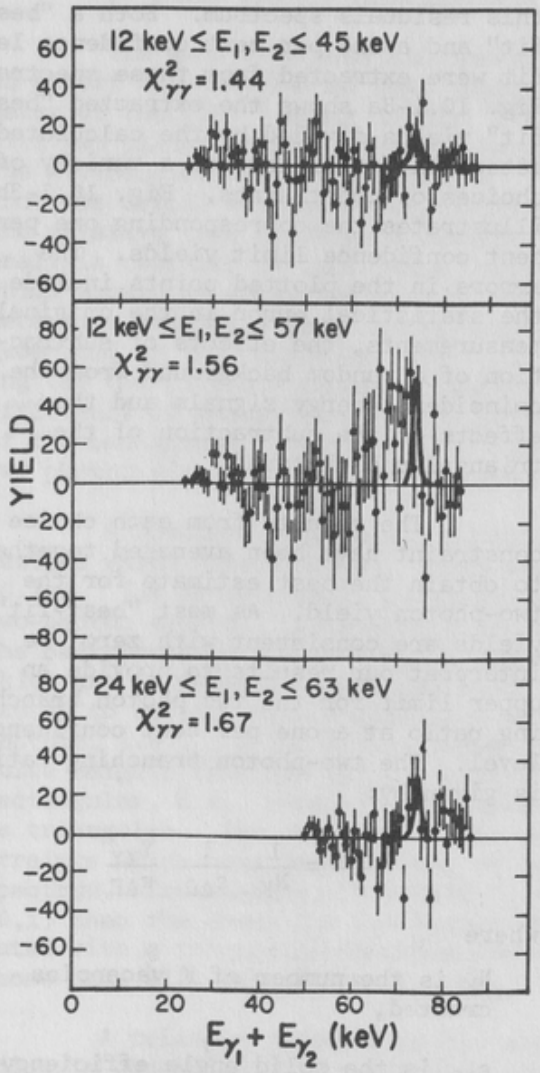

Fig. 10.1-2. Spectra of residuals after subtracting triangular background from the sum spectra. The curve is the "best-fit" yield for a peak of the expected line-shape in the region where the two-photon peak is expected. The chi square is the "best-fit" value for a peak of the expected line-shape in the expected location of two photon decays.

and

$\frac{Y_{\gamma\gamma}}{\varepsilon_{\Delta E}}$ is plotted in Fig. 10.1-3b

$$N_K = 1.8 \times 10^{11}$$

$$\varepsilon_{\Delta\Omega} = 6 \times 10^{-4}$$

We obtain the result that, with a 1% confidence level,

$$\frac{\Gamma_{\gamma\gamma}}{\Gamma} < 6 \times 10^{-6}.$$

The "best-fit" yields indicate that

$$\frac{\Gamma_{\gamma\gamma}}{\Gamma} = (3\pm3)\times10^{-6}.$$

This "best fit" value is one order of magnitude lower than the hydrogenic value for this ratio.[1]

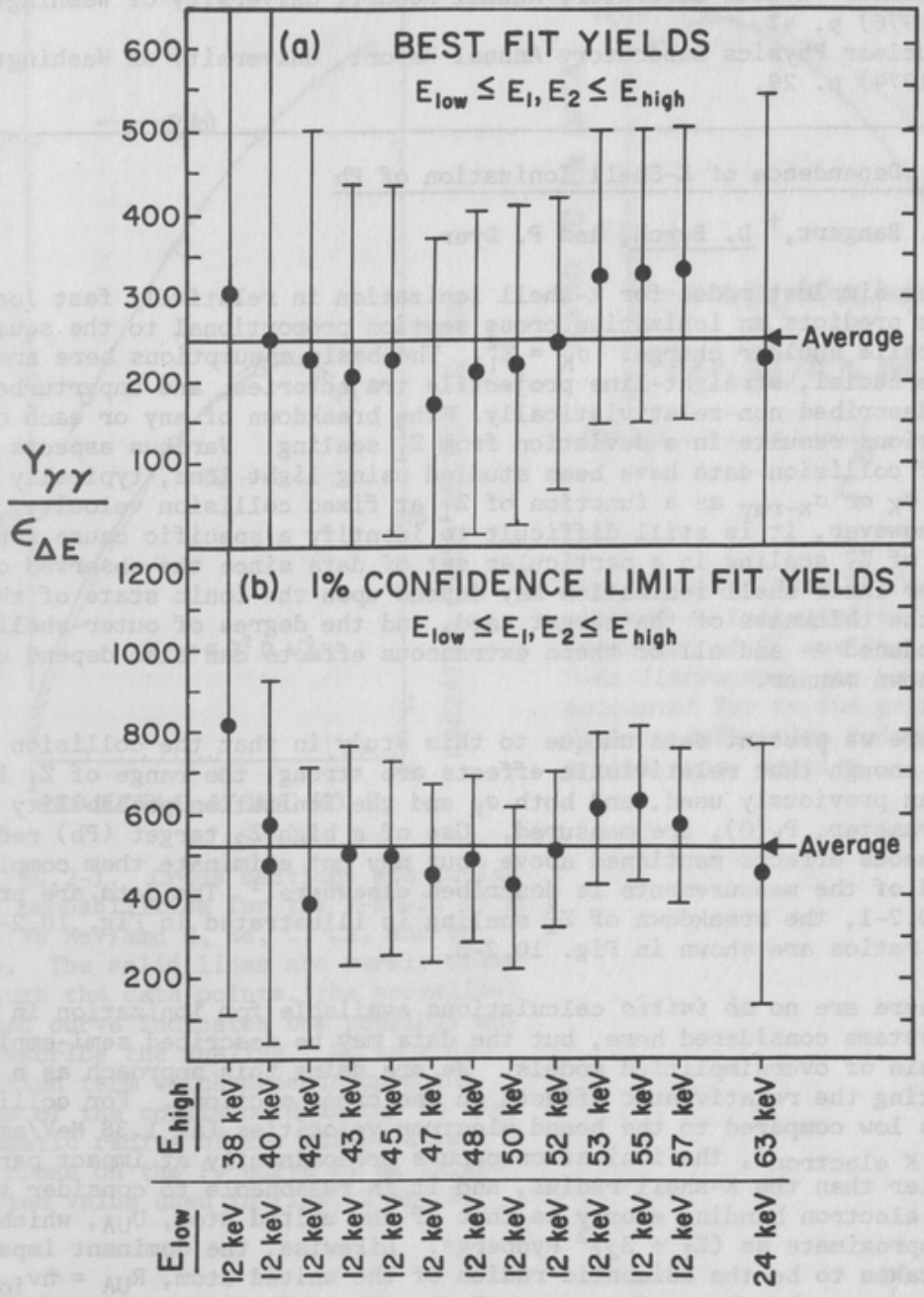

Fig. 10.1-3. Yields extracted from a) "best-fit" values for a peak in the location where two-photon signals are expected and b) one per cent confidence limit values (chi-square distribution with six degrees of freedom) for a similarly placed peak.

1. Nuclear Physics Laboratory Annual Report, University of Washington (1976) p. 47.
2. Nuclear Physics Laboratory Annual Report, University of Washington (1974) p. 29.

10.2 Z_1 Dependence of K-Shell Ionization of Pb

R. Bangert,† D. Burch, and P. Dyer

The simplest model for K-shell ionization in relatively fast ion-atom collisions predicts an ionization cross section proportional to the square of the projectile nuclear charge: $\sigma_K \propto Z_1^2$. The basic assumptions here are: bare projectile nuclei, straight-line projectile trajectories, and unperturbed atomic orbitals described non-relativistically. The breakdown of any or each of these approximations results in a deviation from Z_1^2 scaling. Various aspects of this feature of collision data have been studied using light ions, typically by measuring σ_K or $\sigma_{x\text{-ray}}$ as a function of Z_1 at fixed collision velocity. In general, however, it is still difficult to identify a specific cause for the breakdown of Z_1^2 scaling in a particular set of data since the observed cross section for inner-shell ionization may depend upon the ionic state of the projectile, the thickness of the target used, and the degree of outer-shell excitation produced -- and all of these extraneous effects can also depend upon Z_1 in an unknown manner.

Here we present data unique to this study in that the collision systems are heavy enough that relativistic effects are strong, the range of Z_1 is much larger than previously used, and both σ_K and the ionization probability at zero impact parameter, $P_K(0)$, are measured. Use of a high-Z_2 target (Pb) reduces the extraneous effects mentioned above but may not eliminate them completely. The method of the measurements is described elsewhere.[1] The data are presented in Fig. 10.2-1, the breakdown of Z_1^2 scaling is illustrated in Fig. 10.2-2, and the σ_K/P_K ratios are shown in Fig. 10.2-3.

There are no *ab initio* calculations available for ionization in the complex systems considered here, but the data may be described semi-empirically[2] on the basis of oversimplified models. We are using this approach as a means of estimating the relativistic effects on the cross sections. For collision velocities low compared to the bound electron velocities (at 1.38 MeV/amu, $v_{ion} \sim 0.1\, v_{Pb\ K\ electron}$), the ionization occurs predominantly at impact parameters much smaller than the K-shell radius, and it is reasonable to consider the effective electron binding energy as that of the united atom, U_{UA}, which we crudely approximate as $(Z_1 + Z_2)^2$ Rydbergs. Likewise, the dominant impact parameter is taken to be the adiabatic radius of the united atom, $R_{UA} = \hbar v_{ion}/U_{UA}$. These values can then be used to re-evaluate the various correction factors[1,2] (effectively all maximized by this assumption) and the excess cross section attributed, as a first estimate, to relativistic effects. The main analytical point we will wish to emphasize with this data is that to the extent the presence of Z_1 increases the binding energy (which reduces σ), the relativistic effects (which increase σ) must also be increased. This point may account for the large overestimate of the "binding correction"[1,2] when applied to heavy collision systems.

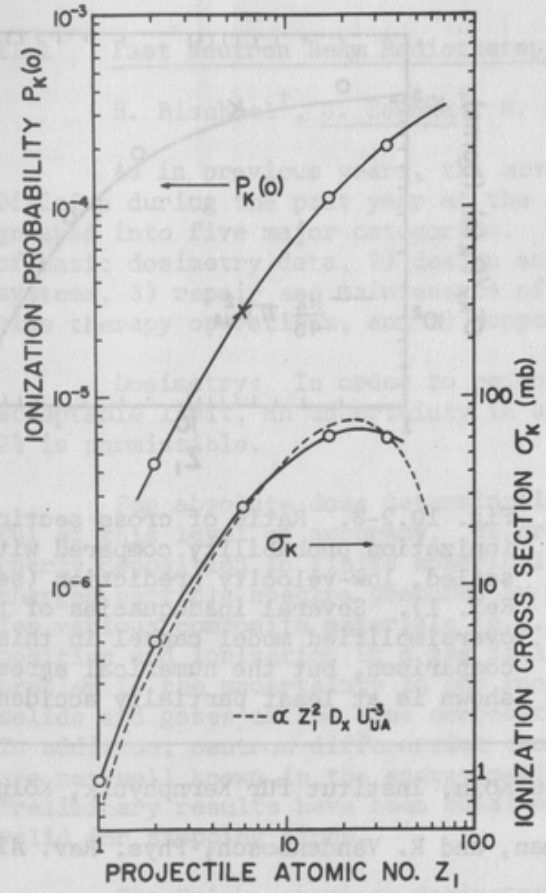

Fig. 10.2-1. Cross sections and ionization probabilities for the K-shell of Pb by 1.38 MeV/amu H, He, C, Cl, and Br ions. The solid lines are merely drawn through the data points, the normalized dashed curve indicates one possible way to describe the scaling. D_x is a deflection term which depends upon the ratio of the collision diameter to the adiabatic radius of the united atom. The cross on the P_K curve is an interpolated value used in Figs. 2 and 3.

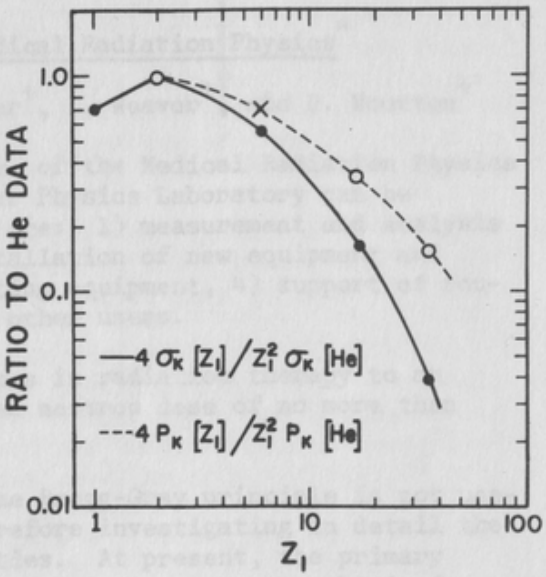

Fig. 10.2-2. Data of Fig. 10.3-1 plotted as indicated to illustrate the breakdown of Z_1^2 scaling. The apparent H-He discrepancy can be quantitatively accounted for as due primarily to a Coulomb deflection reduction of the proton cross section.

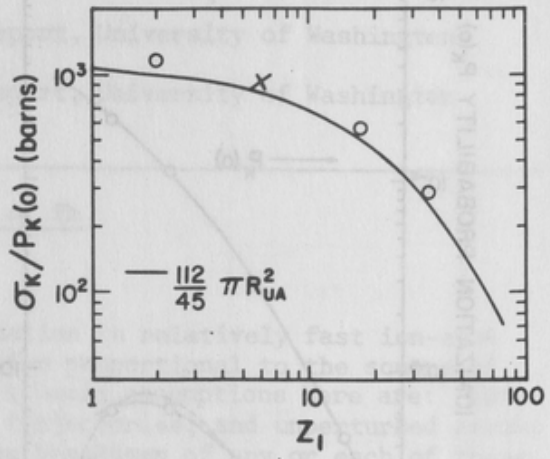

Fig. 10.2-3. Ratio of cross section to ionization probability compared with a scaled, low-velocity prediction (see Ref. 1). Several inadequacies of the oversimplified model cancel in this comparison, but the numerical agreement shown is at least partially accidental.

---

† Present address: Universität zu Köln, Institut für Kernphysik, Köln, Germany.

1. D. Burch, W.B. Ingalls, H. Wieman, and R. Vandenbosch, Phys. Rev. *A10*, 1254 (1974).

2. R. Anholt and W.E. Meyerhof, Phys. Rev. A, to be published (paper III of a IV part series).

---

11. RESEARCH - USERS AND VISITORS

11.1 Fast Neutron Beam Radiotherapy- Medical Radiation Physics*

H. Bischsel+, J. Eenmaa+, R. Seymour+, K. Weaver+, and P. Wootton+

As in previous years, the activities of the Medical Radiation Physics Division during the past year at the Nuclear Physics Laboratory can be grouped into five major categories. These are: 1) measurement and analysis of basic dosimetry data, 2) design and installation of new equipment and systems, 3) repair and maintenance of existing equipment, 4) support of routine therapy operations, and 5) support of other users.

Dosimetry: In order to reduce errors in radiation therapy to an acceptable limit, an uncertainty in absorbed neutron dose of no more than 2% is permissible.

For absolute dose determination, the Bragg-Gray principle is not useful at this level of accuracy. We are therefore investigating in detail the energy deposition in finite spherical cavities. At present, the primary charged particle spectra produced by monoenergetic neutrons are obtained for various composite materials (e.g., Shonka plastic), then energy deposition and ionization in a gas filling the cavity are calculated. A major problem is the uncertainty in our knowledge of stopping power. In particular, solids and gases of the same composition do not have the same stopping powers. In addition, neutron differential cross sections for charged particle production are not well known in the energy region above 8 MeV (except for 14 MeV). Preliminary results have been obtained. The dose calculation code is also valid for stopping pions.

The Fricke chemical dosimeter has been compared to standard ionization chamber methods for absolute dose determination for neutron beams and good correspondence has been obtained between the two techniques. Agreement to better than 2% has been obtained between predicted and measured G-values for the cyclotron neutron beam. This agreement could possibly be improved even more with more accurate determinations of the neutron spectrum.

Specification of tumor dose for neutron radiotherapy is complicated by oblique beam incidence, details of patient contour, tissue inhomageneities in the beam, and the presence of external field-shaping devices. An adequate accounting of these dose-modifying effects must be included in treatment planning. To this end, measurements have been made of effects of tissue inhomogeneities (bone, lung, fat), and phantom geometry and density on neutron dose. Methods of correcting for these effects in treatment planning programs have been investigated. Since neutron beams have a large component of scattered radiation an approximation technique for calculating dose changes due to off-axis scattering has been developed.

Preliminary dosimetric measurements with a high-pressure (33 atm.) D_2 gas target on the Van de Graff accelerator have been completed. The measured dose rate for a 10 x 10 cm field in air at 125 cm SSD was 1.44 ± 0.01 rads/min/μa. Dose buildup measurements indicate a maximum dose at 3.5 mm depth.

Depth-dose measurements for a 10 x 10 cm field in the standard 30-cm tissue-equivalent phantom indicate that the 50% dose occurs at 10.5 cm. The D_2 gas target neutron beam thus exhibits superior dosimetric properties when compared to the beam from the therapy beryllium target, for which the 50% dose occurs at about 9.5 cm. Measurements of beam flatness, photon dose fraction, and biological effectiveness are planned.

New equipment and systems: An automated dosimetry scanning system has been purchased and will be installed for rapid accumulation of dosimetry data for clinical applications.

The Raytheon 704 computer system has been expanded. A multi-featured disc-based file management and text editing system has been installed. Automated setting of patient treatment parameters has been implemented. A Versatec Printer-Plotter and Graf-Pen digitizer have been installed. Patient data storage has been expanded with the implementation of a second disc storage capability. A simple data base management system for random access and processing of patient data has been installed.

For neutron treatment simulation with x-rays, a chair capable of simulating the motions of the therapy chair has been constructed and installed at the University Hospital.

Therapy: Support of therapy operations on a four days per week schedule has continued without interruption during the past year. During alternate weeks the cyclotron is shared with the Division of Nuclear Medicine and the changeover to cancer therapy operations has functioned smoothly.

Intercomparisons: Dosimetry intercomparisons have been conducted with visiting scientists from the National Institute of Radiological Sciences (N.I.R.S.) and from the University of Tokyo, Japan. Also, one of us (H.B.) has visited these institutions in Japan. Measurements conducted on the ^{60}Co beam and on the different neutron beams indicate that the agreement in specification of absolute physical dose is at the 1-2% level. Some discrepancies remain to be resolved in depth-dose determinations.

---

* Supported by NCI Grant No. PO1-CA-12441.

+ Division of Medical Radiation Physics, Department of Radiology, University of Washington

---

11.2 Fast Neutron Beam Radiotherapy - Radiation Biology*

J. P. Geraci[+], K. L. Jackson[+], G. M. Christensen[+], P. D. Thrower[+], and Marinela Mariano[+]

The biology portion of the neutron beam-therapy project has involved determination of the neutron RBE for normal tissue damage in mice. A major emphasis of these studies has been on late radiation effects rather than acute effects since late normal tissue injury rather than acute injury is usually the dose limiting factor in cancer radiotherapy. Furthermore, late effects are the least understood, and have been a problem of neutron radiotherapy in the past.

During the past year we have extended our late spinal cord injury studies by employing 10 fractions of x-rays or neutrons. The biology endpoint used in these studies was the length of the latency period (the time interval between irradiation and paralysis). The results are presented in Fig. 11.2-1. The neutron portion of the curve is complete. However, the animals exposed to x-rays at lower doses than shown in Fig. 11.2-1 are still being followed. Therefore, the uncertainty in the exact position of the x-ray curve is indicated by a dotted line. The numbers in parentheses indicate the number of animals which developed paralysis. The results indicate that the neutron RBE for spinal cord injury may be as high as 4.0 in the range of doses per fraction (100-200 rad) used in neutron therapy.

Another normal tissue that is of concern to the radiotherapist is the kidney. There exists no information on the neutron RBE for late kidney damage to guide the therapist in the treatment of cancers where the kidney is the normal tissue at risk. As a result, during the past year we initiated studies to measure late kidney damage using kidney atrophy, as measured by decrease in kidney weight six months after irradiation as the biological endpoint. The dose response curves for this endpoint following single dose of x-rays or neutrons are shown in Fig. 11.2-2. The numbers in parentheses are the number of animals used for each point. The results show a shoulder on the neutron and x-ray dose response curves. However the neutron curve has a smaller shoulder and a steeper decline in weight than the corresponding x-ray curve,

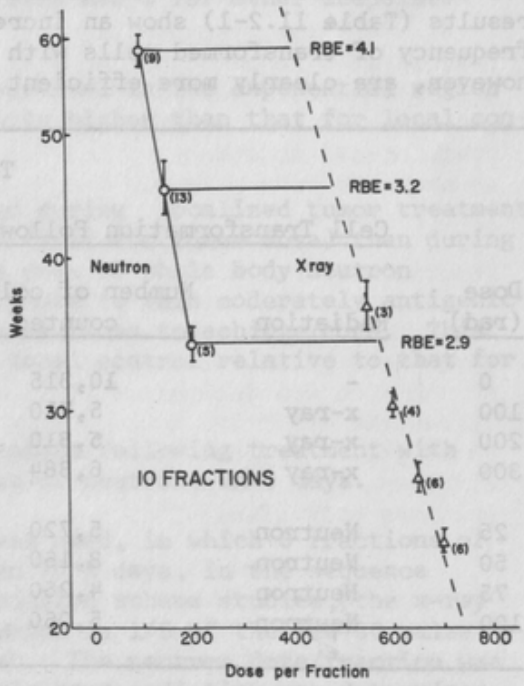

Fig. 11.2-1. Latency period following 10 fractions of x-ray or neutron.

resulting in a neutron RBE of 1.7 at a neutron dose of 1000 rad. Further work is needed at lower doses per fraction to get a clinically relevant RBE for late kidney damage.

A conspicuous late effect of systemic radiation in man and animals is carcinogenesis. Attempts to quantitate the relative carcinogenic risk from the low doses of radiation delivered in the shielded area of a neutron and ^{60}Co facility would require a large number of animals and considerable cost and time. One way to circumvent this problem is to study radiation-induced transformation of normal cells to cancer cells in vitro. During the past year pilot experiments have been carried out using the C3H 10T 1/2 CL8 cell line to determine the RBE of the primary neutron beam for cell transformation. Preliminary results (Table 11.2-1) show an increased frequency of transformed cells with increased neutron and x-ray doses. Neutrons, however, are clearly more efficient per rad than x-rays for cell transformation.

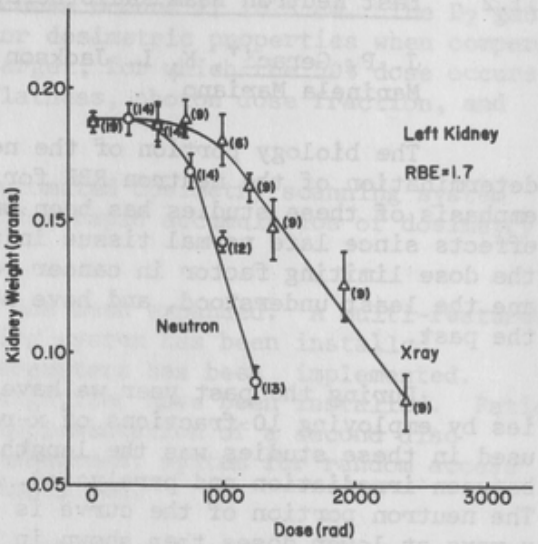

Figure 11.2-2. Dose-response curve for kidney weight loss.

Table 11.2-1

Cell Transformation Following Neutron or X-irradiation in Vitro

Dose (rad)	Radiation	Number of colonies counted	Transformed colonies	Transformation (percent)
0	-	10,315	0	0.00
100	x-ray	5,710	7	0.12
200	x-ray	5,810	16	0.28
300	x-ray	6,384	20	0.31
25	Neutron	5,720	3	0.05
50	Neutron	8,160	9	0.11
75	Neutron	4,260	12	0.28
100	Neutron	5,060	18	0.36

1. R. S. Stone, Neutron Therapy and Specific Ionization. Amer. J. Roentgenol. *59*, 771 (1948).

2. D. H. Hussey, G. H. Fletcher, and J. B. Cordurea, Experience with Fast Neutron Therapy using the Texas A & M Variable Energy Cyclotron. Cancer *34*, 65 (1974).

11.3 Fast Neutron Beam Radiotherapy -- Experimental Oncology*

J. S. Rasey+

The research program in experimental oncology is supportive of the neutron beam therapy project which is currently treating cancer patients with the neutron beam from the University of Washington cyclotron. Our program attempts to answer clinically relevant questions in the neutron radiobiology of tumors and selected normal tissues.

Projects completed, continued, or initiated in the past year include the following:

A. The response of the EMT-6 solid tumor growing in the BALB/c mouse to x-rays or neutrons has been examined using several endpoints as well as variety of fractionation schemes.

Tumors have been treated with single doses of x-rays or neutrons and RBE's** determined for 3 different endpoints: a) local tumor control at 120 days; b) growth delay, and c) clonogenic cell survival, using an *in vitro* colony-forming assay.

An RBE of 2.3 to 2.4 was observed for the growth delay endpoint; this is not statistically significantly different from RBE's for other endpoints of response.

The neutron RBE for clonogenic cell survival in the exponential region of the survival curve -- 3.0 -- is signifivantly higher than that for local control -- 1.7.

The whole body radiation dose received during localized tumor treatment is greater during neutron irradiation (3.5 to 7% of the tumor dose) than during x-ray therapy (0.2% of the tumor dose). This dose of whole body neutron radiation appears to suppress host immune response to this moderately antigenic tumor, requiring a greater tumor cell kill by neutrons to achieve cure. This is consistent with the lower neutron RBE for local control relative to that for clonogenic cell survival.

Local control of EMT-6 tumors was assessed following treatment with 5 fractions of x-rays in 5 days or 5 fractions of neutrons in 5 days.

Mixed neutron-photon radiation also was used, in which 3 fractions of x-rays plus 2 fractions of neutrons were given in 5 days, in the sequence n-n-x-x-x or n-x-x-x-n. In the mixed fractionation scheme studies, the x-ray dose/fraction was held constant at 690 rad, which is 1/5 of the TCD-50 value determined in the 5 fractions x-ray experiment. The neutron dose/fraction was varied over a wide range, and a TCD-50 for this test radiation was determined.

** RBE = relative biological effectiveness = dose of x-rays to produce a given level of damage/dose of neutrons to produce the same damage.

RBE's for neutrons or combined neutron and photon radiation were determined from TCD-50 ratios. The results are summarized in Table 1.

B. Sublethal and potentially lethal damage repair following x- or neutron irradiation was studied using EMT-6 cells growing in vitro. Sublethal damage repair was defined as the re-appearance of a full shoulder on the cell survival curve 6 hours after a priming dose which reduced cell survival to ≈ 0.1.

Sublethal damage repair was examined with all permutations of x- and neutron irradiation, i.e. x-x, n-n, x-n and n-x.

There was partial or complete recovery from sublethal damage with all the above permutations of x- and neutron radiation.

Potentially lethal damage (PLD) repair is seen after both x-rays and neutrons. In cultures plated after the 6-hour delay, there is a substantial increase in absolute survival level at a given dose relative to what occurs with immediate subculture.

In one day old exponentially growing cultures of EMT-6 cells, there is little or no capacity for PLD repair after either x-rays or neutrons.

C. The response of mouse intestinal epithelium to mixed neutron-photon fractionated irradiation, as well as fractionated x-rays only and neutrons only was examined. $LD_{50/4}$†† days was used as the endpoint of response following whole body irradiation. Deaths were tallied 4 days from the midpoint of the 5-day fractionated treatment. The LD_{50} for 5 fractions of x-rays only or 5 fractions or neutrons only given in 5 days was determined first (Table 2).

In a second experiment, mice were irradiated with mixed neutron-photon fractionated radiation, in the sequence n-n-x-x-x or n-x-x-x-n. The x-ray dose/fraction was held constant 427 rad, 1/5 of the $LD_{50/4}$ day determined in the 5 fraction x-ray experiment. The neutron dose/fraction, on those days when neutrons were given, was varied. The total mixed beam dose required to kill 50% of the mice was determined for both mixed fractionation schemes. From these values the effective neutron dose per fraction at the 50% survival level was extracted. For both mixed schemes the dose per fraction is not significantly different from the neutron dose/fraction in the experiment using 5 fractions of neutrons only (Table 2).

D. As part of the U.S.-Japan Cooperative Cancer Research program, studies were begun in the past year to biologically characterize several neutron beams at cancer treatment facilities in both countries. The response of mouse foot skin to irradiation was the test system used. The University of Washington Neutron beam was compared to three different energy beams at the Texas A&M University variable energy cyclotron (TAMVEC), and to neutron beams at the National Institute of Radiological Sciences in Chiba-shi, Japan, and at the

---

††$LD_{50/4}$ day is the dose of whole body radiation lethal to 50% of the mice four days after the midpoint of the fractionated treatment.

Institute of Medical Sciences of Tokyo University, Japan. All neutron beams tested are produced by a $d^{+} \rightarrow Be$ reaction.

The preliminary results are given in Table 3 and are expressed as a relative beam potency, with the University of Washington neutron beam designated as potency = 1.0. The radiation doses required to produce an average skin response has, as a maximum reaction, breakdown and moist desquamation of 1/4 to 1/2 of the skin of the irradiated foot by days 17 to 21 post-treatment This is followed by complete or virtually complete healing by day 35 post-irradiation.

---

* Supported by the National Cancer Institute, Grant No. CA-12441

+ Division of Radiation Oncology, Department of Radiology, University of Washington

---

Table 11.3-1
TCD-50 Values for EMT-6 Tumors

Fractionation Scheme Type of Radiation (# mice in experiment)	TCD-50 (95% confidence limits)	Neutron or Test Radiation RBE* (95% confidence limits)
1 fx X-rays (85)	2360 rads (1710, 3100)	
5 fx X-rays	5 x 690 = 3450 rads (2700, 4409)	
1 fx neutrons (47)	1350 rads (1236, 1474)	1.7 (1.2, 2.3)
5 fx neutrons (56)	5 x 270 = 1350 rads (1080, 1688)	2.6 (1.7, 3.4)
n-n-x-x-x	125n-125n-690x-690x-690x = 2320 rads (2125, 2599)	1.5 (1.1, 1.9)
n-x-x-x-n	170n-690x-690x-690x-170n = 2410 rads (2259, 2571)	1.4 (1.1, 1.8)

* Test radiation is total dose of neutrons + x-rays = TCD_{50} in the mixed fractionation schemes. This was divided into TCD-50 (5 fx x-rays) to determine an RBE for this treatment regimen.

** TGF = $\frac{\text{neutron (or test radiation)RBE - tumor}}{\text{neutron (or test radiation)RBE- skin}}$ for a given fractionation scheme.

TABLE 11.3-2

Fractionation Scheme (# of mice)	LD_{50}/5 day (95% confidence limits) Total dose, rad	Dose/fraction rad [a]	Neutron (or test radiation) RBE [b] (95% confidence limits)
5 fractions x-rays (49)	2,135 (1710, 2700)	427 (342, 540)	
5 fractions neutrons (48)	890 (740,1080)	178 (148, 216)	2.4 (1.7, 3.1)
n-x-x-x-n (48)	190n-427x-427x-427x-190n=1660 (1460, 1940)	190	1.3 (0.9, 1.6)
n-n-x-x-x (48)	154n-154n-427x-427x-427x=1590 (1385, 1820)	154	1.3 (0.9, 1.7)

a. In the mixed schemes, dose/fraction refers to the neutron dose fraction at the 50% survival level, as the x-ray dose/fraction was held constant at 427 rad for all treatment groups.

b. Test radiation RBE = LD_{50} (x-rays and neutrons in mixed scheme)/LD_{50} (x-rays, 5fx).
Neutron RBE = LD_{50} (neutron)/D_{50} (x-rays).

Table 11.3-3

Relative potencies of neutron beams at cancer treatment facilities [a] determined using mouse skin as a biological dosimeter:

TAMVEC 50 MeV[b]	TAMVEC 35 MeV	NIRS 30 MeV	UW 22 MeV	TAMVEC 16 MeV	IMS 16 MeV
0.90	0.99		1.0	1.20[c]	
		0.97	1.0		1.18

a. Abbreviations used are:

TAMVEC - Texas A&M University Variable Energy Cyclotron
NIRS - National Institute of Radiological Sciences, Chiba-shi, Japan
IMS - Institute of Medical Sciences, Tokyo

b. The energies of the deutreron beams are given below the name of each facility. Neutrons were in all cases produced by a $d^+ \rightarrow Be$ reaction.

c. Each line in the table is a separate experiment.

11.4 Total Body Calcium by Neutron Activation

C. H. Chesnut, G. M. Hinn, T. K. Lewellen, R. Murano, W. B. Nelp

The Division of Nuclear Medicine is continuing its measurements of total body calcium by means of whole-body neutron activation and whole-body counting. The cyclotron is used as the neutron source, and the 3.1 MeV gamma ray of 8.7 minute ^{49}Ca is counted.[1]

Two therapy regimes are being tested for the control of post menopausal osteoporosis. 25 patients are being treated with Calcitonin, while 25 more are used as controls. Both treated and control groups are women over 50 years who show several signs of osteoporosis, including a history of fractures. Treatment is continued for a two year period, with 5 neutron activation measurements. A number of other tests are made on these patients, including blood and urine chemistries, photon transmission densitometry of the arm bones, and bone biopsies with tetracycline labeling to measure new bone growth on the microscopic level. A similar group of patients and controls is being studied for the effects of the drug Winstral (Winthrop Laboratories).

More normal subjects were measured. Our normal series now includes 5 males and 5 females in each decade of age from 20 to 80, and a few over 80.

A second system of neutron activation for total body calcium measurement is being developed using the reaction $^{40}Ca(n,\alpha)^{37}Ar$.[2] This new system is being calibrated by comparision to the the ^{49}Ca system. 10 normal and 3 osteoporotic subjects were measured by both systems. The yield of ^{37}Ar divided by the yield of ^{49}Ca is approximately constant, with a standard diviation of 5%(3).

---

1. Nuclear Physics Laboratory Annual Reports, University of Washington, 1968-1976.

2. H.E. Palmer, Journal of Nuclear Medicine *14*, 522 (1973); T. K. Lewellen, C. H. Chesnut, W. B. Nelp, H. E. Palmer, R. Murano, G. M. Hinn, Journal of Nuclear Medicine *16*, 672 (1975).

3. T. K. Lewellen, W. B. Nelp, R. Murano, G. M. Hinn, C. H. Chesnut, Journal of Nuclear Medicine, *in press*.

11.5 Equilibrium Delayed Neutron Spectra

G. W. Eccleston* and G. L. Woodruff+

Directly measured near-equilibrium delayed neutron energy spectra associated with fast-neutron-induced fissions of ^{232}Th, ^{233}U, ^{235}U, ^{238}U and ^{239}Pu have recently been completed.[1] These data were obtained using a cyclical sequence consisting of a 1.0-sec irradiation, 0.08-sec delay, 1.0-sec count and a wait of 0.02-sec. This cycle prevented a significant fraction of the shorter half-life delayed neutron precursors from being measured.[2]

Comparison of these data with spectra measured by others show general agreement at energies in excess of about 250 keV. However, significant differences below this energy exist with our data showing a large fraction of delayed neutrons to exist at the low energies. Measurements of essentially true equilibrium delayed neutron spectra were recently reported by Evans and Krick.[3] Their spectra are also harder than our measured near-equilibrium spectra and it has been suggested that the inclusion in their measurements of more of the shorter half-life precursors, which may have higher mean energies, may partially explain the softer shape of our data.

Modifications to our experimental system have been completed to enable a shorter cycle time to be used to provide equilibrium data.[4] The new cycle consists of 0.1-sec irradiation, 0.02-sec delay, 0.1-sec count and a 0.02-sec wait. A comparison of the delayed neutron group yields between the two second cycle, this new short cycle and the one used by Evans is listed in Table 11.5-1.

Table 11.5-1. Comparison Between Delayed Neutron Yields for an Equilibrium Cycle and the Cycles Used in Measurements

Group	Equilibrium Yields[a]	Evans Cycle (Ref 3)	Two Sec Cycle (Ref 1)	New Short Cycle
1	0.038	0.038	0.004	0.038
2	0.213	0.213	0.224	0.213
3	0.188	0.188	0.197	0.188
4	0.407	0.407	0.421	0.407
5	0.128	0.126	0.108	0.128
6	0.026	0.025	0.010	0.025

[a] Equilibrium yield values from Keepin fast fission data, Reference 5, page 86.

Delayed neutron spectral data produced from cyclical irradiation of the ^{235}U sample using the new short cycle have been collected. This spectrum, shown in Fig. 11.5-1, has a significant fraction of delayed neutrons below 100 keV and is similar in overall shape to the near-equilibrium data collected with the two-second cycle.

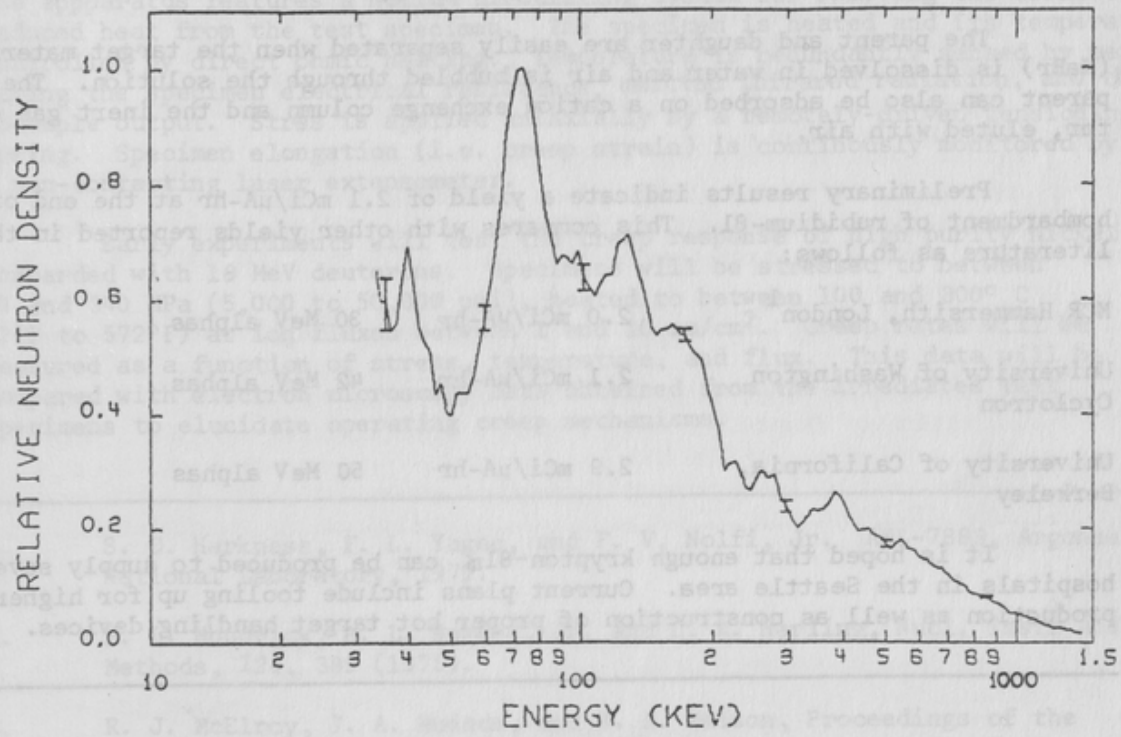

Fig. 11.5-1. Equilibrium ^{235}U Delayed Neutron Spectrum.

* Work supported by AEC Contract AT(45-1)-2225

\+ Department of Nuclear Engineering, University of Washington

1. G. W. Eccleston and G. L. Woodruff, Nucl. Sci. Eng. *62*, 636 (1977).
2. Nuclear Physics Laboratory Annual Report, University of Washington, p. 171 (1976).
3. A. E. Evans and M. S. Krick, Nucl. Sci. Eng., *62*, 652 (1977).
4. G. W. Eccleston and G. L. Woodruff, Progress Report submitted to the Division of Physical Research, ERDA, August (1976).
5. G. R. Keepin, Physics of Nuclear Kinetics, Addison-Wesley, Reading, Mass. (1965).

11.6 Radioisotope Production for Lung Imaging in Nuclear Medicine

G. M. Hinn, W. B. Nelp, W. G. Weitkamp, T. L. Lewellen and R. Murano

The production of ^{81m}Kr ($t_{1/2}$ = 13 sec) for lung imaging in Nuclear Medicine is currently being investigated. Krypton-81m has been produced on the cyclotron using the reaction $^{79}Br(a,2n)\ ^{81}Rb$ to produce the parent rubidium-81 ($t_{1/2}$ = 4.7 hr) which decays to its daughter krypton-81m.

The parent and daughter are easily separated when the target material (NaBr) is dissolved in water and air is bubbled through the solution. The parent can also be adsorbed on a cation exchange column and the inert gas daughter, eluted with air.

Preliminary results indicate a yield of 2.1 mCi/μA-hr at the end of bombardment of rubidium-81. This compares with other yields reported in the literature as follows:

MCR Hammersith, London[1]	2.0 mCi/μA-hr	30 MeV alphas
University of Washington Cyclotron	2.1 mCi/μA-hr	42 MeV alphas
University of California, Berkeley	2.9 mCi/μA-hr	50 MeV alphas

It is hoped that enough krypton-81m can be produced to supply several hospitals in the Seattle area. Current plans include tooling up for higher production as well as construction of proper hot target handling devices.

---

1. T. Jones, J. C. Clark, J. M. Hughes, and D. Y. Rosenzweg, J. Nucl. Med. *11*, 118 (1970).

2. Y. Yano, J. McRae, H. O. Anger, J. Nucl. Med. *11*, 674 (1970).

11.7 Simulation of In-Reactor Creep

P. L. Hendrick[+]

Materials placed under stress and subjected to the elevated neutron fluxes of both breeder and fusion reactors will exhibit a form of accelerated deformation termed irradiation-induced creep. Due to the difficulty, cost, and time required in making precise in-reactor creep measurements, there is world-wide interest in simulating in-reactor creep by bombarding materials of interest with energetic light ions under well-controlled conditions. Such experiments could enhance our understanding of the operating creep mechanisms and permit screening of potential reactor alloys. Several early experiments have demonstrated the ability to simulate irradiation-induced creep and have generated a limited

amount of creep data[1-4].

The Radiation Effects on Metals program supported by the Division of Physical Research/Energy Research and Development Administration at Battelle Northwest has recently initiated a creep simulation program using the Tandem Van de Graaff accelerator at the Nuclear Physics Laboratory. Development of an apparatus located on the straight-ahead line in Cave III, is now underway. The appparatus features a helium circulating system for removing the irradiation-induced heat from the test specimen. The specimen is heated and its temperature controlled by direct ohmic heating. Temperature is redundantly sensed by measuring the specimen electrical resistance, emitted infrared radiation, and thermocouple output. Strss is applied uniaxially by a remotely-driven tensioning spring. Specimen elongation (i.e. creep strain) is continously monitored by a non-contacting laser extensometer.

Early experiments will test the creep response of high purity nickel bombarded with 18 MeV deuterons. Specimens will be stressed to between 34 and 340 MPa (5,000 to 50,000 psi), heated to between 100 and 300° C (212 to 572°F) at ion fluxes between 1 and 10 $\mu a/cm^2$. Creep rates will be measured as a function of stress, temperature, and flux. This data will be compared with electron microscopy data obtained from the irradiated test specimens to elucidate operating creep mechanisms.

---

1. S. D. Harkness, F. L. Yagee, and F. V. Nolfi, Jr. ANL-7883, Argonne National Laboratory, 1972.

2. P. L. Hendrick, A. L. Bement, Jr. and O. K. Harling, Nucl. Instr and Methods, *124*, 389 (1975).

3. R. J. McElroy, J. A. Hudson, and R. S. Nelson, Proceedings of the Int'l Conf on Radiation Effects and Tritium Technology for Fusion Reactors (CONF -750989, Vol. II), 1975.

4. P. L. Hendrick, D. J. Michel, A. G. Pieper, and R. E. Surratt, J. of Nuclear Materials, *59*, 229 (1976).

[+]Battelle Northwest, Richland,Washington

11.8 Radiation Environment Simulation - Mechanical Properties*

R. H. Jones[+], D. L. Styris [+]

The use of penetrating light ions to produce displacement damage in materials offers a degree of control over irradiation parameters not attainable with any neutron source. The long term objective for the ion irradiation for mechanical properties program is the development of an ion irradiation system

with sufficient flexibility to perform a variety of mechanical property experiments while the short term objective is a correlation between the microstructure and mechanical properties of light ion and neutron irradiated materials.

To make the irradiations a high vacuum (5×10^{-10} torr) irradiation chamber with helium cooling gas pumping and purifying system was mated to the 30° beam line (cave 1) of the tandem Van de Graaff accelerator at the University of Washington. The beam line environment is isolated from the irradiation chamber by a 6350 μm thick Havar window. Multiple irradiations of wire tensile test samples (0.125 to 0.254 mm diameter) can be made during any one irradiation. Present experiments use 16 MeV protons to produce damage throughout the gage section of these samples.

Installation of the irradiation chamber began October, 1976. The system is still being conditioned and checked out. Several beam diagnostic runs and one sample irradiation have been completed.

---

*Supported by the Energy Research and Development Administration, Division of Magnetic Fusion Energy

†Battelle Pacific Northwest Laboratories

12. ACCELERATOR AND ION

12.1 Van de Graaff Accelerator Operations and Improvements

Staff

Major improvements and innovations to the three stage tandem Van de Graaff accelerator this year include rebuilding of the low energy end of the tandem, described below, installation and operation of the spin filter on the polarized ion source, described in Sec. 12.3, achievement of the best beam resolution observed to date, described in Sec. 2.7, and successful use of the buncher for heavy ions, described in Sec. 12.7.

Statistics of accelerator operations are given in Table 12.1-1. The injector tank was opened 6 times during the year, the tandem 11 times, mostly to replace stripper foils, but including two openings to replace the charging belt after holes had developed in the fabric.

For several years, a series of problems had been accumulating at the low energy end of the tandem. Examples of these problems are the following: it was determined that several optical elements were not optimally designed (see Sec. 12.4). An accretion of aging components made frequent maintenance necessary, but difficult because of poor accessibility to the components. The lithium charge exchange source housing sat astride the beam line leading to the tandem from all other ion sources so that it was necessary to shut down the entire accelerator while performing the frequently necessary maintenance on this source. And, there was no port at which to permanently install the sputter source.

As a result, it was decided in late 1976 to remove all the components in this region and to replace the lithium charge-exchange source housing with a switching magnet so that additional ion sources could be installed on the accelerator. The revised configuration is shown in Fig. 12.1-1. The electrostatic quadrupole (Sec. 12.4) was installed. The ion pump was relocated so as

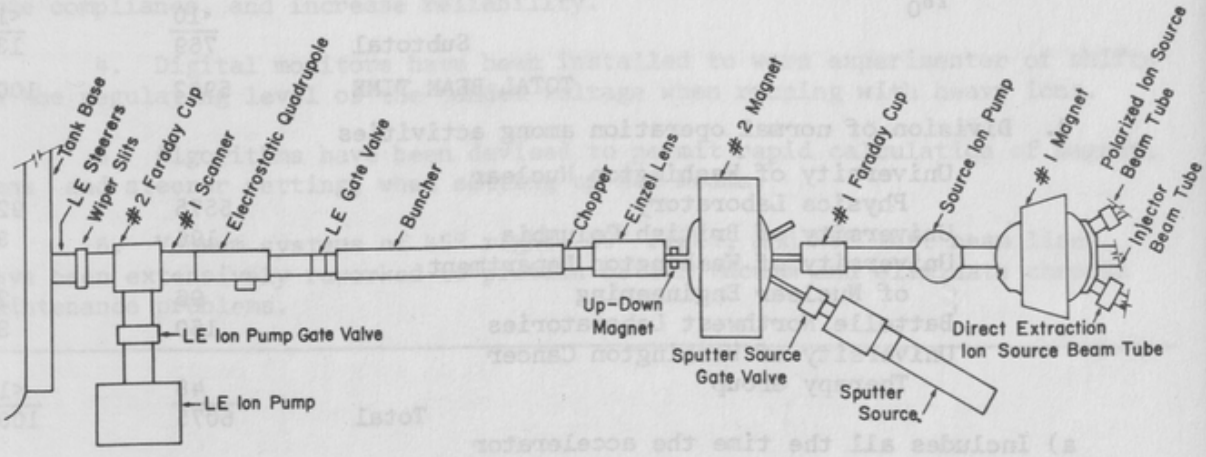

Fig. 12.1-1. Component configuration at the tandem low energy tank base.

Table 12.1-1. Statistics of Van de Graaff Operation from April 16, 1976 to April 15, 1977

1. Division of time among activities	Time (Hrs)	Per Cent
Normal operations[a]	6075	69
Scheduled maintenance	1020	12
Unscheduled maintenance	69	1
Unrequested time	1596	18
Total[b]	8760	100
2. Division of beam time among particles		
a. Two stage operation		
Protons	1306	22
Polarized protons	1277	22
Deuterons	342	6
^{3}He	256	4
^{4}He	708	12
^{12}C	253	4
^{14}N	54	1
^{15}N	121	2
^{16}O	372	6
^{18}O	335	6
^{35}Cl	31	1
^{56}Fe	17	<1
^{79}Br	27	<1
^{81}Br	20	<1
^{107}Ag	14	<1
Subtotal	5133	87
b. Three stage operation		
Protons	365	6
Deuterons	57	1
^{12}C	47	1
^{14}N	96	1
^{16}O	194	3
^{18}O	10	<1
Subtotal	769	13
TOTAL BEAM TIME	5902	100
3. Division of normal operation among activities		
University of Washington Nuclear Physics Laboratory	5575	92
University of British Columbia	196	3
University of Washington Department of Nuclear Engineering	96	2
Battelle Northwest Laboratories	160	3
University of Washington Cancer Therapy Group	48	<1
Total	6075	100

a) Includes all the time the accelerator was under the control of an experimenter.
b) This is the number of hours in a year.

to improve pumping on the low energy beam tube, and a second ion pump was installed near the switching magnet. A stand was built for the sputter source, and the source and its electronics were located permanently at the switching magnet. Revised beam diagnostic components were installed in this region. The rather large amount of rewiring required to bring the sputter source in to operation was completed and documented. The installation of all the components in this region together with the realignment of all upstream beam handling components was accomplished with the loss of only 10 working days of accelerator time.

The new configuration has displayed a number of advantages. The transmission of the beam from the polarized ion source has increased. The sputter source has produced usable beams of heavy ions, and tuning of the beam at the low energy end of the tandem has been simplified. Maintenance on all the systems has been improved. The one disadvantage of the new configuration is that the lithium charge-exchange source cannot be installed on the accelerator without substantial modification of the source housing. Because the polarized ion source has proven capable of producing larger beams of helium ions than the lithium source, it has become the primary source of these ions, and there has been no particular motivation for modifying the lithium source now.

In addition to the major revision at the low energy end of the tandem, a number of other projects have been carried out to improve accelerator operations:

1. A new beam line with beam stop, scanner and air cooled exit foil has been installed on the straight through port of the 90° analyzing magnet for use in the Battelle radiation-induced creep measurements (see Sec. 11.7).

2. A new beam line has been installed on the 30° left port of the switching magnet in Cave 1 for use in the Battelle radiation environment simultation measurement (see Sec. 11.8).

3. Substantial rewiring of both tandem and injector has been carried out and documented to improve maintenance capabilities, increase electrical code compliance, and increase reliability.

4. Digital monitors have been installed to warn experimenter of shifts in the regulating level of the tandem voltage when running with heavy ions.

5. Algorithms have been devised to permit rapid calculation of magnet, lens and steerer setting, when setting up new beams.

6. Vacuum systems of 45° right, 30° right, and 45° left beam lines have been extensively reworked to provide better vacuum and eliminate chronic maintenance problems.

12.2 Cyclotron Operations and Improvements

J.W. Orth and Staff

The cyclotron was used predominently for medical research as in the past few years. Statistics of cyclotron operation are given in Table 12.2-1.

Table 12.2-1. Statistics of Cyclotron Operations from April 16, 1976 to April 15, 1977

	Time (hrs)	Per Cent
1. Division of time among activities		
Normal operation	1664	89
Scheduled maintenance	104	6
Unscheduled maintenance	94	5
Total	1862	100
2. Division of beam time among projectiles		
Alpha particles	14	1
Protons	4	<1
Deuterons	956	98
Total	974	100
3. Division of normal operating time among users		
University of Washington Cancer Therapy Group		
a. Therapy	848	51
b. Physics	154	9
c. Biology	88	5
d. Experimental Oncology	87	5
University of Washington Nuclear Medicine	444	27
University of Washington Nuclear Pharmacy	8	<1
University of Washington Nuclear Physics Laboratory	35	2
Total	1664	100

The most serious trouble with the machine was a problem that prevented the main magnet M.G. set motor starter from latching. This was finally tracked down to wear in the latching mechanism. A new shaft and a readjustment of the linkage and timing finally solved the problem. However, this entire starter as well as the M.G. set is showing a good deal of wear and is sure to give trouble in the near future.

Another area that may give trouble was discovered during a septum change. There is a 4 cm diameter hole melted through the top of the west dee. Fortunately it is between two water lines and as long as it doesn't enlarge too much probably won't affect cyclotron performance. If it should enlarge into a water line the dee would have to be replaced. (There is a 27 year old spare spinning on hand for just such an eventuality.)

A step toward updating the cyclotron was taken this year. The rectifiers in the oscillator power supply were changed from mercury vapor tubes to solid state rectifiers. The 857B tubes and filament transformers were replaced by 6-10 amp 20 kV diodes (IRC-3HV10M10A). Incorporated into the change was a protective circuit of G.E. Varistors which, hopefully, will prevent diode damage from transients.

12.3 Polarized Ion Source

E.G. Adelberger, W.B. Ingalls, H.E. Swanson, and T.A. Trainor

The major polarized ion source improvement during the past year has been the installation of a spin-filter system and associated apparatus for spin-reversal at 1000 Hz. Spin-filter construction and installation required about 10 months at a total cost of about $15,000. Down time during installation was about three weeks.

The ion source now has three operating modes which can be chosen depending on experimental requirements. The original (Sona) source operation is still available with target proton or deuteron currents in the 100-200 nA range and proton beam polarization of 75%. Spin-filter operation with "slow" spin reversal (reversal time > 1 sec) provides proton beams of 50-60 nA on target with 83% polarization and the capability to determine the beam polarization accurately by the quench-ratio method without the need for a separate analyzer. The spin filter with rapid spin reversal (reversal time > 10μs) allows reversal rates up to 1 kHz with spin-correlated beam motion less than 10^{-6} radians and 10^{-5} cm on target. These figures correspond to false asymmetries less than for typical target-detector geometries. For either spin-filter mode the effective deuteron-beam tensor polarization has been increased threefold over the Sona polarization scheme and the vector polarization has increased by 50%. This system has been described in some detail at a recent conference.[1]

The present ion source configuration is shown in Fig. 12.3-1. This figure does not include the Wien processor or acceleration tube immediately downstream, which are discussed in a previous annual report.[2]

The spin-filter solenoid is shown in Fig. 12.3-2. The solenoid contains a 1.6 GHz rf cavity and four-element electrostatic deflection plates. The solenoid bobbin and container have been treated with a "black oxidizing" rust preventive process.

The transverse field coils for the rapid spin-reversal system are shown in Fig. 12.3-3. The coils and associated compensating electric-field plates are mounted on an epoxy flange which allows arbitrary orientation at the transverse fields about the beam axis. The coil forms are split at one end to reduce eddy currents during rapid spin reversal.

Proper adjustment of the compensating electric field reduces to zero the average spin-correlated Lorentz force experienced by charged particles passing through the rapid reversal region. Spin-dependent quenching of

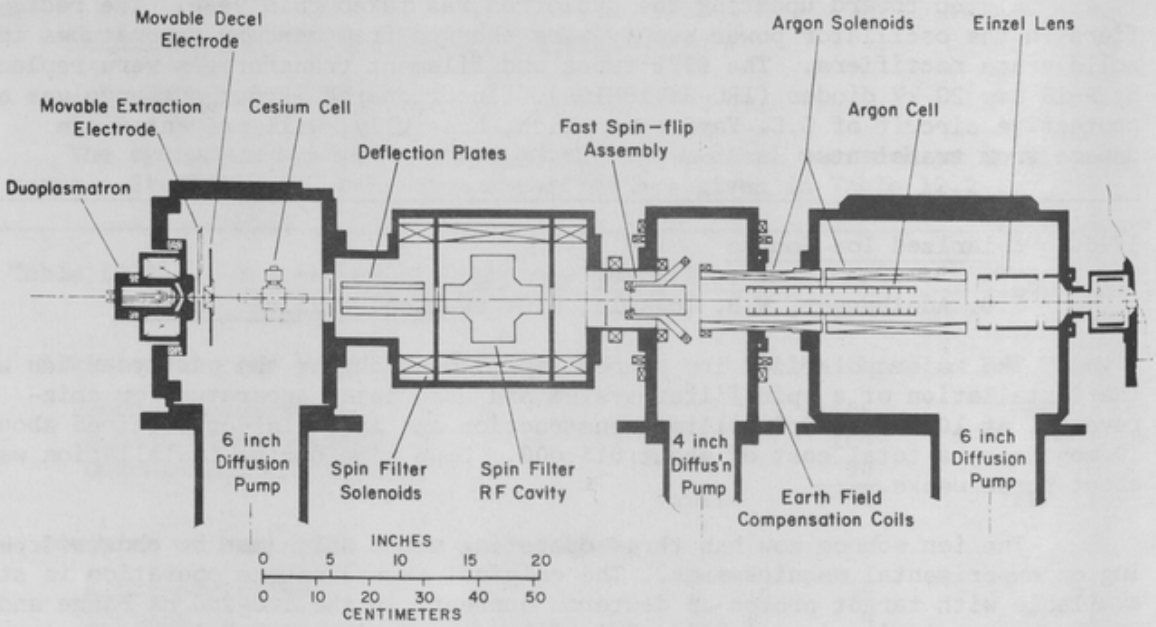

Fig. 12.3-1. Spin-filter polarized ion source.

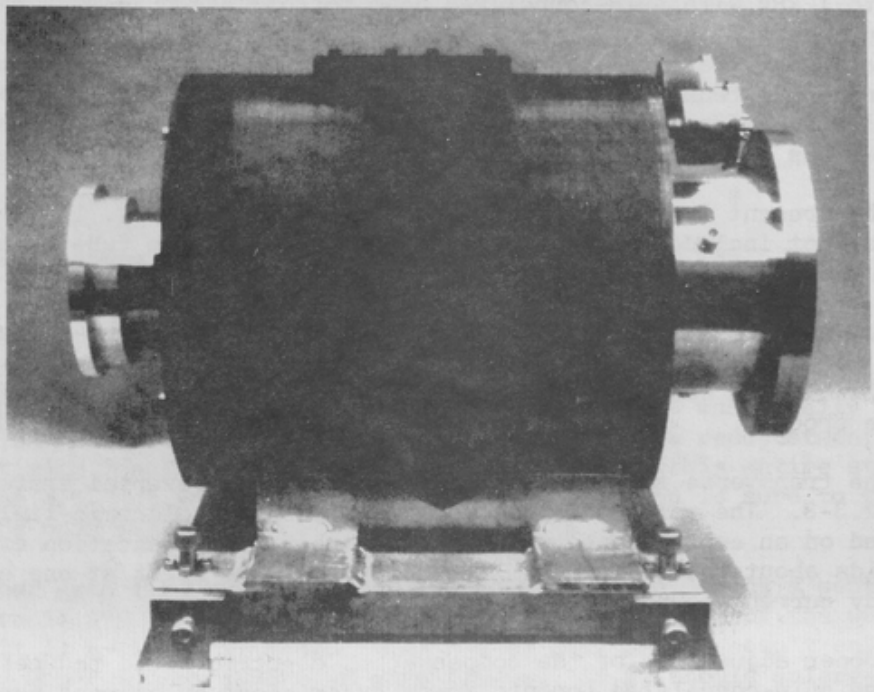

Fig. 12.3-2. Spin-filter solenoid

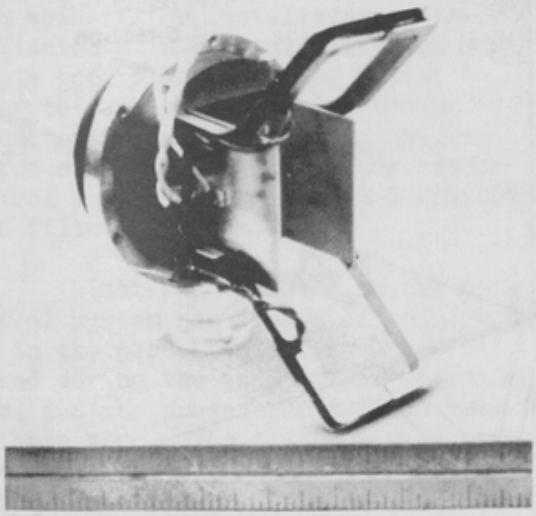

Fig. 12.3-3. Transverse-field coils.

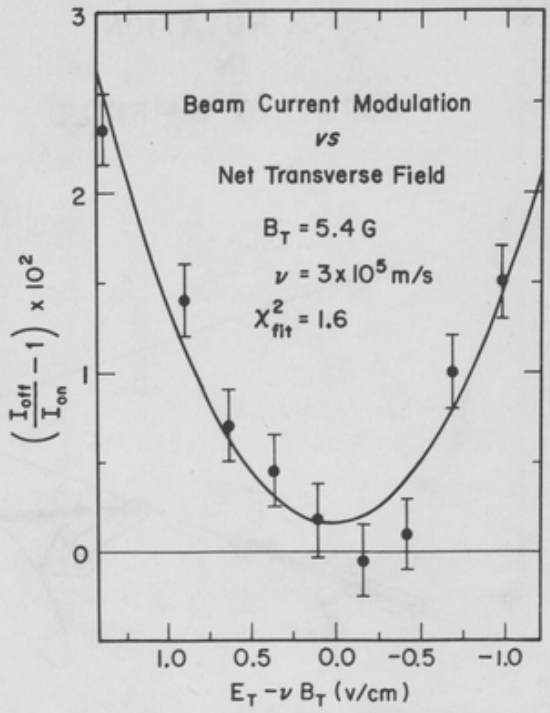

Fig. 12.3-4. Spin-correlated beam-current modulation.

metastable beam passing through this region depends quadratically on the net transverse field and therefore cannot be reduced to zero to the extent that the fields are non-uniform over the beam diameter. The quadratic dependence is illustrated in Fig. 12.3-4. These data correspond to a transverse magnetic field four times larger than normal to enhance sensitivity to spin-correlated effects. The quadratic fit indicates a beam-current modulation less than 10^{-4} at proper field values.

A schematic representation of the rapid spin-reversal process is shown in Fig. 12.3-5. The spin equation of motion in the laboratory system is given by

$$\dot{\vec{S}} = \vec{\omega}_o(t) \times \vec{S}$$

with $\vec{\omega}_o$(MHz) = 8.8$\vec{B}$(t)(Gauss). The atomic spins see a time-dependent field $\vec{B}(t)$ as they pass through the spin-reversal region at a speed v = 3×10^{5}m/s. This field can be described in the reversal region as having a nearly constant magnitude and rotating at a uniform rate ω. In a coordinate system rotating with the magnetic field the atomic spins satisfy the equation of motion

$$\dot{\vec{S}}' = (\vec{\omega}_o' - \vec{\omega}) \times \vec{S}'$$

where $\vec{\omega}_o' - \vec{\omega}$ is a nearly constant vector about which the spin $\vec{S}$ executes simple precession. This motion is represented in Fig. 12.3-5. The transverse and

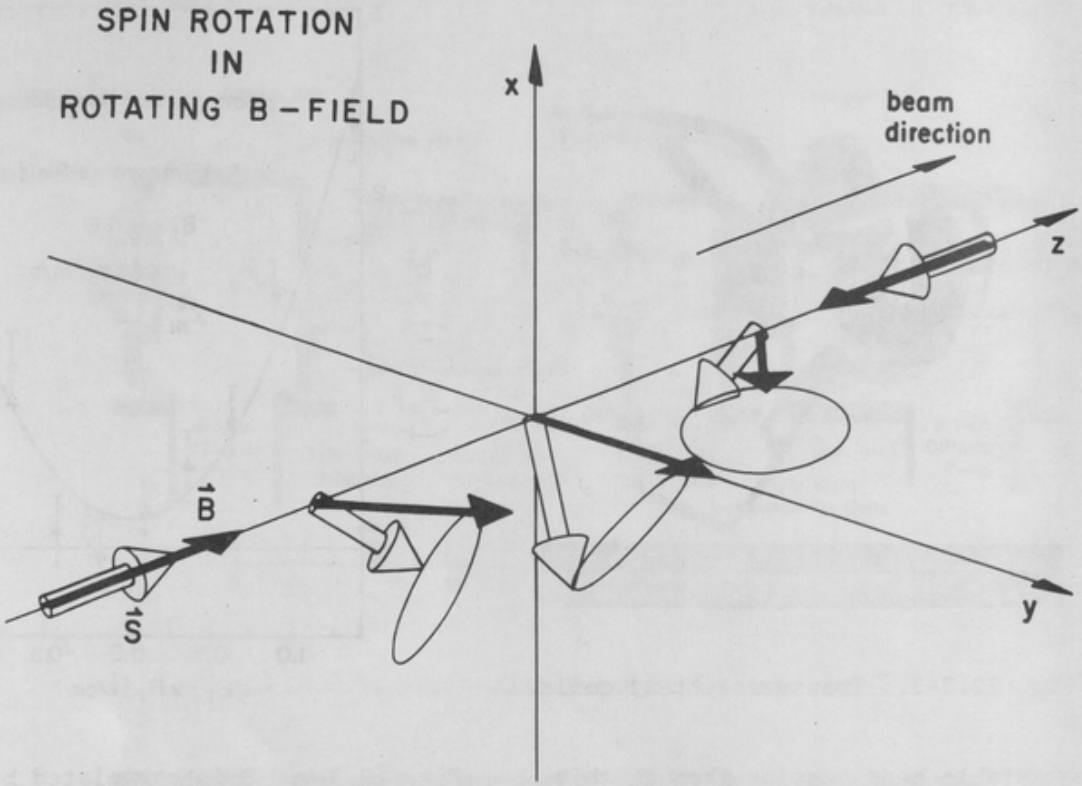

Fig. 12.3-5. Spin precession in the rapid spin-reversal region.

axial fields in the reversal region must be adjusted so that $\vec{S}$ executes one complete cycle in the rotating frame as the net magnetic field rotates through 180° in the laboratory frame. If the transverse field is turned off the axial field undergoes a diabatic reversal and the atomic spin is undisturbed.

Measurement of the beam polarization (Z component of the spin) as a function of the transverse-field strength is shown in Fig. 12.3-6. As the transverse coil is turned on and off the polarization alternates between -0.75 and + 0.80. This spin reversal can be accomplished at rates greater than 1 kHz.

The great reduction in spin-correlated beam motion reported above now makes possible the completion of the ^{19}F parity-violation experiment described in Sec. 2.2 of this report with the assurance that false asymmetries are no longer a possible limiting factor in the experiment.

In connection with the ^{19}F experiment we have successfully developed computer-controlled rotation of the ion-source Wien precessor. The angular position of the precessor is now determined by the position of the polarization vector on target as determined by a "quad polarimeter." The computer, polarimeter and precessor form a feedback loop which maintains the polarization vector in the scattering plane to a few tenths of a degree accuracy.

Other improvements have included installation of a 20 ampere arc-current supply of our own construction, major rewiring of the ion source in connection with spin-filter installations, installation of a digital voltmeter and remote controlled stepping switch in order to sample the growing number of parameters needed to operate the ion source and construction of new remote control panels which include additional spin-filter controls.

Light-pipe failure in the remote-control system has been a chronic problem in the past. This system was reworked during the spin-filter installation, and the subsequent failure rate has been zero. The failures were traced to absence of current-limiting resistors in certain light-pipe channels dating from the original installation.

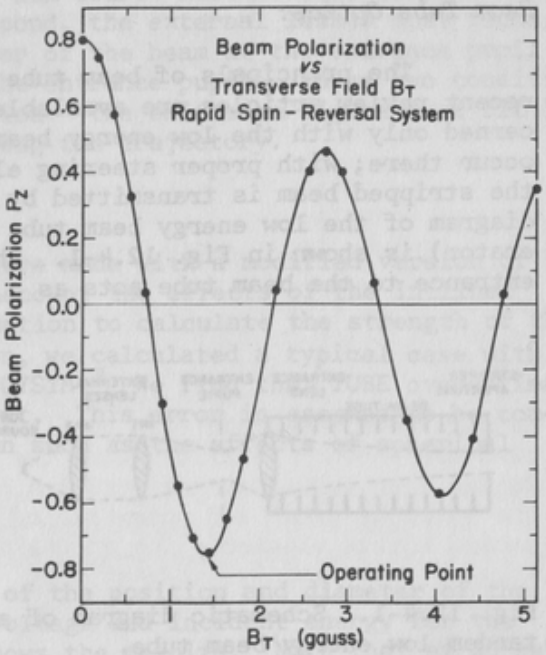

Fig. 12.3-6. Beam polarization *vs.* transverse magnetic field in the rapid reversal region.

The next major improvement to the polarized ion source that we foresee is installation of a cryogenic pumping system for the argon charge-exchange cell. This recently introduced technology provides almost complete localization of argon charge-exchange gas in the ion source, and eliminates charge exchange in unwanted areas. The result is enhanced beam polarization and beam current. More important is elimination of charge exchange in the rapid spin-reversal region with further reduction of spin-correlated beam motion.

---

1. T.A. Trainor, W.B. Ingalls, H.E. Swanson, and E.G. Adelberger, *Proceedings of the Particle Accelerator Conference,* Chicago (1977), to be published in IEEE transactions on Nuclear Science.
2. Nuclear Physics Laboratory Annual Report, University of Washington (1975), p. 18.

12.4 Tandem Beam Transmission Calculations and Improvements

P.J. Grant and W.G. Weitkamp

It is important to minimize the beam lost during acceleration in a tandem accelerator, especially for beams which are difficult to produce with reasonable intensity from the ion source, such as polarized beams or some heavy ion beams. For this reason we have undertaken a quantitative study of improving the transmission, and have tested some possible improvements.

Beam Tube Optics:

The principals of beam tube optics have been known for a long time and recent review articles are available.[1] For present purposes we shall be concerned only with the low energy beam tube of the tandem because most beam losses occur there; with proper steering elements in the terminal, essentially all of the stripped beam is transmitted by the high energy beam tube. A schematic diagram of the low energy beam tube (or the beam tube of a single stage accelerator) is shown in Fig. 12.4-1. The rapidly varying electric field at the entrance to the beam tube acts as a strong converging lens, the *entrance lens*, which focuses the entering beam into the stripper aperture in the terminal of the accelerator. In order for particles to be transmitted through the beam tube, they must pass through an imaginary aperture in front of the tube, the *entrance pupil*. This pupil is the image of the stripper aperture that would be formed by the entrance lens if the beam traveled backwards down the beam tube. The entrance pupil is not fixed in space; instead both the position and diameter of the pupil depend on the terminal voltage, the configuration of electrodes at the entrance to the beam tube, and the energy of the ions from the ion source.

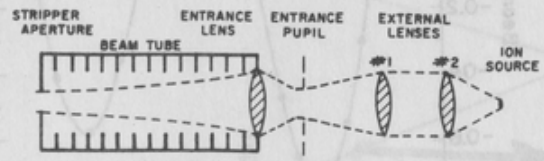

Fig. 12.4-1. Schematic diagram of a tandem low energy beam tube.

It is the function of the external lenses to take the beam emitted by the ion source and focus it into the entrance pupil. The fraction of the beam transmitted by the beam tube depends on how well this can be done. The fraction transmitted also depends on the angular divergence of the beam at the entrance pupil. Obviously, particles with large angular divergence strike the edge of the entrance lens and are lost. For this reason, we must examine the *acceptance* of the beam tube, a quantity characterizing both spacial extent and angular divergence of a beam. If y is the vertical coordinate of a possible trajectory at some point along the trajectory, and y' is the slope of the trajectory at that point, then one can plot a point corresponding to each possible trajectory on the y,y' plane and draw a closed figure around all those trajectories which pass completely through the beam tube. The area of this closed figure in the y,y' plane is called the vertical acceptance of the beam tube. The area of a similar figure in the x,x' plane gives the horizontal acceptance. The acceptance times the square root of the beam energy at a given point along the trajectory is an invarient, i.e., it is independent of position along the beam tube. This follows from Liouville's theorem. Note that only the area of the acceptance figure is invarient; the shape of this figure may change considerably along the trajectory.

Acceptance is a particularly useful concept when compared to the *emittance* of an ion source. The emittance of an ion source is defined in analogy with acceptance as the area of a figure in either the x,x' or the y,y' plane enclosing all trajectories of particles emitted by the ion source. To completely transmit a beam from an ion source through a beam tube, two conditions must

be satisfied: first, the emittance of the ion source must be less than or equal to the acceptance of the beam tube, and second, the external lenses must focus the beam from the ion source so the diameter of the beam at the entrance pupil is smaller than or equal the diameter of the entrance pupil. These two conditions can be combined into a more general condition: the emittance figure must fit inside the acceptance figure at any point along the trajectory.

Computer Codes:

The calculations described below were made with a modified version of TUBE.[2] This first order code takes into account the effects of the inclined fields in beam tubes, but uses an approximation to calculate the strength of the entrance lens. To check this approximation, we calculated a typical case with a more exact (but more time consuming) code CYSYM.[3] We find that TUBE overestimated the strength of the lens by about 20 percent. This error is assumed to be comparable to uncertainties in the calculation such as the effects of spherical aberration, and ignored.

Calculation of the Entrance Pupil:

The first calculation was a study of the position and diameter of the entrance pupil as a function of terminal voltage and incident energy for the normal beam tube geometry. Fig. 12.4-2 shows the results. Note that at 50 keV incident ion energy the entrance pupil moves more than 80 cm as the terminal voltage changes from 2 to 9 MV. Note also that increasing the incident ion energy moves the entrance pupil further from the end of the beam tube and increases the range of motion. Fig. 12.4-2 illustrates an important problem in designing the external lenses. The entrance pupil has a small diameter when it is close to the end of the beam tube (far away from the external lens) and a larger diameter further away. If the external optics consists of only a single lens, the position of the image produced by this lens can easily be adjusted to correspond to the position of the entrance pupil, but because the magnification of the external lens is the ratio of the image distance to the object distance (the fixed distance from ion source to lens) the image is larger when it is further from the lens. This is just the opposite of what is required to put the image inside the entrance pupil. As a result, a single external lens cannot provide maximum transmission for a wide range of terminal voltages; a pair of lenses is required and these must be properly adjusted

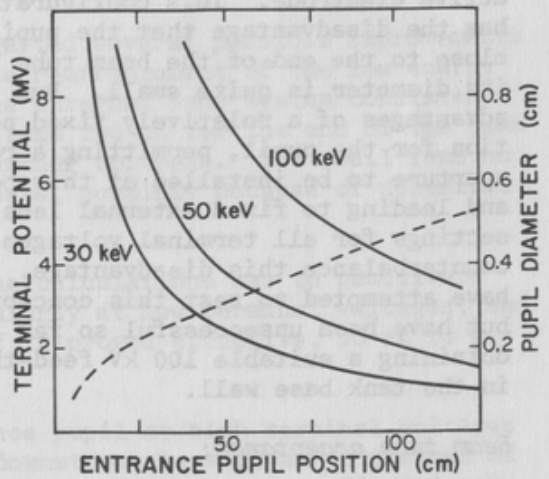

Fig. 12.4-2. Position and diameter of the entrance pupil of a beam tube. Solid curves plot the position as a function of terminal potential (left hand scale). The dashed curve plots the pupil diameter (right hand scale) as a function of pupil position. Distances are measured from the end of the beam tube.

to give maximum transmission, with the upstream lens strong for low terminal voltage and the downstream lens strong for high terminal voltage.

Effects of the tube biasing:

A number of techniques have been utilized to reduce the strong dependence of entrance pupil position on terminal voltage. The most common technique is to weaken the entrance lens by installing a wire grid across the end of the beam tube. This has a number of obvious disadvantages. We have investigated the opposite approach, artificially strengthening the entrance lens. This can be accomplished by biasing the second active electrode from the entrance of the tube with a fixed high voltage. That such biasing tends to stabilize the position of the entrance pupil can be seen in Fig. 12.4-3, where results of calculations made with this configuration are shown. In this figure the dotted line indicates the position of the entrance pupil and potential of the second active electrode for an unbiased tube. It is readily apparent that whereas for a normal beam tube the entrance pupil moves about 80 cm as the terminal voltage changes from 2 to 9 MV, the entrance pupil moves only about 6 cm with a bias of 100 kV on the second active electrode. This configuration has the disadvantage that the pupil is close to the end of the beam tube so its diameter is quite small. But the advantages of a relatively fixed position for the pupil, permitting a real aperture to be installed at this point, and leading to fixed external lens settings for all terminal voltages may counterbalance this disadvantage. We have attempted to test this concept, but have been unseccessful so far in obtaining a suitable 100 kV feed-through in the tank base wall.

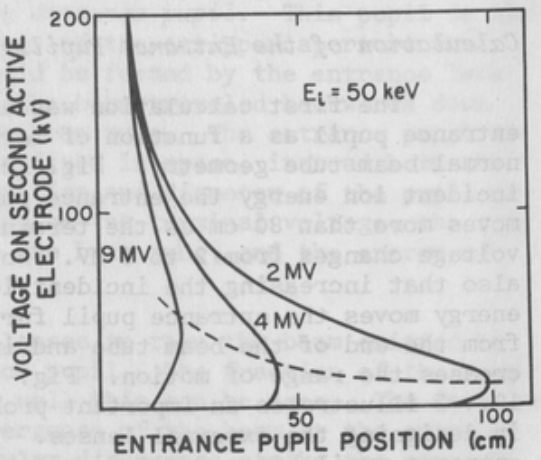

Fig. 12.4-3. Entrance pupil position as a function of bias voltage on the second active electrode. The dashed curve indicates pupil position and second electrode potential for an unbiased tube.

Beam tube acceptance:

The acceptance of the beam tube as a function of terminal voltage V and incident ion energy E_i has been calculated. This acceptance may be expressed

$$A = k\sqrt{V/E_i}$$

where k = 2.7 cm mr in the vertical plane and 7.8 cm mr in the horizontal plane if V and E_i are in the same units. The acceptance is determined by the stripper aperture and the aperture of the tube electrodes. In the vertical case, the limiting trajectories just graze the electrodes about twenty to thirty electrodes from the entrance of the tube. The much larger acceptance in the

horizontal plane is the result of the slotted apertures in the electrodes of a standard inclined-field beam tube.

The acceptance of a beam tube is inversely proportional in the square root of the incident ion energy. A common misconception among tandem users is that since the emittance of an ion source varies inversely as the square root of the ion energy, one can increase the transmission of a beam through an accelerator automatically by raising the acceleration potential of the ion source. Since the acceptance of the tandem varies in exactly the same way with ion energy, nothing can be gained this way. However, raising the ion source accelerating voltage may, in some cases, increase transmission because the image of the ion source more nearly coincides with the entrance pupil, because higher energy beams are less susceptible to deflection by stray magnetic or electric fields, or because of a decreased probability of loss in the collisions with residual gas in the beam tube.

We have measured the emittance of our sputter source to be about 50 cm mr for ^{12}C at 20 keV, in agreement with other measurements.[4] This means we should expect complete transmission of sputter source beams for terminal voltages above about 7 MV. Actual transmission has been substantially poorer than this. The direct extraction ion source has an emittance factor of 10 smaller than a sputter source[4] so beams from it should be transmitted fully over a wide range of terminal voltages. We have observed this.

Revision of the tandem ion optics:

The calculations described above suggested several possible improvements to the ion optics of our tandem. Prior to the rearrangement of the low energy end described in Sec. 12.1 of this report, the external lens system consisted of two einzel lenses, a large 13 cm diameter lens 240 cm for the end of the beam tube and a small 5 cm diameter lens 190 cm further upstream. The small lens had not proven particularly useful in previous tests, possibly because of spherical aberration, so was not in general use.

The first improvement suggested by the calculations was to reactivate the small lens and study its effects, particularly at low terminal voltages, and to replace it with a larger aperture lens, if it proved effective, so as to get rid of spherical aberration.

The very small diameter of the entrance pupil at high terminal voltages suggested that it was important to have the downstream lens close to the end of the beam tube to properly demagnify the image of the ion source to fit into the entrance pupil.

The much larger acceptance of the beam tube in the horizontal plane suggested that one might be able to increase total transmission by using a lens with different focal properties in the vertical and horizontal planes, e.g., a quadrupole, instead of a cylindrically symmetric einzel lens.

To test all of these suggested improvements, we installed a makeshift electrostatic quadrupole doublet 80 cm downstream from the large einzel lens. The quadrupole had 2.9 cm radius cylindrical electrodes 15 cm long, 2.5 cm from

the axis of symmetry. The proton beam from the polarized ion source was used to compare the transmission using the large einzel lens alone with the transmission using the quadrupole alone or, at low energies, using the quadrupole and the reactivated small einzel lens but without the large einzel lens. The polarized source was chosen for these comparison measurements because its transmission had not previously exceeded about 50 percent.

The results of the comparison at four terminal voltages is given in Table 12.4-1. It is, of course, difficult to measure transmission accurately

Table 12.4-1. Comparison of print on transmission with various lenses

Terminal Voltage (MV)	Transmission using large einzel lens alone	Transmission using electrostatic quadrupole
1.1	0.12	0.17*
2.2	0.40	0.77*
5.0	0.56	0.71
8.1	0.51	0.66

* small einzel lens optomized.

since rather minor twiddeling of the settings can sometimes cause major changes in transmission. However, the satisfying trends shown by this table appeared quite real and were observed on two separate occasions. We found that the quadrupole doublet gave best transmission when the upstream lens focused in the vertical plane. Reversing the polarity caused a decrease of about 30% in transmission. Typical voltages on this lens were ±400V.

As discussed in Sec. 12.1 of the report, a permanent quadrupole has been installed and a large diameter einzel lens installed upstream. The substantially improved transmission of the polarized ion source beam has persisted; future efforts will center around improving sputter source heavy ion beam transmission.

1. J.D. Larson, Nucl. Instr. and Meth. *122*, 53 (1974).
2. J.G. Cramer, Nucl. Instr. and Meth. *62*, 205 (1968).
3. Nuclear Physics Laboratory Annual Report, University of Washington (1972) p. 40.
4. G. Doucas, T.J.L. Greenway, H.R. McK. Hyder and A.B. Knox, IEEE Trans. Nucl. Sci. *NS-23*, 1155 (1976).

12.5 Prototype Spiral Resonator Cavity Construction

D. Chamberlin and J.G. Cramer

The components of the prototype cavity structure described in last year's report[1] have been machined, have undergone preliminary checks as an assemblage, and have been electroplated with OFHC copper. The vacuum integrity of the hatch seal and the moving seals has been demonstrated. Final polishing is currently underway and will be followed by assembly and low power tests.

The major deviation from the previous description is the substitution of round for square tubing in the spirals allowing a tighter geometric form for the spirals. This change was made after preliminary checks of the original structure showed the two lower frequency modes to be degenerate when loaded by the surrounding cavity. The round tubing decreased the capacitance of the spirals to various elements and has removed the degeneracy.

The accompanying photograph shows the assemblage at an intermediate stage of plating and polishing. The compensator plate has been omitted as indications from other researchers are that a set of spheres placed relatively close to the spirals will be more effective as a frequency tuning device.[2] The 3" coaxial transmission line fittings may be seen extending out from the top of the cavity at the position of the rotatable, water cooled coupling loop.[3] The close tolerance fit of the hatch into the tank is not evident in the photo. Not shown and only partially machined are the three alternate hatches with their differing spiral and drift tube configurations corresponding to differing resonant modes and particle phase velocities.

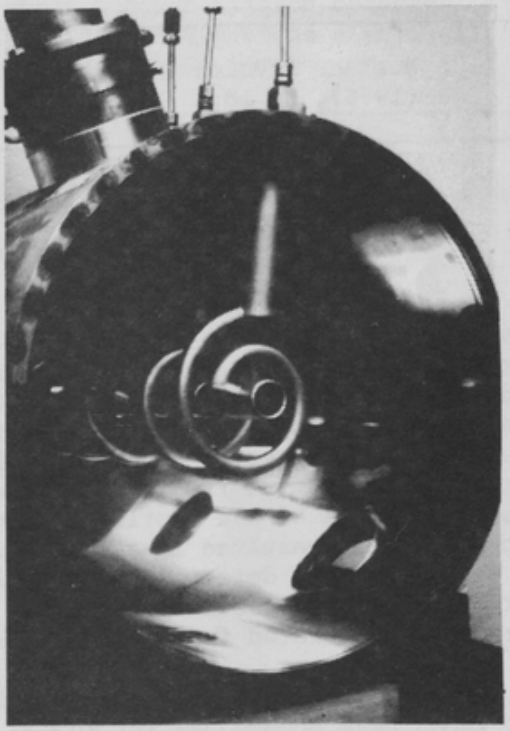

Fig. 12.5-1. Prototype Spiral Resonator Cavity

---

1. Nuclear Physics Laboratory Annual Report, University of Washington (1976), p. 13.
2. A. Schempp and H. Klein, 1976 Linear Accel. Conf., Chalk River.
3. E. Jaeschke, private communication.

12.6 Vacuum tests of Liquid Stripper Foils

J.G. Cramer and R. Roddenberg

We have continued our investigations of the properties of thin films produced at the edge of a rapidly spinning sharpened wheel which is partially immersed in Dow-Corning 200/50 vacuum lubricant, as reported in last year's Annual Report.[1] We have reconstructed the apparatus so that it can be operated in vacuum and have tested it in a vacuum test chamber, at pressures on the order of 10^{-5} torr.

We find that the thin films become even more stable under vacuum conditions, presumably because of the absence of turbulent entrained air which is always present when the apparatus is operated at atmospheric pressure. Thus the method looks very promising as a means of producing "indestructable" thin self-supporting films for stripping and target applications. We plan to run heavy ion beams through these films to study the charge state structure of the stripped ions. These measurements will probably be performed with the magnetic spectrograph in the near future.

---

1. Nuclear Physics Laboratory Annual Report, University of Washington (1976), p. 18.

12.7 Performance of the Klystron-buncher with Beams of Light- and Heavy-Ions

Y-d. Chan, J.G. Cramer, B. Cuengco, H. Fauska, and R. Sielemann

We have checked the bunching performance of the existing Klystron-buncher[1] with protons, ^{16}O- and ^{18}O-ions. To determine the smallest possible packet-width the elastic scattering of protons between 8- and 11 MeV from a C and Co target was measured with a 700μm thick silicon detector. Fast timing electronics was used to measure the time difference between the cooled and over-biased silicon detector[2] and a signal derived from the buncher driver rf. The three-gap buncher at the low energy end of the tandem was tuned to the extraction voltage of 45 kV. Optimizing the buncher parameters (and the associated chopper width) resulted in a best time resolution of (0.8 ± 0.1)nsec (FWHM). We think that the detector contribution to this value is negligible. An even better performance could possibly be obtained if the beam burst timing signal were to be generated from the beam close to the target.

Measurement of the time resolution using a NE 102 plastic scintillator for gamma rays around 500 keV showed a time resolution of (1.1 ± 0.1)nsec (FWHM), the difference compared to the particle detector possibly due to timing contributions from the plastic scintillator.

Because of buncher frequency limitations the bunching of ^{16}O had to be performed on the third harmonic of the basic frequency. At a source extraction voltage of 57 kV we obtained for a beam of ^{16}O at 35 MeV energy time resolutions of 3-4nsec (FWHM), measured between the buncher driving frequency and a

NE 102 plastic scintillator looking at γ-rays from a thin C target.

Bunching of ^{18}O on the third harmonic required more than 60 kV extraction voltage. This could not be stably obtained. We therefore bunched on the fifth harmonic at 34 kV extraction voltage, leading to rather poor transmission of ^{18}O through the tandem. Time resolution measured in the same way as before showed that we still obtained a resolution of 7 to 8nsec (FWHM).

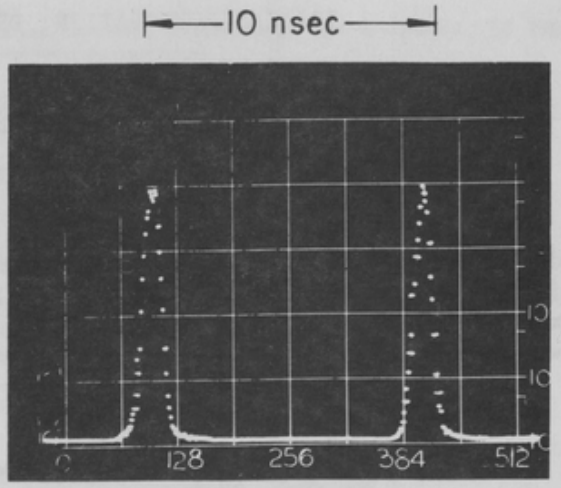

Fig. 12.7-1. Time resolution of the Klystron-buncher-silicon detector system for 8 MeV protons elastically scattered by a Co target.

1. H. Fauska, N.G. Ward, J. Lilley, and C.F. Williamson, Nucl. Inst. Meth. *63*, 93 (1968).
2. Nuclear Physics Laboratory Annual Report, University of Washington (1976), p. 31.

13.1 A Silicon Surface Barrier Detector Telescope for Electrons

P.A. Dickey, J.E. Bussoletti, E.G. Adelberger

The ^{28}Mg beta decay experiment described in Sec. 2.8 required an electron detector with high detection efficiency for 0.5 to 1 MeV electrons, low sensitivity to gamma rays, and good time resolution. We have found these criteria to be met with a simple telescope of silicon surface barrier detectors. In this report we will briefly describe the design and performance of the system.

Design and Operation

The basic telescope consists of three detector elements as shown in Fig. 13.1-1 (for the ^{28}Mg experiment a fourth detector was added behind the telescope to increase the total thickness of silicon for high energy electrons).

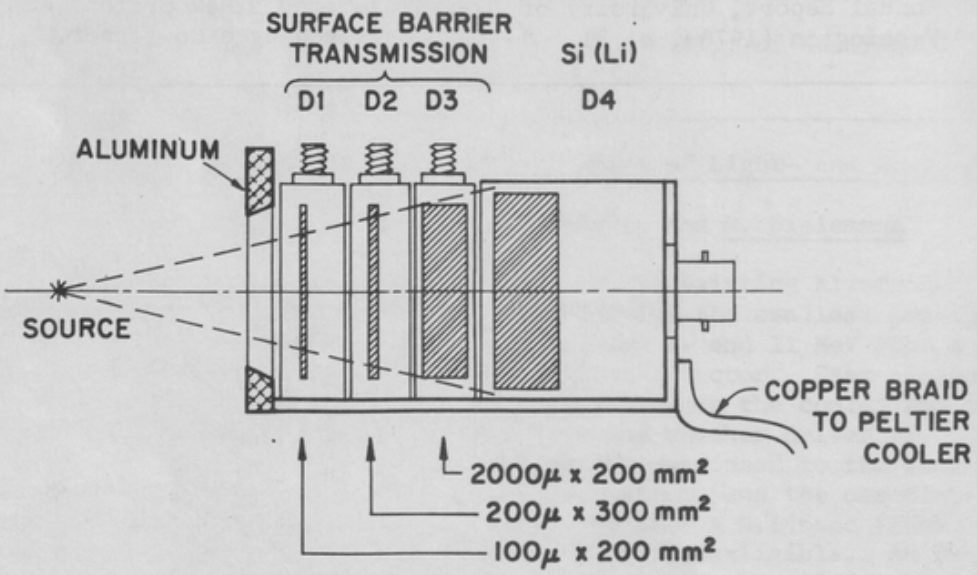

Fig. 13.1-1. Sketch of the physical arrangement of the detector telescope.

The front elements D_1(100μ) and D_2(200μ) are thin compared to element D_3(2000μ); the combined 2.3 mm of silicon stops 1 MeV electrons. In operation, the electronic logic of Fig. 13.1-2 requires a threefold coincidence $D_1D_2D_3$ to announce a valid electron event. Most electrons of 1/2 to 1 MeV produce pulses in all three detectors, and are detected with nearly 100% intrinsic efficiency. Gamma rays, which must Compton scatter in the front detector D_1 in order to be detected, are effectively discriminated against because D_1 is very thin. A two element telescope D_1D_3 would reject gamma rays as effectively as the three element array were it not for the fact that the energy pulses from electrons passing through the

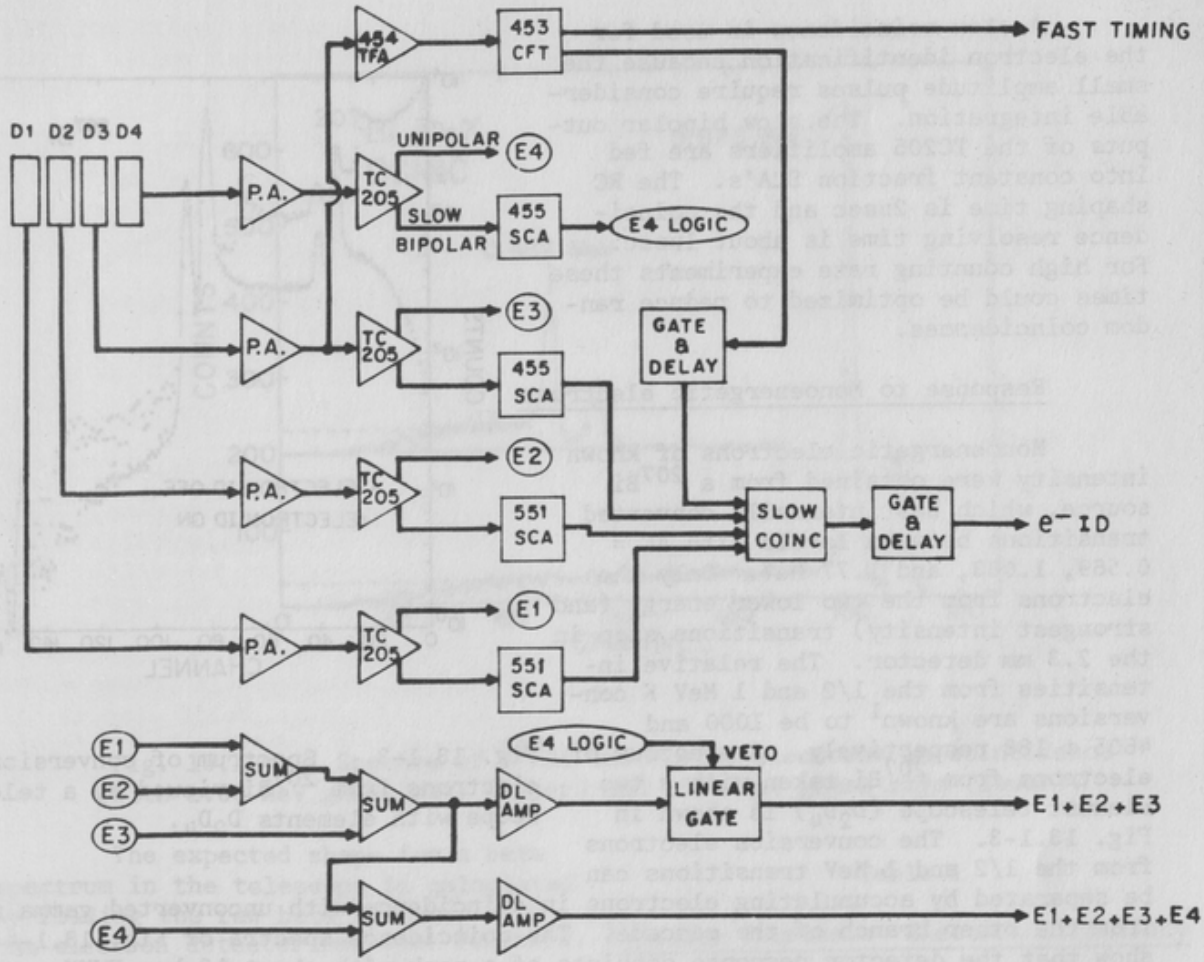

Fig. 13.1-2. Electronic logic for a four element electron telescope.

100μ counter are so small that the discriminator is triggered on noise pulses, thus producing random coincidences with gamma rays Compton scattering in the 2mm counter. The additional 200μ detector between reduces such random coincidences by the factor 200μ/2000μ = 1/10, since now a noise pulse must be in coincidence with a gamma ray scattering in the 200μ detector.

In the ^{28}Mg experiment a fourth detector was added behind the telescope, and events corresponding to electrons which stopped in the third versus the fourth counters were counted separately.

The entire telescope is cooled by a thermoelectric junction to reduce detector noise. The energy resolution is improved and random coincidences between detectors are reduced, thereby increasing the gamma ray rejection.

A slow coincidence is used for the electron identification because the small amplitude pulses require considerable integration. The slow bipolar outputs of the TC205 amplifiers are fed into constant fraction SCA's. The RC shaping time is 2μsec and the coincidence resolving time is about 1μsec. For high counting rate experiments these times could be optimized to reduce random coincidences.

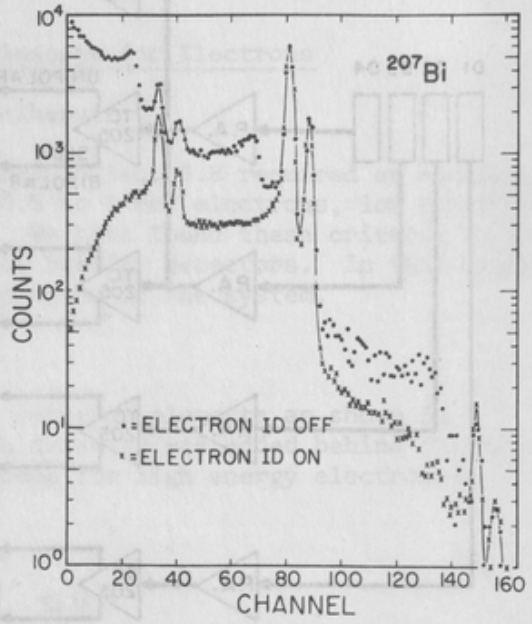

Fig. 13.1-3. Spectrum of conversion electrons from ^{207}Bi viewed by a telescope with elements D_2D_4.

Response to Monoenergetic electrons

Monoenergetic electrons of known intensity were obtained from a ^{207}Bi source, which has internally converted transitions between levels with ΔE = 0.569, 1.063, and 1.77 MeV. Only the electrons from the two lower energy (and strongest intensity) transitions stop in the 2.3 mm detector. The relative intensities from the 1/2 and 1 MeV K conversions are known[1] to be 1000 and 4605 ± 138 respectively. A spectrum of electrons from ^{207}Bi taken with a two element telescope (D_2D_4) is shown in Fig. 13.1-3. The conversion electrons from the 1/2 and 1 MeV transitions can be separated by accumulating electrons in coincidence with unconverted gamma rays from the other branch of the cascade. The coincidence spectra of Fig. 13.1-4 show that the detector response consists of a peak with about 18 kev FWHM resolution plus a flat tail. If the tail is extrapolated horizontally to zero energy it represents 1.8 times the peak area; the peak-tail area ratio is not noticeably energy dependent between 1/2 and 1 MeV.

The absolute intrinsic efficiencies at 1/2 and 1 MeV can be obtained from the known response function and the ^{207}Bi spectrum of Fig. 13.1-3. (The ^{207}Bi source was calibrated by measuring the K - Xray intensity with a 7mm planar Ge(Li). The intensity was normalized to the 60 kev line from a calibrated ^{241}Am source standard.) Table 1 lists the measured intrinsic efficiencies for three element ($D_1D_2D_3$) and two element (D_2D_3) telescopes; the efficiency was calculated by summing over the entire response function-extrapolated to zero energy and dividing by the geometric efficiency based on the nominal 200mm detector area. Deviation from unit efficiency occurs because multiple scattering in detectors D_1 and D_2 deflects some electrons sufficiently that they do not reach D_3.

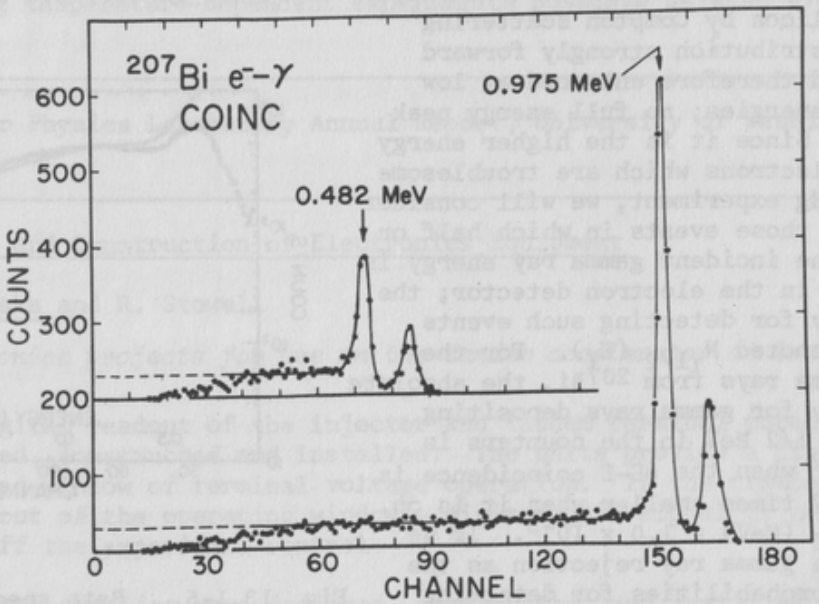

Fig. 13.1-4. Spectra of ^{207}Bi conversion electrons in coincidence with 1.06 MeV gamma rays (upper) and .569 MeV gamma rays (lower).

The expected shape for a beta spectrum in the telescope is calculated by folding the raw beta spectrum with the electron detector response function. Fig. 13.1-5 shows measured and calculated beta spectra for a ^{90}Sr - ^{90}Y source; the detector configuration was $D_2D_3D_4$.

Table 1

Absolute Intrinsic Electron Efficiency

	$D_1D_2D_3$	D_2D_3
1 MeV	0.98±.05	1.00±.05
1/2 MeV	0.76±.05	0.88±.05

Response to Gamma Rays

In the ^{28}Mg experiment, or wherever a small beta branch is measured, the rejection of gamma rays can be crucial. The gamma ray detection efficiency must be small and accurately known. We have measured the gamma ray efficiency by deflecting away the ^{207}Bi conversion electrons with a permanent magnet and looking at the remaining gamma rays in the telescope.

Gamma rays of 1/2 to 2 MeV interact in silicon by Compton scattering with a distribution strongly forward peaked and therefore enhanced at low electron energies; no full energy peak is seen. Since it is the higher energy Compton electrons which are troublesome in the ^{28}Mg experiment, we will consider here only those events in which half or more of the incident gamma ray energy is deposited in the electron detector; the efficiency for detecting such events will be denoted $N_{\gamma 1/2}(E_\gamma)$. For the 1 MeV gamma rays from ^{207}Bi, the absolute efficiency for gamma rays depositing more than 1/2 MeV in the counters is 1.8×10^{-2} when the ΔE-E coincidence is off and 17 times smaller when it is on. Thus $N_{\gamma 1/2}$ (MeV) = 1.0×10^{-3}. If we define the gamma ray rejection as the ratio of probabilities for detecting electrons and gamma rays with energy greater than half that of the incident particle, we find

$$R \equiv \frac{N_{e1/2}(1\ \text{MeV})}{N_{\gamma 1/2}(1\ \text{MeV})} = 630$$

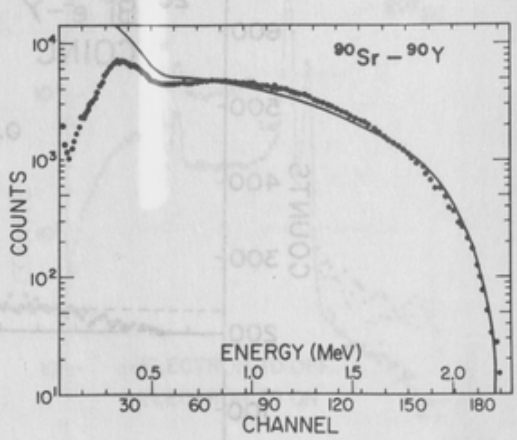

Fig. 13.1-5. Beta spectrum from ^{90}Sr-^{90}Y source obtained with three element telescope $D_2D_3D_4$. Solid line is calculated spectrum based on theoretical beta spectrum shape folded with telescope response function.

Since this number is energy dependent, it should be measured at energies near those expected for electrons and gamma rays.

---

1. F.T. Avignone, Nucl. Inst. and Meth. *116*, 521 (1974).

13.2 Construction of a Target Heating System for In-Beam Experiments at Elevated Temperatures

B.A. Scott and R. Sielemann

For certain types of experiments it is desirable to have the possibility of keeping a target at elevated temperatures. We have constructed an inset for the small T-shaped scattering chambers which is essentially a resistance-heated target holder. Small thick targets can be inserted in a BN rod which has a W wire wound on its outside. This rod in turn is inserted into an Alumina tube which has metallic reflectors on the outside. Ta or C apertures prevent the beam from hitting non-target areas. Target temperatures up to 800° C can be easily achieved, an upper limit is presently given by the tolerable heating of the brass chamber. The temperature is measured by two independent thermocouples. An easily interchangeable inset is made for larger targets at lower temperatures.

An exising target cooler with liquid nitrogen can be connected to our target holder A making temperature-dependent experiments possible between -70° C and +800° C.

---

1. Nuclear Physics Laboratory Annual Report, University of Washington (1976), p. 34.

13.3 Design and Construction of Electronics Equipment

H. Fauska and R. Stowell

Electronics projects for use on the tandem accelerator or ion sources:

1. Two digital readout of the injector and tandem terminal potentials were designed, constructed and installed. The units provide a digitally selected window of terminal voltage operation. If the terminal voltage falls out of the operating window a digital gate signal is generated to turn off the experiment control.

2. Two power supplies were designed, constructed, and installed in the analyzing and switching magnet power supplies to allow the use of the full range of the respective regulator.

3. One 10MHZ reference unit was designed and constructed for the HP. 5254 A/C freq. meter to provide for its use on the polarized ion source.

4. One switching magnet degaussing supply was constructed and installed.

5. The remote control of the number two ion source magnet was constructed and installed. The chassis includes a degaussing power supply for the magnet.

6. New logarithmic pre-amplifiers for the image slit pre-amplifiers have been designed and constructed and are going through final testing.

Other electronics projects:

1. An alpha counter which is power line operated and runs as a continuous radiation monitor was designed and constructed.

2. One five channel scaler unit was constructed. Each channel is one decade and allows cascading.

3. An overflow scaler was designed and constructed.

4. A scaler was designed and constructed for use in experimental setup at the control console.

5. A scaler routing system used in fast flip experiments was constructed and is being tested. The unit will provide data switching for 10 channels.

6. A digitally selected frequency stabilizer with crystal reference was designed and constructed for use in testing the spiral resonator.

7. A standing-wave ratio meter was constructed for testing the spiral resonator.

8. The series power transistor bank of the cyclotron magnet were changed to silicon transistors.

9. The field regulator for the cyclotron magnet was redesigned and built.

10. A beam intensity controller for use in the Battelle radiation induced creep experiments was designed and constructed. It uses the chopper on a time domain regulator principle. The low energy chopper is driven by a variable length pulse so as to repeditively remove a controlled fraction of the beam and maintain a precisely constant average output beam.

11. A high precision analog divider and multiplier circuit was designed and constructed to provide the Battelle radiation creep measurement a signal proportional to target heater current and target heater power.

14. THE COMPUTER AND COMPUTING

14.1 Computer Hardware Improvements

N.R. Cheney

A lite pen has been incorporated into the display hardware used with the laboratory's off line computer. Software development is presently underway to include this capability in off line data analysis programs.

Construction of an interface to allow the laboratory's on line computer to access data from up to 16 ADC's (Tracor Northern model TN1213) is over 90% complete. This project has taken longer than originally anticipated in our funding proposal due to several post proposal suggestions made by experimenters.

14.2 RALPH/EDNA: Data Collection/Analysis Programs for Multiple Parameter Coincidence Experiments

J. Bussoletti, P. Dickey, J. Sanislo

These two programs expand the capabilities for collecting multiple parameter coincidence data beyond those offered by SCOSINDHAP/SCOSINEAP. The new more powerful programs can replace SCOSINDHAP/SCOSINEAP in all applications. The data tape formats are not compatible, but a conversion program exists.

RALPH is the on-line data collection program and offers the following important features:

1) Up to four coincident parameters may be processed by the program.

2) Simultaneous collection of coincidence and singles data through the same ADC in the manner of SCOSINDHAP.

3) Two different coincidence event formats may be defined simultaneously through the use of event validity conditions.

4) On-line collection and display of up to eight spectra. These spectra may be one dimensional, two dimensional or particle identification spectra. Any combination of spectra types may be in operation simultaneously.

5) Up to four digital gate conditions may be applied to each spectrum.

6) Ability to replay data tapes during a temporary halt in data collection.

7) Tape handling has been simplified from that used by SCOSINDHAP so that no load point markers are needed.

8) Minimum processing time for a simple three parameter coincidence is about 800 μsec.

EDNA is the off-line program for analyzing data tapes written by RALPH. Significant features of EDNA are:

1) Use of the disk as temporary storage space to minimize the number of tape reads required for sorting.

2) Sorting can be performed into one dimensional or two dimensional spectra of parameters or functions of one or more parameters.

3) Up to four gate conditions may be set on each spectrum and these gates may be defined by a single parameter or a function of parameters.

4) Ability to add/subtract both one dimensional and two dimensional spectra.

5) Facilities for dumping spectrum and/or event information to tape for interfacing with specialized user-written programs.

Each of these programs and their operation is completely described in separate user's manuals.

14.3 HOPFLUX: Modification of HOPTHREE to Generate Optical Model Particle Fluxes for Heavy Ion Reactions

M.B. Tsang and R. Vandenbosch

In order to visualize the refractive, reflective and absorptive effect of complex potentials in heavy ion scattering, it is useful to be able to examine the flux trajectories in the angle-distance plane.

Subroutine NUMEROV of the optical model program HOPTWO[1] has been modified to give wave functions for each partial wave. The program was first developed on the Laboratory SDS 930 Computer and later on the CDC 6400 Computer of the University of Washington. On the latter computer HOPTHREE[2] (a modification of HOPTWO capable of handling up to 1,000 partial waves) was used. The program consists of two parts. HOPFLUX calculates the wave functions and writes them on a tape which is read by another FORTRAN program FLUX that gives particle fluxes, as a function of distance and angle. The fluxes calculated for 18 MeV alphas on argon were checked against those reported by I.E. McCarthy[3]. They were in excellent agreement.

1. J.G. Cramer, Nuclear Physics Laboratory Annual Report, University of Washington (1974), p. 26.
2. R. Vandenbosch, Nuclear Physics Laboratory Annual Report, University of Washington (1975), p. 44.
3. I.E. McCarthy, Nuclear Phys. *10*, 583 (1959).

14.4 RESFIT: An Optical Model Plus Resonance Fitting Program

N. L. Back

The program RESFIT, which generates elastic scattering cross section and analyzing power excitation functions for low-energy protons[1], has been revised. The new version 2.1, like the old one, includes both direct (optical model) and resonant (Breit-Wigner) contributions. In addition, modifications have been made to allow for both spin-0 and spin-1/2 targets, and a fitting routine has been included so that searches can be made on the resonance parameters. Some of the capabilities and limitations of the program are: (a) it is written for the Laboratory's SDS 930 computer, (b) up to three excitation functions can be calculated, each with up to 55 energies, (c) up to seven resonances can be included, (d) up to 10 parameters can be varied, (e) only 16 partial waves are allowed, (f) the user can decide whether or not to use the fitting routine, and whether to fit to cross section data, analyzing power data, or both, and (g) the data and final calculations are printed out, but are not plotted.

---

1. Nuclear Physics Laboratory Annual Report, University of Washington (1973), p. 29.

14.5 Classical Trajectory Program

R. Vandenbosch and R. Weisfield

This program calculates classical trajectories for a particle moving in a central pontential. The trajectory is numerically integrated from infinity to the classical turning point (distance of closest approach) and then is reflected about this point back to infinity. The asymptotic scattering angle is printed, along with the distance of closest approach and the scattering angle obtained for a purely Coulomb potential. The calculation can be repeated over integral steps of angular momentum, all of whose orbits can be plotted on the Calcomp plotter.

The calculation uses the real part of an optical model potential, composed of an attractive Woods-Saxon nuclear part, and repulsive Coulomb and centrifugal parts. A recent addition to the program optionally calculates the time the projectile takes to reach the turning point from a previously specified starting distance. The time is printed as a function of decreasing distance, whose decrement can be varied to the system of interest.

An example of trajectories calculated for the $^{86}Kr + ^{139}La$ system is shown in Fig. 14.5-1. These calculations, which as yet do not take into account energy and angular momentum loss along the trajectory, nevertheless reproduce some of the qualitative features of the experimental data. There is a concentration of the largest ℓ waves near the grazing angle. These trajectories are identified with the sharp peak in the observed cross section for the partially damped events. The lower partial waves have trajectories leading to smaller angles or orbiting around to negative angles. Experimentally, events

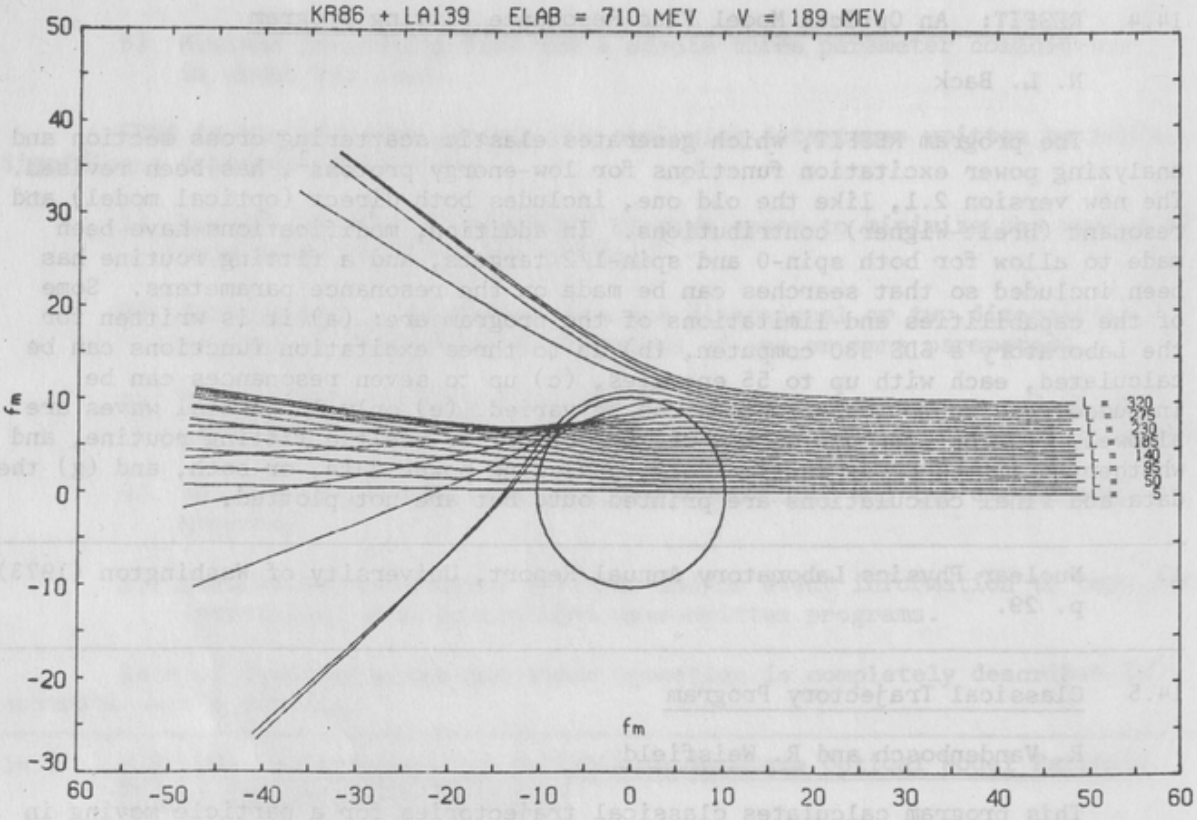

Fig. 14.5-1. Example of a trajectory for the $^{86}Kr + ^{139}La$ system at E_{Lab} = 710 MeV. The nuclear potential used is one of a family which reproduces the elastic scattering, and has a central depth consistent with adiabatic merging of the target and projectile into a single sphere of normal density.

with larger energy loss are found to be primarily forward peaked, but also extend to larger angles. It would be desirable to include energy and angular momentum losses in a future version of this program.

14.6 KGPHASE: A Subroutine for Calculating Coulomb Phase Shifts for Non-integer and Complex Angular Momentum L-values

John G. Cramer

When a relativistically-invariant wave equation such as the Klein-Gordon equasion is used to describe the scattering of spinless particles, as discussed in Sections 6.6 and 9.4 the effective angular momentum values which must be used in the evaluation of Coulomb wave functions become used in the evaluation of Coulomb phase shifts and Coulomb wave functions become non-integers. For cases where the product of charges ZZ' is greater than 68.5 there will arise an even more pathological situation in which the effective angular momentum value becomes complex. For this case the Coulomb phases and wave functions are undefined,[1] and if one is not to abandon the usual treatment of the Coulomb-

nuclear scattering problem altogether, a model is required for dealing with this catastrophe. This is discussed further in Section 6.7.

The Coulomb phase shifts are defined by the equation:

$$e^{2i\sigma_\lambda(\eta)} = \frac{\Gamma(\lambda+1+i\eta)}{\Gamma(\lambda+1-i\eta)} \qquad (1)$$

where η is the Sommerfeld parameter and λ is the effective angular momentum value, and these are given by the equations:

$$\eta = ZZ'e^2/\hbar v = ZZ'\alpha/\beta \quad \text{and} \quad \lambda = [(\ell+1/2)^2-(ZZ'\alpha)^2]^{1/2}-1/2$$

where α is the fine structure constant and β is the velocity relative to c. As long as λ is real, the numerator and denominator of (1) are equal in magnitude so the Coulomb phase will be real. However, when λ becomes a complex quantity, if we take (1) literally then its numerator and denominator magnitudes will be unequal and $\sigma_\lambda(\eta)$ must also become complex, its imaginary part being the logarithm of the magnitude ratio. This is effectively an analytic continuation of the definition of the Coulomb phase shift into the complex L-plane.

We have written a subroutine to evaluate the real and imaginary parts of the analytically continued Coulomb phase, using the extended Stirling approximation given by eqn. 6.1.41 of the Handbook of Mathematical Functions[2], considering the z-value to be complex and using separate expansions to evaluate the real and imaginary parts.

The subroutine call is:

```
CALL KGPHASE(ETA,ALR,ALI,CPR,CPI)
```

where ETA is the Sommerfeld parameter, ALR and ALI are the real and imaginary parts of the effective angular momentum λ, and CPR and CPI are the real and imaginary parts of the Coulomb phase shift which is calculated.

Note that the usual procedure of evaluating a Coulomb phase of large ℓ and recurring downward will not work for the relativistic case because the λ-values are neither integers nor evenly spaced in λ. Thus each Coulomb phase must be calculated individually in a relativistic Coulomb scattering calculation.

---

1. N.F. Mott and H.S.W. Massey, The Theory of Atomic Collisions, pp. 40-41, Oxford at the Clarendon Press (1949).
2. M. Abramowitz and I.A. Stegun, Handbook of Mathematical Functions, p. 257, U.S. Government Printing Office, Washington, D.C. (1964).

14.7 KGRUTH: A Program for Calculating the Rutherford Scattering Amplitude for the Klein-Gordon Equation

John G. Cramer and John G. Wills*

As discussed in Sec. 14.6 above and in Sec. 6.6 below, Coulomb scattering with a relativistic wave equation such as the Klein-Gordon cannot be calculated with the usual Rutherford scattering formula. In fact, no closed expression is known for the evaluation of relativistic Rutherford scattering. Nevertheless, the conventional treatment of the Coulomb-nuclear scattering problem requires that the Rutherford amplitude be factored out of the partial-wave sum so that the radial integration can be terminated when the nuclear potential cuts off at R_{max} and so that the partial wave sum can be truncated at approximately $\ell = kR_{max} - \eta$.

The Rutherford cross section calculated with the Klein-Gordon wave equation is also interesting in itself, in that there will be, in some cases, experimentally observable differences between Schrodinger and Klein-Gordon derived Rutherford cross sections which make it possible to experimentally test the form of the wave equation.

For these reasons, we have written a program to calculate the Klein-Gordon-Rutherford amplitude by means of a partial wave sum. The basic expression for the Rutherford amplitude is:

$$f^{KG}_{ruth} = \frac{1}{2ik}\sum_{\ell}(2\ell+1)P_\ell(\cos\theta)\{\exp\{2i[\sigma_\lambda(\eta) + \pi(\ell-\lambda)/2]\} - 1\} \qquad (1)$$

where the effective angular momentum value for the Coulomb phase is given by:

$$\lambda = \sqrt{(\ell+1/2)^2 - (ZZ'\alpha)^2} - 1/2 \qquad (2)$$

Here η is the Sommerfeld parameter ZZ'e2/hv and α is the fine structure constant. Unfortunately, the series given in (1) does not cut off at finite values of ℓ, but one can add and subtract the non-relativistic amplitude f_{ruth} given by:

$$f_{ruth} = \frac{1}{2ik_\ell}\sum_{\ell}(2\ell+1)P_\ell(\cos\theta)\{\exp[2i\sigma_\ell(\eta)] - 1\} = -\frac{\eta}{2k}\left(\sin\frac{\theta}{2}\right)^{-2-2i\eta} e^{2i\sigma_0} \qquad (3)$$

Equation (1) then becomes:

$$f^{KG}_{ruth} = f_{ruth} + \frac{1}{2ik}\sum_{\ell}(2\ell+1)P_\ell(\cos\theta)\exp[2i\sigma_\ell(\eta)] \times \{\exp\{2i[\sigma_\lambda(\eta) - \sigma_\ell(\eta) + \pi(\ell-\lambda)/2]\} - 1\}. \qquad (4)$$

Clearly the second exponential factor approaches 1 as $\lambda \to \ell$ so the series converges, but this happens relatively slowly, and requires a summation of thousands of partial waves for very heavy ions. This situation can be improved by a slight modification of equation (4) in which instead of using f_{ruth} and $\sigma_\ell(\eta)$ for the actual η-value, we use a slightly modified value η' given by:

$$\eta' = \eta - \frac{\eta^2\beta^2}{2L+1}\left[\mathrm{Tan}^{-1}\left(\frac{\eta}{L+1}\right) + \frac{1}{2L+2} - \frac{\pi}{2}\right] \pm \{1\,\eta(L+1) - 1/(2L+2)\} \qquad (5)$$

where L is the angular momentum value at which we wish to truncate the series. With this procedure we can calculate f^{KG}_{ruth} with a few hundred partial waves and use this for Rutherford scattering predictions and for optical model calculations.

For the case where ZZ'>68 the effective angular momentum λ will become complex for the low partial waves. When this happens, there is no "correct" procedure for evaluating the Coulomb phase shifts and Rutherford amplitude, since, strictly speaking, both are undefined[1]. In the program KGRUTH, we have provided three alternative procedures for dealing with this problem, which may be taken as models. These are: (1) use only the real part of λ when it becomes complex, so that $\lambda = -1/2$; (2) use only the real part of the analytically continued Coulomb phase shift $\sigma_\lambda(\eta)$; and (3) use the full complex value of the analytically continued Coulomb phase shift $\sigma_\lambda(\eta)$. The analytic continuation procedure employed in (2) and (3) is discussed in Sec. 14.6 above. It is not at present clear which of these procedures (if any) is most successful in dealing with the Coulomb catastrophe which occurs for ZZ'>68. Our present feeling is that procedure (2) is probably best in that it gives the smoothest transition between the questionable low partial waves and those for which this problem does not arise.

The program KGRUTH employs complete fully relativistic reaction kinematics and is capable of dealing with identical or non-identical particles. It employs the subroutine KGPHASE[2] to evaluate the Coulomb phase shifts and can handle partial wave sums with up to 1600 partial waves. It compares the normal and Klein-Gordon amplitudes and cross sections and produces a high-density plot of both.

We plan to incorporate this program in a pair of new optical model programs, one for pion scattering and one for heavy ion scattering which use the Klein-Gordon as their wave equation and treat the Coulomb part of the problem as accurately as possible.

---

* Permanent address: Physics Dept., Indiana University, Bloomington, Indiana.

1. N.F. Mott and H.S.W. Massey, The Theory of Atomic Collisions, pp. 40-41 Oxford at the Clarendon Press, (1949).
2. See Sec. 14.6 of this report.

14.8 KGCOU: A Subroutine for Calculating Coulomb Wave Functions and their Derivatives for Non-integer Angular Momentum L-values

John G. Cramer

When a relativistically invariant wave equation such as the Klein-Gordon equation is used to describe the scattering of spinless particles, as discussed in Sec. 6.7, the effective angular momentum values which must be used in the evaluation of Coulomb wave functions are not integers. Therefore, the usual procedures for evaluation of Coulomb wave functions, which involve recursion in unit steps in angular momentum, cannot be used. It is therefore necessary to

devise a new procedure for the evaluation of Coulomb wave functions of arbitrary, and in particular fractional, angular momentum values.

Fortunately, the Manchester group has recently published a description[1] of a computer program for calculating Coulomb wave functions which employs a continued fraction procedure which does not depend on recursion relations or on the integer character of the angular momentum values. We have written the subroutine KGCOU based on the Manchester program which calculates the regular and irregular Coulomb wave functions $F_\ell(\rho,\eta)$ and $G_\ell(\rho,\eta)$ and their derivatives with respect to ρ, $F'_\ell(\rho,\eta)$ and $G'_\ell(\rho,\eta)$. The calling sequence of this program is:

```
CALL KGCOU(RHO,ETA,AL,FC,FCP,GC,GCP)
```

where RHO and ETA are the ρ and η values, AL is the value of the effective angular momentum, and FC, FCP, GC, and GCP are the output quantities F_ℓ, F'_ℓ, G_ℓ, and G'_ℓ. Note that the program must be called separately for each value of AL rather than in the usual way of filling an array in a single call. Note also that the program does not calculate Coulomb phase shifts, which are calculated with the subroutine KGPHASE described in Sec. 14.6 above.

The subroutine KGCOU calculates the Coulomb wave functions very rapidly as long as AL is less than the cutoff L-value defined by:

$$L = \sqrt{\rho(\rho - 2\eta) + 1/4} - 1/2 \qquad (1)$$

If AL is larger than this value, the program employs a Runge-Kutta integration procedure to integrate inward from a larger value. This procedure is quite time consuming, and these wave functions require about 100 times longer to evaluate than the lower AL values. Fortunately, in a typical calculation only a few of the largest AL values fall in this region.

This program will be employed in two new optical model programs, one for pion scattering and one for heavy ion scattering, which will employ the Kelin-Gordon equation as their wave equation. This program does not deal with the problem of complex effective angular momentum values, as discussed in Sec. 14.7. However, we recommend that for this case the Coulomb functions be evaluated for AL= $^-$0.5, and the resulting G+iF Coulomb Hankel function be multiplied by the phase factor $\exp[2i(\sigma_\lambda - \sigma_{-\frac{1}{2}})]$. This procedure is consistent with those described in Sec. 14.7 above.

---

1. A.R. Barnett, D.H. Feng, J.W. Steed, and L.J.B. Goldfarb, Computer Physics Communications 8, 377 (1974).

14.9 AUTOPEAK: An Automatic Peak Search Program with Least Squares Fitting

K. Green

In conjunction with the ^{24}Mg(α,α') experiment described in section 7.4 of this report, an automated analysis program was developed to handle the large

amounts of data in a consistant manner. It is designed to function without operator intervention, requiring only a tape drive and the line printer.

AUTOPEAK reads standard MULTSING data tapes and scans designated spectra for peaks by a method similar to that of Blok, DeLange and Schotman[1]. The method is sensitive to multiplets and will operate with completely arbitrary peak shapes. Peaks located in this manner are then fit with Bevington's CURFIT[2], using a fitting function consisting of up to 4 peaks on a quadrative background. The width, height and centroid of each peak is variable, peaks which fail to converge are discarded.

Output consists of a brief line printer plot for each peak, giving the source data, fit and background. The centroid, RMS width, background subtracted area and statistical error of each peak is also printed.

---

1. H.P. Blok, J.C. DeLange and J.W. Schotman, Nuclear Instruments and Methods, *128*, 545-556 (1975).
2. Philip R. Bevington, Data Reduction and Error Analysis for the Physical Sciences (McGraw=Hill, 1969), pp. 237-239.

14.10 PRECESS: A Program to Calculate Spin Precession in a Time-varying Magnetic Field

R. Von Lintig and T.A. Trainor

This program was written in connection with the design of the rapid spin-reversal system recently installed in the polarized ion source (see Sec. 12.3 of this report). Computer simulation of this system is desirable because proper operation depends critically on magnetic fields generated by six separate coils in the rapid-reversal region of the ion source, and because trial-and-error adjustment of the system would require a significant amount of accelerator time.

The program integrates the spin equations of motion

$$\frac{d\vec{P}(t)}{dt} = \vec{\omega}(t) \times \vec{P}(t)$$

where $\hbar\vec{\omega}(t) = \mu_0 \vec{B}(t)$ and $\vec{B}(t)$ is the magnetic field in the rest frame of the spin. The spin is that of a neutral hydrogen atom moving at 3×10^5 m/s through a region of varying magnetic field which is static in the laboratory system.

Transverse and axial magnetic field values are entered as data or generated internally with appropriate analytic expressions. The transverse and axial fields can be separately normalized and/or shifted with respect to one another along the atomic-beam axis prior to integration of the equations of motion.

The program calculates three spin components as functions of position along the beam axis. It also calculates the final z component of spin as a function of either field-normalization parameter or the relative displacement of axial and transverse fields.

14.11 VOYEUR: Automatic Analysis of Excitation Function Spectra

J. Osborne

VOYEUR is an off-line analysis program, for use on our 930 computer. Detailed instructions for use of the program are available from the VOYEUR self-loading tapes. VOYEUR is designed to automatically produce excitation functions from data tapes produced by the program MULTSING. Peak regions are defined by the user. The final excitation function can be output on cards, listed on the line printer, plotted on the line printer, or plotted by the Calcomp plotter in a form suitable for publication.

In the calculation of yields, VOYEUR automatically normalizes to a current integrator scaler and corrects for ADC dead time. Up to 40 peaks at 50 energies can be calculated in one pass. The windows defining the peaks can be defined so that they automatically track changes in the calculated centroid of the peak. Background subtraction, which is also optional, is accomplished using a straight line interpolation between user-defined high and low background regions. The files are read back into the computer, and the user can then define a weighted sum of the yields. This allows him to add or subtract peaks and to convert yields to cross-sections. The user can also define the yield of one peak to be divided by the yield of another, for the purpose of normalization or comparison of yields.

15. ENERGY STUDIES

15.1 Energy Studies

D. Bodansky and F.H. Schmidt

The book discussed in last year's report; The Energy Controversy: The Fight Over Nuclear Power was published in September, 1976 (Albion Publishing Co., San Francisco). About a dozen newspapers carried a six-part condensed version of the book during the fall of 1976. In view of the rapidly changing national energy situation, at the present time we are considering a revision to bring the book up-to-date.

Another part of our work, also mentioned in last year's report, led to the preparation of a chapter entitled "Safety Aspects of Nuclear Energy", which has now appered in The Nuclear Power Controversy, edited by Arthur Murphy for the American Assembly, Columbia University (Prentice-Hall, October, 1976).

In addition to the above writing, we have given a number of seminars and colloquia on diverse aspects of the energy problem in various departments of our own and other Universities, have made presentations before government bodies, and have spoken to a broad range of general audiences. Some of our comments have been published as letters-to-the-editor.

In recent months, in collaboration with members of the Nuclear Engineering Department, we have begun more intensive study of one of the most important issues on the national energy scene: the connection between nuclear power plant operation and weapons proliferation. A contributed talk on this subject will be presented at the Washington, D.C. meeting of the American Physical Society, in April, 1977.

In March 1977 one of us served as a Moderator at an assembly held by the Air Force Academy in Colorado Springs. These yearly assemblies follow the pattern of the American Assemblies and are sponsored jointly by the A.F.A. and Columbia University. The three days of sessions brought together a group of about eighty students selected from Universities across the country, and about fifteen specialists in diverse fields of energy drawn from Universities, National Laboratories, and Government Agencies.

The overall objectives of our studies remain unchanged from those mentioned previously[1]---to evaluate as best we can the energy problem as a whole, and to communicate our evaluations.

---

1. Nuclear Physics Laboratory Annual Report, University of Washington, p. 163, (1976).

16. APPENDIX

16.1 Nuclear Physics Laboratory Personnel

Faculty

Eric G. Adelberger, Professor
Norman Austern, Visiting Professor[1]
John S. Blair, Professor
David Bodansky, Professor, Chairman, Department of Physics
David F. Burch, Research Assistant Professor
John G. Cramer, Professor
Klaus A. Eberhard, Visiting Associate Professor[2]
George W. Farwell, Professor
I. Halpern, Professor
Donald R. Maxon, Visiting Professor[3]
Fred H. Schmidt, Professor
Kurt A. Snover, Research Assistant Professor
Thomas A. Trainor, Research Assistant Professor
Robert Vandenbosch, Professor
William G. Weitkamp, Research Associate Professor; Technical Director, Nuclear Physics Laboratory

Research Staff

Konrad Aniol, Research Associate
Hans-Holger Bohn, Research Associate[4]
Philip A. Dickey, Research Associate
Peggy L. Dyer, Research Associate
Lynn D. Knutson, Research Associate[5]
Raymond J. Puigh II, Research Associate
Rainer Sielemann, Research Associate[6]

Laboratory Supervisory Personnel

Harold Fauska, Research Electronics Supervisor; Assistant Technical Director, Nuclear Physics Laboratory
John W. Orth, Accelerator Engineer; Assistant Technical Director, Nuclear Physics Laboratory

Predoctoral Research Associates

Chemistry

Man-Yee B. Tsang
Michael P. Webb[7]

Physics

Norman L. Back
Klaus G. Bernhardt[2]
Hyoung C. Bhang
John E. Bussoletti
Yuen-dat Chan
David T. C. Chiang
Bernardo D. Cuengco
Katsuyaki Ebisawa
Kwok-Leung Liu[8]
William G. Lynch

Research Assistants

Physics

Kelly C. Green
Loren F. Stokes
Richard D. Von Lintig
James C. Wiborg[9]

Full-Time Technical Staff

Professional Staff

Noel R. Cheney, Computer Systems Engineer[12]
Sally A. Hoffman, Research Scientist
William B. Ingalls, Research Engineer
Shirley Kellenbarger, Chemist, Detector Maker
Gary W. Roth, Accelerator Engineer
Alan G. Seamster, Research Engineer
Rod E. Stowell, Electronics Engineer
H. Erik Swanson, Research Engineer

Accelerator Technicians

Barbara L. Lewellen
Carl E. Linder
Georgia J. Rohrbaugh
George E. Saling

Design and Drafting

Peggy Douglass, Graphics Des./Illustrator
Lewis E. Page, Designer

Instrument Makers

Louis L. Geissel, Student Shop Leadman
Normal E. Gilbertson
Charles E. Hart, Foreman
Gustav E. Johnson
Byron A. Scott, Student Shop Leadman[10]
Allen L. Willman, Leadman

Administrative Staff

Julie L. Anderson, Secretary
Dana Jones, Administrative Secretary
Christina O. Rios, Administrative Secretary[12]
Helene Turner, Administrative Secretary[11]

Part Time Technical Staff

John F. Amsbaugh	Roger Lapthorne
Michael Bizak	Bruce Magnuson
David Chamberlin	Kevin L. Michelsen
Yuma Chou[12]	John L. Osborne
Ronald Dickens	Jan Sanislo
Lila Graham[12]	Christopher Scofield
Patrick J. Grant	Steven Stradley[12]
Lynn D. Green	Robert J. Thoreson[12]
Richard Holladay[12]	Kody Van Dyk[12]
Wilbur Jones	Tim Van Wechel
Mark H. Killinger	Richard Weisfeld

---

1. On leave from the Department of Physics, University of Pittsburgh, Pittsburgh, PA 15260.
2. Present address: University of München, Sektion Physik D-8046, Garching, Germany.
3. On leave from the Department of Physics, Brown University, Providence RI 02912.
4. Present address: Institute für Kernphysik and Nukleare Festkörperphysik, Technische Univ. München, D-8046 Garching, Germany.
5. Present address: Department of Physics, University of Wisconsin-Madison, Madison WI 53706.
6. On leave from the Hahn-Meitner-Institut für Kernforschung Berlin, 1 Berlin 39, Germany.
7. Present address: Physics Division, Oak Ridge National Laboratory, P. O. Box X, Oak Ridge, Tenn. 37831
8. Present address: Rocket Research Corp., Redmond, WA.
9. Present address: Westinghouse, Richland, WA.
10. Retired March 31, 1977.
11. Retired February 28, 1977.
12. No longer associated with the Nuclear Physics Laboratory.

16.2 Advanced Degree Granted, Academic Year 1976-1977

M. P. Webb: Ph.D. "Nuclear Reaction Mechanisms in the $^{18}O + ^{12}C$ and $^{86}Kr + ^{139}La$ Systems."

16.3 List of Publications

Published Papers:

"Scattering of Polarized Protons from ^{12}C from 11.5 to 18 MeV," H.O. Meyer, W.G. Weitkamp, J.S. Dunham, T.A. Trainor and M.P. Baker, Nucl. Phys. *A269*, 269 (1976).

"Isospin Mixing in ^{12}C," E.G. Adelberger, R.E. Marrs, K.A. Snover, J.E. Bussoletti, Phys. Lett. *62B*, 29 (1976).

"Application of the Direct-Semidirect Model to the Interpretation of E1 and E2 Strengths in $^{14}C(p_{pol},\alpha)^{15}N$," K.A. Snover, J.E. Bussoletti, K. Ebisawa, T.A. Trainor and A.B. McDonald, Phys. Rev. Lett. *37*, 273 (1976).

"Investigation of E2 and E3 Radiation above the Giant Dipole Resonance in $^{89}Y(p,\gamma_0)^{90}Zr$," F.S. Deitrich, D.W. Heikkinen, K.A. Snover and K. Ebisawa, Phys. Rev. Lett. *38*, 156 (1977).

"Radiative Transitions and Isospin Mixing in ^{12}C," E.G. Adelberger, R.G. Marrs, K.A. Snover and J.E. Bussoletti, Phys. Rev. C. *15*, 484 (1977).

"Isospin-Forbidden Particle Decays in Light Nuclei (I).T=3/2 Levels of ^{9}Be, ^{9}B," A.B. McDonald, T.K. Alexander, D. Hausser, D. Disdier, E.G. Adelberger, H.B. Mak, A.D. Shukla and A.V. Nero, Nucl. Phys. *A273*, 451 (1976).

"Gamma Decays of Some T=0, T=1, and T=2 States in ^{20}Ne above E_x = 9.5 MeV," R.G. Marrs, E.G. Adelberger and R.A. Snover, Nucl. Phys. *A277*, 429 (1977).

"Question of Inner-Shell Electron Pickup during α Decay," P. Dyer, D. Burch, Phys. Rev. Lett. *36*, 903 (1976).

"High Energy Levels in ^{13}N (II)," D. Berghofer, M.D. Hasinoff, R. Helmer, S.T. Lim, D.F. Measday and K. Ebisawa, Nucl. Phys. *A263*, 109 (1976).

"Neutron Pickup by Alpha Particles to Unbound States," D.R. Brown, I. Halpern, J.R. Calarco, P.A. Russo, D.L. Hendrie, H. Homeyer, Phys. Rev. C. *14*, 896 (1976).

"Effects of Non-local Potentials in Heavy Ion Reactions," J.G. Cramer and R.M. DeVries, Phys. Rev. C. *14*, 122 (1976).

"Application of Austern-Blair Theory to the Interference between Coulomb and Nuclear Excitation in the Inelastic Scattering of Heavy Ions," C.K. Gelbke and J.G. Cramer, Phys. Rev. C. *14*, 1048 (1976).

"A 'Unique' Energy-independent Woods-Saxon Optical Potential for ^{16}O + ^{28}S: Elastic Scattering," J.G. Cramer, R.M. DeVries, D.A. Goldberg, M.S. Zisman and C.F. Maguire, Phys. Rev. C. *14*, 2158 (1976).

"Deeply Inelastic Scattering of ^{84}Kr from ^{208}Pb," R. Vandenbosch, M.P. Webb and T.D. Thomas, Phys. Rev. C. *14*, 143 (1976).

"Energy, Angular and Charge Distributions for Deeply Inelastic Scattering of Xe by Ta and Pb," R. Vandenbosch, M.P. Webb, T.D. Thomas and M.S. Zisman, Nuclear Physics *A269*, 210 (1976).

"Nuclear Reactions in the ^{86}Kr + ^{139}La System at 710 MeV," M.P. Webb, R. Vandenbosch and T.D. Thomas, Physics Letters *62B*, 407 (1976).

"How Strong is the Absorption in the ^{12}C + ^{20}Ne System?" M.P. Webb, R. Vandenbosch and K.G. Bernhardt, J. Physique Lett. *37*, L161 (1976).

"Elastic Scattering of ^{84}Kr from ^{208}Pb," R. Vandenbosch, M.P. Webb, T.D. Thomas, S.W. Yates and A.M. Friedman, Phys. Rev. C. *13*, 1893 (1976).

"The Rotational Band of the ^{236}U Shape Isomer," J. Borggreen, J. Pedersen, G. Sletten, R. Heffner and E. Swanson, Nucl. Phys. *A279*, 189 (1977).

"Neutron Radii of Calcium Isotropes from Pion Total Cross-Section Measurements," M.J. Jakobson, G.R. Burkson, J.R. Calarco, M.D. Cooper, D.C. Hagerman, I. Halpern, R.H. Jeppeson, K.F. Johnson, L.D. Knutson, R.E. Marrs, H.O. Meyer and R.P. Redwine, Phys. Rev. Lett. *38*, 1201 (1977).

Book:

"The Energy Controversy: The Fight Over Nuclear Power, " Fred H. Schmidt and David Bodansky, Albion Publishing Company, San Francisco (1976).

Papers Submitted or in Press:

"Radiative Proton Capture to the Ground State and First 3 Excited States of ^{12}C," K.A. Snover, P. Paul and H.M. Kuan, submitted to Nucl. Physics.

"Electromagnetic Decays of T = 2 States in T_z = 1 Nuclei," D.P. Balamuth and E.G. Adelberger, Phys, Rev., to be published.

"Electromagnetic Transitions in ^{13}C and ^{13}N," R.E. Marrs, E.G. Adelberger and K.A. Snover, Phys. Rev., to be published.

"Cross Sections for K-Shell Ionization by Electron Impact," K. Green and D. Burch, submitted to Atomic and Nuclear Data Tables.

"A Possible Photon-detection Method for Distinguishing between Stars and Galaxies Composed of Matter and Antimatter," J.G. Cramer and W.J. Braithwaite, submitted to Phys. Rev. Letters.

"Spontaneously Fissioning Isomers," R. Vandenbosch, Annual Rev. Nucl. Sci., to be published.

"Angular Momentum Transfer in Deeply Inelastic Scattering of 610 MeV ^{86}Kr by ^{209}Bi," P. Dyer, R.J. Puigh, R. Vandenbosch, T.D. Thomas and M.S. Zisman, submitted to Phys. Rev. Letters.

"Heavy Ion Elastic Scattering II: 142 MeV ^{16}O on ^{28}Si, ^{56}Co and ^{60}N," G.R. Satchler, M.L. Halbert, N.M. Clarke, E.E. Gross, C.B. Fulmer, A. Scott, D. Martin, M.D. Cohler, D.C. Hensley, C.A. Ludermann, J.G. Cramer, M.S. Zisman, and R.M. DeVries, submitted to Nuclear Physics.

"The Transition between Light and Heavy Ion Elastic Scattering," R.M. Devries, D.A. Goldberg, J.M. Watson, M.S. Zisman, and J.G. Cramer, submitted to Phys. Rev. Letters.

"Back-angle Anomalies in ^{6}Li Scattering from ^{40}Ca and ^{44}Ca," H. Bohn, K.A. Eberhard, R. Vandenbosch, K.G. Bernhardt, R. Bangert, and Y-d. Chan, Phys. Rev. C, to be published.

Invited Papers and Talks:

"Production of Li, Be and B at Low Energies," D. Bodansky, presented at the American Chemical Society Meeting, San Francisco, Sept. 2, 1976.

"Isobaric Analog Resonance Spectroscopy with Polarized Protons," M.P. Baker, presented at the Chicago APS Annual Meeting, Bull. Am. Phys. Soc. *22*, 85 (1977).

"Radiative Proton Capture and Direct-Semidirect Model," K.A. Snover, Informal Conference on Radiative Capture, Stanford University, August, 1976.

"Radiative Capture of Polarized Protons on ^{14}C and ^{15}N," J. Bussoletti, Informal Conference on Radiative Capture, Stanford University, August, 1976.

"Parity Violation in Nuclei," E.G. Adelberger, presented at Gordon Research Conference on Nuclear Structure, July 9, 1976.

"Systematic Heavy Ion Elastic Scattering Measurements: A Map of the Optical Potential," J.G. Cramer, Invited paper at the APS/DNP Meeting at East Lansing, Mich., Bull. Am. Phys. Soc. *21*, 991 (1976).

"The Excitation of Giant Resonances by Hadrons," I. Halpern, 4 x 50 Symposium, Copenhagen, Denmark (June, 1976).

"Neutron and Proton Radii of the Calcium Isotopes from $\pi^{\pm}$ Total Cross Section Measurements," I. Halpern, EPS Conference on Radial Shapes of Nuclei, Cracow, Poland (June, 1976).

"The Need for Nuclear Power in the Energy Mix," D. Bodansky, Invited talk presented at the WETA Regional Energy Conference, Portland, Oregon, (Sept. 16, 1976).

"Techniques for Diagnosing and Reducing Van de Graaff Terminal Sparking," W.G. Weitkamp, presented at 1976 Symposium of Northeastern Accelerator Personnel, Tallahassee, Fla. (Nov. 3, 1976).

"Parity Violation Experiments in Nuclear Physics," E. Adelberger, Bull. Am. Phys. Soc. *22*, 627 (1977).

Conference Proceedings publications:

"Safety Aspects of Nuclear Energy," David Bodansky and Fred H. Schmidt, in *The Nuclear Power Controversy*, American Assembly, Columbia University, Arthur W. Murphy, ed., Prentice-Hall (1976).

"Relativistic Coulomb Effects in Pion Scattering," J.G. Cramer, W.J. Lynch and J.G. Wills, to be published in the Proceedings of the VIIth Conference on High Energy Physics and Nuclear Structure, Zurich (1977).

Contributed Abstracts:

"Inelastic Scattering of 60 MeV Pions to Continuum Excitations," D. Chiang, I. Halpern, L. Knutson, M.D. Cooper, J.F. Amann, P.D. Barnes, M. Doss, S.A. Dytman, R.A. Eisenstein, J.D. Shermann, J.N. Craig and W. Wharton, Bull. Am. Phys. Soc., *22*, 525 (1977).

"Isospin Forbidden Beta Decay of ^{28}Mg," P.A. Dickey, J.E. Bussoletti, and E.G. Adelberger, Bull. Am. Phys. Soc. *22*, 527 (1977).

"Particle Decays of the Lowest T=2 State in ^{36}Ar," S.J. Freedman, M.A. Oothoudt, R.G.H. Robertson, F.J. Zutavern, E.G. Adelberger, and A.B. McDonald, Bull. Am. Phys. Soc. *22*, 527 (1977).

"A Possible Method of Distinguishing between Stars and Galaxies Composed of Matter and Antimatter," J.G. Cramer and W.J. Braithwaite, Bull. Am. Phys. Soc. *22*, 538 (1977).

"A Proposal for Monitoring Nuclear Power Plants," F.H. Schmidt and G.L. Woodruff, Bull. Am. Phys. Soc. *22*, 547 (1977).

"Cross Sections Relevant to Gamma-Ray Astronomy," P. Dyer, D. Chiang, and D. Bodansky, Bull. Am. Phys. Soc. *22*, 583 (1977).

"Angular Momentum Transfer in the ^{86}Kr + ^{209}Bi Reaction," R. Vandenbosch, P. Dyer, R. Puigh, T.D. Thomas and M.S. Zisman, Bull. Am. Phys. Soc. *22*, 594 (1977).

"Parity Violation Experiments in Nuclear Physics," E. Adelberger, Bull. Am. Phys. Soc. *22*, 627 (1977).

"Decays of the Lowest T=2 State in ^{44}Ti," S.J. Freedman, A.V. Nero, M.A. Oothoudt, R.G.H. Robertson, F.J. Zutavern, E.G. Adelberger and A.B. McDonald, Bull. Am. Phys. Soc. *21*, 980 (1976).

"Width of the Lowest T=2 State of ^{24}Mg," J.L. Osborne and E.G. Adelberger, Bull. Am. Phys. Soc. *21*, 965 (1976).

"Decays of T=0, T=1, and T-2 Levels of ^{20}Ne," E.G. Adelberger, K. Ebisawa, R.G. Marrs and K.A. Snover, Bull. Am. Phys. Soc. *21*, 965 (1976).

"Decays of T=0, T=1 and T=2 Levels of ^{20}Ne," E.G. Adelberger, K. Ebisawa, R.E. Marrs and K.A. Snover, Bull. Am. Phys. Soc. *21*, 965 (1976).

"Does the ^{15}N(p,γ_0)^{16}O Reaction Show a Giant E2 Resonance?" J.E. Bussoletti, K.A. Snover, K. Ebisawa, T.A. Trainor, H.E. Swanson and E.G. Adelberger, Bull. Am. Phys. Soc. *21*, 996 (1976).

"A Comparison of Sona and Spin-filter Polarization Schemes for a Lambshift Polarized Ion Source," T.A. Trainor, W.B. Ingalls, H.E. Swanson and E.G. Adelberger, Bull. Am. Phys. Soc. *22*, 157 (1977).

"Mass of Lowest T=2 State of ^{12}C," R.G.H. Robertson, T.L. Khoo, G.M. Crawley, A.B. McDonald, E.G. Adelberger and S.J. Freedman, Bull. Am. Phys. Soc. *22*, 551 (1977).

"Isospin Forbidden Particle Decays of the Lowest T=2 Levels of ^{16}O," A.B. McDonald, S.J. Freedman, M.A. Oothoudt, R.G.H. Robertson, F.Z. Zutavern and E.G. Adelberger, Bull. Am. Phys. Soc. *22*, 552 (1977).

Other Publications by Members of Our Laboratory:

"The K-Matrix Parameterization of the $^{12}C(\alpha,\gamma)^{16}O$ Cross Section," J. Humblet, P. Dyer, B.A. Zimmerman, Nucl. Phys. *A271*, 210 (1976).

"Influence of Impurities on the Solute Electric Field Gradient in Non-cubic s-p Metals," W. Leitz, W. Semmler, R. Sielemann and T.H. Wichert, Phys. Rev. B.*14*, 5228 (1976).

Row 1

Cuengco, Weisfield, Killinger, Bussoletti, Geissel, Cramer, Trainor, Lewellen, Stowell, Yagel, Page, Von Linting, Ebisawa, Aniol, Dyer, Hoffman, Rohrbaugh, Lapthorne, Jones, Snover, Adelberger

Row 2

Bhang, Green, Rodenberg, Ingalls, Linder, Dickens, Dickey, Schmidt, Orth, Fauska, MacLellen, Van Wechel, Johnson, Puigh, Saling, Chamberlin, Roth, Lynch, Willman, Seymour, Hart, Weaver, Maxson, Swanson, Sielemann, Blair, Eenmaa, Anderson, Weitkamp, Chan, Eqbal